First attempt toward a quasi-Pandemonium free β-delayed spectroscopy of Ge using PARIS at ALTO

Ren Li

université
PARIS-SACLAY

First attempt toward a quasi-Pandemonium free β-delayed spectroscopy of ^{80}Ge using PARIS at ALTO

Première tentative vers une spectroscopie β-retardée de ^{80}Ge quasi-libre de l'effet de Pandémonium avec PARIS à ALTO

Thèse de doctorat de l'université Paris-Saclay

École doctorale n°576, Particules, hadrons, énergie et noyau : instrumentation, imagerie, cosmos et simulation (PHENIICS)
Spécialité de doctorat : Structure et réactions nucléaires
Graduate School : Physique, Référent : Faculté des sciences d'Orsay

Thèse préparée dans l'unité de recherche **IJCLab** (Université Paris-Saclay, CNRS), sous la direction de **David VERNEY**, Directeur de recherche, et le co-encadrement de **François DIDIERJEAN**, Ingénieur de recherche

Thèse soutenue à Paris-Saclay, le 29 Avril 2022, par

Ren LI

Composition du jury

Fadi IBRAHIM Directeur de recherche, CNRS, IJCLab, Orsay	Président
Berta RUBIO BARROSO Professeure des universités, Universidad de Valencia	Rapporteure & Examinatrice
Olivier STEZOWSKI Directeur de recherche, CNRS, IP2I, Lyon	Rapporteur & Examinateur
Muhsin N. HARAKEH Professeur des universités, University of Groningen	Examinateur
David VERNEY Directeur de recherche, CNRS, IJCLab, Orsay	Directeur de thèse

THESE DE DOCTORAT
NNT: 2022UPASP042

université PARIS-SACLAY

ÉCOLE DOCTORALE
Particules, hadrons, énergie et noyau : instrumentation, imagerie, cosmos et simulation (PHENIICS)

Titre: Première tentative vers une spectroscopie β-retardée de ^{80}Ge quasi-libre de l'effet de Pandémonium avec PARIS à ALTO

Mots clés: physique nucléaire expérimentale, décroissance β, distribution Gamow Teller, ISOL, spectroscopie γ, Résonance Dipolaire Pygmy

Résumé: La désintégration β, processus précisément décrit au niveau le plus élémentaire (quarks), devient une sonde riche et complexe lorsqu'elle est impliquée dans le milieu multi-nucléons en forte interaction qu'est le noyau atomique. Dans ce système corrélé, la transformation d'un neutron en proton (ou inversement) décrite par les opérateurs de Fermi et Gamow-Teller donne lieu à des états collectifs impliquant de manière cohérente une grande partie des nucléons sous la forme d'une résonance géante. Proches de la stabilité, pour les noyaux riches en neutrons, ces résonances géantes se situent bien au-dessus de la fenêtre d'énergie accessible dans la désintégration β (Q_β), et cette désintégration doit passer par les composantes de queue de ces résonances en compétition avec les premières transitions interdites. Cependant, l'avènement d'une nouvelle génération d'installations de faisceaux d'ions radioactifs permettant des études de désintégration β de noyaux avec des fenêtres Q_β toujours plus grandes, au-delà de 10 MeV, change désormais cette perspective. Par exemple, la désintégration β de noyaux exotiques peut fournir une méthode nouvelle et unique pour étudier le mouvement collectif plus sensible à la peau des neutrons, la résonance dipolaire pygmée (PDR) et également une opportunité pour une compréhension plus approfondie des phénomènes exotiques impliqués dans la désintégration β nucléaire à travers mesure précise de la distribution de force de transition Gamow-Teller, B(GT).
L'objectif de cette thèse est d'améliorer la compréhension de la structure dans la région du seuil neutron (S_n) des noyaux exotiques etl'influence de cette structure sur la force Gamow-Teller B(GT) en étudiant une source mixte $^{80g+m}$Ga collectée sur la station de désintégration BEDO de l'installation de type Isotope Separation On Line (ISOL) ALTO à Orsay. Les états émetteurs β ^{80g}Ga et ^{80m}Ga ayant pour couple spin-parité 6^- et 3^- respectivement, cette source a l'avantage de pouvoir peupler une plage de spins inhabituellement étendue dans les états excités du noyau fils ^{80}Ge. L'objectif de ce travail couvre donc trois aspects : étudier le PDR dans le ^{80}Ge, démêler les schémas de niveaux de décroissance alimentés par les deux états émetteurs β du ^{80}Ga et parvenir à une détermination précise du B(GT) associé dans toute la fenêtre Q_β. Pour atteindre cet objectif, un spectromètre gamma hybride composé de phoswiches PARIS NaI/$LaBr_3$ associés à des détecteurs Ge haute résolution a été utilisé.
Une analyse détaillée est présentée dans ce manuscrit, les résultats suggèrent une manifestation de la PDR dans ^{80}Ge. Des schémas de niveaux de décroissance séparés et des distributions B(GT) de $^{80g+m}$Ga sont proposés pour la première fois. De plus, par comparaison avec des calculs de type quasiparticle random phase appproximation (QRPA) avec blocage, le mécanisme microscopique de la PDR dans ^{80}Ge est discuté.

université PARIS-SACLAY

ÉCOLE DOCTORALE
Particules, hadrons, énergie et noyau : instrumentation, imagerie, cosmos et simulation (PHENIICS)

Title: First attempt toward a quasi-Pandemonium free β-delayed spectroscopy of ^{80}Ge using PARIS at ALTO

Keywords: experimental nuclear physics, β-decay, Gamow Teller strength, ISOL, γ spectroscopy, Pygmy Dipole Resonance

Abstract: The β-decay, a precisely described process at the most elementary (quark) level, becomes a rich and complex probe when involved in the strongly interacting multi-nucleon medium which is the atomic nucleus. In this correlated system the transformation of a neutron into a proton (or vice versa) described by the Fermi and Gamow-Teller operators gives rise to collective states involving coherently a large fraction of the nucleons under the form of a giant resonance. Close to stability, for neutron-rich nuclei, these giant resonances lie far above the energy window accessible in the β-decay (Q_β), and this decay must proceed through tail components of these resonances in competition with first-forbidden transitions. However, the advent of a new generation of Radioactive Ion Beam facilities making possible β-decay studies of nuclei with ever larger Q_β windows, beyond 10 MeV, now changes this perspective. For instance β-decay of exotic nuclei can provide a new and unique method to investigate the more neutron-skin-sensitive collective motion Pygmy Dipole Resonance (PDR) and also an opportunity for a deeper understanding of exotic phenomena involved in nuclear β-decay through precise measurement of the Gamow-Teller transition strength distribution, B(GT).

The objective of this thesis is to improve the understanding of the structure in the neutron threshold (S_n) region of exotic nuclei and the influence of this structure on the B(GT) by studying a mixed $^{80g+m}$Ga source collected at the BEDO decay station of the ALTO Isotope Separation On Line facility in Orsay. The ^{80g}Ga and ^{80m}Ga β-decaying states having spin-parity 6^- and 3^- respectively, this source has the advantage that it can populate an unusually large spin-range of daughter states in the nucleus ^{80}Ge. The goal of this work therefore covers three aspects: investigate the PDR in ^{80}Ge, disentangle the decay level schemes fed by the two β-decaying states of ^{80}Ga and achieve a precise determination of the associated B(GT) in the whole Q_β window. To achieve this goal, a hybrid gamma spectrometer composed of PARIS NaI/$LaBr_3$ phoswiches associated to high resolution Ge detectors was used.

A detailed analysis is presented in this manuscript, the results suggest a manifestation of PDR in ^{80}Ge. Separated decay level schemes and B(GT) distributions of $^{80g+m}$Ga are proposed for the first time. In addition, through comparison with state-of-the-art nucleons-blocked quasiparticle random-phase approximation (QRPA) calculations, the microscopic mechanism of PDR in ^{80}Ge is discussed.

Acknowledgements

With the interest of further understanding of the strucutre and fundamental interaction in subatomic nuclei and motivation of discovering some new physical phenomenons, the decision of starting a Ph.D study in nuclear physics was made at the end of 2017 in Lanzhou, which was followed by an exciting message, an opportunity to perform my Ph.D study in Paris-Saclay, France.

After trudging valley of first year and along with the occurrence of global pandemic COVID-19 in the left two-and-a-half years, when time has come to being awarded with title of "doctorat de l'université Paris Saclay", in addition to my own efforts, I would like to express my sincere acknowledgements to the people who contributed to this thesis.

Firstly, I want to thank my juries, Dr. Fadi Ibrahim, Prof. Berta Rubio Barroso, Dr. Olivier Stezowski, Prof. Muhsin N. Harakeh, Dr. David Verney and Dr. Francois Didierjean for their contributions to my thesis with reviewing my manuscript, writing reports, attending my defense and proposing scientific questions and comments. Particularly, I thank Prof. Muhsin N. Harakeh for his very detailed check of my spelling and grammar mistakes for whole dissertation.

I would like to present my special appreciation to my supervisor, David Verney, who guided the direction of this thesis. I thank him for his organization of experiment and discussions throughout data analysis. Usually, meeting was organized by David every one or two weeks and lasted for around one hour each time. It was not only a supervision of the progress of my thesis but also an important occasion to trigger new inspirations which are critical for mining the experimental data. Notably, discussions were kept as usual during COVID-19 quarantine in 2020 and 2021. For this manuscript, David performed a very detailed revision for the two most important chapters, "experimental data analysis" and "experimental results for $^{80g+m}$Ga β-decay study", one sentence by one sentence. The related pages were dyed with blue-line (sentence reconstruction) and yellow-zone (comments) almost fully and few sentences survived. He accuralized and optimized my statements but did not change my contents. Especially, I am grateful to David for large degree of freedom (free atmosphere of research) he provided, which allowed me to explore whatever I was interested in the data even though somethimes it was a waste of time. In addition, I thank my co-supervisor, Francois Didierjean, for his efforts in experiment and participation in discussions sometimes during COVID-19 quarantine.

I address my gratitude to Dr. Isabelle Deloncle for her very detailed correction for the chapters of "introduction and motivation" and "discussion", which constituted the complementary for David's revision. In particular, the statements become more rigorous after many hyperbolic words being deleted under her serious comments: "do not write very pompous sentences" and "at the inverse also, do not use, I think, super: super interesting, super good...very is largely sufficient". Furthermore, she, to-

gether with Dr. Sophie Peru Desenfants, performed theoretical calculation to reproduce experimental results of this thesis using HFB+QRPA* method.

The significant contributions of Dr. Clément Delafosse, post-doctoral researcher, to my thesis development have to be acknowledged. Clément played the role of initial reader of this manuscript who provided many advices for some improvements. His funny but full of wisdom comments made my modification process far away from boredom, e.g., "detector does not have mission. it is our mission!", "meV is too small." et al.. Moreover, Clément brought me humorous encouragement sometimes when I was highly stressed and anxious like "calm down Ren. every Ph.D is unique!".

I thank Dr. Carole Gaulard, the leader of our team FIIRST, who offered precious advices for my defense slides to make it more logical and understandable.

I have to say their rigorous correction not only improved the quality of my thesis but also presented an example of how to help a newcomer. I will cherish these correction documents in the future as a critical memory of my Ph.D training.

For the organizations including the people involved, I thank great "Laboratoire de Physique des 2 Infinis Irène Joliot-Curie (IJCLab)" and Université Paris-Saclay for providing me an opportunity to perform my PhD thesis. International colloborations of ALTO-ISOL and PARIS are acknowledged for their work in radioactive beam $^{80g+m}$Ga and detectors including Fadi Ibrahim, David Verney, Abdelhakim Saïd, Clément Delafosse, Matthieu Lebois, François Le Blanc, Francois Didierjean, Brigitte Roussiere, Julien Guillot, Maher Cheikh Mhamed, Isabelle Deloncle, Carole Gaulard, Guillem Tocabens, Céline Gaubert-Rosier, Adam Maj, Michal Ciemala and Kasia Hadynska-Klek et al..

For funding resource, I gratefully acknowledge the support from China Scholarship Council under Grant No.201804910509. Simultaneously, I thank Dr. Xiaohong Zhou, my Chinese supervisor, and Dr. Song Guo, Guangshun Li and Jianguo Wang, my Chinese colleagues, for their guidance in the scholarship application.

In the end, I prefer to thank my parents, Huaiqiang Li and Yanhua Wang, for their unconditional support for my PhD study while they never know what is a nucleus. I appreciate my wife, also my friend, Mrs. Ruirui Dong, for her warm accompanying and love.

Ren Li
Université Paris-Saclay
May 2022

Contents

1 Introduction and motivation

Sommaire

The atomic nucleus was discovered in 1911 by Ernest Rutherford in the Geiger–Marsden gold foil experiment in 1909 - The Scattering of α and β Particles by Matter and the Structure of the Atom [1]. As a self-organized many-body finite system, it exhibits both microscopic single-particle and macroscopic collective-mode of excitations. These two views constitute two facets of a single object that can be reconciled through microscopic theories thanks to the recent theory developments [2, 3, 4]. Single-particle degrees of freedom are manifested by shell structure [5, 6] providing an interpretation of the observation of magic numbers while collective degrees of freedom are in general associated to vibration and/or rotation of various nuclear shapes [7, 8, 9, 10, 11] providing the interpretation of the observation of rotational band spectroscopy.

The purpose of this chapter is to provide a general review of β-decay theory and the existing challenges in the understanding of nuclear β-decay process. The structure of β strength function and its implication for nuclear study are also introduced. Furthermore, the structural evolution along N = 50 isotonic chains toward the hard-to-reach double magic nucleus ^{78}Ni is introduced. In this introduction, we introduce the concepts behind the nuclear shell model, collective model and the nuclear force. Experimental results achieved during the last few decades in these exotic regions will be also presented. The existing debate concerning the collectivity evolution in the neutron-rich Ge isotopes toward N=50 will also be introduced in this chapter. This discovery may provide a candidate solution to the open question of the neutron-skin thickness of ^{208}Pb.

Recent experimental results on unusually strong γ/neutron competition following β-decay in the neutron-rich Ge nuclei were interpreted as a possible manifestation of Pygmy Dipole Resonance (PDR) effects. The possibility of using beta decay as an additional (complementary) probe for studying high-lying collective states in exotic nuclei will be introduced here.

Finally, three new experimental landscapes of β-decay study are introduced: trap-assisted decay spectroscopy, TAGS and PARIS.

1 Nuclear structure and β-decay

1.1 Nuclear β-decay and its complexity

Nuclear β-decay

Even though, in principle, the mechanism of β decay at the nucleon (respectively quark) level is currently understood, considerable efforts are still needed in order to achieve a quantitatively satisfactory description of the β-decay processes of an atomic nucleus, a complex many-particle system wherein residual interactions of various types may lead to a more complex β-decay process than free neutron. This has a strong infludence on the distribution of the β strength as a function of the excitation energy in the daughter nucleus, B(GT), and consequently on the β decay properties. This complexicity includes β-decay operator part: two-body current and tensor current and complex final state wave function part of the daughter nucleus: collective excitations, nucleon multi-correlation, Δ excitation and Direct sea excitation. B(GT) distribution determines not only the half-life, the rates of β-delayed neutron emission and fission, but also the shape of the emitted electron and neutrino spectra. Furthermore, B(GT) measurements are important to numerous applications in nuclear physics, astrophysics

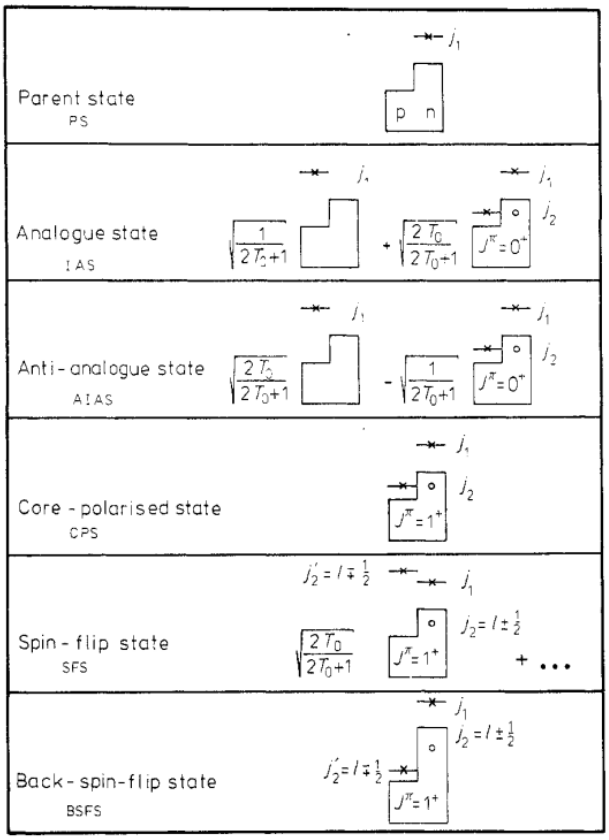

Figure 1.1 – The configurations which exhaust the β strength in Gamow-Teller β^- decay: anti-analogue states, spin-flip states, back-spin-flip states and core-polarised states. These states also exhaust the M1 γ strength in the γ decay of the isobaric analogue state (IAS) that is populated by supperallowed Fermi β transition [12].

and nuclear engineering.

In nuclear β decay, from Fermi theory, a neutron-hole proton or a proton-hole neutron excitation is created. The single nucleon concentrates the main part of the β transition strength for the different multipolarities to small regions of transition energy, i.e. giant resonances (GR) that will deprive the β decays to levels outside the resonance of their single-particle strength. It is important to note that due to the Pauli principle the pn^{-1} and np^{-1} states with ground-state isospin T > 0 have different properties when compared with the $p^{-1}p$ and $n^{-1}n$ states as E1 or M1 giant resonances.

The Standard Model SU(3) $\times$ SU(2) $\times$ U(1) composed of three fermion families with left-handed components of quarks $q_{Li} = (u_L, d_L)_i$ and leptons $\ell_{Li} = (\nu_L, e_L)_i$ (i = 1, 2, 3) forming doublets and the right-handed components u_{Ri}, d_{Ri}, e_{Ri} singlets of isotopic symmetry SU(2) of weak interactions. The charged current weak interactions in QCD are described by coupling

$$\frac{g}{2\sqrt{2}} W_\mu^+ \overline{(u\ c\ t)} \gamma^\mu (1-\gamma^5) V_{CKM} \begin{pmatrix} d \\ s \\ b \end{pmatrix} + h.c. \tag{1.1}$$

Therein V_{CKM} is the Cabibbo-Kobayashi-Maskawa matrix. In the SM context, V_{CKM} should

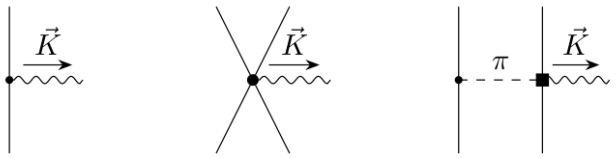

LO, $\sigma\tau$ | Heavy meson exchange c_D | Pion exchange $c_3,\ c_4$

Figure 1.2 – Diagrammatic representations of the axial-vector charge-changing current. $\bar{K}$ is the momentum transferred to the resulting electron and anti-neutrino pair. The solid lines represents nucleons, the dashed lines pions and the wavy line the coupling to the electron and anti-neutrino. The leftmost figure represents the standard (one-body) transition operator ($\sigma\tau$) and the others form the leading two-body current (2BC) [15].

be unitary and any deviation can be a signal of new physics beyond SM. However, recent precise measurements of V_{us} and V_{ud} indicate the violation of the first row, $|V_{ud}|^2 + |V_{us}|^2 + |V_{ub}|^2 < 1$, at the level of around two or three standard deviations and propose the solution: vector-like up quark [13, 14]. These latest developments in SM demonstrate the incomplete understanding of the weak interaction even at the particle level. The β-decay in many-body system nucleus is more complex due to the transformation of a neutron into a proton in nucleus (the vice versa), which happens in a strongly interacting and correlated medium and the system reacts as a whole, which is different from free neutron decay.

Two-body current effect

In order to understand the origin of the quenching factor of nuclear β-decay, an international group performed a first-principle theoretical calculation of some light and medium-heavy nuclei plus ^{100}Sn and declared that they addressed this puzzle [15]: the quenching factor arises, to a large extent, from the coupling of the weak force to two nucleons as well as from strong correlations in the nucleus. There, effective field theory (EFT) was used to describe the coupling of weak interactions to two nucleons via two-body currents (2BC). In the EFT approach, 2BC work as subleading corrections to the one-body standard Gamow-Teller operator $\sigma\tau$. They are smaller but significant corrections to weak transitions like the importance of three-nucleon forces in nuclear interaction. The new β-decay operator was newly defined as formula 1.2 and as shown in the related diagram Figure 1.2[15]. Figure 1.3 shows the results with 2BC. One can easily observe that the new operator reproduces experimental data better than the conventional one-body operator. Recently, this method (2BC) was extended to tensor current and obtained a good result especially in the calculation of neutrinoless double β-decay matrix (physics beyond SM) [16].

$$\hat{O}_{GT} = \hat{O}^{1b}_{\sigma\tau} + \hat{O}^{2b}_{2BC} \tag{1.2}$$

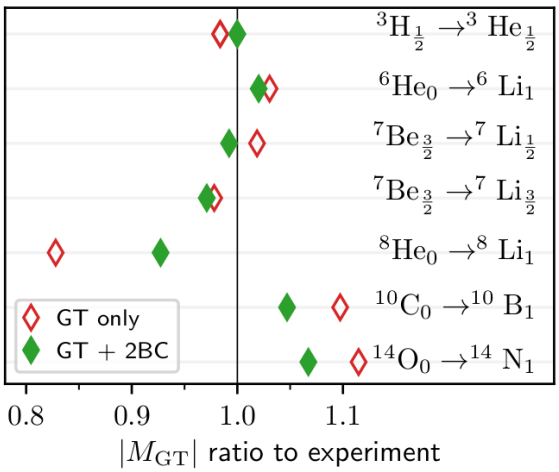

Figure 1.3 – Theory-to-experiment ratio for the Gamow-Teller matrix elements with and without 2BC [15].

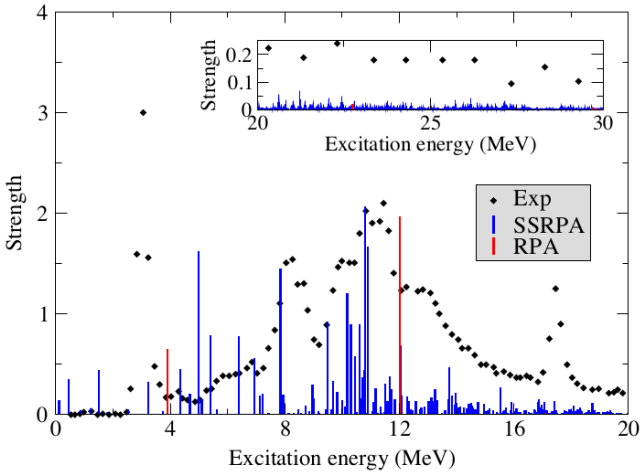

Figure 1.4 – B(GT) distributions for ^{48}Ca of experiment MeV^{-1} (black points), RPA and SSRPA calculations. Notice: to better display the results, the RPA and SSRPA strengths were rescaled as RPA strength was divided by nine and multiply the SSRPA strength by two [17].

Nuclear multi-correlation effect

Very recently, another theorical group developed a self-consistent second random-phase approximation (SSRPA) without quenching factor for charge-exchange processes with Skyrme energy-density functions where two-particle–two-hole (2p2h) configurations were included [17]. The theory was tested through calculating Gamow-Teller strength of the doubly-magic nucleus ^{48}Ca and ^{78}Ni. The amount of B(GT) below 20 or 30 MeV is considerably smaller than with other energy-density-functional calculations and keeps better agreement with experimental results as presented in Figure 1.4. Especially, it reproduces experimental results much better than does the traditional RPA. In addition, the density of B(GT) distribution progressively increases with excitation energy leading to a long high-energy tail in the spectrum. The authors attributed these successes primarily to their many-body method, the key ingredient of which is the inclusion of 2p2h configurations.

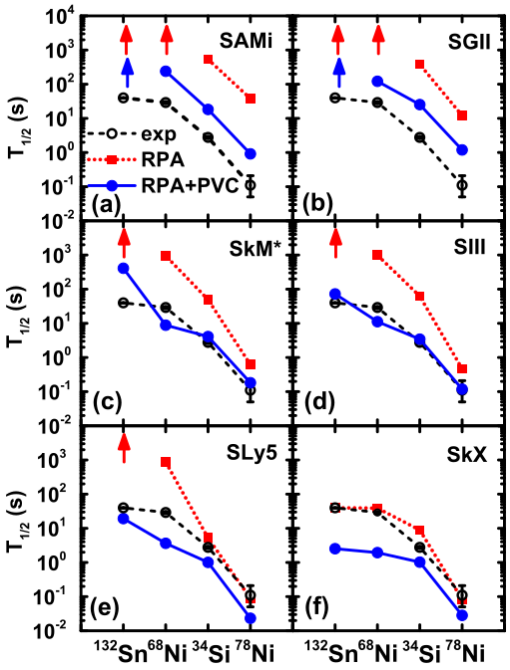

Figure 1.5 – $T_{1/2}$ of ^{132}Sn, ^{68}Ni, ^{34}Si and ^{78}Ni calculated by RPA and RPA + PVC approaches in comparison with experimental values [18].

Nuclear collective effect

One group reproduced the nuclear β-decay data of magic nuclei like ^{78}Ni and ^{132}Sn including B(GT) and $T_{1/2}$ with taking into account the coupling between particles and collective vibrations on top of self-consistent RPA based on Skyrme density functionals (RPA+PVC) [18]. The calculated $T_{1/2}$ are reduced along with the increasing of the phase space available for the decay. Consequently, in case of ^{34}Si and ^{78}Ni, good agreement between theoretical and experimental hal-lives have been achieved especially in the case of the Skyrme force SkM as shown in Figure 1.5 [18].

Therefore, this "particle-vibration coupling effect" was expected to play important role in other weak interaction processes.

1.2 Structure in the β strength function and consequence for nuclear physics

As shown in Figure **??**, for a μ_τ = -1 transition, there are four different particle-hole configurations: core-polarised states (CPS), spin-flip states (SFS), anti-analogue states (AIAS) and back-spin-flip states (BSFS). The configurations of these states for a neutron-rich parent nucleus are given in Figure 1.6. Therein, BSFS is only accessible for nuclei with a large neutron excess and it will be the lowest states that can be reached by allowed β-decay. The SFS is usually referred to as the Gamow-Teller giant resonance. In the following, the distributions of the allowed β strength of these states is introduced. Based on the assumption of a supermultiplet symmetry, the Gamow-Teller strength would concentrate in the SFS and this state will be degenerate in energy with the IAS. However, the supermultiplet symmetry is broken by the spin dependence of nuclear forces which results in a transfer of some Gamow-Teller strength going to the lower-lying pygmy resonances. But, note that 90% or more of

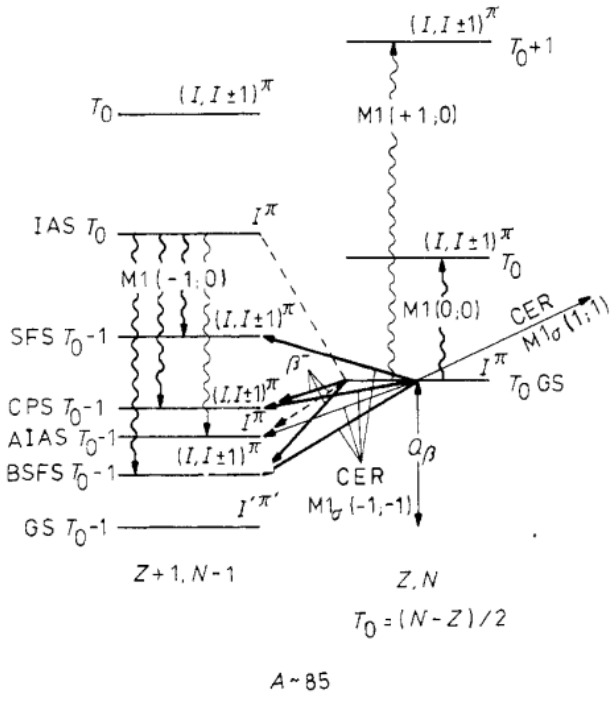

Figure 1.6 – Scheme of Gamow-Teller and M1 strength distribution in neutron-rich nuclei [19].

the total Gamow-teller strength still concentrates in the SFS (GTGR) and the rest is in the CPS and BSFS. The AIAS exhausts some β strength only for nuclei with N $\approx$ Z.

The collectivity of these states and their Gamow-Teller strength increases along with increasing neutron excess. The SFS is energetically not accessible in β^- decay. However, other lower-lying collective states (BSFS and CPS) are accessible in β^- decay for very neutron-rich nuclei and consequently generate the pygmy resonances.

Energy estimates of these structured states are:

Fermi transition

According to the selection rule ΔT = 0, ΔI = 0, the only state that can be reached by "superallowed" Fermi transition is the Isobaric Analogue State (IAS). However, the IAS is beyond the Q_β window in nuclei with N > Z. Only for β^+ decay in N < Z nuclei can the IAS be reached energetically.

Gamow-Teller transition

Gamow-Teller transitions are a mode of β decay in which the β and neutrino spins are coupled with total spin 1 (triplet states). It dominates the decay in medium-mass neutron-rich nuclei. It can be described by classical fermi current-current interaction theory, phenomenological effective field theory based on the hypothesis of the interaction of 4 pointlike fermions and modern fundamental standard model. However, after more than half century development, grand challenges still exist for these two theories to reproduce the experimental nuclear B(GT) distributions accurately.

In practice, the ft values and Gamow-Teler strength can be calculated from four-fermion points

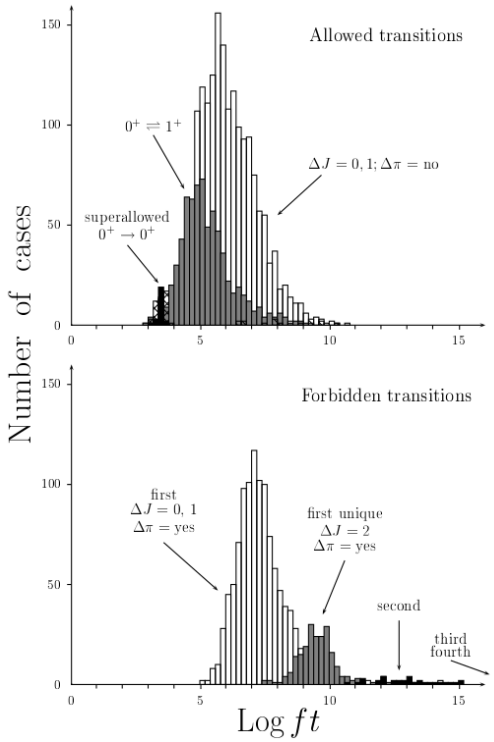

Figure 1.7 – A summary of logft values from [21].

interaction theory as formulas 1.3 (the first three) and can be defined again with correction terms like last formula in 1.3 [20]:

$$\begin{cases} B^-_{GT} = \frac{g_A^2}{2J_i+1} | < \phi_f || \sum_j \bar{\sigma}(j)\tau^-(j) || \phi_i > |^2 \\ \frac{dW}{dt} = \frac{G_\beta^2 m_e^5}{2\pi^3} f(B^-_F + B^-_{GT}) \\ ft = \frac{K}{g_V^2 B(F) + g_A^2 B(GT)} \\ Ft \equiv ft(1+\delta'_R)(1+\delta_{NS}-\delta_C) = \frac{K}{2G_V^2(1+\Delta_R^V)} \end{cases} \tag{1.3}$$

Therein $K/(\hbar c)^6 = 2\pi^3\hbar \ln 2/(m_e c^2)^5 = 8120.27648(26) \times 10^{-10}$ GeV^{-4}s, δ'_R and δ_{NS} comprise the transition-dependent part of the radiative correction as δ'_R is a function of electron's energy and Z of the daughter nucleus and δ_{NS} depends on the detailed nuclear structure; δ_C is the isospin sysmmetry breaking correction; Δ_R^V is the transition-independent radiative correction and G_v is the vector coupling constant for the semileptonic weak interaction.

Figure 1.7 is a summary of logft values from about 3900 β transitions [21].

The mystery of β-decay of nuclei, to a large extent, hides behind the quenching factor, q $\approx$ 0.75 used to reproduce the B(GT) values in nuclei, which mechanism is explained variously from two-body currents in weak interaction, Δh excitation, Dirac sea states excitation to nucleon multicorrelations in a finite many-body nuclear quantum system, shell effect, nuclear collective motion, nuclear tensor force and so on. All of thses explanations seem to work to a certain extent. Anyhow, quenching factor still keep elusive nowadays even though some resolutions were proposed like B(GT) is carried away by the ΔN^{-1} excitation in the quark model [22]. In the next contents of this subsection, three cases with

latest developments are introduced, which are important to help to understand the β-decay process in nucleus.

Furthermore, for disentangling these mechanisms and test related theories, the precisely measured B(GT) information plays the vital role surely as a experimental touchstone. However, only a fraction of the total Gamow-Teller strength within the decay energy window can be observed. Toward more neutron-rich nuclei, this window becomes larger. Nervertheless, it is still experimentally challenging to detect Gamow-Teller strength accuratly due to Pandemonium effect. This effect is more detailed in a next section.

Application in nuclear structure

Nuclear β-decay provides a unique opportunity to investigate the nuclear structure in particular those hard-to-reach nuclei located far from stability. Particularly, if precusor presents an isomeric state, a mass of states with rich spin information will be available. For example, ^{80}Ga has two isomers with similar half-lives, 1.57(1) s and 1.91(3) s, but quite different spins 3^- and 6^-. Therefore, the excited states with spin 1-8 are available for the daughter nucleus ^{80}Ge through the β-decay study of $^{80g+m}$Ga. In addition, the extracted logft value from β-decay can be used to assign the spin-parity of the excited states of daughter nucleus through super-allowed $\sim$3, allowed (3-6), first forbidden (6-9) and second forbidden (11-13) β-transition identification [19]. These assignments are very difficult for the nucleus far from stability using traditional method as the low production prevents the angular distribution and angular correlation measurement of excited states, which are essential to assign the spin-parity information.

Furthermore, as introduced above, even though the mechanism of β-decay at particle level is understood somehow, considerable effort is still needed to describe the β-decay processes of atomic nuclei. It is because the nucleus is a complex many-body system where various residual interactions may lead to collective excitations. This characteristic provides a precious chance to study the collective motion of a daughter nucleus like γ-vibration and PDR.

Application in nuclear reactor security: decay-heat calculation

The precise calculation of the decay heat emitted by thermal neutron-irradiated nuclear fuel is an important factor to ensure security of reactor design and operation, removal of spent fuel from the core, the subsequent storage prior to and after reprocessing and nuclear waste disposal. Decay heat can be calculated from the nuclear decay properties of the related fission products and their decay products generated within the irradiated fuel. However, much information came from experimental measurements obtained with HPGe detectors in which populations of high-energy states through β-feeding were underestimated due to the low detection efficiency for γ-rays at high energy. It was caused by the so-called pandemonium effect as introduced above and as shown in the Figure 1.8.

Decay-heating are contributed by three components: heavy particles (H_{HP} like p, α, neutron, fragments), light particles (H_{LP} like electron) and photons (H_{EM} like X γ-rays). So, the energy of

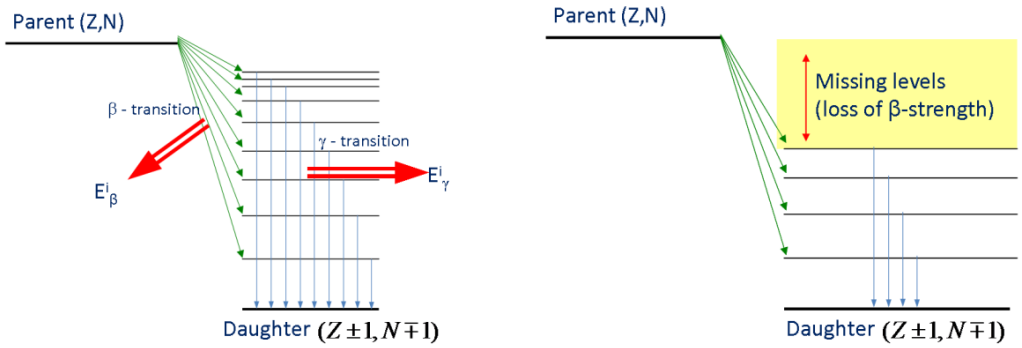

(a) Real feeding levels (b) Detected feeding levels

Figure 1.8 – Schematic representation of the pandemonium effect in beta decay.

decay-heating can be achieved by summing them.

$$\begin{cases} H_{HP}(t) = \sum_{i=1}^{M} \lambda_i^T N_i(t) \bar{E}_{HP}^i \\ H_{LP}(t) = \sum_{i=1}^{M} \lambda_i^T N_i(t) \bar{E}_{LP}^i \\ H_{EM}(t) = \sum_{i=1}^{M} \lambda_i^T N_i(t) \bar{E}_{EM}^i \end{cases} \tag{1.4}$$

Where $\bar{E}$, λ_i^T and N are the mean energy released per disintegration, total decay constant and the number of the individual nuclides.

Commercial nuclear reactors generate roughly 1040 different nuclei and a large fraction are unstable. Therefore, the energy released in their decays produces heat known as decay-heat, estimated to be approximately 8% of the total heat produced in the reactor [23]. Hence, this contribution must be taken into account in the energy production. Therefore, in conclusion, re-precision measurement with new setups, which can overcome Pandemonium effect like TAS, and re-evaluation of this important energy are critically needed.

1.3 Nuclear structure in the vicinity of ^{78}Ni

Nuclear shell model

Actually, in the early days of nuclear physics, the shell structure of the atoms was known, but the experiments did not allow to shed light on the shell structure of nuclei. Some other descriptions seemed more natural like the analogy with a charged liquid drop. However, along with the accumulation of the experimental evidence, e.g. the extra binding related to some precise values of the number of neutrons and protons (magic numbers) and the systematical measurements of spins and parities, the existence of shell structure in a nucleus was noticed in 1930s. Then a decades of explaining the regularities of the nuclei associated with magic numbers began. Otto Haxel, J. Hans D. Jensen, Hans E. Suess [24] and Maria Goeppert Mayer [5] proposed a model of independent of nucleons, confined by a surface-corrected, isotropic harmonic oscillator well, and critically, hamiltonian which contains a strong spin-orbit coupling term. Eq. 1.5 of this model obtained a success in the end, which generated the naive shell model. The key point of the success is that the spin-orbit coupling leads to the l

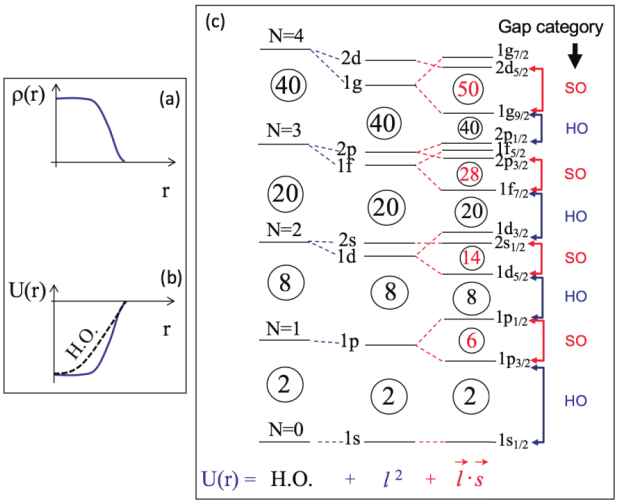

Figure 1.9 – (a) density distribution of nucleons in nuclei; (b) a mean potential (solid line) and an approximation by a Harmonic Oscillator potential (dashed line). (c) The shell structure with magic numbers: see details in [25].

splitting of degenerate j states into j = l ± s and spin-orbit coupling favors the state of higher total angular momentum.

$$U(r) = \frac{1}{2}\hbar\omega r^2 + D\overrightarrow{l^2} + C\overrightarrow{l}\cdot\overrightarrow{s} \tag{1.5}$$

However, for a nucleus with the number of protons and neutrons far from the magic numbers, it becomes indispensable to include in the so-called “residual” interactions terms like tensor force, isospin-dependent nuclear force and so on. At this point, it is difficult to reproduce the experimental data of exotic nuclei with simple mean field (monopole force) only. At this crossroad, some shell model practitioners choose to persist this way - "simple shell model (difficult in practice)". Some other nuclear theoreticians select another path to develop: the modern nuclear force - first principle calculation like lattice QCD based on gauge field theory.

Nuclear collective motion

The early shell model seemed disconnected from the idea of the compound nucleus and the liquid-drop model. With the observation of rotational motion, the reconciliation seemed to become harder. Then a resolution came in which the collective rotors were associated with “intrinsic states” very well described by deformed mean-field determinants and wherein the eigenstates can be extracted by projection to good angular momentum. Along with the nuclear superfluidity, it was added to the nuclear picture [26, 27], allowing the unified model to be born. Later, Nilsson performed the calculations of functions using a harmonic oscillator potential for positive (prolate) and negative (oblate) deformations in his PhD. thesis. Then such "Nilsson diagrams", which were carefully revised on the basis of empirical data, became an essential tool in nuclear physics [28].

The nuclear collective properties can be described through a coordinate α characterizing the spatial distribution of the nucleon density that, in turn, defines the nuclear field. Such coordinates are

symmetric functions for the individual nucleon coordinates.

For a nuclear system with a small compressibility, the collective excitations of lowest energies are associated with changes in shape with an approximate preservation of volume. Assuming such system to have a sharp surface, the normal coordinates of these oscillations would be an expansion parameter $\alpha_{\lambda\mu}$ of the surface as defined by Eq. 1.6

$$R(\theta,\phi) = R_0[1+\sum_{\lambda\mu}\alpha_{\lambda\mu}Y_{\lambda\mu}(\theta,\phi)] \tag{1.6}$$

R_0 is the equilibrium radius and the $Y_{\lambda\mu}$ is the normalized spherical harmonic function of order λ,μ. These surface oscillations are associated with a collective flow having the same velocity field as that of an incompressible classical liquid drop, which leads to the expression 1.7 for the parameters in terms of the polar coordinates (r_p,θ_p,ϕ_p) of individual nucleon.

$$\alpha(\lambda,\mu) = \frac{4\pi}{3A}\sum_{p=1}^{A}(\frac{r_p}{R_0})^{\lambda}Y^*_{\lambda\mu}(\theta_p,\phi_p) \tag{1.7}$$

For quadrupole deformation ellipsoid nuclei, one can get Eq. 1.8,1.9,1.10 and as it is detailed in [26, 27].

$$R(\theta,\phi) = R(\pi-\theta,\phi) = R(\theta,-\phi),\ \ \alpha_{21} = \alpha_{2-1} = 0, \alpha_{22} = \alpha_{2-2} \tag{1.8}$$

$$\begin{cases} R(\theta,\phi) & = R_0[1+\alpha_{20}Y_{20}(\theta,\phi)+\alpha_{22}Y_{22}(\theta,\phi)+\alpha_{2-2}Y_{2-2}(\theta,\phi)] \\ \alpha_{20} & = \beta\cos\gamma \\ \alpha_{22} & = \frac{1}{\sqrt{2}}\beta\sin\gamma \end{cases} \tag{1.9}$$

$$\begin{cases} R(x) = R(y) = R_0(1-\frac{1}{2}\sqrt{\frac{5}{4\pi}}\beta) \\ R(z) = R_0(1+\sqrt{\frac{5}{4\pi}}\beta) \\ \delta = \frac{R_z-R_x}{R_0} = \frac{3}{2}\sqrt{\frac{5}{4\pi}}\beta = 0.946\beta \\ Q_0 = \frac{3}{\sqrt{5\pi}}ZR_0^2\beta(1+\sqrt{\frac{5}{65\pi}}\beta) \end{cases} \tag{1.10}$$

In the case of nuclear oscillations, under the assumption that the frequencies ω_p for particle excitation are large compared with the frequencies ω_c of the collective motion, the relationship between the particle and collective motion is especially simple.

For the shape vibration, the system can be described in terms of collective coordinates representing the amplitude. The equations of motion have the same form in the classical theory and the quantal features can be achieved by the canonical procedure of quantization. The basic dynamic variables are the operators associated with the creation and annihilation of quanta. Then the quanta can be regarded as noninteracting entities if the excitations can be superposed without modifying the vibrational mode. In this approximation, the boson operators, Hamiltonian and related energy are defined as in Eq. 1.11. Under the assumption that the quanta involved in the process act independently

[27], the total decay rate is proportional to the number of quanta (n + 1).

$$\begin{cases} C^{+}|n>=(n+1)^{1/2}|n+1> \\ H=\hbar\omega c^{2}+c+E(n=0) \\ E(n)=(n+\frac{1}{2})\hbar\omega \end{cases} \tag{1.11}$$

For the ratational model, with separating the intrinsic and rotational components, the corresponding Hamiltonian and energy (for even-even nuclei) can be writen in the form of Eq. 1.12 wherein g represent the moment of inertial.

$$\begin{cases} H=H_{intr}(q,p)+H_{rot,\alpha}(P_{\omega}) \\ \Phi_{\alpha,I}=\Psi_{\alpha}(q)\phi_{\alpha,I}(\omega) \\ E_{rot}^{core}=\frac{\hbar^{2}}{2g}I(I+1) \end{cases} \tag{1.12}$$

Modern nuclear force

Besides the shell model and collective model, one emerging nuclear theory is so-called "modern theory of nuclear forces" based on quantum chromodynamics (QCD). It benefits from the success of QCD in particle physics especially along with the import of gauge field theory [29]. Because the nucleus is composed of protons and neutrons (except interaction particles) that are formed from quarks and gluons, it is natural to extend the theory describing basic particles (QCD) to the theory describing the matter (hadron and nucleus) made up by them. Eq. 1.13 is the Lagrangian of QCD, more details can be found in [30] where $\mathcal{L}$ represents the Lagrangian, ϕ=$\phi_{\alpha i}$ quark fields and $\phi_{\alpha i}$ is a 4-component Dirac-spinor, γ_{μ} the Dirac matrices, A^{μ} gluon fields, g color charge (strong coupling constant) and $G_{\mu\nu}$ gluon field strength tensor.

$$\mathcal{L}_{QCD}=\bar{\phi}(i\gamma_{\mu}(\partial^{\mu}-iA^{\mu})-m)\phi-\frac{1}{2g^{2}}trG_{\mu\nu}G^{\mu\nu} \tag{1.13}$$

Lattice QCD (LQCD) is a practical tool to calculate hadron properties from the QCD Lagrangian on a discretized Euclidean space-time. Today's computer power is sufficient to allow for full QCD simulations at small quark masses, large enough volumes (2.5 fm), and sufficiently fine lattice spacing ∼0.05 fm so that the results can really be connected to the physical quark masses. For the nuclear force problem, one important development in LQCD is the first attempts to construct a nuclear potential, however, groundbreaking studies. However the present results have not yet got an accuracy to achieve high-precision predictions for nuclear properties due to many problems like wave functions of hadrons in terms of quark fields, neutrino's mass, multi-body currents interaction, methodology to normalize QCD to Schrödinger wave mechanics and tensor force in nucleus.

Before discussing the nuclear forces from QCD, it is necessary to clarify the relation between the chiral Lagrangian for pions together with nucleons and the nuclear Hamiltonian. One method in the framework of chiral EFT, besides the already mentioned time-ordered perturbation theory, is based on S matrix, therein the nuclear potential was defined through matching the amplitude to the Lippmann-Schwinger equation [31]. Another one is based on the unitary transformation where the potential is

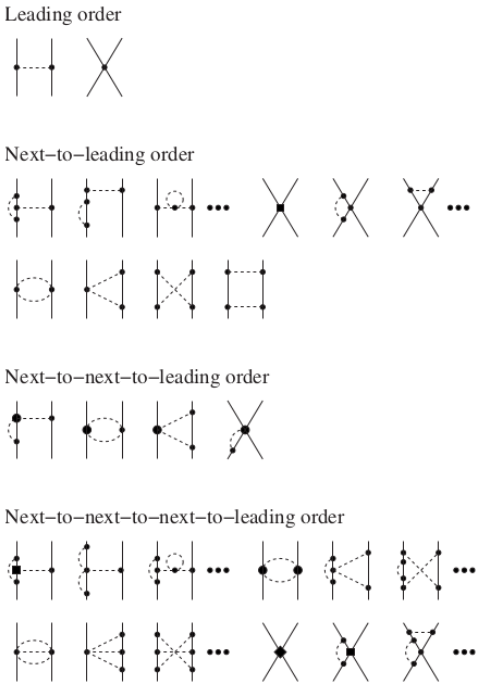

Figure 1.10 – Chiral expansion of the two-nucleon force. Solid dots, filled circles, squares, and diamonds denote vertices with $\Delta_i = 0$, 1, 2, and 3 respectively [33].

achieved by applying an appropriately chosen unitary transformation to the underlying pion-nucleon Hamiltonian [32]. Both methods lead to energy-independent interactions that is a welcome feature enabling applications to three- and more-nucleon systems.

By expanding the effective Lagrangian in powers of the pion fields, one can verify that the only tree diagrams connecting two nucleons are the one-pion exchange as shown in the first line in Fig. 1.10 and yielding the following potential in the two-nucleon center-of-mass system

$$V_{NN}^{(0)} = -\frac{g_A^2}{4F_\pi^2}\frac{\bar{\sigma_1}\cdot\bar{q}\bar{\sigma_2}\cdot\bar{q}}{4F_\pi^2\bar{q}^2+M_\pi^2}\tau_1\cdot\tau_2 + C_S + C_T\bar{\sigma_1}\cdot\bar{\sigma_2} \tag{1.14}$$

Where superscript (0) denotes the chiral order, σ_i and τ_i are the Pauli spin matrices and isospin Pauli matrices, $\bar{q}$=$\bar{p}$-$\bar{p\prime}$ is the nucleon momentum transfer and $\bar{p}(\bar{p\prime})$ are the initial (final) nucleon momentum. F_π=92.4 MeV and g_A = 1.267 refer to the pion decay and the nucleon axial coupling constants, respectively. C_S and C_T are the low-energy constants determining the strength of the leading NN short-range interaction. Higher order interaction $V_{NN}^{(2)}$ and $V_{NN}^{(3)}$ can be found in reference [33].

Reduced electromagnetic transition probabilities

Reduced electromagnetic transition probabilities B(XL) for partial γ-ray transitions and for certain multipolarity are given in the following equations [34].

$$B(XL; I_i \to I_f) = \sum_{\mu, M_f} | < I_f M_f | M_{XL,\mu} | I_i M_i > |^2 \tag{1.15}$$

$$B(XL; I_i \to I_f) = (2I_i + 1)^{-1} | < I_f || M_{XL} || I_i > |^2 \tag{1.16}$$

$$B(XL; I_i \to I_f) = \frac{L[(2L+1)!!]^2 \hbar}{8\pi(L+1)} (\frac{\hbar c}{E_\gamma})^{2L+1} P_\gamma(XL; I_i \to I_f) \tag{1.17}$$

where (2L+1)!! $\equiv 1 \times 3 \times 5 \ ... \ \times (2L+1)$;

$P_\gamma(XL; I_i \to I_f)$ is the partial γ-ray transition probability.

Formula 1.18 presents the relations between the reduced transition probabilities $B(XL; I_i \to I_f)$ and the partial gamma-ray transition probabilities $P_\gamma(XL; I_i \to I_f)$ for different multipole transitions in which the transition energy E_γ is given in MeV [34]. The $B(EL; I_i \to I_f)$ unit is in $e^2(fm)^{2L}$, $B(ML; I_i \to I_f)$ in $(e\hbar/2M_pc)^2(fm)^{2L-2}$ and the decay rate $P_\gamma(XL; I_i \to I_f)$ is in sec^{-1}.

$$\begin{cases} B(E1; I_i \to I_f) = 6.288 \times 10^{-16} E_\gamma^{-3} P_\gamma(E1; I_i \to I_f) \\ B(E2; I_i \to I_f) = 8.161 \times 10^{-10} E_\gamma^{-5} P_\gamma(E2; I_i \to I_f) \\ B(E3; I_i \to I_f) = 1.752 \times 10^{-3} E_\gamma^{-7} P_\gamma(E3; I_i \to I_f) \\ B(M1; I_i \to I_f) = 5.687 \times 10^{-14} E_\gamma^{-3} P_\gamma(M1; I_i \to I_f) \\ B(M2; I_i \to I_f) = 7.381 \times 10^{-8} E_\gamma^{-5} P_\gamma(M2; I_i \to I_f) \\ B(M3; I_i \to I_f) = 1.584 \times 10^{-1} E_\gamma^{-7} P_\gamma(M3; I_i \to I_f) \end{cases} \tag{1.18}$$

Formula 1.19 is the partial γ-ray half-lives according to the Weisskopf estimates for different multipole transitions when the nuclear radius is given in $1.2A^{1/3}$ fm (A = mass number) where E_γ=transition energy is in MeV[34].

$$\begin{cases} T_{1/2\gamma w}(E1) = 6.762 A^{-2/3} E_\gamma^{-3} \times 10^{-15} sec \\ T_{1/2\gamma w}(E2) = 9.523 A^{-4/3} E_\gamma^{-5} \times 10^{-9} sec \\ T_{1/2\gamma w}(E3) = 2.044 A^{-2} E_\gamma^{-7} \times 10^{-2} sec \\ T_{1/2\gamma w}(M1) = 2.202 E_\gamma^{-3} \times 10^{-14} sec \\ T_{1/2\gamma w}(M2) = 3.100 A^{-2/3} E_\gamma^{-5} \times 10^{-8} sec \\ T_{1/2\gamma w}(M3) = 6.655 A^{-4/3} E_\gamma^{-7} \times 10^{-2} sec \end{cases} \tag{1.19}$$

In order to disentangle the different modes of excitation one can, among few other observables, make use of the values of the reduced electromagnetic transition probabilities B(XL). In addition, from the $P_\gamma(XL; I_i \to I_f)$, one can learn that for same multipolarity, the decay rate is inversely proportational to energy of γ-ray. Therefore, due to selection rule of β-decay, lower multiplicity of cascade is prefered, which means that, in principle, one can achieve 100% β transition intensity with a few of γ detector, i.e. low granularity.

Here, the short overview of the nuclear models and theoretical observables needed is stopped. We will use them in the part devoted to the interpretation of my experimental results. In this chapter, I

would like also to outline the experimental evidences and their interpretation what makes this nuclear region ^{78}Ni so interesting.

Evolution of neutron shells near ^{78}Ni

Recent advances in the technique of radioactive ion beams have made the nuclei near double magic ^{78}Ni (Z=28 and N=50) more accessible for experimental studies. It is interesting in terms of nuclear structure. Firstly, some nuclei are the waiting-points in the r-process. Secondly, the experimental results of this region are important to provide information for the nuclear theory development like shell model and extracting the effective interactions.

The binding energy of the "last" neutron in the N = 50, 51 isotones is drawn as a function of proton number in the left part of Fig. 1.11[35] based on the atomic mass table [36]. One can observe a clear evolution of the N=50 shell gap from Z=28 (Ni) to Z= 50 (Sn), which is 3.0(5) MeV for ^{78}Ni and 3.9(4) MeV for ^{100}Sn [35]. In addition, one can easily observe an inflexion point at Z=40 in the binding energy curve as a function of the proton number for the N=49 isotones (ground state $9/2^+$) as compared to the curve for the N=51 isotones (ground state $5/2^+$). It can be related to the evolution of the interaction strength along the filling of the proton $f_{5/2}$, $p_{3/2,1/2}$ orbits for $Z \leq 40$ and $g_{9/2}$ for $Z \geq 40$. It means that the filling of the $\pi g_{9/2}$ shell binds the $\nu g_{9/2}$ orbit less than the $\pi f_{5/2}$ and $\pi p_{3/2,1/2}$ shells are doing. In other words, the matrix element $V^{pn}_{g_{9/2}g_{9/2}}$ is weaker than $V^{pn}_{(f,p)g_{9/2}}$, the latter contains an attractive component from the tensor interaction that may enhance its strength with respect to other monopoles when the former (Z>40) includes a repulsive term arising from the tensor part of the nucleon–nucleon interaction. Another role in the N=50 gap evolution is the proton-neutron interactions between the proton $\pi f_{5/2}$, $\pi p_{3/2,1/2}$ and $\pi g_{9/2}$ orbitals and the neutron $\nu d_{5/2}$ and $\nu g_{7/2}$ orbitals, $V^{pn}_{\pi(f,p,g)\nu d_{5/2}}$ and $V^{pn}_{\pi(f,p,g)\nu g_{7/2}}$. The $7/2^+$ states energies have been extracted from the (d,p) stripping reactions on ^{86}Kr, ^{88}Sr, ^{90}Zr and ^{92}Mo and are reported in Fig. 1.11.

In the right part of Figure 1.11, the monopole part of the interaction V^{pn} can be tentatively derived from the evolution of binding energy as function of the proton number. From the constancy of the slope for $\nu d_{5/2}$ orbit before and after Z = 40, one can derive that the monopoles involving this orbit have values of about 440 keV. For the $\nu g_{9/2}$ and $\nu g_{7/2}$ orbits the monopole matrix elements are $V_{g9/2g9/2}$ with ∼350 keV and $V_{g9/2g7/2}$ with ∼750 keV. The energy difference between the two values (400 keV) could be ascribed to the tensor part of the interaction for these l = 4 orbits.

Evolution of proton shells near ^{78}Ni

Figure 1.12, calculation from [37], shows that the Z = 28 proton gap is eroded gradually in neutron-rich nuclei, which means that the ^{56}Ni core used up to now in shell model (SM) calculations in this region of nuclei is not as appropriate as thought. The calculation is based on two experimental constraints: the sizes of the N = 48 and N = 50 gaps, which correspond to the gaps in ESPE, shown in Figure 1.12, 5.8 MeV in ^{68}Ni (gap between $f_{7/2}$ and $p_{3/2}$ orbits) and 4.6 MeV in ^{78}Ni (between $f_{7/2}$ and $f_{5/2}$ orbits). This reduction behavior clearly reflects the difference in the strength of the $V^{pn}_{\nu g9/2\pi p3/2}$ and $V^{pn}_{\nu g9/2\pi f5/2}$ proton-neutron interactions, which lead to the crossing of the single-particle levels p and f. This obtained shell evolution is crucial for understanding of the observed nuclear structure in the

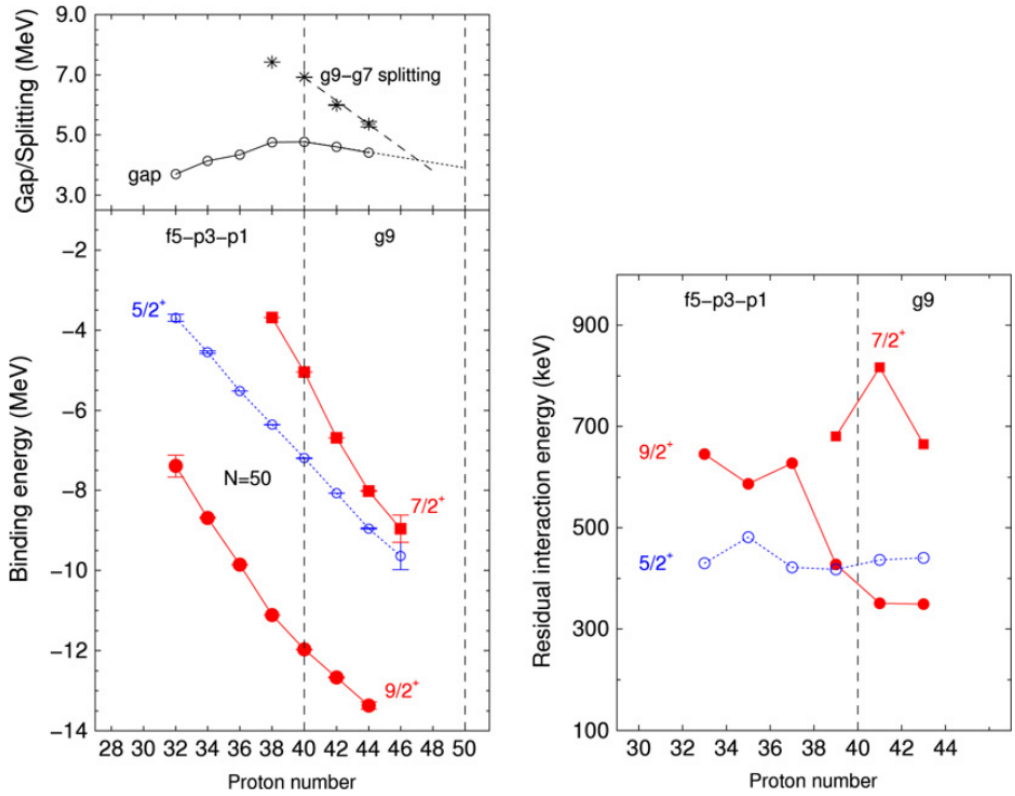

Figure 1.11 – Left-down: evolution of the binding energies of $\nu g_{9/2}$ (ground states of the N = 49 isotones) and $\nu g_{7/2}$ states compared to those of the $5/2^+$ states (ground states of N = 51 isotones). The $7/2^+$ states extracted from the (d,p) stripping reactions on ^{86}Kr, ^{88}Sr, ^{90}Zr and ^{92}Mo. Left-up: energy splitting and the N = 50 gap. Right: Evolution of the proton–neutron residual interactions V^{pn} extracted from the slopes of the binding energy of the neutron states in left part. Figure is taken from [35]

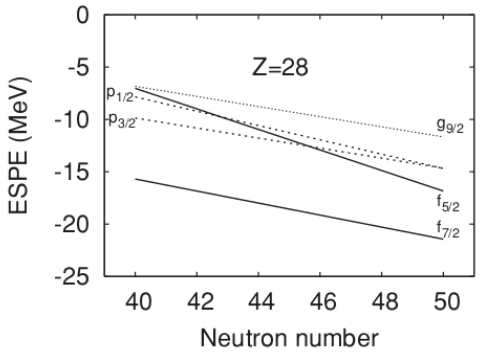

Figure 1.12 – Evolution of proton effective single-particle energies between ^{68}Ni and ^{78}Ni [37].

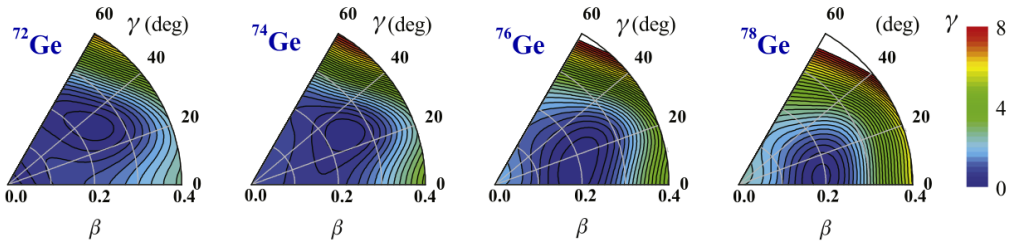

Figure 1.13 – The potential energy surfaces for ^{72,74,76,78}Ge calculated by constrained triaxial covariant density functional theory newly proposed PC-PK1. The energy difference between each contour line is 250 keV [41].

^{78}Ni region.

1.4 Debate on the evolution of collectivity in germanium isotopes

Besides axially symmetric shapes like quadrupole deformation, some nuclei exhibit triaxial deformation and present observables such as γ-band and hot-debated wobbling motion. The triaxial deformation in the closed shell region like doubly-magic ^{78}Ni has a special and critial importance as it can prove the fundemental role of nuclear collective motion and its contributions to the binding energy, particularly, in the neutron-rich region. This mechanism was interpreted as quantum-mechanical self-organization.

Among these nuclei, the even–even Ge isotopes have attracted many endeavors including experimental and theoretical work. In ^{72,74,76,78}Ge it has been experimentally proved the existence of a γ-band indicating the triaxiality [38, 39, 40, 41]. However, no experimental data can help to distinguish between a γ-soft or γ-rigid asymmetry.

Nowadays, a new increasingly intense debate concentrates on the shape evolution of Ge isotopes as the ^{80,82}Ge$_{48,50}$ remain triaxial and γ-soft ($\gamma \sim 30°$) as shown in Figure 1.14 from the previous data from ALTO combining the related "JUN45" and "JJ4B" calculation [42] or opposite like publication [41]: ^{74}Ge from soft to rigid triaxiality (going toward the N=50 closed shell) shown in Figure 1.13? Some signals of gamma vibration have been found in the present work of this thesis through beta-delayed spectroscopy of ^{80}Ge in ALTO data. However, further confirmation measurement is needed.

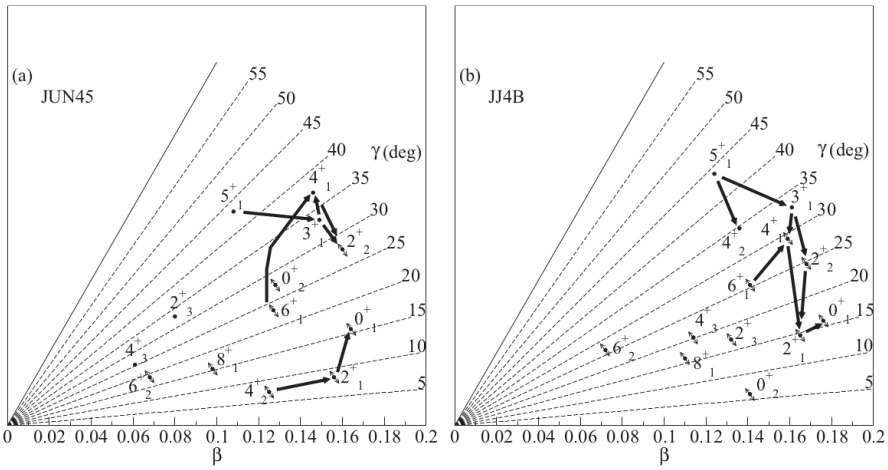

Figure 1.14 – Centroids of the intrinsic deformation parameters β_s and γ_s of ^{80}Ge (subscript s means state). The shell model wave-functions were obtained using the JUN45 and JJ4B residual interaction parameters. States marked with thin double arrows are γ-soft [42].

1.5 A brief overview of the QRPA framework

Hartee-Fock Bogolyubov

The Hartree-Fock solution came rather late in the nuclear theory for solving the many-body nuclear problem. It uses an effective force (in this work it would be D1M) for the interaction between two nucleons, which is adapted to the HF calculation and process. The process for obtaining the HF solution is iterative. Starting from a given single-particle level spectrum (e.g., the density), one evaluates the field created by the A-1 nucleons felt by a nucleon, and enters it in a matrix. The matrix is then diagonalized in order to obtain a new single-particle level spectrum. So, iteration after iteration the system self-consistently determines itself the single-particle level spectrum that minimizes its potential energy for a given deformation. This calculation is performed at different deformations (here restricted to quadrupole, axially symmetric, ones) and the lowest HF energy is considered as the HF solution. The pairing is included in the HFB formalism, making use of the Bogolyubov quasi-particle basis. When using Bogolyubov's pairing treatment it is the same effective force that is used to determine the pairing field, contrary to the BCS treatment which implies to add an interaction, often under a seniority hypothesis.

HFB is then convenient to obtain the single-particle level spectrum (the equivalent of the Nilsson diagram, but self-consistent in HFB) of deformed or spherical nuclei in their ground state.

The HFB process can also be used to obtain the single-particle level spectrum associated with a one- or several- quasi-particle excitations. It allows for example to obtain the excitation energies of N-qp (isomeric) state. In this work we have performed HFB calculations, not only for obtaining the single-particle level spectrum associated with the ground state (0 qp excitation) but also the ones lowering the excitation energy of different 2qp excitations, those 2qp found to be principal building blocks (or 2qp components) of the first $K^\pi=2^+$ QRPA excited state.

Quasi-particle random-phase approximation

Contrary to the HFB framework, the QRPA is dedicated to study dynamical nuclear phenomena: the phonon (or vibrational) excitations. Starting from a single-particle level spectrum obtained in HFB calculations, for each nucleon species, all the 2qp excitations corresponding to a given δ-K enter the QRPA matrix that is diagonalized. After diagonalization one obtains the wave-function and the energy of each eigen-state (i.e. excited state) of the given δ-K and parity π. From the wave-function one can calculate the B(EMλK) of this state to the ground state of QRPA (the 0 phonon states i.e. the HFB wave function). One can also determine the main 2qp contributions of each phonon excitation.

QRPA* calculations: an approximate second QRPA calculation

For this thesis, preliminary calculations have been performed as a kind of "iteration" of the HFB+QRPA process. Having determined the main 2qp contributions to the first $K^\pi=2^+$ QRPA state,we have used HFB calculations, with the blocking technique, for obtaining the single-particle level spectrum associated with each of these major 2qp excitations. Then we have performed a QRPA* calculation for determining the $k=1^+$ phonon excitations that can be built on this "excited" single-particle level spectrum. This is along the same line as the QRPA calculations that were performed for the odd ^{83}Ge in [43]. Here, the result is an approximate second-QRPA calculation, with approximate "2p2h" or "4qp" excitations.

p-n QRPA calculations: a charge-exchange QRPA

In a QRPA calculation, as mentioned above, the 2qp excitations entering the matrix are evaluated for the proton and the neutron single-particle level spectrum separately. In the contrary, for the description of the beta-decay, one considers the proton-neutron 2-qp excitations only and only for $K^\pi=0^+$, $\pm1^+$. Some developments are under way in order to extend the description to other beta-decay modes, still limited to Gamow-Teller transitions.

The results obtained with these codes for the beta-decay of ^{80}Ga$\Rightarrow$ ^{80}Ge and for the phonon excitations in ^{80}Ge will be discussed in Chapter 5.

2 Nuclear pygmy dipole resonance

2.1 Milestones of PDR study

Discovery of PDR

Pygmy Dipole Resonance(PDR) [44], denoted as a new collective excitation on the top of the low-energy tail of the Isovector Giant Dipole Resonance (IVGDR) [45], was defined originally as an enhancement of electric dipole γ-ray transitions (E1) around neutron separation threshold (S_n) region and neutron star born temperature (10 MeV) [46] in the "neutron capture gamma rays" study in 1961 [47] as shown in Figure 1.15. The enhancement of E1 strength was interpreted as due to an oscillation of all proton against all neutrons (IVGDR) or due only to the excess neutrons oscillating against a proton-neutron saturated core (PDR) by three-fluid hydrodynamical model [48]. The interest of PDR

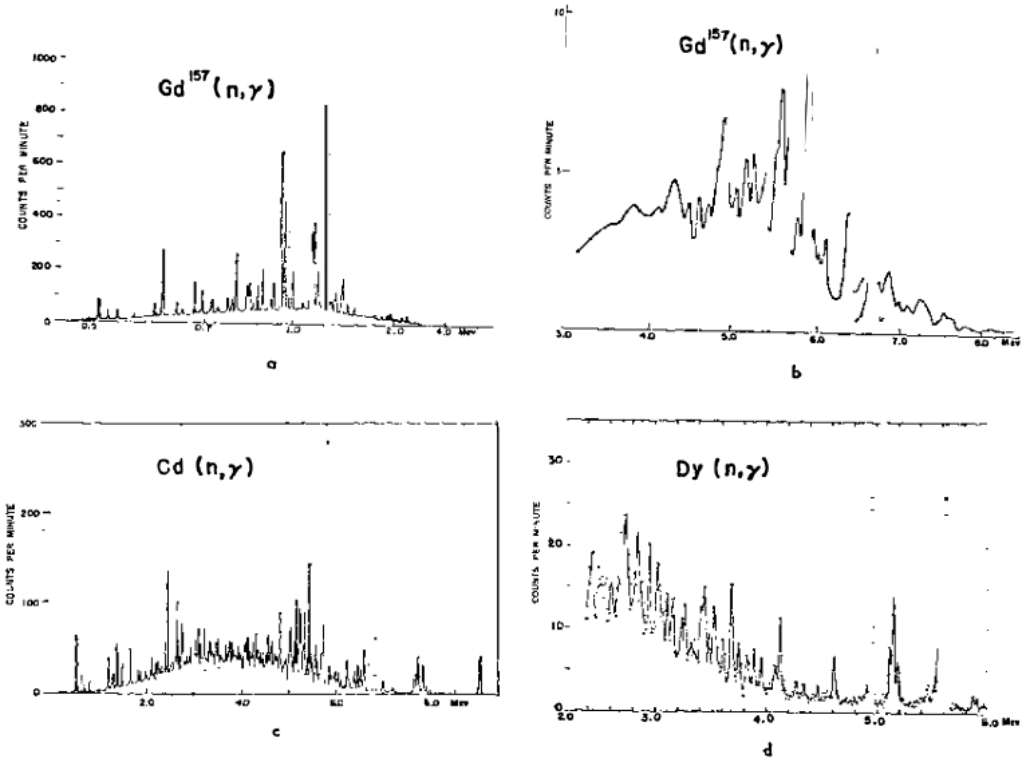

Figure 1.15 – Heavy element capture γ-ray spectra observed with various high resolution spectrometers. (a)Low-energy spectrum from ^{157}Gd (n,γ).(b) High-energy spectrum from ^{157}Gd(n,γ) (c) Spectrum from Cd(n,γ).(d) Spectrum from Dy(n,γ) [47].

study is driven by its correlation to the thickness of neutron skin [49, 50, 51], like showed in Fig. 1.24 ^{208}Pb case, and its influence on the astrophysical r-process [52, 53, 54].

Isospin vector and isospin scalar spliting

However, the underlying structure of PDR still remains elusive and is under intense scrutiny nowadays. The PDR is more dependent on the properties of the underlying nuclear force than IVGDR [44, 56, 55], and the related microscopic model calculations are still a challenging task [57]. Experimentally, one milestone of PDR study is the observation of isospin splitting: E1 distributions difference between the (α, α' γ) and (γ, γ') reactions in nuclei ^{138}Ba [58], ^{140}Ce [59] and ^{124}Sn [60]. The theoretical interpretation [61, 62] is that PDR splits into lower-energy isoscalar, surface mode, and higher-energy isovector components as shown in Fig. 1.17.

New decay pattern

Another milestone is the observation of the new decay mode of PDR, decaying to low-lying states, that can provide complementay information on the wave function of these states. First suggestion of existence of the new decay mode was introduced in a ^{142}Nd PDR study [63]. But the direct evidence in this experiment, i.e. observation of low-lying γ-rays from these excited states, lacked because of the large γ-ray background at the transition energy due to beam interaction with electrons in the

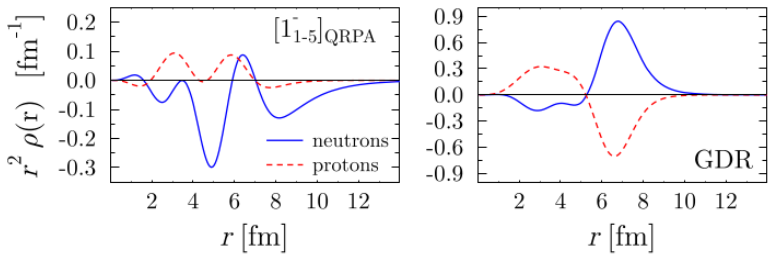

Figure 1.16 – Cumulative transition densities for the first five 1^- QRPA states for ^{208}Pb where all five states are dominantly neutron 1p-1h configuration. For comparison, summed transition densities for the IVGDR are shown [55].

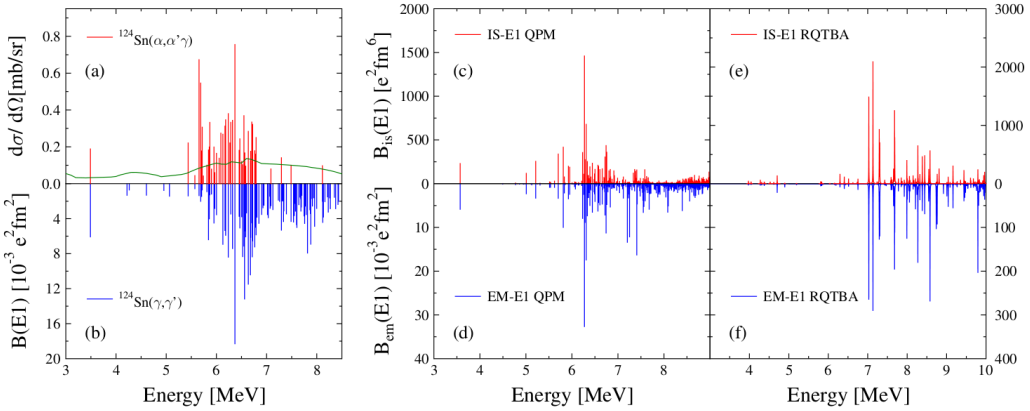

Figure 1.17 – (a)Singles cross section for the excitation of 1^-states in ^{124}Sn obtained in the (α,$\alpha'\gamma$) experiment. The green line is the experimental sensitivity limit; (b) B(E1)↑ measured with the (γ, γ) reaction; (c) The quasiparticle-phonon model (QPM) calculation for the isoscalar operator; (d) QPM calculation for the electromagnetic dipole operator. (e) The relativistic quasiparticle time-blocking approximation (RQTBA) strength functions in ^{124}Sn for the isoscalar operator; (f) The RQTBA strength function for the electromagnetic dipole operator [60].

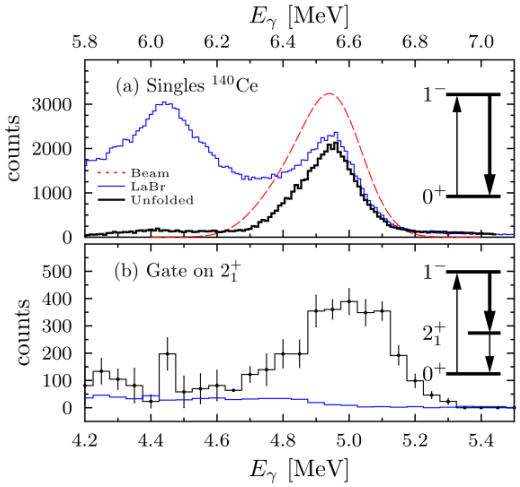

Figure 1.18 – The measured energy spectra from $LaBr_3$ detectors for ^{140}Ce with a beam energy of 6.5 MeV corresponding to the transitions in the simplified level schemes. (a) Spectra from $LaBr_3$ (blue: measured, black: unfolded, red: beam energy distribution). (b) Spectrum in the $LaBr_3$ of γ-rays gated by $2_1^+ \rightarrow 0_1^+$ transition (1.596 MeV) detected by the $LaBr_3$ spectrometers. The blue histogram represents the random coincidence background [66].

target. In recent years, this new decay mode study was researched in three nuclei ^{60}Ni [64], ^{130}Te [65] and ^{140}Ce [66], as shown in Fig. 1.18, using fully linearly polarized quasimonochromatic, Compton-backscattered photons, which revealed that the levels associated with PDR have a regular behavior and that ∼25% of them decay to excited states. Above all, these researches show that the decay of PDR states is not the inverse reaction of its excitation by photons. This discovery extraordinarily challenges the traditional knowledge of PDR structure that was assumed to 100% decay to the ground state due to large 1p1h components. However, PDR decay pattern research is restricted to stable nuclei currently due to the limitations involving secondary beam intensity, excitation cross section and detection efficiency of high energy γ rays. Notice, in addition, that these studies still rest on the investigation of deexcitation behavior of 1^- states.

2.2 β-decay: a new method to study PDR

From experimental metholodogy, the E1 strength distribution varies dramatically depending on the employed experimental technique. One has real-photon scattering with photons from bremsstrahlung or compton backscattering, virtual-photon scattering such as coulomb excitation and hadronic interaction involved with proton or alpha scattering. At present, (p, p′) inelastic scattering at small forward angles seems the most complete approach that allows the extraction of the complete B(E1) below and above the neutron threshold [67]. But, this completeness is still an open question. Particularly, the angular-momentum transfer of the Nuclear resonance fluorescence (NRF) reaction is almost entirely limited to the $1\hbar$ intrinsic angular momentum of the photon due to its massless character. Note that this characteristic actually is a double-edged sword. On one side, NRF allows the energences of J = 1 levels, dipole-excited states, embedded in a sea of levels with other various spins [68]. On the other side, this "advantage" limits the PDR existence border in the spin dimension because direct excitation

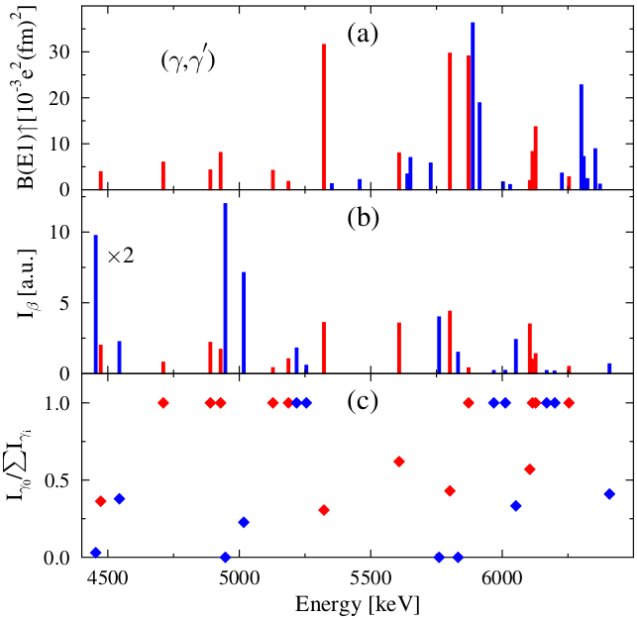

Figure 1.19 – Candidate states of 1^- in ^{136}Xe. (a) B(E1) strength distribution as extracted from (γ,γ') reaction; (b) 1^- population intensity in the ^{136}I β-decay; (c) The ground-state branching ratios of γ-deexcitation in β-decay. Red: states populated in both reactions [68].

of two-phonon states from the ground state by the electromagnetic field is strongly hindered as compared to the excitation of one-phonon states although it is possible only due to the internal fermion structure of phonons [69]. Based on these, for even-even nuclei, 1^- is the default spin-parity for PDR states until now.

Whereas, from the basic definition of PDR or its intrinsic physics picture, excess neutron or saturated core oscillation, the character of PDR is only E1 transition enhancement instead of 1^- states. Hence, a medium-spin PDR could naturally exist that can be built on 2^+ or 4^+ quadrupole collective states. However, such PDR states are hardly available for conventional experimental methods but an opportunity exists for β-decay experiment, thanks for its precursor states-like specificity. Exotic nuclei, since having high Q value, make β-decay a new playground for PDR research. Moreover, one important advantage of β decay is that it can avoid the tail of IVGDR, all protons versus all neutrons out-of-phase vibration, intrinsically because it is difficult to generate all proton and all neutron out-of-phase motion in β-decay reaction; this contamination was a continuous difficulty in the past decades. Another unique advantage in the β-decay is the population of two particle two hole (2p2h) multi-correlation states [17, 70], which is due to the weak interaction's character and its complexity including multicorrelations, two-body currents [15, 16, 71] and Dirac sea states excitation [72]. This perspective was verified by a recent B(E1) distribution comparison investigation between (γ, γ') reaction and β decay [68] as shown in Fig. 1.19. Another positive signal was released by total absorption γ-ray spectrometry (TAGS) research following β decay, which revealed considerable population probabilities for high-lying states associated with the precusor-like spin and parity [73, 74].

Therefore, β decay study will challenge the completeness of PDR response populated by previous methods including real photon, virtual photon and hadron induced excitations, which are sensitive to

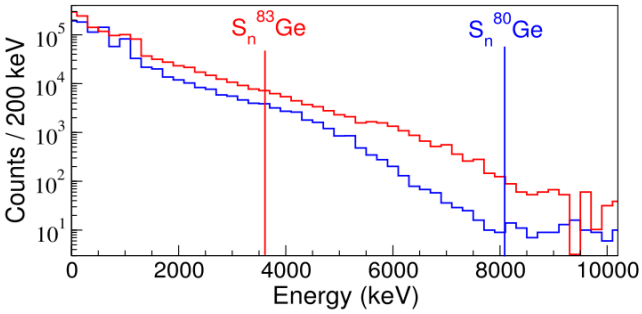

Figure 1.20 – The γ-spectra measured in coincidence with β electrons from the decay of ^{80,83}Ga. The two spectra are normalized to the same number of β-decay events [43].

J = 1 states. But, simultaneously, it will be imporatant complementary component for other methods also. A new experimental window will be opened for investigating PDR's internal structure and decay pattern. In particular, it would extend the PDR's existence border in spin dimension. Besides, the nuclear β decay properties play key role in r-process. So, the measurements of its generated PDR states following the B(GT) distributions can not be replaced by other reactions though it populates only a fraction of PDR states. Nervertheless, it is experimentally still a formidable challenge to observe them due to Pandemonium effect [75].

2.3 Achievements at ALTO

Recently, the BEDO decay station was equipped by a modular versatile detectors array PARIS coupled with HPGe detectors and optimized to cover the full β-delayed γ-strength allowed in the full Q_β window. There are two other important achievements in ALTO, happened in 2017, that have been the triggers of the launch of the experimental program of this PhD thesis at ALTO ISOL in Orsay to investigate the structure of the neutron-threshold region of Ga isotopes. Firstly, it is the unexpected observation of the β-delayed "ultra"-high-energy γ-rays (8-9 MeV) [43] in the β-delayed emission products of $^{83}_{31}Ga_{52}$ ($T_{1/2}$ =312 ms; Q_β =11.7 MeV) sources collected at the BEDO station as shown in Figure 1.20.

Secondly, it is the observation of the abnormal reduction of β-delayed neutron emission probability (P_{1n}) from ^{83}Ga to ^{84}Ga while the $Q_{\beta n}$ window increases from 8087(3) keV to 8811(30) keV [36]. This result, shown in Figure 1.21, have been obtained in one single experiment using the ^{3}He neutron-counter TETRA [76]. It indicates a higher γ deexcitation branch ratio (Γ_γ) above the neutron separation energy S_n of ^{84}Ga, which is important side evidence (signal) of the existence of PDR.

2.4 Applications of PDR study for neutron skin and r-process

Neutron-skin thickness measurement is one direct methodology to determine the slope parameter of the symmetry energy in the equation of state (EOS) that is a key equation in the description of dense astrophysical objects such as neutron stars [77] and quark star [78] and, consequently, that constrains their radius. While the electric dipole (E1) response of nuclei is dominated by the isovector giant dipole resonance (IVGDR) that is a highly excited collective mode above the particle emission

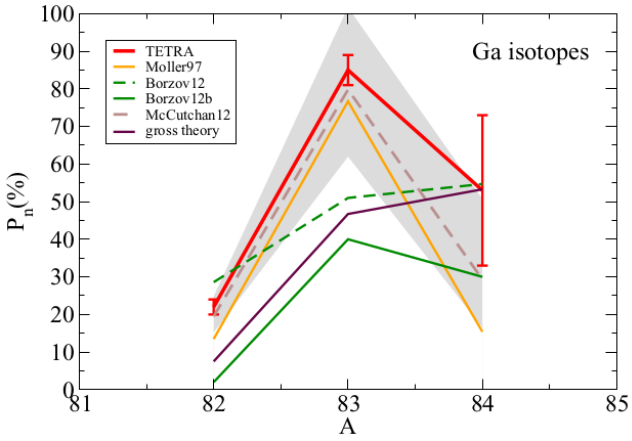

Figure 1.21 – P_{1n} for the $^{82-84}$Ga precursors from measurement in TETRA compared to theoretical results using QRPA approaches ("Moller97" and "Borzov12b,Borzov12"), the gross theory and results from empirical formula by McCutchan ("McCutchan12") [76].

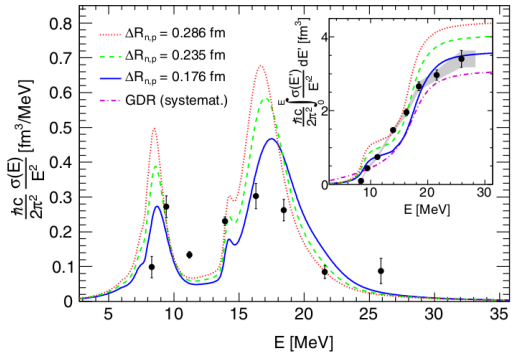

Figure 1.22 – The inverse energy-weighted dipole strength (black dots) with FSUGold calculation for ^{68}Ni. Inset: cumulative experimental dipole polarizability and the corresponding FSUGold calculations. For comparison, the curve for the GDR is shown as well [79].

threshold, the pygmy dipole resonance (PDR) attracts wide interest especially for neutron-rich nuclei. Its mechanism was assigned to the oscillation of excess neutrons against an isospin-saturated core. Consequently, PDR is more sensitive than IVGDR to nuclear structure and may shed light on the neutron skins in nuclei. Figure 1.22 is a case of ^{68}Ni used to demonstrate the relationship between the thickness of neutron skin and the strength of PDR.

The PDR state, if located above or around S_n, is not only the doorway states in the neutron-capture process but is also the dominant in the following nucleosynthesis path: depopulation by γ emission (n, γ) to form a new nucleus or by subsequent neutron emission (n, n$'$). Furthermore, in the photon bath of the astrophysical r-process environment, the PDR above S_n enhances the reverse process of (γ, n) photodisintegration. Therefore, the width of PDR and its distribution relative to S_n of neutron-rich nuclei impact significantly the production of heavy elements beyond iron in the universe [80, 81, 82].

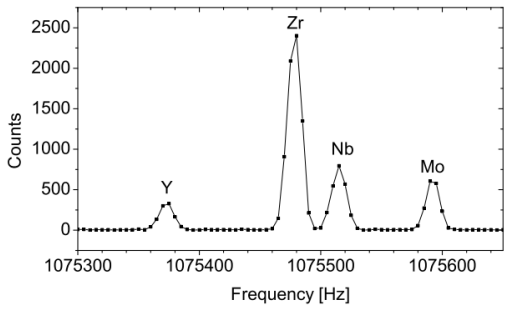

Figure 1.23 – A quadrupole frequency scan in the JYFLTRAP purification trap for mass A = 100 in which each point is accumulated for 50 cycles and the spectrum was plotted with collection of 30 min [83].

3 New experimental landscapes of β-decay study

3.1 Trap-assisted decay spectroscopy

Penning trap is an excellent high-precision mass spectrometer for radionuclides. Its high-resolving power for separating isobaric and isomeric contaminants can be used to improve β-delayed spectroscopy study through delivering purified isotopes. This coupling is very important for ISOL-type facilities to overcome the suffering from strong isobaric and isomeric contaminations, which is especially disturbing for nuclear β-delayed spectroscopy experiments.

The first experiment with a Penning trap purified beam for decay spectroscopy was performed at Jyväskylä with JYFLTRAP mass spectrometer as shown in Figure 1.23 [83]. Now, these trap-assisted systems have been installed in a few laboratories like ISOLTRAP at ISOLDE/CERN [84, 85] and MLLTRAP at ALTO [86]. They have a resolving power reaching 10^6 which can provide isomeric selectivity. Figure 1.24 presents the frequency scan in a recent trap-assisted decay spectroscopy study of ^{81}Ge performed at IGISOL with JYFLTRAP. In this scan, the closely-lying isomeric state ^{81m}Ge $(1/2^+)$ has been identified and separated in the trap [87].

3.2 Total Absorption γ-ray Spectroscopy

Pandemonium effect

In 1977, Hardy, Carraz and Jonson performed a β-decay simulation using statistical model of a fictional nuclide: Pandemonium. Suprisingly, much γ-ray intensity remains unobserved under normal experimental conditions actually when compared with its simulated γ-ray spectrum as shown in Figure 1.25. From this case ^{145}Gd, the authors doubted many decay schemes of other nuclei determined from such spectra, based on γ-peak analysis and intensity balances, if Q_β window is large and, consequently, the number of transitions is large. Furthermore, the authors pointed that the decay branching ratios for all but the strongest transitions could be wrong by orders of magnitude and the "measured" ft values for most β-transitions need to be reevaluated.

Then, in the following years and nowadays, in order to solve this so-called Pandemonium effect in β-decay studies, total absorption γ spectroscopy (TAS) setups were developed around the world. On

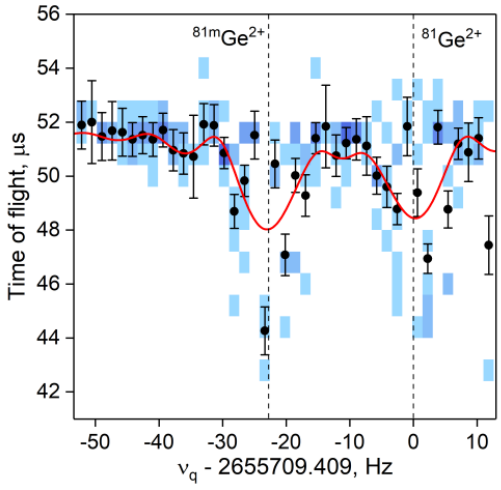

Figure 1.24 – ToF-ICR spectrum with 100 ms quadrupolar excitation in the second trap in JYFLTRAP for $^{81}Ge^{2+}$ after the in-trap β-decay of ^{81}Ga [87].

the other hand, many people doubt this conclusion and confirm that complete I_β is unavailable for high-resolution γ spectroscopy (HRGS). However, they believe that HRGS can build 100% I_β decay level scheme even for nuclei with high Q_β value if the statistics are enough. Anyhow, one should be careful of the high-energy γ-ray detection in case of consequent misoperation due to non-observation of them in β-decay study of nuclei with high Q_β value.

TAS technique

Total absorption gamma-ray spectroscopy (TAGS) was designed to overcome the so-called Pandemonium effect. Along with the development of radioactive beam technique, the exotic nuclei located in the neutron drip-line region with high Q_β value (>10 MeV) become available. Consequently, the states at high excitation energy of the daughter nuclei can be populated. So, the γ deexcitation energy also becomes high accordingly. In addition, the related energy distribution of β transitions vary largely. However, for the traditional high resolution γ-ray spectrosopy (HRGS) technique, the collection of information for individual γ-rays becomes difficult due to the low detection efficiency of high-pure germanium detectors of high energy γ-rays. It is caused by so-called the Pandemonium effect.

TAS uses large 4π scintillation detectors like in Figure 1.26 with NaI crystals, which is based on the direct detection of energy of the full de-excitation cascade rather than individual γ-rays. It is the logic to overcome the Pandemonium effect. TAS technique owns the powerful ability for looking for the missing β intensity from HRGS technique and in the correcting of the distortion of the β intensity obtained from balance method.

The nuclear decay study with TAS technique has impacts on three topics of interest: 1. high-energy γ-ray detection from neutron unbound states and the related subjects like PDR study, B(GT) distribution in β-decay, nuclear structure near S_n and neutron capture reaction in astrophysics (n,γ); 2. reactor decay heat calculations; 3. reactor antineutrino spectrum calculations [88].

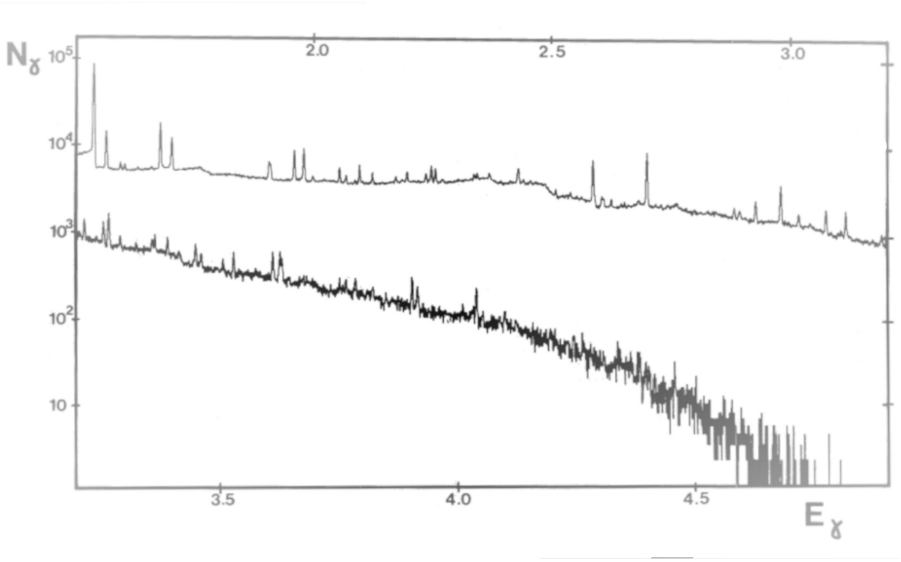

Figure 1.25 – β-delayed γ spectrum of Pandemonium from computer simulation (upper) and data (lower) for the nucleus ^{145}Gd [75].

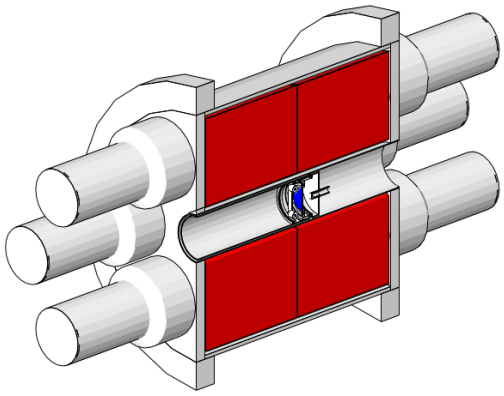

Figure 1.26 – Cross-sectional view of the detector geometry from Geant4 simulation. Red: BaF_2 crystals. Blue: Si detector. The beam is deposited on the tape, in front of the Si detector, from left direction [88].

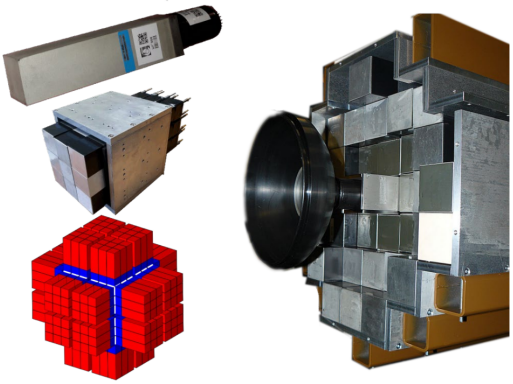

Figure 1.27 – Left, from top to bottom: a phoswich, a cluster, a 4π cube of 24 clusters. Right: Wall geometry of 33 phoswiches [89].

3.3 PARIS technique

In the measurement of γ-rays, one of the important observables during the nuclei decay study, the good detector in principle should own excellent time and energy resolution, good detection efficiency of full energy peak and low internal radiation. Obviously, it is difficult for single type of detectors to own all of these advantages. For example, HPGe has the best energy resolution but its time resolution and detection efficiency at high γ-ray energy are far from being ideal. And, currently, a large volume single HPGe crystal (vol. $>$ 1 liter) is not commercially available. In the past decades, large volume BaF_2 and NaI detectors (several liters volume) have been utilized for the detection of high-energy gamma rays to achieve high full energy peak efficiency and good time resolution at the expense of energy resolution.

However, there is a feasible solution that is to combine different scintillator materials in a phoswich geometry for realizing the benefits from the different "features" of the different scintillators. PARIS (Photon Array for studies with Radioactive Ion and Stable beams) is an international project that aims to develop and build a new 4π γ-ray calorimeter. it is also planned to play the role of an energy-spin spectrometer. It is composed of phoswich detectors with two shells: the scintillators $LaBr_3$ for the inner shell providing simultaneously excellent time resolution, high detection efficiency and relatively good energy resolution in a large energy range and NaI for the outer shell that can be used for add-back and also can work as a veto detector performing anticoincidence to supress the background. In addition, PARIS has high granularity that allows for the multiplicity measurement of γ-rays. It is designed to detect in beam γ radiation at typical high counting rate (decades of kHz in a single phoswich) and in a wide energy range, 1 MeV to 50 MeV. Currently, 2022 PARIS array has 8 clusters. One cluster means a bunch of 9 phoswich $LaBr_3$/NaI detectors as shown in Fig. 1.27 left-middle one.

The main goals of PARIS are the studies: nuclear new modes of excitation like PDR; structure near S_n of exotic nuclei; the properties of hot exotic nuclei produced in fusion-evaporation reactions by γ-decay measurement of IVGDR; the nuclear reaction dynamics [89].

4 Summary of motivations

The β-decay, a precisely described process at the most elementary (quark) level, becomes a rich and complex probe when involved in the strongly interacting multi-nucleon medium which is the atomic nucleus. In this correlated system the transformation of a neutron into a proton (or vice versa) described by the Fermi and Gamow-Teller operators gives rise to collective states involving coherently a large fraction of the nucleons under the form of a giant resonance. For neutron-rich nuclei close to stability, these giant resonances lie far above the energy window accessible in the β-decay (Q_β), and this decay must proceed through tail components of these resonances in competition with first-forbidden transitions. However, the advent of a new generation of Radioactive Ion Beam facilities making possible β-decay studies of nuclei with ever larger Q_β windows, beyond 10 MeV, now changes this perspective. For instance, β-decay of exotic nuclei can provide a new and unique method to investigate the more neutron-skin-sensitive collective motion Pygmy Dipole Resonance (PDR) and also an opportunity for a deeper understanding of exotic phenomena involved in nuclear β-decay through precise measurement of the Gamow-Teller transition strength distribution, B(GT).

The objective of this thesis is to improve the understanding of the structure in the neutron threshold (S_n) region of exotic nuclei and the influence of this structure on the B(GT) by studying a mixed $^{80g+m}$Ga source collected at the BEDO decay station of the ALTO Isotope Separation On Line facility in Orsay. The ^{80g}Ga and ^{80m}Ga β-decaying states having spin-parity 6^- and 3^- respectively, this source has the advantage that it can populate an unusually large spin-range of daughter states in the nucleus ^{80}Ge. The goal of this work therefore covers three aspects: investigate the PDR in ^{80}Ge, disentangle the decay level schemes fed by the two β-decaying states of ^{80}Ga and achieve a precise determination of the associated B(GT) in the whole Q_β window. To achieve this goal, a hybrid gamma spectrometer composed of PARIS NaI/$LaBr_3$ phoswiches associated to high resolution Ge detectors was used.

2 Production of radioactive ion beams at ALTO and experimental setup

Sommaire

The exploitation of exotic nuclei beams is the new direction in nuclear science and, surely, is precondition for the research of these exotic nuclei's fundamental characteristics. The new techniques development allows the exotic nuclei to be accessible experimentally, which provides the possibility to understanding the structure of exotic nuclei exhibiting new phenomenons not observed in stable nuclei. In neutron drip, these line are triggered by the high isospin asymmetry or their low binding energy. This chapter will introduce the production methods of radioactive ion beam, ^{80}Ga at ALTO France including photo-fission, Ion source and the techniques used in isotope on-line separation.

1 Production of radioactive-ion-beam $^{80g+m}$Ga

1.1 Production and separation methods of secondary beams

Production method

For radioactive beam production, there are various reactions over a wide energy range being used to produce exotic isotopes. It includes:

1. induced fission(neutron, proton, photon, heavy ions, Coulomb): the disintegration of heavy nuclei near uranium into two large fragments, which play an important role in the production of exotic nuclei;

2. Fragmentation of relativistic heavy ions: at high energies above the Fermi domain, only the overlapping parts of the colliding nuclei participate in the interaction. Consequently, the heavy fragments outside this region are sources of exotic nuclei that cover the entire periodic table up to uranium. In addition, it owns the advantage to populate the neutron-rich side of the nuclear chart because the fragments profit from the neutron excess of the heavy nuclei;

3. Multi-nucleon transfer: exotic nuclei in the vicinities of both projectile and target are created by nucleon exchange in the peripheral collisions at Coulomb energies, which is an efficient way to produce neutron-rich heavy elements otherwise difficult to achieve;

4. Complete fusion: only known reaction to synthesize the super-heavy and hyperheavy elements [90].

One key parameter of a secondary beam facility is the intensity of exotic beams that is determined by several contributions such as primary beam intensity, the selected reaction, the target thickness and the separation efficiency. The luminosity (L) is the important performance characteristic of a secondary beam facility that is defined by the product of the projectile intensity (N_P) and the target thickness (N_T). However, the intensity (N_F) for a specific fragment exotic beam at the exit of a separator is determined as L by the reaction cross section (σ) and the separation efficiency (ϵ) (see equation 2.1[90]):

$$N_F = N_P N_T \sigma \epsilon = L \sigma \epsilon \tag{2.1}$$

Considerable inroads have been made in improving the luminosity of the ion sources. As shown in the formula 2.1, another crucial contribution to the intensity of secondary beams is the transportation efficiency of the separation system including the decay loss that can range from 10^{-6} to 1 depending on

the used reaction and the separation method. The selectivity of separation method is also responsible for the amount of contaminations present in a secondary beam. While the production rate is crucial to study exotic nuclei, beam purity is also basically important. Isobaric contaminations from non-selective ion products and/or ionization as well as molecular contaminants produced by chemical reactions are often present with much higher intensities than the ions of interest, which prevents certain types of measurements.

There are two main separation principles applied in existing and planned exotic beam facilities. The first one, Isotopic separation on-line (ISOL) technique, it was developed to complement nuclear chemistry tools for short-lived nuclei far from stability [91, 92]. The second method is in-flight separation. Using this method, one often takes advantage of the specific reaction kinematics to separate selected nuclear reaction products from contaminants with a high suppression factor ($> 10^{-12}$) [90]. ISOL method and the in-flight technique can be considered as complementary to some extent.

When ompared with In-Flight separation method, the ISOL production has several advantages: 1. Secondary beams can be produced from very low energy (keV) to high energy, at the cost of a post-accelerator for reaction products; 2. The beams produced by ISOL and reaccelerated present a high quality emittance such as ensuring a small beam size on target and small energy dispersion; 3. Pure isotopic beam as the transmission and rates exclusively depend on the isotopes due to chemical selectivity. For every element (isotope) an ionization process has to be developed before the beam becomes available. Therefore, good-quality beams of exotic nuclei of interest can be produced via the ISOL technique.

1.2 Production of radioactive isotopes with photo-fission at ALTO ISOL

In the ISOL method, an intermediate or heavy-mass thick production target is used. It is bombarded with light beam including neutrons, protons, electrons, gamma-rays or heavy ions. Nuclear reactions vary from fusion-evaporation to fission, multi-nucleon transfer reactions, fragmentation and spallation, which is dependent on the energy of the primary beam, from a few tens of MeV per nucleon to 1 GeV for proton. The reaction products are stopped inside the target and only those, being thermalized, diffusing as neutral atoms outside the target material can contribute to produce a radioactive beam. Then, some of the reaction products reach at an ion source, therein they are ionized and accelerated with an electrostatic field. The target catcher array can also be integrated into the ion source. They are often reaccelerated to the typical level 10-100 keV. As a result of the time cost of diffusion, effusion, ionization and extraction processes from the production target, ~ 100 ms, ISOL system is limited to radioactive nuclei with half-lives longer than 10 ms, depending on the chemical and solid-state characters of the reaction products. In spite of this disadvantage, it still is a powerful tool to locating the exotic nuclei with doubly-magic numbers of N = 50 and N = 82, in the vicinity of ^{78}Ni [93] with half-life 110^{+100}_{-60} ms and ^{132}Sn with half-life 39.7(8) s, respectively [94]. The exotic nuclei of secondary beam are separated by electromagnetic fields according to their mass-over-charge ratio. Nowadays, some of the most known and advanced beam facilities using proton beams are ISOLDE at CERN (Switzerland), IGISOL at Jyväskylä (Finland), SPIRAL2 at GANIL (France), ISAC at TRIUMF (Vancouver, Canada). ALTO ("Accélérateur et Tandem d'Orsay") is a unique one using photo-fission.

For nuclear physicists, the availability of intense neutron-rich radioactive beams will open new perspectives in the research of nuclei very far away from the valley of stability. It will allow to apprehend the behaviour of the nuclear matter under extreme isospin asymmetry conditions, which also opens many new perspectives, e.g. detailed nuclear structure researches in yet unexplored region, ^{78}Ni and ^{132}Sn doubly magic region. Several laboratories are focussing on researches aimed at producing high enough intensities to guarantee a new generation of experiments like EURISOL project in Europe. Fission is a powerful mechanism to produce a number of such beams. A large effort have already been spent to investigate the production of neutron-rich isotopes in photofission at ALTO.

Nuclear fission, where the nucleus splits preferentially into two smaller fragments along with massive energy release, is a important tool with unique characteristic for producing the exotic radioactive nuclei. Nuclear fission is exothermal process since the nuclear binding energy per nucleon for the produced medium mass nuclei is significantly higher than that of the original heavy nucleus. However, to be able to fission the nucleus has to stretch to a certain elongated shape firstly, which requires energy for the deforming nucleus to pass the so-called saddle point. Then the energy is released. There are several methods to bring energy to nucleus as electromagnetic radiation (photofission) or nuclear reaction via a particle (e.g., proton, alpha, deuteron or neutron). The potential barrier against the fission for medium heavy nuclei is of the order of 50 MeV while for actinides (^{233}U, ^{235}U, ^{239}Pu ^{241}Pu, ^{241}Am, etc.) of the order of 5 MeV. In the last half century, fission reaction has led to the production and discovery of more than 400 new isotopes. After more than 80 years since its discovery [95], the underlying microscopic mechanism of the fission process still remains elusive and under intense scrutiny nowdays such as the angular momentum generation of the primary fission fragments.

ALTO has developped a program to optimize the production of radioactive beams from ^{238}U fission using in a first time the deuteron beams of the Tandem and finally the electron beams. The research and development (R&D) project PARRNe (Production d'Atoms Radioactifs Riches en Neutrons) was initiated at the Institut de Physique Nucléaire d'Orsay (IPN Orsay) in 1997, and is now an important constituent of today's new laboratory: Laboratoire de Physique des 2 Infinis Irène Joliot-Curie (IJCLab, Orsay France).

The program PARRNe (Production d'AtomesRadioactifs Riches en Neutrons) at ALTO aimed to study the parameters to optimize the production of radioactive beams from ^{238}U fission. The PARRNe 1 project was developed in order to measure the online production of rare gases. These measurements gave relative and empirical information on the productions of radioactive beams. In order to investigate the production of the other elements as well as the optimization of the target ion source unit, PARRNe 2, an isotopes separator on-line, was then installed at the Tandem of IPN Orsay. The influence of the energy of the deuteron beams from 20 to 130 MeV along with the nature of the converter materils Be, C, U has been investigated within the European RTD program SPIRAL2. These "PARRNe 1" measurements have been done at Orsay with 20 and 26 MeV , Louvain la Neuve with 50 MeV, KVI with 80 and 130 MeV with an UC_x target and at 26 MeV with a molten U target. The main advantage of the "PARRNe 1" is the utilization of an identical set-up at various accelerators. The performed experiments demonstrated that fast-neutron–induced fission method is a highly interesting way for future RNB facilities. But, this method requires the further development of very intense primary beams (i.e. deuteron or proton) for the neutron production. An interesting alternative way

to neutron-induced fission would be the bremsstrahlung-induced photo-fission of uranium.

This program was mainly devoted to research the production of neutron-rich fragments beams extracted from the thick target fission with ISOL method [96]. In the framework of the PARNNe program different techniques were utilized to characterize the release properties of the isotopes of interest from a UC_x target [97]. Along with the R&D program, the related physics research of the neutron-rich isotopes was started also [98, 99]. At the beginning, the fission of ^{238}U was induced by the deuteron beams provided by the Tandem accelerator (a 15 MV Tandem electrostatic accelerator). An experimental programme to investigate the implementation of photo-fission was initiated at Orsay in 2000. Isotopic cross sections were measured with a 50-MeV electron beam from the LEP Pre-Injector (LPI) at Cern, a machine that was subsequently transferred and installed at Orsay in 2005. Consequently, the first electron beam at the new site was accelerated in 2006. After a long development programme including reinforcement of the radiation shielding around the target and a major facelift of the PARRNe mass separator, the licence for operation at the full nominal intensity of 10 μA was granted in 2012. Nowdays, the ALTO linear accelerator provides 50 MeV electron beam of 10μA intensity.

Photo-fission producing radioactive isotopes was proposed by Diamond [100] and Oganessian [101] et al. using the electrons as the primary beam. As known, in the interaction between electrons and converter material, bremsstrahlung, having an energy E_e and γ-radiation with a continuously falling spectrum down to $E_\gamma^{max} = E_e$ is generated, which induces fission in the target (photo-fission). Photo-fission with diverse energies is determined by the region of isovector giant dipole resonance (IVGDR).

In the case of ^{238}U, the fission cross section at the IVGDR energy region reaches 0.16 barn [102]. The dependence of the uranium fission cross section $\sigma_f(E_\gamma)$ on the electron beam energy, in fact determining the IVGDR structure, is presented in Figure 2.1. As shown, the yield of γ-quanta in the IVGDR region, 10 - 17 MeV, depends on the energy of electrons. As shown in Figure 2.1, it is easy to derive the dependence $\sigma_f(E_\gamma)$ and evaluate the probability of uranium fission in the optimal size target per every electron, with energy E_e reaching the target. As can be seen, the energy of γ generated by the bremsstrahlung radiation varies and grows up to a maximum value corresponding to E_e. And the trend increases gradually with raising the electron beam energy. To induce fission the photon energy must be larger than the fission threshold energy of ^{238}U which is 6 MeV. From Figure 2.1, fission cross section as a function of incident photon energy, the fission fragment yield sharply grows with E_e increasing up to $E_e = 30$ MeV and then continues to smoothly and slowly grow up to $E_e = 50$ MeV and higher. Thus, 50 MeV seems to be the optimal energy for photo-fission. At $E_e =$ 50 MeV, the calculated fission yield is about 0.6% per electron. Therefore, according to Diamond's calculation, with 30 MeV and 100 kW electron beam it is possible of induce more than 10^{13} fissions/s. It was validated by Oganessian experimentally. In that experiment, a 25 MeV and a 0.5 kW electron beam was delievered on a tantalum converter to induce photo-fission in a sheet of uranium. The resulted fission rate in the target was measured to be order of 10^{11} fissions/s [101]. Fig. 2.2 presents the power of photo-fission in production of neutron-rich Sn isotopes than other types of fission.

ALTO is the only installation worldwide that presently delivers low-energy radioactive ion beams from the photo-fission of ^{238}U using an electron linear accelerator, which is surrounded by a great

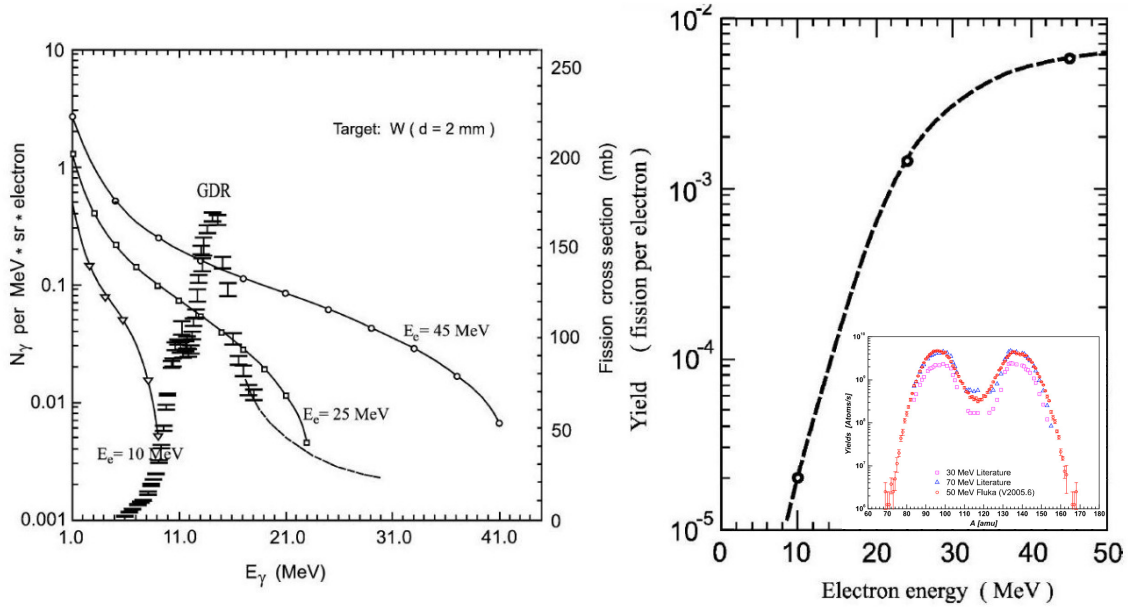

Figure 2.1 – Left: the solid lines are the γ-quanta spectra, the left-hand scale, produced by electrons with various energies as indicated in the figure. The experimental points, the right-hand scale, correspond to the ^{238}U photofission cross section [102, 101]; Right: the fission yield per electron for ^{238}U as a function of the electron energy [101]. The inner plot on the right-hand presents the photofission mass distributions for electron beam energies of 30 MeV [103, 104], 50 MeV (simulations) [104] and 70 MeV [103, 104].

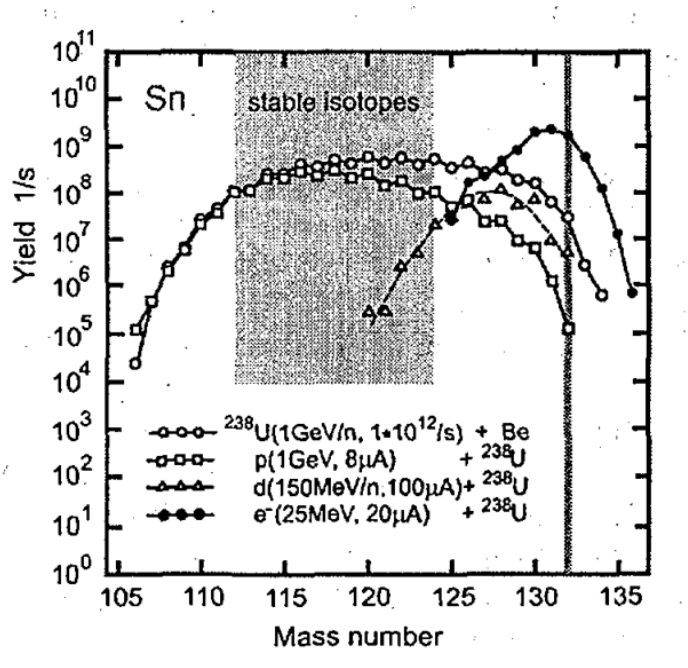

Figure 2.2 – The yield of Tin isotopes in different reactions as indicated in the figure [101].

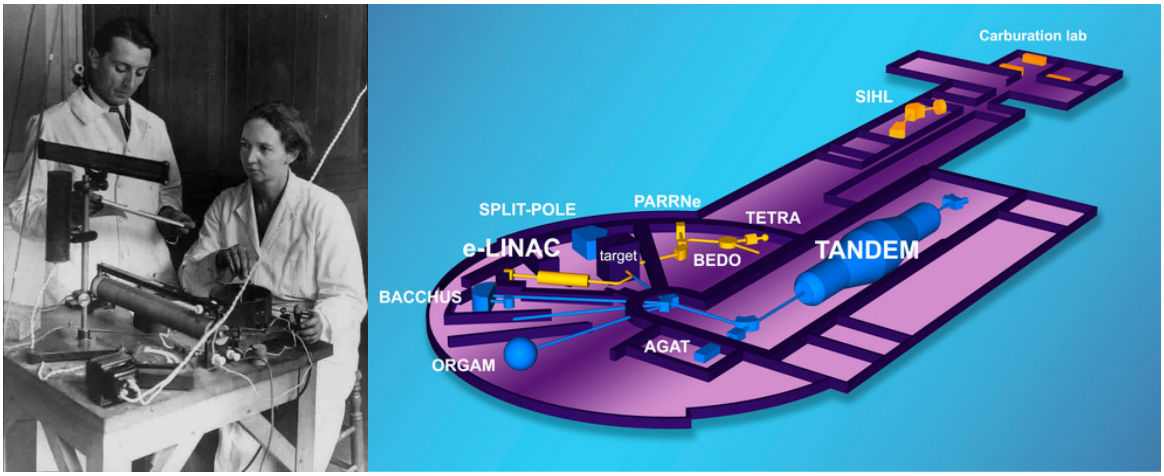

Figure 2.3 – IJCLab ALTO Facility. Note: left Irène et Frédéric Joliot-Curie picture from website of Musée Curie

variety of experimental instruments/devices on 6 different beam lines for physics research. It was initiated at Orsay in 2000. The isotopic cross sections were measured with a 50 MeV electron beam from the LEP Pre-Injector (LPI) at CERN, a machine which was then transferred and installed in Orsay in 2005. The first electron beam on the new site was accelerated in 2006. After a long development program including the reinforcement of the radiological shielding around the target and a major facelift of the separator PARRNe, the authorization to operate at full nominal intensity of 10 μA was granted in 2012. This marks the start of ALTO-LEB (Low-energy beams).

1.3 ALTO-ISOL facility

ALTO facility has two-accelerators located in Orsay science compus, France (see figure 2.3). The first accelerator is a 15 MV tandem utilized to accelerate ions from proton to gold as well as clusters and molecules. It is operated since 1970 with constant maintenance and upgrades. It is, for instance, the first installation in the world accelerating fullerene molecules. The second one is a Linear accelerator ("LINAC") which accelerates electrons up to 50 MeV is utilized for photo-fission with a uranium carbide target for the production of neutron-rich radioactive beams. It is the first facility in the world applying this pioneering and advanced technique.

1.3.1 LINAC

The electron Linear Accelerator (LINAC) generates electron beams with an energy up to 50 MeV and an intensity of ≈10 μA. It is used to produce radioactive ion beams by electron bremsstrahlung induced photo-fission in a uranium carbide (UC_x) target heated to 2000°C. A general view of the LINAC is shown in Figure 2.4. The main components of the LINAC are the injector including the accelerator section and the transmission line. The injector made up of an electron gun that delivers a pulsed electron beam of 100 Hz, an adjustable pulse width between (0.2 - 2 μs) length and brings electron to 90 keV. Following the electron gun there are two high frequency cavities (a pre-buncher and a buncher) that makes it possible to form and pre-accelerate electron bunches for acceleration up

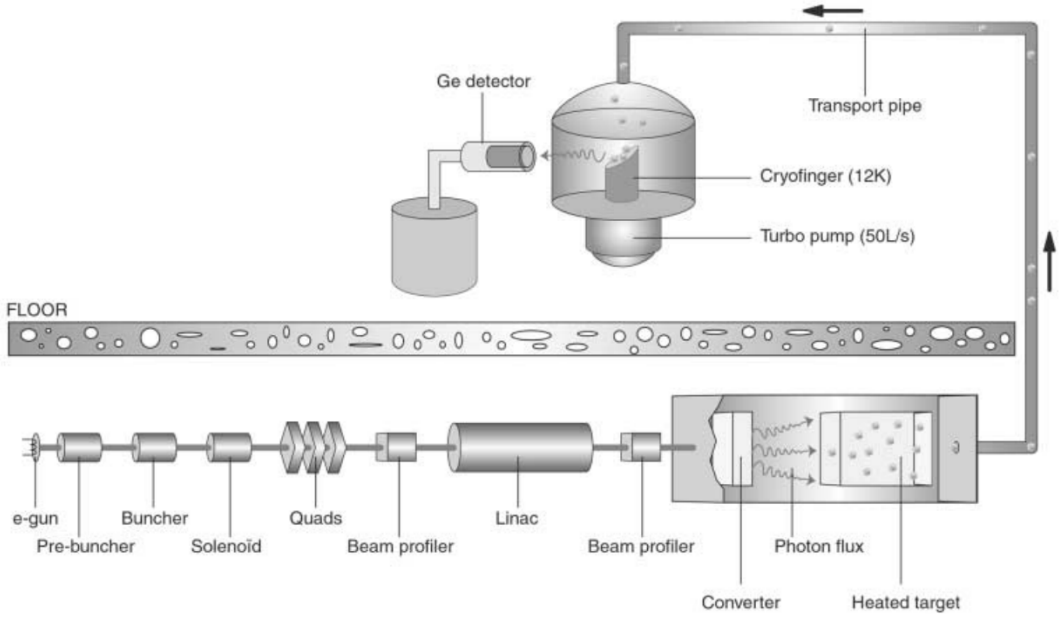

Figure 2.4 – Schematic view of the PARRNe1 experimental set-up LEP Pre-Injector at CERN [98].

to 3MeV. Electrons leaving the injector will be accelerated up to 50 MeV in the accelerator LINAC section, 4.5m length. The acceleration section is in fact the former LEP pre-injector. Once the beam has been formed, with average maximum current of 10 μA and a width of 15 ps under a repetition period of 333 ps, the transmission line will ensure its routing to the target-source assembly under the required focusing conditions. The line is equipped with two magnetic dipoles deflecting the beam at 130°. Note: the transmission line can also be utilized for a deuteron beam for experiments with fast neutrons. The characterization of the beam throughout the transmission line is guaranteed, thanks to the various beam diagnostic elements implemented along the line.

1.3.2 ISOL UC_x target at ALTO

After the first deflection in the magnetic dipoles, the electron beam bombards a uranium carbide target ($^{238}UC_x$). Electrons are converted into photons through bremsstrahlung in the first centimeters of the target. The generated gamma cascade initiates the uranium fission process. The ALTO $^{238}UC_x$ target is a thick target that consists of 143 pellets, disks of 14 mm in diameter, 1 mm thick and with the apparent density of 3.2 g/(cm^2) that are assembled in a 140 mm length cylindrical graphite or carbon nanotubes container. Totally, it contains 60.8 g of ^{238}U [104]. By means of two blocks, the cylinder is trapped inside a 20 cm long and a few millimeters thick tantalum ($_{73}$Ta) oven to have a homoneous heating of the target up to 2000 °C, which makes the produced radioactive elements to be released fastly. There is an 8 mm diameter hole in the center of the oven where a transfer tube is welded, which guarantees the diffusion and effusion of the elements to the ionization source as shown in Figure 2.5. The diffusion and effusion of a given element from the target depend on its various physical-chemical characteristics. Therefore, the most volatile elements (e.g., Rb and Cs ...) and noble gases (e.g., Ar and Xe ...) have a relatively lower boiling temperature as shown in Fig. 2.6. The

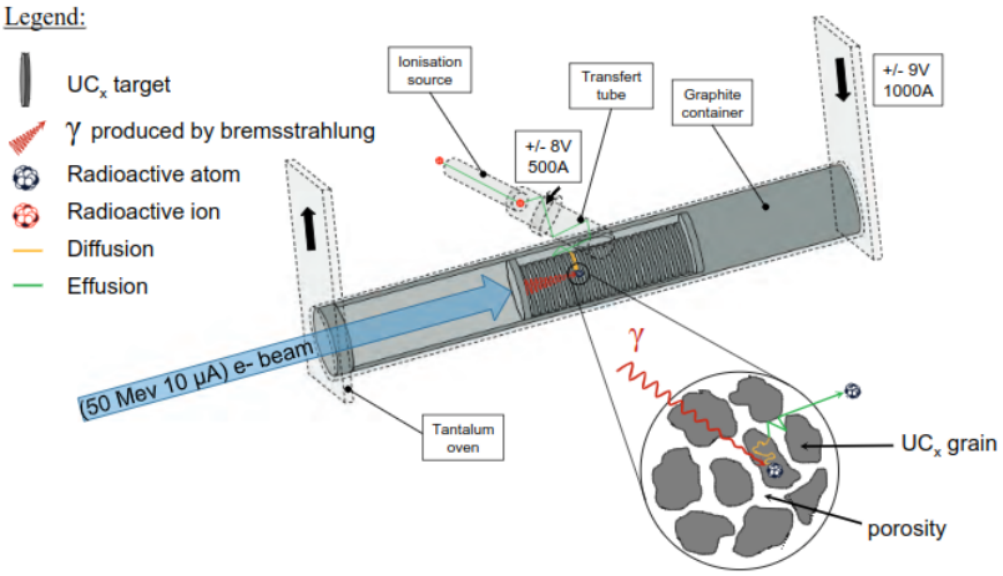

Figure 2.5 – UC$_x$ ISOL target at ALTO IJCLab Orsay [108].

saturation vapor pressure makes them diffuse from the target and then effuse to the ion source quickly. However, for other elements such as metals (like Ga, In, Sn, Tl ...) or earth alkaline metals (like Sr and Ba ...), the boiling temperature is high enough to cause them to remain possiblly in a solid form and difficult to be extracted. A typical research program and a targeted team at IJCLab is aimed at the studies of production of neutron-rich radioative beams extracted from thick targets of the ALTO design [105, 96, 104, 97]. Fig. 2.7 presents the absorption of γ-rays as function of U-target thickness in photo-fission. Many "easy" radioactive beams have already been sent to experimental beam lines. For elements far away from stability with short half-lives and low production cross sections further investigations are still needed as shown in the above cited articles. Different materials were also tested at ISOL IJCLab Orsay. The release performances of molten U and UC$_x$ thick targets were investigated at PARRNe [106, 107], which is fundamental investigation for the next generation ISOL facilities such as SPIRAL2, EURISOL, HIE-ISOLDE and SPES.

In formula 2.2, used to describe the radioactive beam intensity, ϵ includes three efficiencies, respectively, release, ionization and transpor efficiency. One main factor of the UC$_x$ is efficiency of release controlled by diffusion and effusion in the material:

$$\epsilon_{release} = \epsilon_{(diffusion+effusion)} \tag{2.2}$$

1.3.3 Ion sources

After release from the UC$_x$ target the radioactive atoms have to be ionized and then accelerated at least to several tens keV for subsequent downstream magnetic mass separation and electrostatic beam guiding. In the following, three different types (mechanisms) of ion sources used at ISOL Orsay facility are discussed: resonant laser ionization, surface ionization sources and MK5 plasma. Their

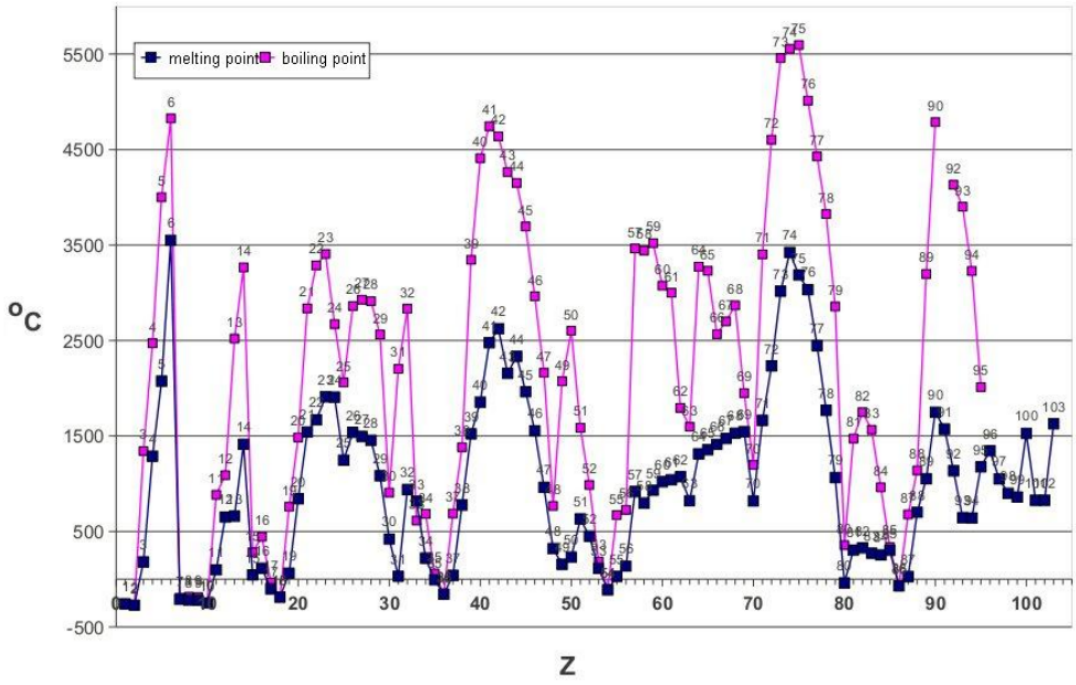

Figure 2.6 – The melting and the boiling points for different chemical elements. [109].

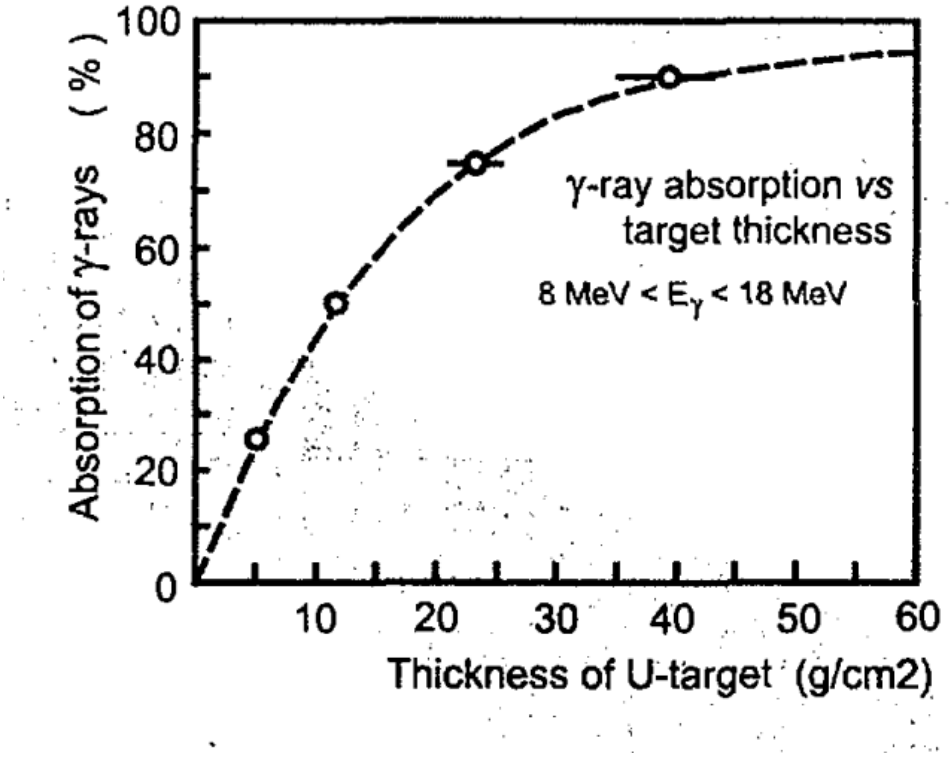

Figure 2.7 – Target γ-rays absorption as function of target thickness. [101].

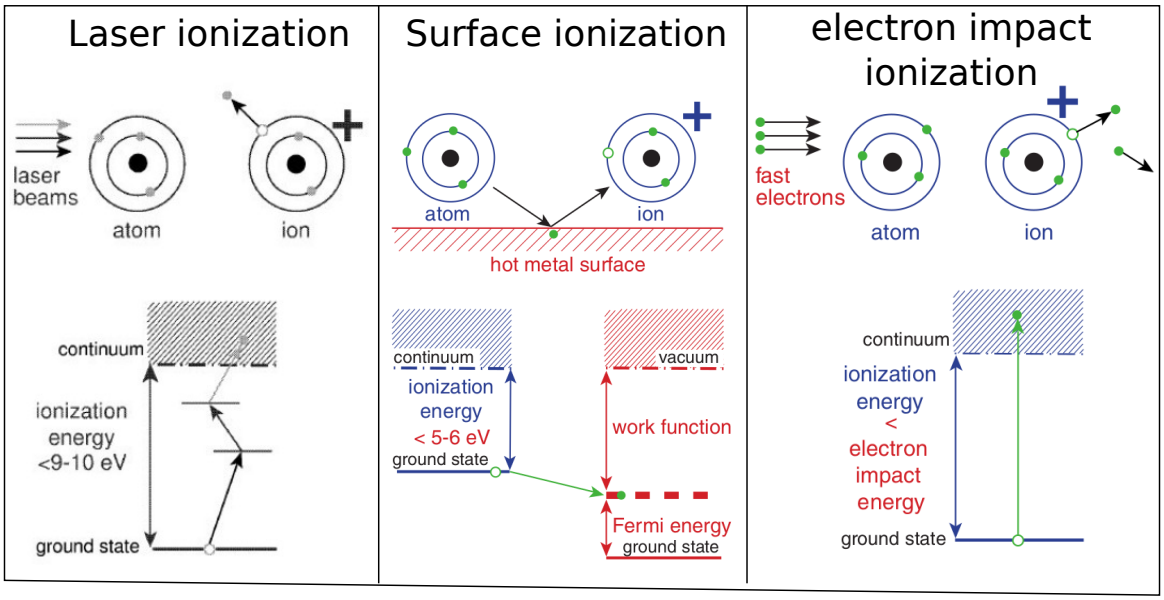

Figure 2.8 – Schematic representation of resonant laser ionization, surface ionization and electron impact ionization. [110, 109].

performance has to be evaluated according to the same criteria: efficiency – selectivity – rapidity that are decisive for all steps of the whole ISOL process. The efficiency of ionization is the ratio of the number of an isotope extracted from the ion source to the amounts of the injected isotope. The selection of source to be employed depends on the ionization potential of the interesting element such as the required charge state. At ALTO the choice of laser ionization, surface ionization or plasma ionization depends on the specific requirements. Over the past few years a strong effort has been put in developing the laser ionization source from ALTO laser team (RIALTO project [111]) to achieve the best isotopic selectivity that the ISOL technique can provide. After several upgrades of the setup, the reliability of the ion source has been largely improved and can be considered fully operational now. After the ion source, the intensities of the radioactive beams extracted from the $^{238}UC_x$ target can reach, e.g., 3 x 10^7 pps for ^{132}Sn nowdays in ALTO [112].

The laser ion source

The laser ion source of the ALTO research platform at IJCLab/in2p3/CNRS Université Paris-Saclay aims to produce pure ion beams utilizing resonant laser ionization source. Resonance Ionization Spectroscopy (RIS) can provide a highly efficient and selective way to ionize exotic atoms through a multistage laser excitation process. The laser room located above PARRNe mass separator is equipped with two Nd:YAGs operating at 10 kHz and pumping three dye lasers (540-850 nm) as two from Radiant Dyes and one from Lioptec with their doubling units BBO (270-425 nm) to reach the ionization schemes to two and three stages. To test the ionization patterns of the different elements, an online test bench is available in RIALTO that is equipped with an Atomic Beam Unit (ABU) used to determine the optimal operation parameters, which is necessary for on-line operation with radioactive beam. This device makes it possible to adjust the different laser wavelengths by measuring

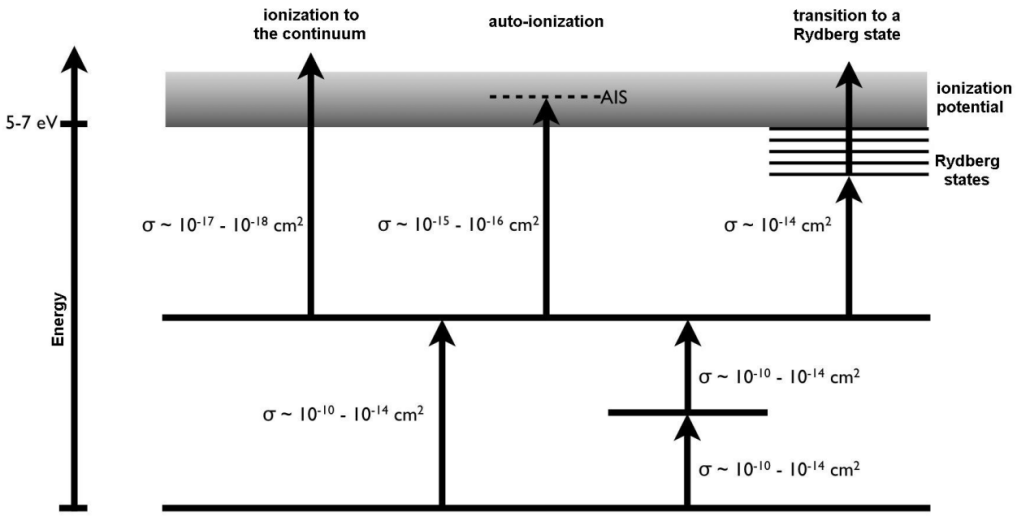

Figure 2.9 – Schematic of different ways of ionization and the corresponding cross sections (figure from [117]).

the current of the ions of interest obtained by the interaction of lasers and an atomic beam [111]. Resonant photo-ionization is a good ionization method that provides high selectivity and many choices of construction materials for the ion source chamber in which the valence electron is brought to the continuum through resonant absorption of photons via several excited levels. The used theory and techniques in a resonance ionization laser ion source (RILIS) are quite similar to those of standard RIS [113, 114]. RIS is a multistep photon absorption process where the final state is the ionization continuum of an atom, which can comprise two or three steps as shown in Fig. 2.9. The first step is always resonant and chemically selective due to the unique level structure of a specific element. But be careful about the overlap of first excited state of some atom such as Ga and Rb, which could generate the Rb contamination in Ga beam. The first step takes an atom to an intermediate state. In the second step of laser ionization, atoms are excited by laser photos to the continuum or to an auto-ionizing state or to highly excited states that are close to the continuum [115, 116].

However, if the auto ionizing states or Rydberg state are unknown, the second step will be directly to the continuum, nonresonant ionization, with relatively smaller cross section $\sigma \approx 10^{-17}$ cm^2 to 10^{-18} cm^2 as shown in 2.9[117], which requires a strong laser about 5 mJ/pulse. In contrast, in the case of resonant reactions, e.g., excitation to auto-ionizing states and low-lying Rydberg states, the requirements for the laser power are more relaxed thanks to the higher cross section as $\sigma \sim 10^{-14}$ cm^2. The auto-ionizing state is a state with two electrons excited above the atomic ionization potential and it will decay by a radiationless transition into an ion and an electron with lifetime $\sim 10^{-10}$ - 10^{-15} s. When one electron is ejected, the other one drops to the ground or excited states of ion. Although all multiple-electron atoms have auto-ionizing states, the information about them is not sufficient. About Rydberg states ionization, to excite an electron from the Rydberg state to the continuum a strong static field $\sim$ 10 kv/cm is needed, which makes this method difficult to be applied.

In the following some features of RIS are discussed that are important for the using of a RILIS.

An atom exposed to a photon flux ϕ of wavelength $\lambda = hc/E_{12}$ will be excited with the rate:

$$W_{12} = \phi\sigma_{12}(\lambda) \tag{2.3}$$

E_{12} is excitation energy, $\sigma_{12}(\lambda)$ is the absorption cross section for atoms from the ground state. If the absorption rate W_{12} is larger than the spontaneous emission rate from the related excited level, the occupation of the ground state and excited state as well as the rates of absorption and stimulated emission will come into equilibrium, called transition saturated. The transition from the first excited level to another higher excited state can be treated analogously. If enough photons for each excitation are provided simultaneously, the occupation reaches equilibrium among all participating levels, and the highest state located above the ionization threshold (including continum, auto-ionization and Rydberg state), then the excited atom will emit an electron (being ionized). The electron and the ion can be separated rapidly in a small electrical field. Therefore, for the last step the upper level is always empty and stimulated emission does not happen. If using non-resonant transitions into the continuum with a typical cross section of 10^{-17} cm^2 and the spontaneous emission rate to metastable states of 10^6 s^{-1} , a photon flux with order of 10^{23} cm^{-2}s^{-1} is needed. Given a beam spot of some mm^2 area and visible light, this laser corresponds to a power of some kW. Such strong power can presently only be provided by pulsed lasers. Therefore, raising the efficieny of the laser ionization is strategy due to low duty cycles. If the atoms can be confined for a while in the region irradiated by the laser beam, the overlap in time can be improved considerably and higher efficiencies can be reached even with low duty-cycle lasers. Three ways have been used to store the atoms for enhancing the overlap interaction time between atom and laser: 1. collection on and desorption from a cold surface; 2. stopping in a buffer gas cell remaining for some tens ms before being evacuated; 3. diffusion through a hot cavity with a small outlet hole, being heated to avoid excessive adsorption to the walls. To have at least one chance to interact with the atom, the laser should have a repetition rate of the order of 10 kHz. Higher repetition rate has higher interaction chance. The core “ingredients” for the efficient operation of a "hot cavity type" RILIS are: 1. the ionization scheme; 2. the laser system; 3. the ionizer cavity; 4. equipment for beam tuning and monitoring; find more details in [110]. Furthermore, a modification of the technique where detecting a single electron (or single ion) using a channel electron multiplier permits the precise measurement of a single-atom in individual ionization tracks.

Surface ionization ion source

If an atom having a low ionization potential (IP $<$ 6 eV) hits the hot surface of a material with high work function like a noble metal, it has a high probability to give its valence electron to the metal and to be ionized as shown in Figure 2.8. This process is called positive surface ionization with charge 1^+. Similarly, negative surface ionization exists for elements with high electron affinity that hits a hot surface of a material with low work function like LaB_6 and be ionized negatively. The efficiency of positive surface ionization can be particularly enhanced when utilizing a hot cavity where a thermal plasma consisting of surface ionized ions and thermionic electrons is generated. Although the surface ionization source can not produce multi-charged ions the advantage of this source is its simplicity and selectivity as only elements with low ionization potential are ionized.

The ionization tube of the source utilized at ALTO has a diameter of 3 mm and length of 3 cm. Ionization efficiency of this ion source for alkalis varies between 50% to 100% [118]. For gallium (Ga), the efficiency of this source measured at ISOLDE is 1% [119].

Plasma ion source

As introduced above, elements with low IP can be ionized selectively and efficiently with a surface ion source. But, there are many interesting elements with higher IP that require another type of ion source. Plasma ion source is a universal tool for ionization of many different elements. If the temperature T_p of plasma is high enough ($kT_p \geq$ IP), practically all atoms entering the plasma can be ionized by electron impact as shown in Figure 2.8 and charge changing collisions. Traditionally, the plasma is generated in an arc discharge. The electrodes are used up very rapidly. Therefore, these need to be exchanged frequently (several hours), which leads to problems in the environment of a radioactive ion beam facility where the target area is difficult to access. Nowadays, several other types of plasma ion sources with less maintenance cost have been applied successfully at ISOL facilities like MK5 so-called "hot plasma source" where the transfer line is maintained around 1900 °C. It also permits to ionize the less volatile elements. In a medium temperature version like MK3 and MK6 the transfer line is kept between 200 and 400 °C mainly for the selective separation of Cd and Hg elements. Finally, the MK7 owns a water-cooled transfer line kept at room temperature to condense all elements except the noble gases. In addition, the atoms to be ionized have to stay in the ionization region long enough. Therefore, the MK5 is very efficient for elements heavier than argon.

The plasma ion source applied in ALTO facility is MK5-ISOLDE [120]. The mechanism of its work is based on the Forced Electron Beam Induced Arc Discharge (FEBIAD) source that was developed by Kirchner and Roeckl for the GSI on-line separator [121]. It can reach high efficiency of around 50 % [121] for elements above argon and works stably even at low gas pressures (10^{-5} mbar). MK5 is called hot plasma source where the transfer line is maintained around 1900 °C . And it can ionize the less volatile elements. The whole source is heated by an electric current with 300-400 A flowing through a closed circuit consisted by a cathode, an anode, a transfer tube and a support of the target. The anode is a molybdenum cylinder connected with a voltage of 100 to 200 V where a vacuum of 10^{-4} bar is maintained. The end point faces the cathode composed of a graphite grid. The holes in the grid let electrons pass through the anode to form the arc discharge. The cathode is composed of a cylinder of tantalum wherein the atoms move and reach to the discharge chamber. The distance from the anode to the cathode is a few millimeters. The potential between the anode and cathode will remove electrons from the atoms. The ions are subjected to a potential difference of 30 kV at the output of the source and then translated to the mass separator [122].

Laser ion source of radioactive gallium isotopes

In case of the gallium atoms ionization by two-step excitation to the continuum, two laser beams are needed. Figure 2.10 presents the ionization scheme for gallium atoms composed of two steps: 1. the first excitation of the electron is from the electronic ground state $4s^2 4p\ ^2P_{1/2}$ (44.7%) or $4s^2 4p\ ^2P_{3/2}$ (55.3%) to the intermediate excited state $4s^2 4d\ ^2D_{3/2}$, which requires a UV laser with wavelength of

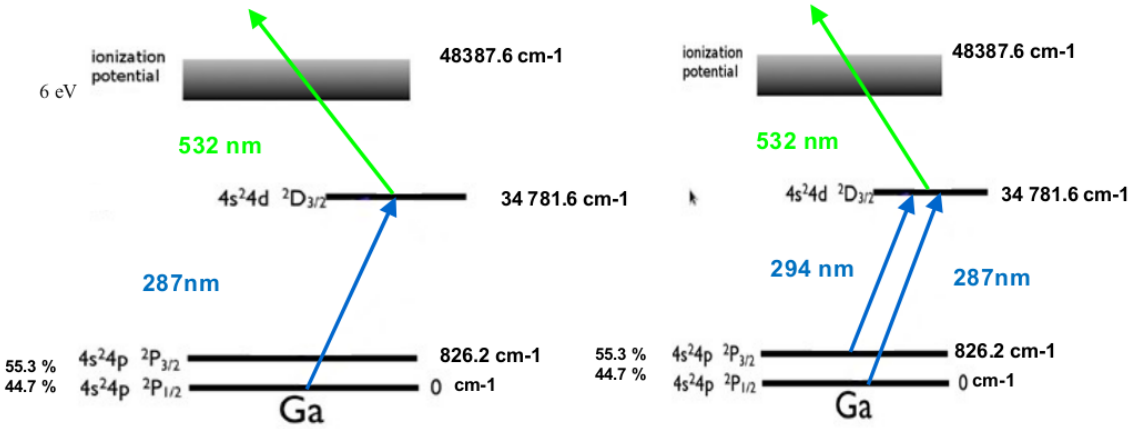

Figure 2.10 – Ionization scheme for gallium in two steps [117]. a) left figure: ionization from the ground state; b) right figure: ionization from the ground and metastable states. The maximum efficiency for the ionization of gallium atoms by laser ion source achieved at ISOLDE was 21% [110].

287.4 nm and 294 nm, respectively; 2. The second step is the ionization from the $4s^24d\ ^2D_{3/2}$ state to the continuum utilizing a green beam with 532 nm wavelength. The efficiency achieved at ISOLDE was 21% by the laser ion source for gallium atoms [110]. In order to ensure the maximum ionization of gallium atoms the new laser ion source system was built at ALTO.

The first successful use of laser ion source at maximum intensity of the electron beam performed at ALTO was in 2011 as described in [109] and below. A two-step nonresonant laser ionization scheme was applied (Figure 2.10a). The schematic view of the laser ion source system is presented in Figures 2.11 and 2.12. It includes two lasers: 1. The pump laser Edgewave Nd: YAG with model INNOSLAB IS2011-E aims to provide vertically polarized 532 nm laser beam with a frequency of 10 kHz and a pulse width of 10 ns [109]. The maximum power of the laser is 100 W; 2. The dye laser with commercial-type Lambda Physik model FL3002 can deliver beams with wavelengths from 300 nm to 900 nm. In order to obtain the wavelength of interest (UV light) a Rhodamine 6G dye was utilized. The dye laser contains an oscillator, a preamplifier and two amplifiers. The oscillator and the preamplifier compose a cell wherein the dye flows with high speed. This unit operates with two steps. Firstly, the oscillator, through pumping the cell, generates the laser beam with required wavelength. Secondly, the preamplifier amplifies the beam.

Two laser beams are obtained simutaneously in the following procedure: 1. Inside the Nd:YAG laser, the cavity generates a light with wavelength of 1064 nm. The frequency of this beam is doubled with a nonlinear BBO crystal (barium borate crystal BaB_2O_4) to extract as output green laser beam of 532 nm. The beam is split into two branches when coming out from the Nd:YAG (carrying 30% and 70% initial power for the first and second beam, respectively [109]). The first 532 nm beam is continually guided directly to the ionization tube. Because the cross section for this excitation is low ($\sigma \approx 10^{-18}$ - 10^{-17} cm^2) the power of the laser is relatively high with 30 W. The transmission efficiency of the laser beam to the ionization tube is about 67%, i.e. 20 W, when arriving at the ion source. 2. The second beam is sent to pump the dye lasers. After the 532 nm laser beam enter the dye laser, a beam with new, desired wavelength is generated (in gallium case is 574.8 nm) and then the beam

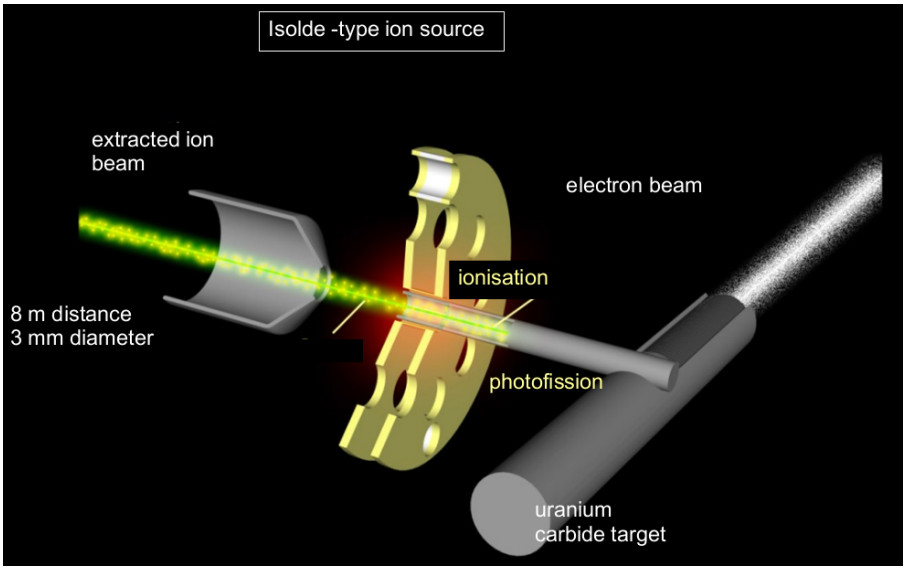

Figure 2.11 – Schematic view of the ISOLDE ion source.

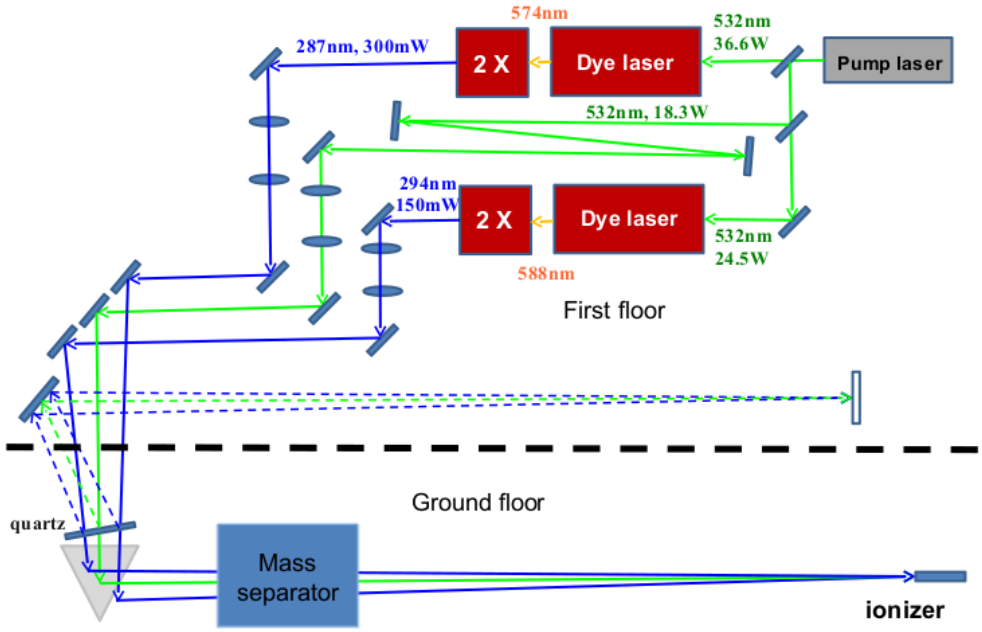

Figure 2.12 – Laser ion source at IJCLab ALTO [123] (figure from B. Lesellier).

is amplified also. 3. Following this, the dye laser beam with 574.8 nm is sent to BBO crystal to get the UV beam of 287.4 nm. The power of this laser is much lower than that of the Nd:YAG pump laser but sufficient because the cross section of this transition is higher ($\sigma \approx 10^{-14}$ - 10^{-12} cm^2). This UV light is also sent to the ionization tube. The transmission of this UV beam to the ionization tube was 24%, 120 mW at the ion source. The wavelengths of the laser beams are monitored by an optical spectrometer, "lambdameter". The ionization tube with diameter of 3 mm is placed 8 m away from the last optical element (prism) that sends beams towards the tube, see Figure 2.11. To manipulate the position of the beams in the tube, a partial reflection of the optical prism was monitored on a screen, placed 8 m upstream, to image the ionization tube.

The performance of the laser ion source was tested with a stable ^{69}Ga beams in one week time. The number of ions was calculated by measuring the current with two Faraday cups, one mounted behind the mass separator and the second one before the beam collection point on the tape. The ionization efficiency of ^{69}Ga with the laser was ten times higher than that with the surface ionization (as the current was 10 nA with laser). Figure 4.9 in the PhD thesis of Dmitry Testov shows the comparison of two γ-ray spectra measured with laser ON(red)/OFF(blue) for ^{80}Ga performed in 2014 [123]. One can easily notice a great improvement in the statistics and the purity of the spectrum when the laser is ON, which necessitates shielding of the mass separator to prevent the random coincidences of rubidium which was very abundant in the previous experiment and Vancouver facility.

A new way found to enhance the efficiency of the laser ionization, at least by factor 2, is the ionization from the metastable state $4s^24p\ ^2P_{(3/2)}$ (2.10 b) that is highly populated (excited) by the high temperature applied to the ionization tube. The population of this metastable level (55.3%) was estimated to be similar to the ground state (44.7%) [123]. So, in order to ionize the atoms from this metastable state, a second UV laser was installed 2.12, another dye laser. Then, the on-line laser ionization of Ga isotopes with the new dye laser system was operated again in November 2012 with a 287/294-532 nm scheme, see Figure 2.12. Note: One pump laser, 532 nm, was split into three beams as shown in 2.12. One with 532 nm (10W) was guided directly to the ionization tube with transmission of 60%. The rest of the power was equally sepratated into two beams pumping the two dye lasers, 287 nm (300 mW) and 294 nm (150 mW). The ϵ_{laser} measured, with the same ionization scheme, for the stable isotope was higher compared with the previous experiment in 2011, which is caused by the different alignment of the laser allowing it to ionize more atoms in the ionization tubes. Unfortunately, ϵ_{laser} drops suddenly possibly due to violation of laser alignment or synchronization, wrong wavelength, quality of dyes, etc. Although all these factors are considered, laser efficiency could not be brought back. Hence, in the end, the experiment using a radioactive beam, the ϵ_{laser} didn't exceed 5% [123].

1.3.4 Mass separator PARRNe

After exiting from the ion source, accelerated by a 30 keV potential, the interesting ions travel to the mass separator (PARRNe). The mass separator, an H-shaped electromagnetic dipole separator [124], is separated from the target-ion source unit by a 1.5 m thick concrete wall, which is a shield against background radiation including fission fragments, γ-rays and neutrons from the target accumulating

in the magnet. In addition, to suppress background contamination further protecting the experiments and personal environment, the mass separator is surrounded by a concrete wall with 15 cm thickness and a shield "pie". "Pie" is composed of a 10 cm polyethylene to slow down neutrons, then a 0.5 thick Cd layer to absorb neutrons and finally some lead bricks to absorb the γ-rays produced by the (n,γ) reaction in cadmium layer, which can decrease the neutron background precisely. The secondary beams in ALTO have good optical quality and are well focused, which is helpful for optimizing the transmission efficiency and the mass separator's resolution. The mass separator has a homogeneous and adjustable magnetic field B with deflection angle of 65° and radius of curvature ρ of 60 cm. The selection of targeted ions is done according to the deflection radius (the magnetic rigidity) when ions pass through the magnet, which is proportional to the mass number A and inversely proportional to the charge of the ion q as described as $B\rho = \frac{mv}{q} = \frac{\sqrt{2mE}}{q}$. Because most of the ions have charge 1^+, those are mass separated. The separation parameter Δx between two isotope beams of masses m and m + Δm is expressed as $\Delta x = D\frac{\Delta m}{m}$ where D is the dispersion of magnet with value 1370 mm. For example, Δx for the masses 100 and 101 is 13.7 mm [125].

In the γ-spectra, there is no contaminations due to ^{80}Kr deexcitation populated by ^{80}Rb Electron Capture (EC) beta-decay as there is no peak observed belonging to ^{80}Kr. Even though the strongest γ-line 616.8 keV ($2^+ \rightarrow 0^+$ in ^{80}Kr with Iβ^+=21.2%[126]), there is no event observed in the β-gated spectra of this work. A beam composition 78% of ^{80}Rb was produced in TRIUMF proton fission facility with 480 MeV proton beam while ^{80}Ga production ratio was only 22%[127]. It was contributed by surface ionization effect since the transfer tube is a W ionizer heated up to 2000 °C, which ionizes alkalies and also other elements with particularly low first ionization potentials selectively. In principle, the Rb isotopes can be stopped within the separator chamber that was additionaly shielded with lead bricks. However, some of the γ-rays of Rb decay appear sometimes as a random coincidences with γ events. A shielding around the focal plane of the magnet in ALTO allowed us to have no contaminants from the Rb isotopes. In addition, the contaminant γ-rays can be discriminated through their half-lives and γ-γ coincidence technique.

1.3.5 Beam line for TETRA, BEDO, LINO, POLAREX and MLLTRAP

Two new beam lines for the BEDO/TETRA terminals were constructed at IJCLab-ALTO in addition to the one existing before. The detailed optimum values of these elements of the beam line optics set for Ga isotopes beams can be found in [123], table on page 87. During the ^{80}Ga and ^{134}Sn beam periods, the temperature of the source was set to ≈2000 °C and the extraction potential was around 30 keV. Extracted fission fragments travel firstly through quadruples Q_1 and Q_2 to a Faraday Cup (CF1) placed just afterwards. Once the optimal values for T_{target}, E_{extr}, Q_1, Q_2 are found, the current at CF1 will reach the maximum. Then the beam is led further to Q_3, Q_4 and the following mass separator. Note: Q_3 is eliminated from the beam guidance and governed by the DAQ system, which allows to deflect the beam as the beam is "ON" when HV(Q_3) = 0 and beam "OFF" when HV(Q_3) = 1 kV. Q_4 is an important quadrupole because that it impacts the beam right before the mass separator. Generally, the applied high voltage for HV(Q_4) = 0.2-0.3 kV is relatively lower when compared with other quadruples. After mass selection (separator) and CF2, the secondary beam is

guided by deflector to BEDO/TETRA or straight forward to the old ALTO-line. After Q9 and Q10 the beam is deflected again by the deflector (Deflecteur) with 60° in order to achieve a large operation space. Then the beam's heights are corrected by the "steerer" followed by a beam profile detector, BP6, that can be moved inside the beam line by remote control. Alternatively, CF6 can also be used at the same position to monitor the beam current. Normally in this section of beam transport, the fluctuations of the beam profile between BP6 (CF6) and BP8 (CF8) are under control. Between them the beam passes through Q11 and then a "Kicker" kicks the beam to the Bender that guides the beam finally to the TETRA/BEDO terminal. Two pairs of slits are placed to cut the beam for the purpose of making it exactly the size of the tape (1 cm × 1 cm at maximum). In the end, CF9 is the last Faraday Cup in the radioactive beam line located just before the detection system. Couple of CFs are mounted sectionally monitoring the beam quality to guarantee the best transmission rate. The final transmission rate obtained between CF2 and CF9 was 70% [123]. There are 42 wires composing the beam profile monitor system including the beam distribution both in vertical and horizontal directions. Note: The theoretical magnetic field of the separator usually needs to be adjusted using rations of isotopic abundances for two neighboring masses, e.g., A = 80 and A = 82 by the current in CF2.

2 Experimental setup

The β-delayed γ-spectroscopy of ^{80}Ge was performed taking advantage of the presence of PARIS at ALTO in July 2019 alongside the β-delayed γ-spectroscopy of ^{80,82,83,84}Ge with beam time 10.03h, 4.90h, 39.03h, 15.52h individually. This research is a series study of gallium isotopes in BEDO (BEta Decay studies at Orsay). This program aims to investigate the nuclear structure of the neutron-rich region, in the vicinity of ^{78}Ni.

BEDO is a state-of-the-art movable-tape-based experimental setup currently operated at ALTO, which provides opportunities to build a more complex detection system with radioactive beam offered by the completion of a new secondary beam line sections at ALTO. BEDO is dedicated for nuclear structure studies after beta-decay of neutron-rich fission isotopes produced at ALTO. The trajectory of the tape in BEDO is set to maximize the available space around the beam collection point, ideally 4π, allowing the closest positioning of different types of detectors to reach the maximal efficiency. The mechanical support frame was also designed to host various detector assemblies: the beam collection point is surrounded by a cylindrical plastic scintillator for β detection as trigger of beta-decay event, 2 HPGe and 3 PARIS clusters comprising 27 $LaBr_3$ + NaI phoswitch detectors for fast timing and high-energy γ-rays measurement. In this hybrid assembly, HPGe was responsible for 0 - 6 MeV energy region, using its high energy resolution advantage to suppress the descendants' contamination, and PARIS was for 6 - 10 MeV pure precursor decay region. This whole Q_β window covered detection setting aims to extract the detailed information of excited states and to address the Pandemonium effect simultaneously.

2.1 Tape system

The ^{80}Ga source was built by collecting the beam on an aluminum-coated mylar tape at the center of the array. The source was surrounded by a cylindrical (4π) 2 mm thick plastic detector for β-tagging. γ-rays were detected by a set of HPGe detectors and the PARIS array. During the measurement period, the daughter and granddaughter nuclei also experience β decay. Therefore, in order to supress unwanted radioactivity from these isotopes the movable tape system was necessary with a cycle move setting that depends on the lifetime of the interesting isotopes to be studied.

The Al-coated mylar tape is rolled on two reels above the detection system. As it goes down the collection point it collects the beam and extends a bit farther down and turns back again storing in the second reel. The system is kept in vacuum, the same as the beam line. This design, moving in cycles to keep the previous collection tape 1.3 m away, is to obtain the clean spectrum of interesting nuclei and to try to keep the contaminations of the descendants at a minimum. The time required for tape once-cycle move is 2 s as shown schematically Figure 2.13. The tape system gives a signal when it starts moving. This signal is split into two for FASTER system one working as tape moving and the other one as moving finished (beam collecting starts). Therefore, the event building, first step of data analysis, should start from the second signal (beam collecting starts) and end at the next signal (tape moving starts). This signal jumping procedure in the events building process aims to exclude the data generated during the tape moving period.

Tape setting

$$N_t = N_0 e^{-\frac{t \ln 2}{T_{1/2}}} \tag{2.4}$$

The time choice of one cycle including measurement period of background, beam collection and decay depends on the half-life of the isotopes of interest and also the half-lives of the daughters. So, the determined half-lives are needed as well. Actually, the choice of cycle is a balance selection between the wasting of beam time (2 s for tape moving every cycle) and the spectrum purity (avoiding the contamination from descendants). The former prefers a longer cycle while the later benefits from a shorter cycle. The longer cycle can reduce the beam wasting during to tape movement and consquently can obtain more possible γ - γ coincidence events but at the same time a longer cycle generates more descendants and more peaks will appear in the spectra recorded with detectors. The maximum speed of 1 m is 0.1 s with a precision of about $\pm$1 mm for ALTO tape system [123].

One law that can be obtained from the radiation rule as shown in 2.4 is that 50% precursors decay after $1T_{1/2}$, 75% after $2T_{1/2}$, 87.5% after $3T_{1/2}$, 93.75% after $4T_{1/2}$ and 96.875% after $5T_{1/2}$. So, it would be better if the cycle can be set less than $1T_{1/2}$ of daughter and granddaughter nuclei.

Background measurement: 0.5 s is set usually for the background measurement, which is useful for background substraction when counting the events' statistics during Bateman equation handling process (see details in the data-analysis section).

Beam collection: the number of nuclei present on the tape increases owing to the beam collection and also decreases simultaneously owing to the radioactive decay Eq. 2.4. As shown in the formula 2.4, the amount of decay in unit of time is proportional to original accounts, which means the number of

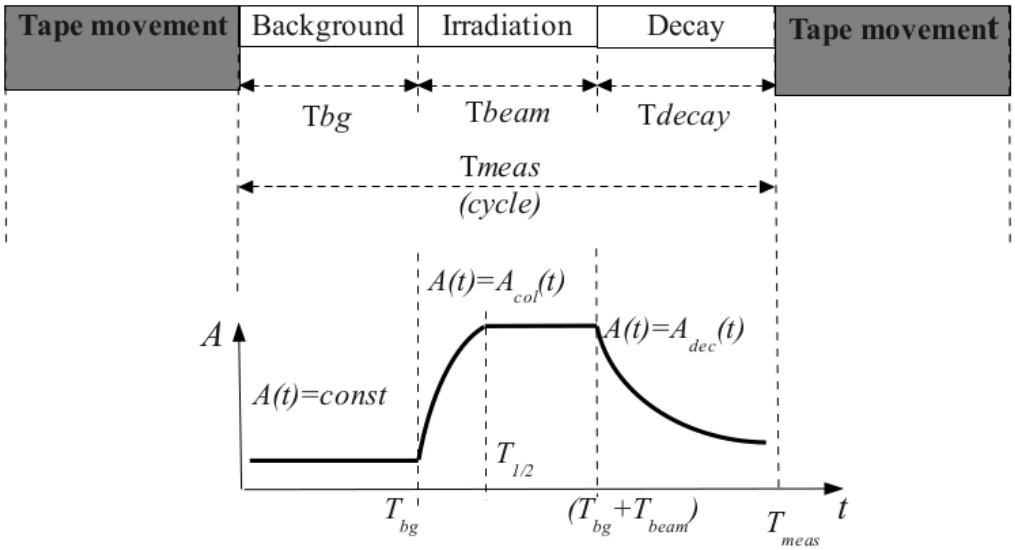

Figure 2.13 – Schematic diagram of tape system movement showing the particles' activities of three periods: background measurement, beam collection, decay process [123].

decay in unit of time increases along with the precursors' accumulation but the beam injection rate is stable. So, in the end, the particles' activity curve will reach a flat level, balance (saturation) between injection and decay, as shown in Figure 2.13. The time needed to reach this saturation depends on the beam intensity and the halflife of the nuclei. Hence, this beam collecting period can be set as long as possible but trying to guarantee the time of the whole circle being less than $1T_{1/2}$ of daughter and granddaughter nuclei.

Decay process: decay time can be set $\sim 3T_{1/2}$ of precursor to ensure the 87.5% decay possibility for the last injections. However, it would be better if it can be compatible with the former principle: whole cycle being less than $1T_{1/2}$ of daughter and granddaughter nuclei.

Table 2.1 lists the details of tape setting of ^{80}Ga during the experiment. The half-lives of $^{80g+m}$Ga is 1.9(1) s and 1.3(2) s, ^{80}Ge is 29.5(4) s and ^{80}As is 15.2(2) s. The $\%\beta^- n$ (P_n) of ^{80}Ga is 0.86(7) [126].

Table 2.1 – Choice of tape cycles

Isotope	T_{bg} (s)	T_{beam} (s)	T_{dec} (s)
^{80}Ga	0.5	5	5

2.2 Detector system

2.2.1 Beta detector

The calculated geometrical efficiency of the β detector is $\sim$70% of 4π. Another unique feature of BEDO as shown in Fig. 2.14 and TETRA is the tape setup is transparent, material as Poly (methyl methacrylate) (PMMA) $(C_5O_2H_8)_n$, which helps to monitor visually tape movements and facilitate repairing in case of accident. However, the outside of the plastic has to be covered by thin layer of

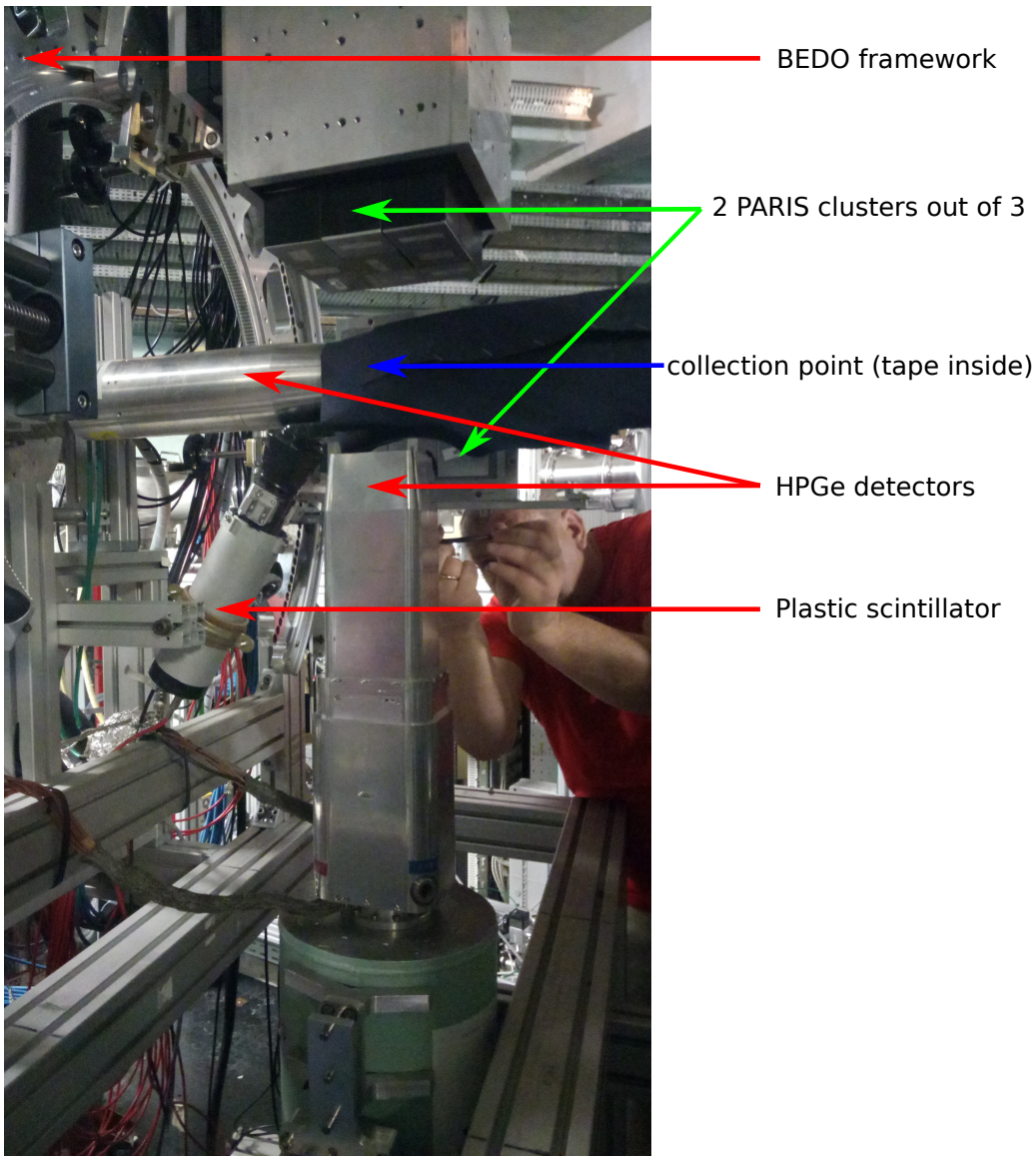

Figure 2.14 – BEDO decay station mounted with PARIS array coupled with HPGe.

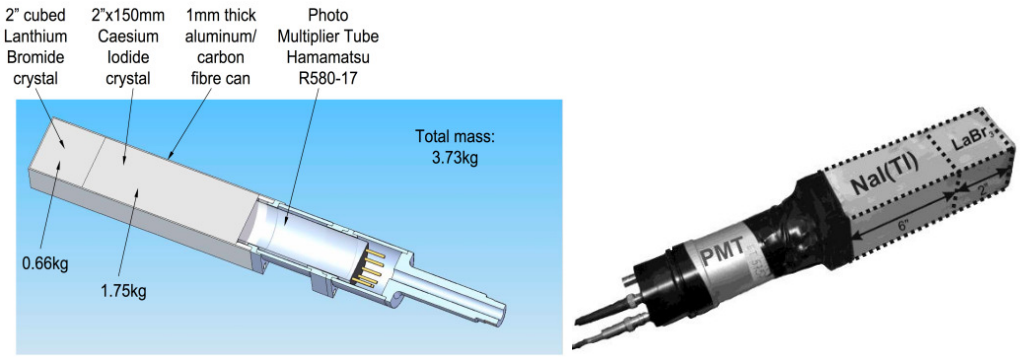

Figure 2.15 – Schematic and real diagram of single phoswich of PARIS detector [128].

dark material (a few micron thick), consequently, the energy deposited from outside β particle in the scintillator is insufficient for ionization and/or the light from outside seen by the photomultiplier is also too weak and then is cut by the discriminator threshold. Another factor to reduce the contamination of light, emitted from detectors, in PMT is the relative big distance (50 mm and 74 mm for HPGe and 120 mm for PARIS) between the source and the γ detectors. That means that PMT is relatively far from detectors. So the light contamination from the detector is negligible.

2.2.2 High-purity germanium detector

Two High-purity germanium detectors were used during the experimental measurement as shown in Fig. 2.14, one Clover in the bottom of the focal plane and another Coaxial faced with the beam direction. The idea is that one can combine the advantage of HPGe (high energy resolution) and advantages of PARIS (high detection efficiency and fast timing) together. It makes the hybrid detection system have the abilities to satisfy many requirements: γ-γ coincidence from HPGe-HPGe detectors for low energy decay level scheme building, low-high energy coincidence through putting a narrow gate on HPGe (4 keV) for looking for ultra-high-energy γ-rays. It makes the construction of a whole Q_β window covered decay level scheme possible.

2.2.3 PARIS modular array

PARIS is a novel 4π γ-ray calorimeter that is composed of phoswich detectors with two shells each: the scintillators with advanced technology ($LaBr_3$(Ce) or $CeBr_3$) in the inner volume providing high efficiency, excellent time resolution and relatively good energy resolution simultaneously in a large energy range and a more conventional scintillator (NaI) in the outside shell, as presented in Fig. 5.19.

PARIS consists of "phoswich" detectors each with two components: a frontal 2 * 2 * 2 inch $LaBr_3$(Ce) scintillators coupled to a 2 * 2 * 6 inch NaI scintillator. However, the light outputs generated in both scintillators are collected by a common photomultiplier PMT. One crucial advantage of PARIS is its high efficiency proportional to the solid angle covered by the detectors. Another characteristic property is its high granularity, which allows for the measurement of gamma-rays multiplicity that is important for the determination of the spin and parity of excited states. In the first experiment, three clusters including 9 phoswich detectors each was used in conjunction with HPGe detectors. More

information is available in the website of PARIS collaboration [128].

2.3 DAQ system

2.3.1 electronic system

Plastic detector 4π β: the signal from the plastic detector was sent directly to FASTER and passed through CRRC4 filter [129]. This signal was applied in the analysis process as the trigger of β decay.

Germanium detectors: the signal from the detector was first sent to the inside preamplifier located close to the crystal in order to reduce the thermal noise and to obtain an optimum charge collection. After the preamplifier, the signal was sent to the Linear Amplifier where it was amplified and shaped into semi-Gaussian shape. The decay part of the signal was determined by the feedback circuit of the preamplifier. In order to avoid so-called undershoots, through the differentiation of the exponential tail from the preamplifier, which may cause the amplitude defect when the second signal arives just after the first one, the pole-zero cancelation circuit was utilized. Then the signal was sent to the fast digital acquisition system FASTER, combining TDC and ADC together, and then was digitalized by 14 bit, 125 MHz converter under triggerless model.

PARIS detector: each photoswich of PARIS cluster was connected to a photomultiplier (PMT). The signal from each PMT was sent to FASTER directly with one output but two gates for the signal integration corresponding to a longer one [-20,800] ns and a shorter one [-20,100] ns, which was set for later data analysis: extracting the signal from $LaBr_3$(Ce) and NaI from one PMT and output label.

2.3.2 Digital modular acquisition system: FASTER

The pre-amplified, anode or amplified signals from the electronics were sent to fully digital acquisition system called FASTER (Fast Acquisition System for nuclEar Research) developed at the Laboratoire de Physique Corpusculaire (LCP) in Caen, France where they were converted into numeric format: see figures 2.16 and 2.17. It is used to record the relevant observables including deposited energy and time of each hit extracted online from the traces. FASTER has been built to be modular and integrated to satisfy the needs of nuclear experiments particularly those combining different types of detectors together with significantly different characteristics. Each card has 4 channels. The energy signal is coded in dual channel 12-bits up to 500 Msps ADC capability, which is ideally suited for time of flight, charge, and energy measurement. The number of bits for the amplitude and the sampling rate are two important properties used to define the performance of a fast digitizer as the former defines the amplitude resolution and the later defines the time resolution. The FASTER system is a triggerless system. Each detector including plastic scintillator, germanium detector and $LaBr_3$(Ce) is considered as an independent source for which the physical signal assigned with an absolute time is coded. The time accuracy, according to designed goal, can reach 250 ps for $LaBr_3$(Ce) detector. The FASTER card can encode up to 500 million events per second per channel, which is above the counting rate observed in β-decay experiments.

FASTER digitizer is a flash analog-to-digital converter recording samples of the input signal with a super high repetition rate and transfering them for signal processing. It is a modular digital acquisition system based on a synchronized tree model aiming to handle the medium size experiments from

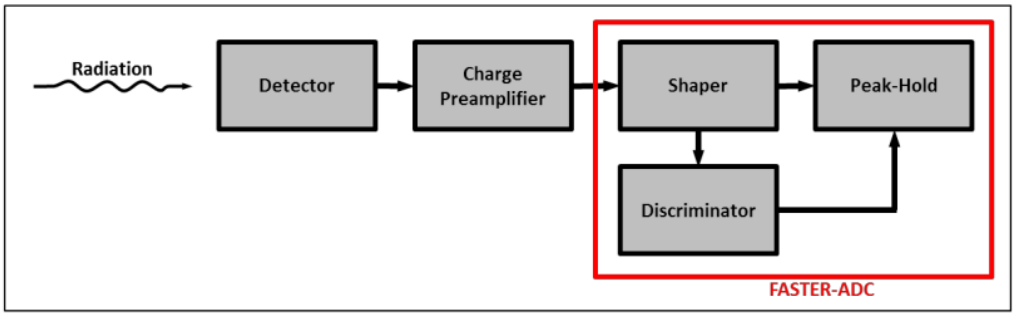

Figure 2.16 – Essential modules of FASTER in a spectroscopy set-up [129].

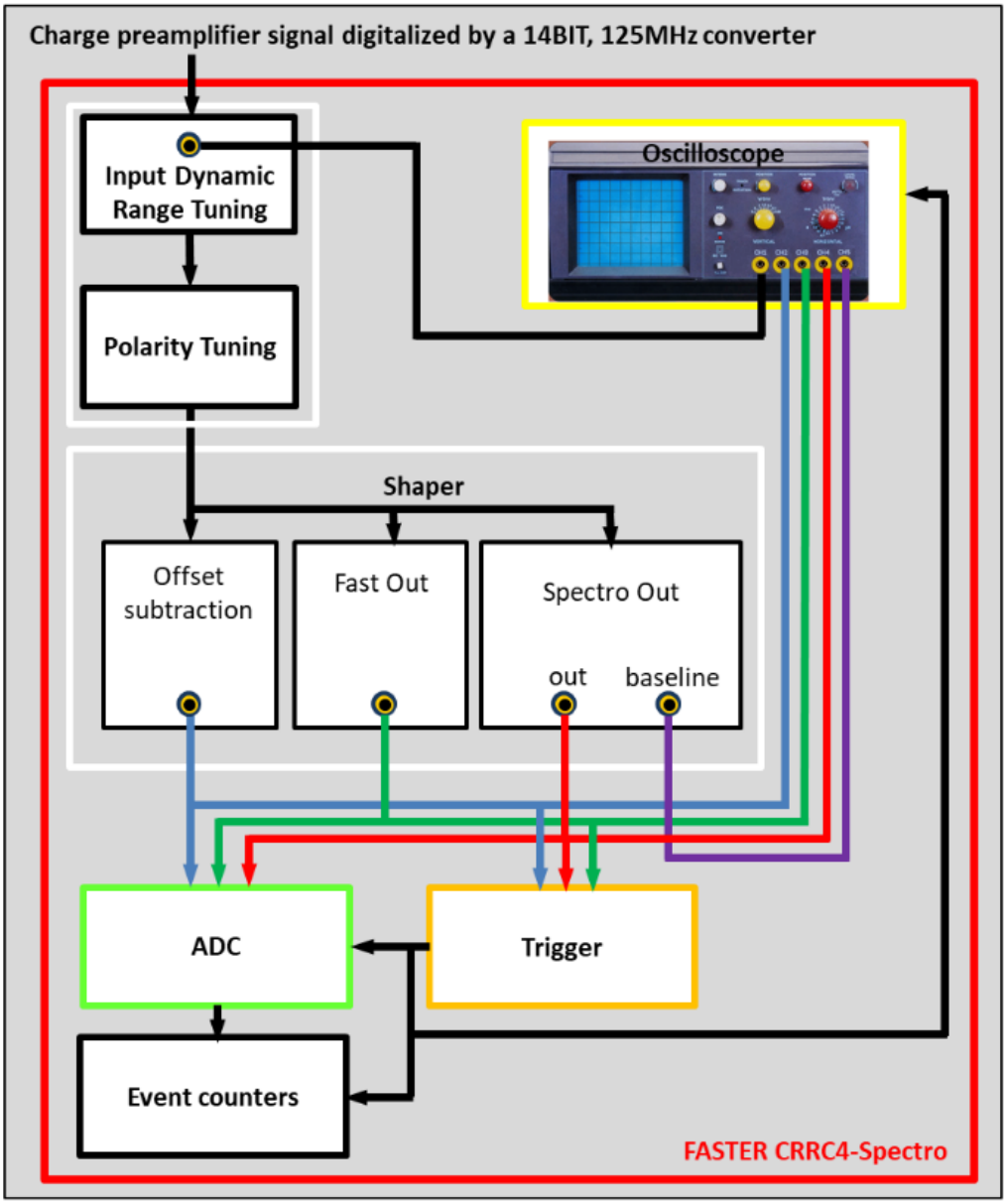

Figure 2.17 – Diagram of the FASTER-CRRC4-Spectro signal processing [129].

one to several hundred detectors. It includes n-ary tree where each node performs the following functions: 1. synchronize and aggregate the data streams received from the daughter nodes; 2. make decision on the resulting data stream; 3. deliver the resulting stream to the parent node. In addition, FASTER is a triggerless system where all the data is timestamped, allowing nodes to perform online correlations between measurements according to user-defined time windows. Using components of standard hardware and software, users can build an acquisition system tailored to their needs. Standards like UDP/IP protocol, Ethernet gigabit connection, microTCA crate or standalone box and VITA 57 daughter boards can be used [129].

The FASTER DAQ system contains two different types of cards that can be connected to a single motherboard [129, 130]: 1. CARAS daughterboard: The main character of this card is a 500 Msps 12 bits digitizer discretizing the incoming pre-amplified signals. Then different algorithms are applied to mimic the operations performed by an ADC, QDC or TDC and those can be uploaded on an embarked FPGA processor. Note: ADC converts a voltage into a digital representation. However, in experiment, we have a current and we are interested in the total charge. Hence, we need a QDC (Charge to Digital Converter) that is essentially an integration step followed by an ADC and its integration requires limits. In the context of the first experiment of the PhD thesis, "Beta-decay study of ^{80}Ga in BEDO" (more detail in next section), these cards are used to process the signals from scintillator detectors. For the PARIS ($LaBr_3$(Ce) + NaI) signals, the QDC algorithm is used, which features a digital constant fraction discriminator mode with a zero-crossing interpolation to provide the best time resolution. Same QDC/TDC way was applied to 4π plastic detector to extract best time resolution as signals from plastic detector is the trigger for beta-decay, time beginning of event building. For the beam ON/OFF signals, an ADC integrator-differentiator algorithm called CR-RC4 was used. In addition, the CARAS cards also possess a "RF" module that digitizes the high frequency (2.5 MHz) signals of the beam producing time stamps and sends them to the data stream. Due to the period measured with a ps precision, every beam-time-stamp (precursor-time-stamp) can be precisely reconstructed offline also in later data analysis process, which provides a precise reference clock for an entire measurement.

2. MOSAHR daughterboard [129, 130]: The main character of this card is a 125 Msps 14 bits digitizer to process the incoming pre-amplified signals. But the FPGA can only accept the ADC algorithm such as trapezoidal or CR-RC4 to calculate the amplitude and time stamp of each signal. In both experiments, all the signals from germanium crystals are sent to these MOSAHR cards. In order to minimize low-energy walk and obtain the best timing properties, the trapezoidal filter was selected because that it uses a constant fraction discrimination module instead of the leading edge discriminator module. All motherboards were located in one μTCA crate. The DAQ can be run in two modes: disk and setup model. In the setup mode, a standard FASTER graphical user interface can be used to adjust tuning parameters, implement a trigger condition and visualize online spectra during the experiment period using the versatile ROOT Histogram Builder (RHB) software [131]. The disk mode skips the graphical part and delivers the data sent by each motherboard and then writes it on a data server. The transfer rate from the crates to main operating computer is about 70 Mb/s when the rate of writing to disk ranges from 5 Gb/h to 100 Gb/h depending on the trigger conditions. This limitation corresponds to the maximum transfer rate achieved by using two coupled 1 Gb optic

fibers connection between crates and server. So, the maximum counting rates obtained during the experiment in each detector are: 3 kHz for the LaBr3, few hundreds Hz for the HPGe, 7-8 kHz in plastic.

3 Experimental data analysis

Sommaire

1 Outline

The FASTER Data Acquisition system (FASTER DAQ) registers all signals on each channel independently in a triggerless mode. Events are given a time stamp and are registered in chronological order in the specific FASTER system format. Since the data analysis was performed using the ROOT software, the data generated by the FASTER DAQ in the FASTER format were converted to a ROOT format for further treatment. The data were stored in the ROOT trees (TTree) and each one has several branches containing specific information like two ADC values with long and short signal integration time, time, label (identification of detector). The data type of each branch was declared according to the size of the information it contained, which helped to optimize the size of the data through compressing each branch independently. In particular, the branches could be read independently from each other according to the user's needs. The data analysis was separated into two steps: 1. Physical event reconstruction (detectors' time alignment, energy calibration and coincident with β particles). 2. Further data sorting and organizing according to physical events relationships including building various coincidence matrices, applying clover and PARIS addback procedures and so on.

The first step of the data analysis is the construction of physics events from raw data. An event will be considered physical if it originates from the beta decay of a nucleus. So, considered events are β particle, γ-ray and neutron. During this process the reference time (clock time zero) adopted is the signal from β detector considering the β particle is the signal of beta-decay and the fast response of scintillator (sub-ns level). A window length of 500 ns was adopted for the event building in order to avoid losing relevant data (since at least one excited state of ^{80}Ge is already known to be a ns isomer). As said previously a physical event is considered originating from the beta decay of a nucleus collected onto the tape, this means one should consider an additional condition related to the tape cycle : with the ^{80}Ga setting, the beta particle should be detected in a time window corresponding to the duration of the beam collection + 10 s.

The second step consists in building coincidence relationships between physical events like γ-γ matrices filling (HPGe-HPGe, HPGe-$LaBr_3$, HPGe-$LaBr_3$(cluster addback), HPGe-$LaBr_3$(addback all), HPGe-$LaBr_3$+NaI, All-All and so on), clover, PARIS addback and fast timing and so on. In this step, the time window for γ-γ coincidence was set as 50 ns which is enough considering the time resolution of detectors as introduced in experimental setup section.

In the two following subsections, the procedure of the data analysis is described in detail. Firstly, I will detail all corrections of calibration procedures applied to the raw data. In the second part, I will detail the analysis procedure and the main information extracted from it with an emphasis on the ^{80g}Ga and ^{80m}Ga lifetime determination and the determination of the individual feedings from both beta decaying states.

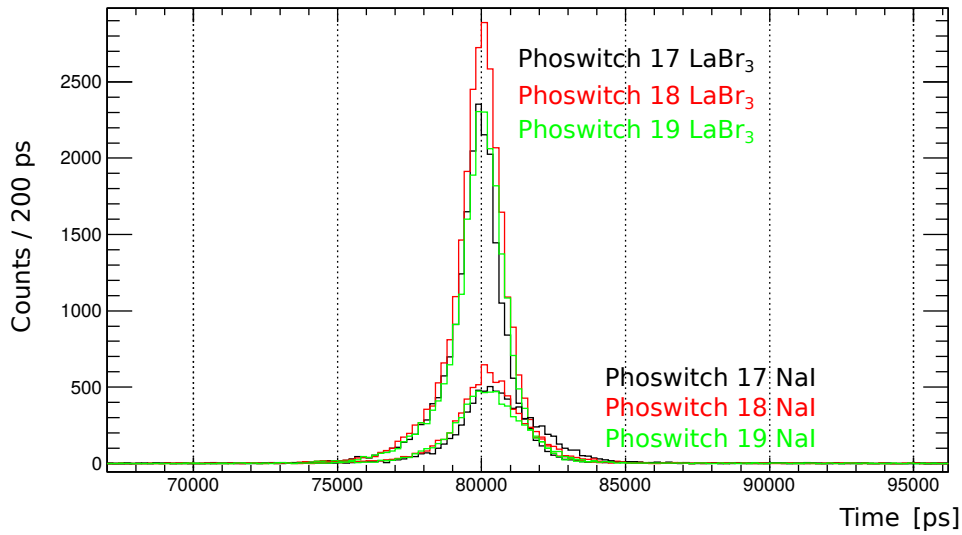

Figure 3.1 – Time signal distribution of a few of NaI or LaBr3 channels relative to β particle signal, arbitrarily aligned to the 80 ns position. The 1109 keV γ-ray was used during this alignement process in order to avoid γ-rays from 8^+ isomer.

2 Detectors calibration and correction

2.1 Time alignement of detectors

It is essential for the whole data analyzing process to have the same reference time for each detector. Delays may appear between different signals due to several reasons like different signal rising time or cable lengths. It is also essential to build a clean β-gated γ energy spectrum, free from the lines originating from activities located outside the beam collection region (room background, or accidental collection off the tape). Figure 3.1 presents the results of time alignment of labels 17, 18, 19 corresponding to three PARIS phoswich channels. They were aligned to 80 ns arbitrarily. For each phoswich the times of $LaBr_3$ and NaI events were corrected separately. The quality of time corection is critical for fast timing analysis especially for $LaBr_3$(Ce) to extract lifetime of state around 1 ns. Otherwise, one will obtain a worse time resolution after summing the spectrum from different channels together if the quality of alignement is not good enough. Then, the $LaBr_3$ can only be used individually during the fast timing analysis process. The cost is losing statistics.

After this step, one can build the β-gated γ-spectrum and perform β-γ-γ coincidence with time window 50 ns.

2.2 Beta detector

Time resolution

The time resolution of the plastic detector can reach ps magnitude, the time identification limit of FASTER DAQ.

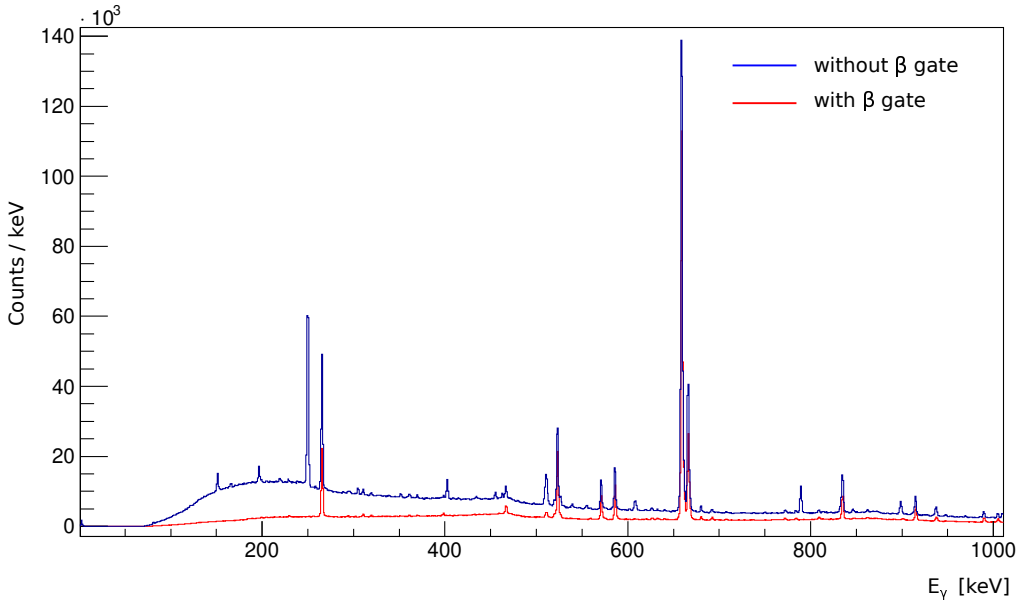

Figure 3.2 – The comparison of γ spectrum from ^{80}Ge between β-gated and without β-gate demonstrates the role of β-trigger in the suppression of background contaminations.

Detection efficiency

An effective detection efficiency for the beta detector can be obtained by comparing peak surface areas in beta-gated and beta-ungated spectra (see Fig. 3.2). In the end, the efficiency of the BEDO cylindrical plastic detector for this is 74.6(2)% as shown in Figure 3.3. In principle, if the β particles have a sufficiently large energy, it will deposite energy in plastic and generate a signal. Then the detection efficiency will be just geometric efficiency. However, the β particle energy spectrum is continuum. So the β with energy below the plastic threshold will not be detected. The parameters determining the shape of β spectrum include Q_β, S_n, precusor nucleus's and daughter's structure. Therefore, the ϵ_β would be different during studying different neutron-rich nuclei with diverse Q_β values. Hence, ϵ_β should be determined individually for each mass (A) extracted directly from γ and γ-β gated spectra comparison method instead of from source like ^{60}Co.

2.3 High-Purity Germanium (HPGe) detector

Time resolution

The determination of the HPGe time resolution is important to perform half-life time measurement of excited states, at $\approx$ dozens of ns or μs magnitude, and to decide the time window for the event building and γ-γ coincidences. Figure 3.4 presents the distribution of the time differences between HPGe and beta-detector events. Note that as the obtained plot includes all data, the time structure around 65 ns must be interpreted as due to an instability in the response of detectors or FASTER DAQ. But it has no effect when operating 500 ns time window events building and 50 ns γ-γ coincidence. The green curve in Fig. 3.4 is distinguished by its lowest staistics which is due to a relative larger distance

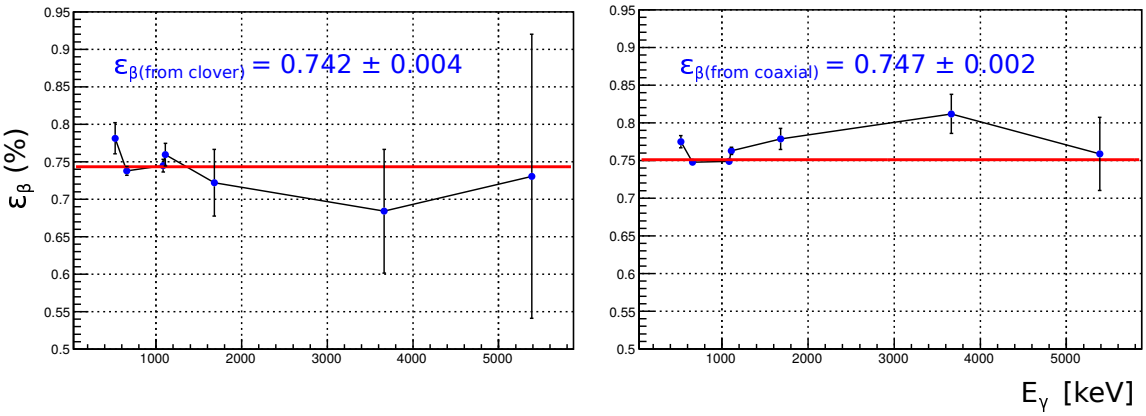

Figure 3.3 – β detection efficiency of 4π plastic scintillator in BEDO extracted from clover and coaxial HPGe.

to the CLOVER end cap, hence a lower geometrical efficiency. The extracted time resolution value for the CLOVER and Coaxial HPGe, as shown in table 3.3, are 12.65(5) ns and 10.39(2) ns respectively.

Energy drift and linearity (ADC instability)

There is a energy drift (maybe due to some ADC instability) in HPGe detectors found during the experiment and a pathological "sine wave figure" appeared when drawing the residuals values between the calibrated values (when all files using same calibration parameters) and the evaluated values from NNDC [126]. Figure 3.5 presents a typical example of an energy drift for a given HPGe channel between "run091(0001)" (blue) taken at 0h - 1h on 05/07/2019 and "run104(0008)" (red) taken at 14.23h - 15.23h on 05/07/2019. Therefore, if the γ energy calibration of all these data is taken from the same calibration parameters obtained from the source calibration run of the beginning or the end of the experiment, there will be a $\sim$1 keV energy walk appearing as presented in Table 3.1. Consequently, the energy resolution of the total sum γ-spectrum including all data will be deteriorated seriously.

Table 3.1 – Calibrated γ energy values of different files with same calibration parameters. The numbers in parentheses, (), are experimental error bars.

Evaluated values	659.14(4) (keV)	1083.47(4) (keV)	3664.37(7) (keV)
File run104(0008) values	659.15(0.27)	1083.48 (0.29)	3664.28(0.57)
File run091(0001) values	659.99(0.27)	1084.96 (0.29)	3668.26(0.57)
Residuals(between run091 and run104)	0.84 (0.38)	1.48 (0.41)	3.98(0.81)

Energy resolution

High-Purity Germanium detector (HPGe with high purity 99.999%) is known for its high energy resolution under cooling condition 77 K with liquid nitrogen. The effects of the observed energy drift highlighted in the previous subsection prevents any global energy calibration including linear, quadratic and Spline methods. Due to this fact, the only solution is to separate the data into 4 subgroups inside which the energy drift remained limited as 1: run081, run91 and run092; 2: run093, run094 and

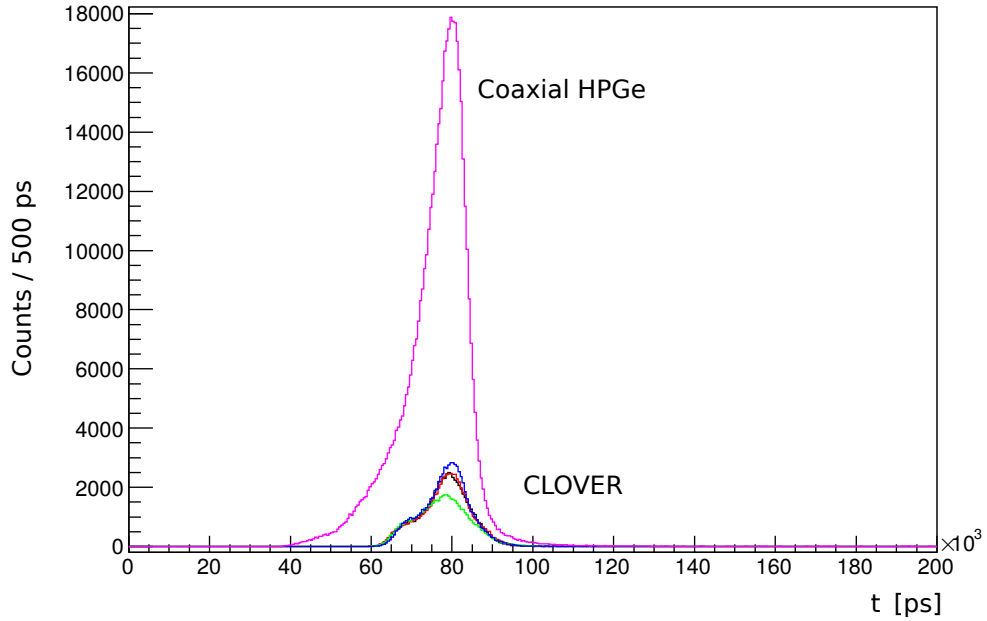

Figure 3.4 – Time resolution of γ detectors at 1109 keV: CLOVER and Coaxial HPGe.

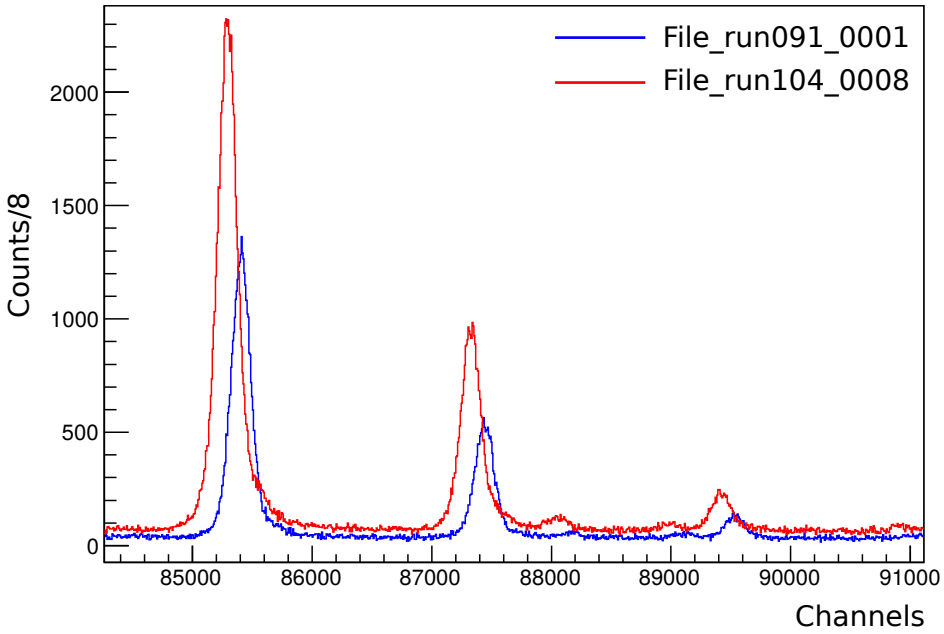

Figure 3.5 – Plot of γ-spectrum from Coaxial HPGe detector as blue one from file run091 and red one from file run104. The strongest peak corresponds to 1083 keV γ-ray belonging to ^{80}Ge.

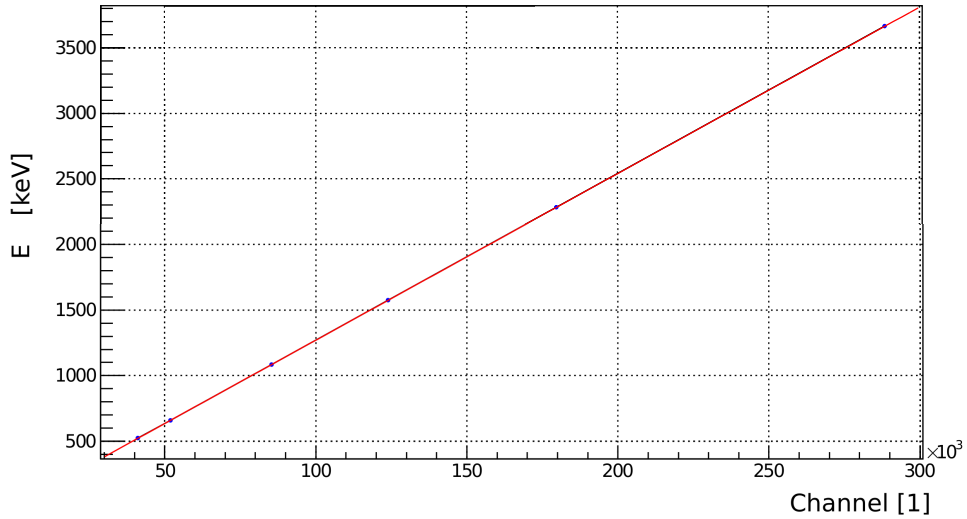

Figure 3.6 – Linear calibration of coaxial HPGe using inner-source.

run095; 3: run104 and run105; 4: run106 and then perform the energy calibration individually using a selection of reference lines in the A = 80 decay chain. The known γ-rays adopted to perform the calibration are 523.18(4), 659.15(4), 1083.47(4), 1573.57(5), 2283.22(6), 3664.37(7) keV as shown in Figure 3.6, which was selected to cover a large energy range. The results of calibration were checked with other γ-rays of ^{80}Ge and also with γ-rays from daughter nuclei activities because the data of these daughter nuclei were from other, independent decay experiments. After applying this calibration procedure, the corrected data show a very linear channel-energy relationship up to 6 MeV, which means that a linear calibration is sufficient. Table 3.2 shows the quality of the energy calibration and that the residuals related to evaluated values remain below 0.5 keV. The energy resolution of HPGe detector is presented in Figure 3.7 achieved from summed spectra including one clover and one coaxial HPGe. The FWHM is 2.55 keV at 1109 keV.

Table 3.2 – Residuals of γ-rays between evaluated values from ENSDF [126] and this work; (), are error bars.

Nuclei	^{80}As	^{80}As	^{80}Se	^{80}Se	^{80}Ge
Evaluated values	265.36(7) (keV)	936.97(8) (keV)	666.2(2) (keV)	1645.2(3) (keV)	4443.4(3) (keV)
This work	265.4(3)	937.3(3)	666.2(3)	1644.8(3)	4443.6(7)
Residuals	-0.09(31)	-0.47(31)	0.03(36)	0.36(42)	-0.21(76)

Detection efficiency

The detection efficiency of the HPGe detectors was measured using ^{152}Eu sources placed at the outside the tape chamber 1 cm away from the collection point in the coaxial HPGe direction. However, for ^{80}Ga decay study, the Q_β value is 10312(4) keV and S_n of ^{80}Ge is 8080(4) keV [126]. Therefore, γ-ray detection at energies up to 10 MeV is required. As known, the higher the γ-rays' energy is, the harder an experimental determination of the efficiency becomes. In this experiment, the HPGe detection

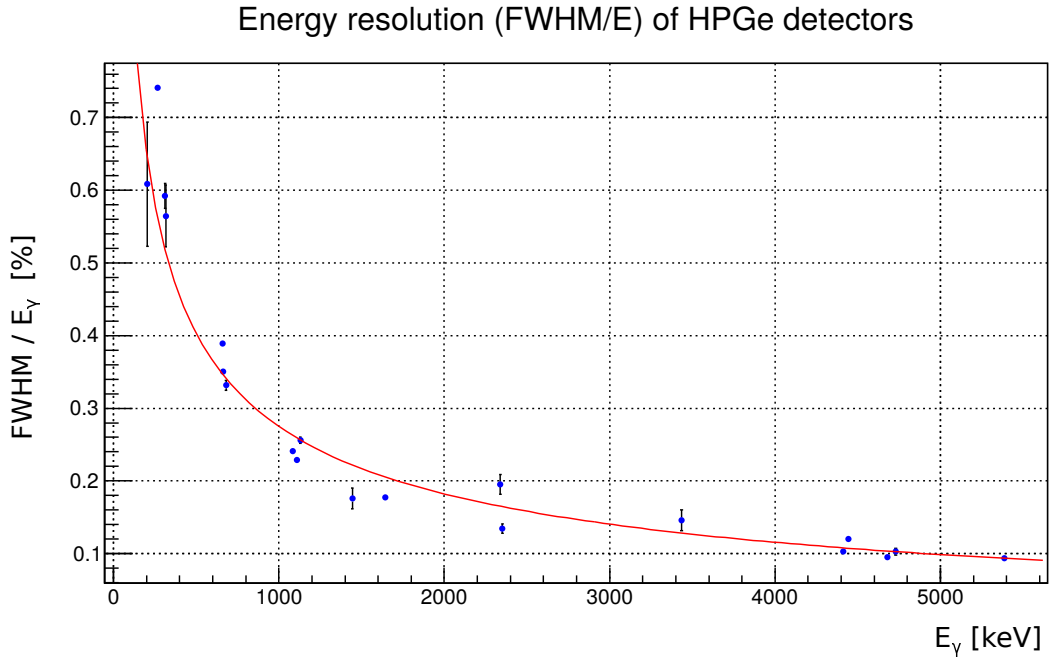

Figure 3.7 – Energy resolution of γ detectors (from summed spectra CLOVER and Coaxial HPGe). Fitting function: $\mathrm{FWHM/E_\gamma = a \times (E_\gamma + b \times E_\gamma^2)^{-1/2}}$.

energy range was set to 0-6 MeV for coaxial.

Since no physical calibration source is available for the highest energy part of the spectrum, it is necessary to use numerical simulations. This was done for the clover and coaxial HPGe detectors using GEANT4 [134]. These simulations must first reproduce the data obtained at lower energy with the ^{152}Eu source. The most sensitive parameter is the distance between each crystal and the endcup that is different for each crystal, poorly known and difficult to measure directly. Therefore, it was considered as an adjustable parameter of the simulation that one has to adapt manually and patiently. The four values adopted at the end of this procedure were 6 mm, 4 mm, 23 mm, 18 mm for the four individual crystals of the clover detector. These values were verified by a M1 internship work using "γ ray imaging technique for the clover detector" and obtained a rough average value of 5 mm for the 4 crystals. Additionally, the determination of the dead-layer thickness is another challenge. The front layer can be affected by aging effects, neutron-induced damage and damages caused by lithium or boron doping. The dead layer around the cooling finger could be created by the lithium doping of the core and diffused further into the detector over time. The easier method to take into account those effects is to adjust slowly the dead layer thickness so as to reproduce the low energy range efficiency extracted from physical ^{152}Eu source data. More detailed method of dead layer estimation can be found in the literature and Ref. [135] therein.

Figure 3.8 presents all the parameters used during the Monte Carlo simulation in the modeling geometry of HPGe detector and the open access code can be found in the literature [132]. Figure 3.9 shows the efficiency as a function of the energy of CLOVER calibrated by ^{152}Eu source and associated fit. Based on the better (than coaxial HPGe) agreement between fitting function and data and the sufficient statistics of the γ-rays appearing in the decay level scheme, while the coincidence

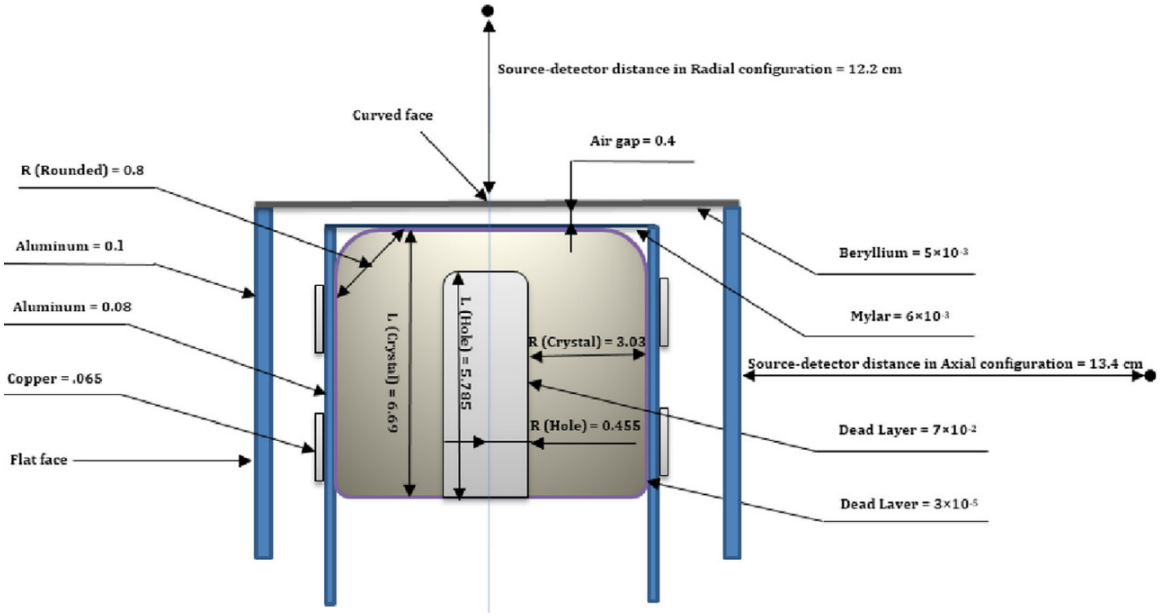

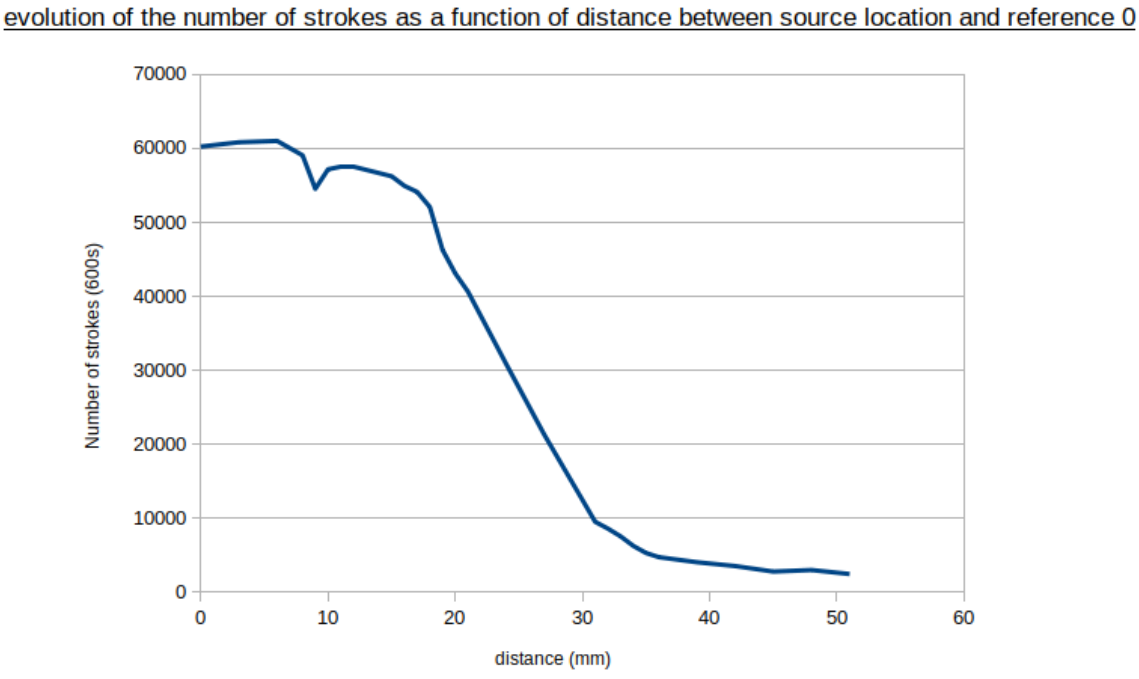

Figure 3.8 – Up: clover detector geometry modeling and configurations (in cm units); see details in reference [132]. Down: imaging spectra of clover detector. One can observe the source meet endcup at 10 mm and meet crystal begin ∼20 mm and totally behind crystal at ∼30 mm.

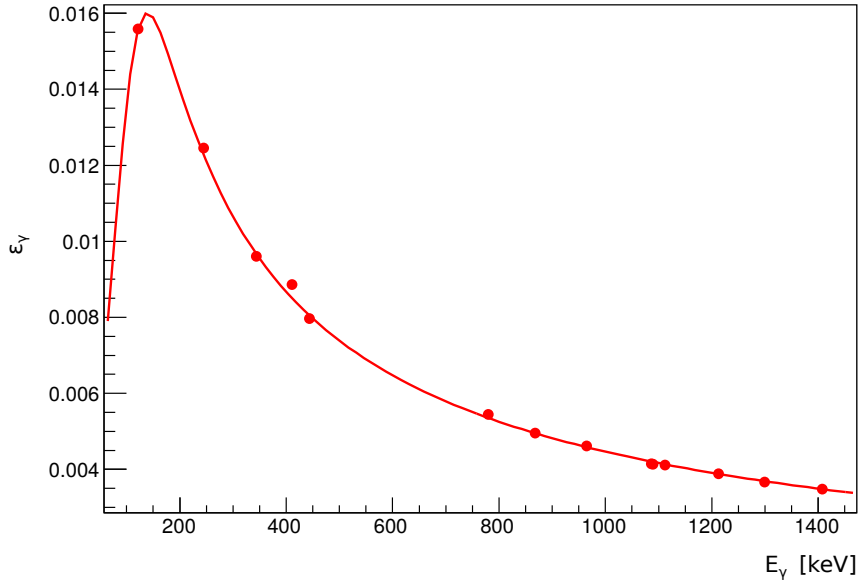

Figure 3.9 – Absolute efficiencies of clover HPGe detectors calibrated by ^{152}Eu source. Fit function used from radware framework [133]: eff = EXP[(A+Bx+Cx^2)$^{-G}$ + (D+Ey+Fy^2)$^{-G}$]$^{-1/G}$, where x = log(EG/E1) and y = log(EG/E2), E1 = 100 keV; E2 = 1000 keV.

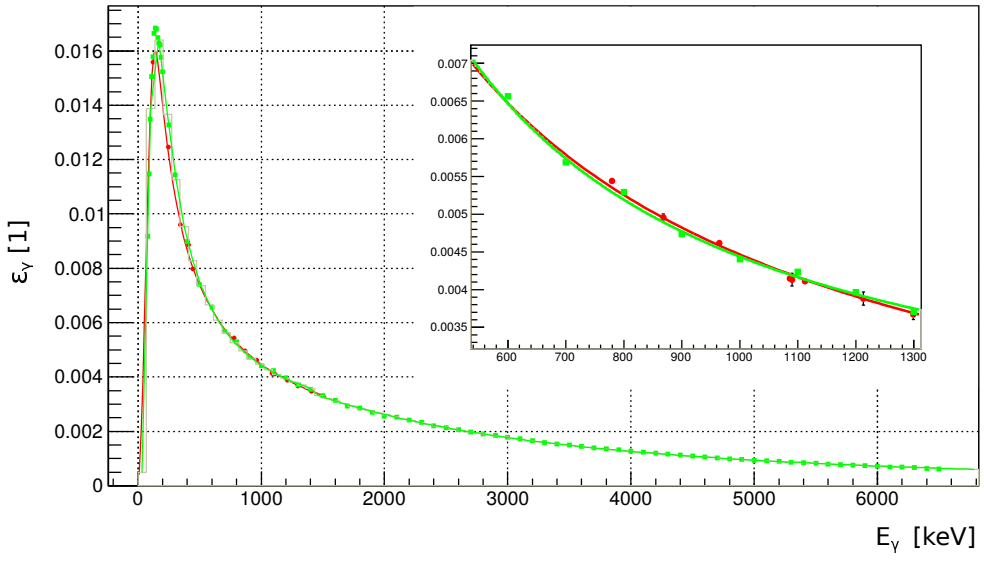

Figure 3.10 – Absolute photo-peak efficiency of clover summing of the 4 crystals: red points and the fitting curve present results from ^{152}Eu source; green points and fitting curve show efficiency obtained from Geant4 data. Fit function used from radware framework [133]: eff = EXP[(A+Bx+Cx^2)$^{-G}$ + (D+Ey+Fy^2)$^{-G}$]$^{-1/G}$, where x = log(EG/E1) and y = log(EG/E2), E1 = 100 keV; E2 = 1000 keV. Insert window is zoom on 550-1300 keV region to show the consistency of source data and simulation data.

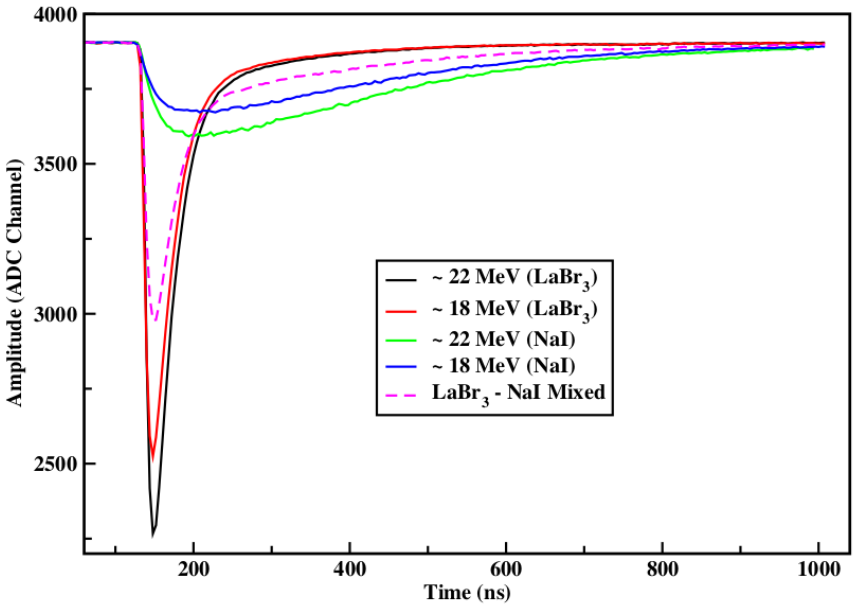

Figure 3.11 – The pulses of signals in one phoswich generated by a high energy gamma ray in a test measurement of PARIS in Ref. [136].

relationships were extracted from whole HPGe detectors, the absolute branching ratios I_β and logft values were obtained using the set of data of the CLOVER only. So, the Geant4 simulation was also performed for the clover to extend the efficiency curve to high energy region up to 6 MeV as shown in Figure 3.10. Good agreement can be found between the data collected from ^{152}Eu source and generated from Geant4 simulation.

2.4 PARIS array

PARIS was designed as a calorimeter for measurements of γ-rays covering a wide energy range of 100 keV–50 MeV. The PARIS array consists of phoswich detectors each with two shells of scintillator detectors. The inner shell $LaBr_3$ can provide fast timing, direction, and γ-rays multiplicity and Total Absorption Spectrum (TAS) like measurements with veto by outside NaI. In addition, the total energy of a high energy photon, if it punches through and forms an electromagnetic shower in the outside shell, can be reconstructed in an add-back mode exploiting the energy information from the outer shell.

Signals separation

The first step of using PARIS is to separate the signals coming from $LaBr_3$ and NaI, which is essential for their individual calibrations. Pulse Shape Analysis (PSA) methods are used to resolve the two phoswitch signals using their widely different shaping and decay times as shown in 3.11. So, one can save two values generated by FASTER DAQ system: one was obtained with a shorter time gate 120 ns for the QDC process and second one obtained with longer time gate of 820 ns for the QDC coding window.

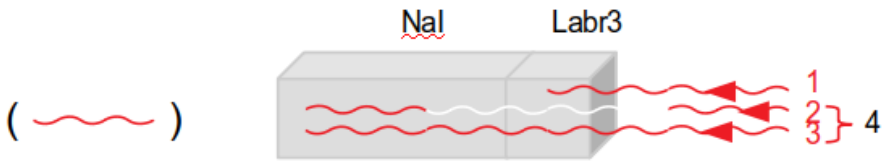

Figure 3.12 – Energy deposit situations when a γ-ray hits one phoswitch.

There are more than four different situations when a γ-ray arrives into the phoswich as illustrated with Fig. 3.12: 1. the γ-ray hits the $LaBr_3$ crystal only and deposits its full energy inside. Now, one can observe the same value in Q_{short} (collected charge in PMT) with shorter QDC time gate (120 ns) and Q_{long} with a longer time gate (820 ns) as shown in Figure 3.13, the separated line. Hence, the θ_y (as defined in Fig. 3.12) is 45 degree; 2. γ-ray goes through $LaBr_3$ but deposits zero energy and then hits NaI and deposites full energy there, this gives rise to another clear line in the diagram of Fig. 3.13. One can measure the θ_x (as defined in Fig. 3.13) through this line; 3. γ-ray punches through LaBr3 and NaI and deposites energy in both crystals partly, these events are localized in the crossing part in Figure 3.13. 4. If more than two γ-rays hit the phoswich at the same time (pileup events), the corresponding events appear only in the longer QDC time window 820 ns. In that situation, Q_{long} is larger than usual as visible in region number 4 in Figure 3.13; 5. The photon escapes the phoswich from the bottom or side direction. This last situation is more complex. Firstly, one can remove part of the bottom escape events from the spectra by using NaI as veto detectors. Secondly, in the case of side escape one can, in principle, get rid of these by a cluster addback procedure. But the material (Aluminum) between phoswich reduces the efficiency of this procedure.

$$\begin{aligned} Q_{short} &= q_1(E_{LaBr_3})\cos\theta_y + q_2(E_{NaI})\sin\theta_x \\ Q_{long} &= q_1(E_{LaBr_3})\sin\theta_y + q_2(E_{NaI})\cos\theta_x \end{aligned} \tag{3.1}$$

The next step consists in using the measured values Q_{short} and Q_{long} to generate quantities q_1 and q_2 which contain the $LaBr_3$ and NaI energy deposit information exclusively: $q_1(E_{LaBr3})$ and $q_2(E_{NaI})$. The transformations from Q to q parameters requires two parameters, θ_x and θ_y, as shown in Eq. 3.1. Once this is done, E_{LaBr_3} and E_{NaI} can be obtained by calibrating $q_1(E_{LaBr_3})$ and $q_2(E_{NaI})$ using reference γ sources. Figure 3.13 shows the result of this procedure. This process is so-called signals separation procedure. At the moment, the γ spectra from $LaBr_3$ and NaI crystal are obtained.

The pure $LaBr_3$ (NaI) γ spectrum is then obtained by setting $E_{NaI} = 0$ ($E_{LaBr_3} = 0$) and the $LaBr_3$-NaI addback spectrum by adding the $LaBr_3$(Ce) and NaI(Tl) signals, $E_{LaBr_3} + E_{NaI}$. Using this addback procedure allows recovering the full energy peaks part of the statistics spread over the 511 keV simple- and double-escape events. This is particularly important for the highest energy part of the gamma spectrum. However, it should be pointed out that for the PARIS array this $E_{LaBr_3} + E_{NaI}$ addback is also far away from ideal. The addback results in a spectrum distortion, a regular energy walk. It could be due to the complicated response function when combining two different scintillators together. It remains of utmost importance to understand how the performance of the $LaBr_3$(Ce) is modified by coupling to NaI(Tl) and how to settle this problem to get a good addback spectrum.

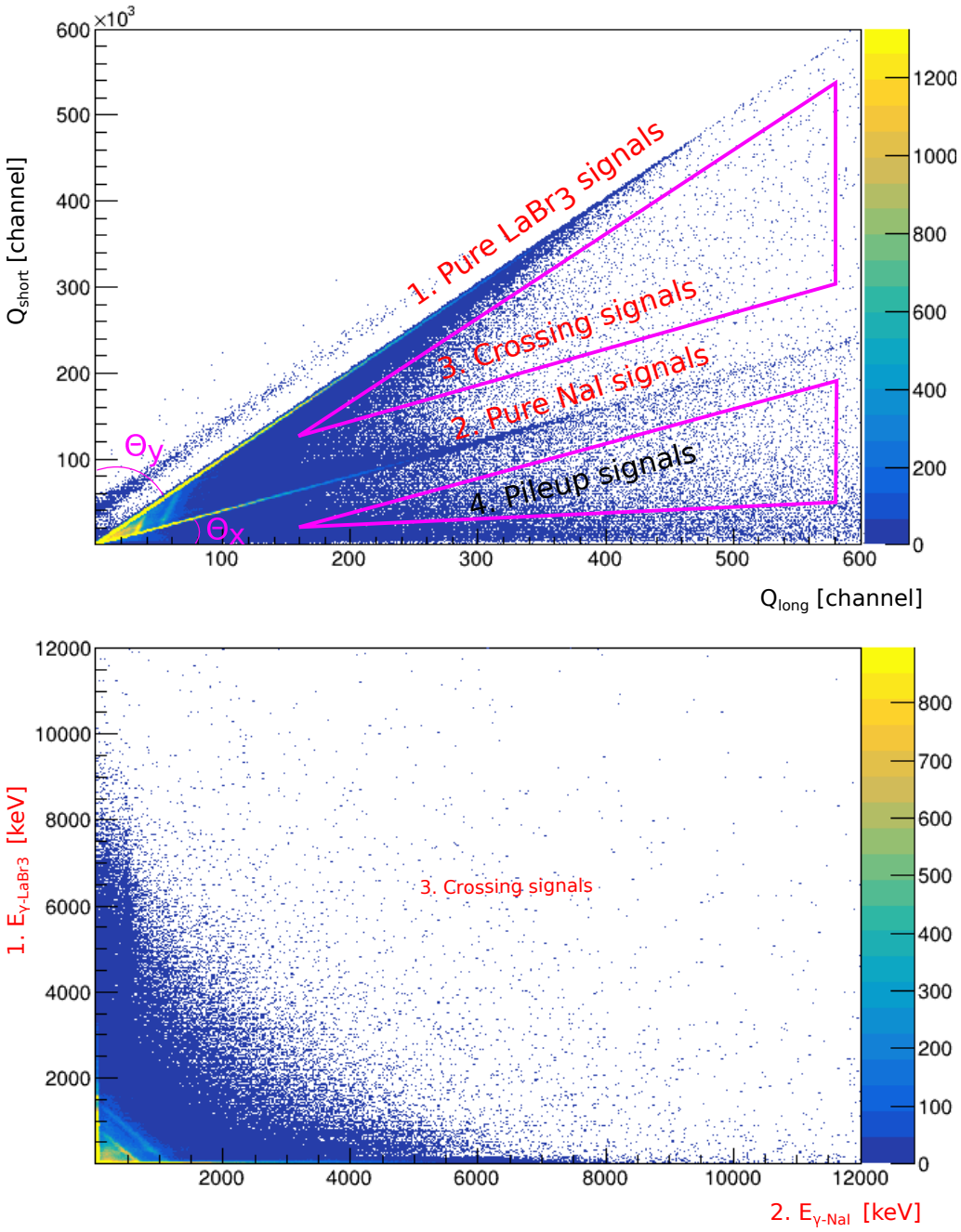

Figure 3.13 – 2D histogram of Q_{short}:Q_{long} two output signals from one phoswich (upper part) and its projection histogram E_{LaBr_3}:E_{NaI} (lower part).

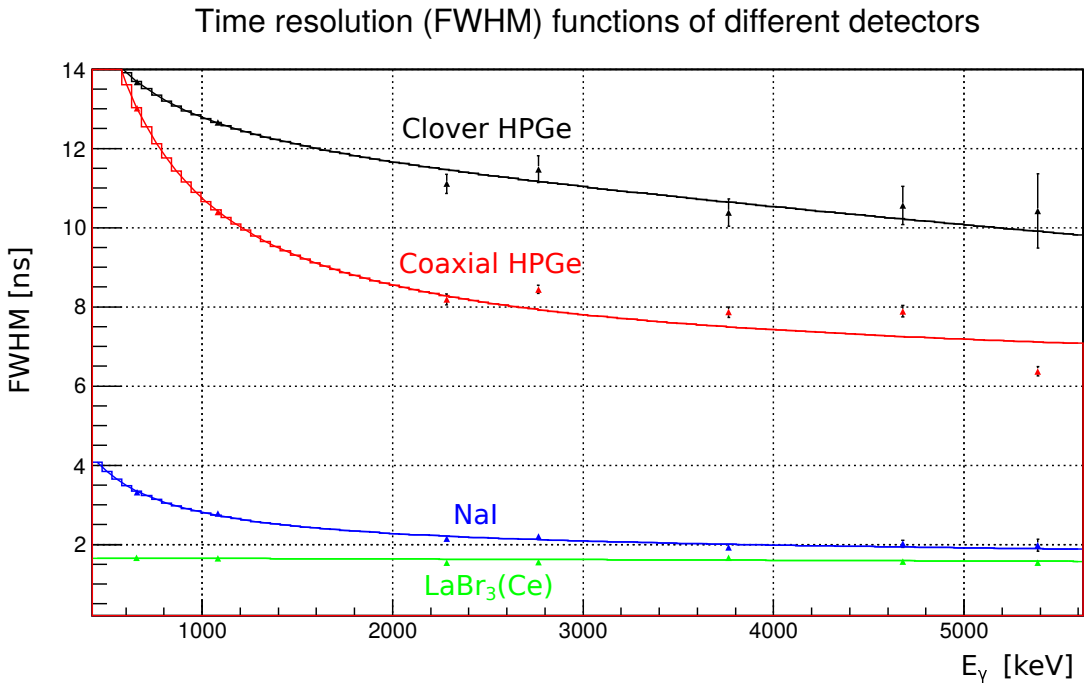

Figure 3.14 – Time resolution function of different types of γ detectors. Fitting function: FWHM = $a(E_\gamma + bE_\gamma^2)^{1/2}$

Time resolution

One advantage of the PARIS detector is its excellent time resolution, which originates from the fast response of $LaBr_3(Ce)$ detector. It gives to PARIS fast timing measurement capabilities in additional to other functions. The design objective of time resolution of PARIS at 1 MeV is 250 ps, which makes many lifetime measurement possible for nuclear excited states with half-lives around or longer than 1 ns using easy data analysis method. However, the time resolution performance of PARIS ($LaBr_3$ crystal) in this experiment is 1.65(2) ns at 1083 keV as listed in Table 3.3. The time resolution of NaI crystal in PARIS, coaxial HPGe and clover HPGe are also presented in Table 3.3. The time resolution functions of different types of detectors and γ-rays energy are presented in Figure 5.20. It is very important information for further data analysis like time window determination of events building, γ-γ coincidence and so on, as will be explained in the forthcoming data analysis section. Note that the time resolution information was extracted from the time difference between signal of γ-ray in each detector and signal of β particle in the plastic scintillator.

Table 3.3 – Time resolution of different detectors at 1083 keV.

Detectors	$Labr_3(Ce)$ (ns)	NaI (ns)	Coaxial HPGe (ns)	Clover HPGe (ns)
FWHM at 1083 keV	1.65(2)	2.78(4)	10.39(2)	12.65(5)

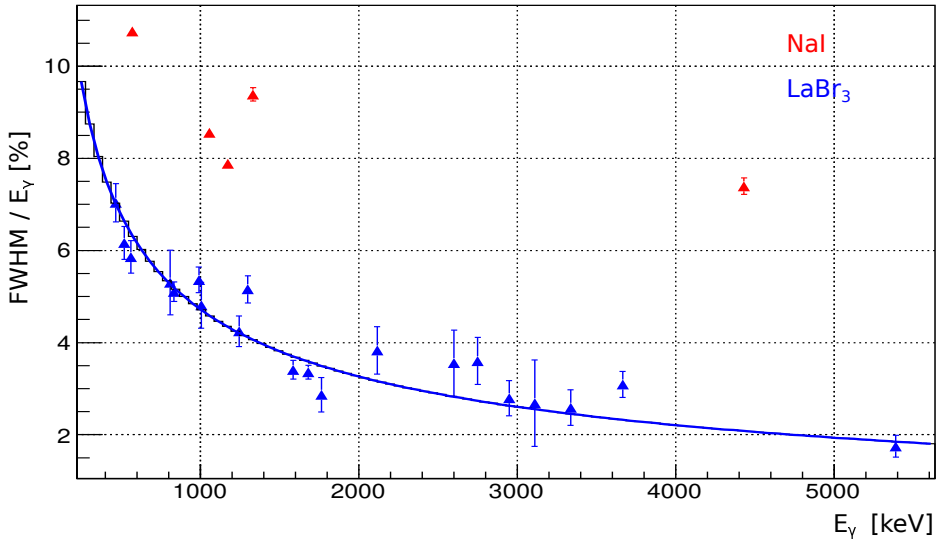

Figure 3.15 – Energy resolution as a function of the γ-ray energy of the individual $LaBr_3$ and NaI components of the PARIS phoswich detectors. Fitting function used is $FWHM/E_\gamma = a(E+bE^2)^{-1/2}$.

Energy resolution

As introduced above, PARIS is a complex modular array as each phoswich contains two crystals but is connected to a common PMT. So, the energy calibration of PARIS was decomposed into 4 steps:

(1). Separate $LaBr_3$ and NaI components of the signal;

(2). Calibrate $LaBr_3$ and NaI detectors separately for low energy part, below 4.5 MeV, using standard γ sources including ^{137}Cs (661.66 keV), ^{60}Co (1172.23 keV, 1332.49 keV, 2505.72 keV), ^{207}Bi (569.70 keV, 1063.66 keV, 1770.23 keV), AmBe (4439.82 keV 3.2) and some γ-rays from background like ^{2}H (2223.25, populated by hydrogen neutron capture), ^{214}Bi (2204.06 keV) and ^{208}Tl (2614.51 keV);

(3). Correct low energy part calibration using well established gamma rays from the collected ^{80}Ga sources: for NaI the following lines 659.15 keV, 1083.47 keV and 1109.36 keV were used; for $LaBr_3$(Ce) 659.15 keV, 1083.47 keV, 1109.36 keV, 1235.74 and 1312.91 keV;

(4). Calibrate $LaBr_3$ and NaI crystal separately for high energy part, above 4.5 MeV using AmBe (4439.82 keV issued from reaction 3.2) and AmBe + Ni (8998.63 keV issued from reaction 3.3).

$$Am \rightarrow \alpha + {}^{9}Be \rightarrow {}^{13*}C \rightarrow n + {}^{12*}C_{(2^+ \rightarrow 0^+ : 4439.82 keV)} \tag{3.2}$$

$$n + {}^{58}Ni \rightarrow {}^{59*}Ni_{((1/2)^+ \rightarrow (3/2)^- : 8998.63 keV)} \tag{3.3}$$

After this energy calibration, the energy resolution as a function of the γ-ray energy, was obtained, it is an important control parameter of the quality of the PARIS data. The value (FWHM/E) at 1 MeV for $LaBr_3$ is ≈5% and for NaI is ≈9% as shown in Figure 3.15. This result was obtained without the necessity to resort to the run-grouping technique used for the HPGe detectors because, as seen

previously, the amplitudes of the observed energy shifts were of a few keV, which is smaller or of the same order of magnitude as the scintillator resolutions. In addition, one should pay attention to the non-linearity of $LaBr_3$ during the energy calibration, which is due to the intense light yield that saturates the response of PMT, (63 photon/keVγ [137]). In the previous PARIS test measurement, this non-linearity appears when E_γ>10 MeV [138], which also depends on the applied HV.

Detection efficiency

The role of the PARIS detectors in the present hybrid array is to provide the major contribution to the γ-ray efficiency in the highest part of the spectrum (above 6 MeV). In order to increase this efficiency one should aim at the most compact geometrical positioning of the PARIS detectors. However one still has to differentiate the gamma and neutron signals by their time of flight. For that reason, a distance of 120 mm between the source and the detector end caps was chosen for the 3 PARIS clusters, which gives an 8.5 ns flight time difference between 1 MeV neutrons and gammas (to be compared to 50 mm source-cap distance for the coaxial HPGe and 74 mm for the HPGe clover).

The SToGS package was developed by the Lyon group for PARIS Monte Carlo simulation [139]. In the following process, it will be further developed to extract the detection efficiency of PARIS under different modes that vary according user's demands.

In order to proceed with a detailed analysis it is interesting to arrange the PARIS data into 6 sorting modes. For each modes, it is necessary to determine the individual detection efficiency. There is one Monte Carlo simulation SToGS package developed by the Lyon group [139] that is available for PARIS simulation. These 6 possible modes (see Table 3.4) are as follows: 1. Only $LaBr_3$ and working individually (no addback procedure, NaI are used as veto detectors); 2. Only $LaBr_3$ (vetoed by NaI) but addback inside one cluster (9 phoswich detectors); 3. Only $LaBr_3$ (vetoed by NaI) but addbacked totally (27 phoswich detectors); 4. Summed spectra from individual $LaBr_3$(vetoed by NaI) and individual NaI; 5. Addback the signals from $LaBr_3$ and NaI crystals inside one phoswich (considering the cross talking signal between two crystals; 3rd part in Figure 3.13); 6. Add-back the signals from $LaBr_3$ and NaI crystals inside one cluster (considering the cross-talk signal inside one cluster including 9 phoswich detectors). The detailed difference of these modes will be discussed later on. Figure 3.16 shows the γ-ray detection efficiency for three of them, which was obtained through normalizing them to clover detector.

Table 3.4 – Different Data sorting modes of PARIS array

Data sorting modes	Description
mode 1	Only $LaBr_3$ working individually (vetoed by NaI)
mode 2	Only $LaBr_3$ (vetoed by NaI) but addback inside one cluster (9 phoswich detectors)
mode 3	Only $LaBr_3$ (vetoed by NaI) but energy being added totally (27 phoswich detectors)
mode 4	Summed spectra from individual $LaBr_3$(vetoed by NaI) and individual NaI
mode 5	Addback the signals from $LaBr_3$ and NaI inside one phoswich (considering the cross talking signals between two crystal)
mode 6	Addback the signals from $LaBr_3$ and NaI but inside one cluster (considering the cross talking signals between 9 phoswich detectors)

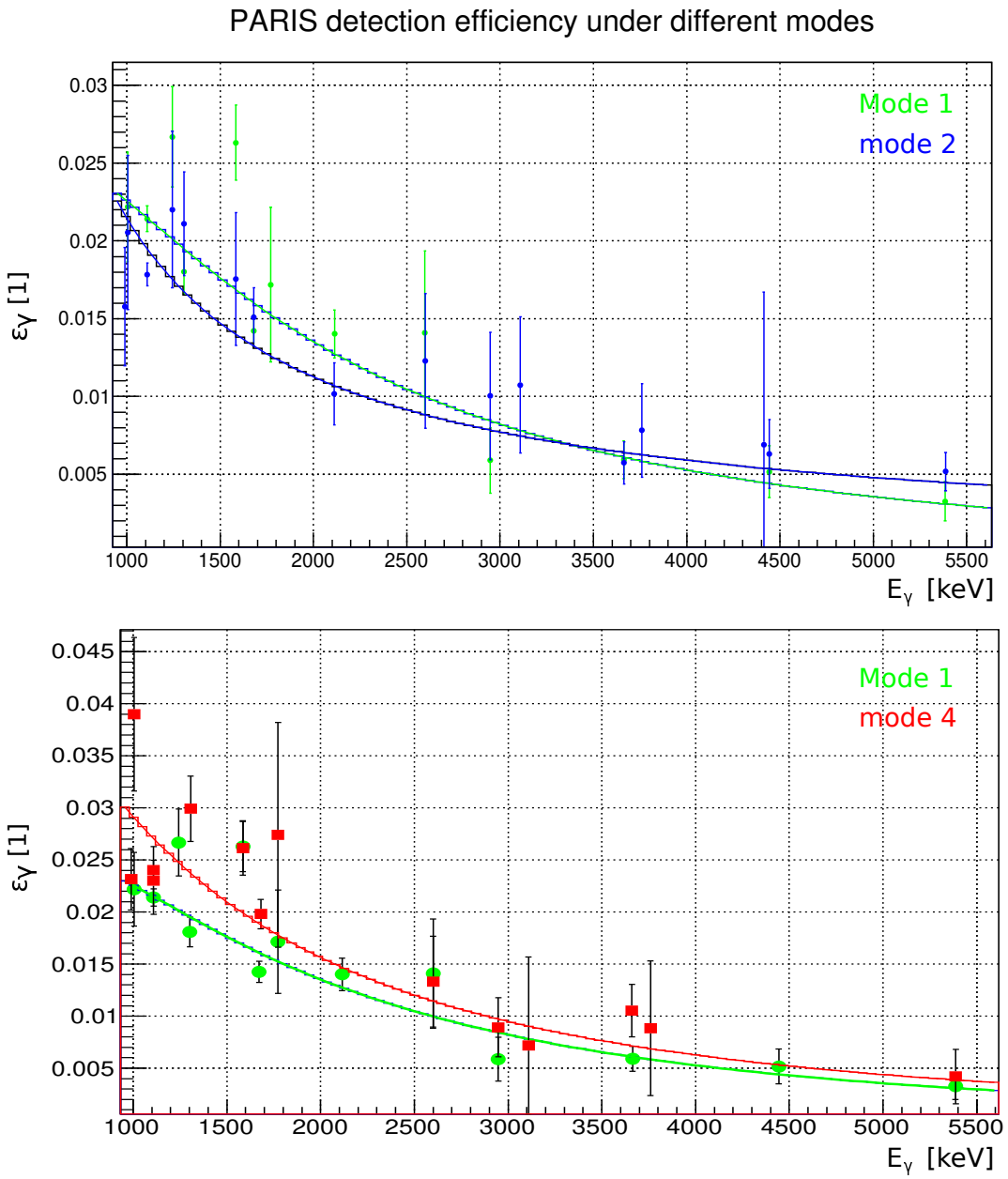

Figure 3.16 – PARIS detection efficiency under different modes (each one is compared with mode 1). Fit function used from radware framework [133]: eff = EXP[(A+Bx+Cx^2)$^{-G}$ + (D+Ey+Fy^2)$^{-G}$]$^{-1/G}$, where x = log(EG/E1) and y = log(EG/E2), E1 = 100 keV; E2 = 1000 keV.

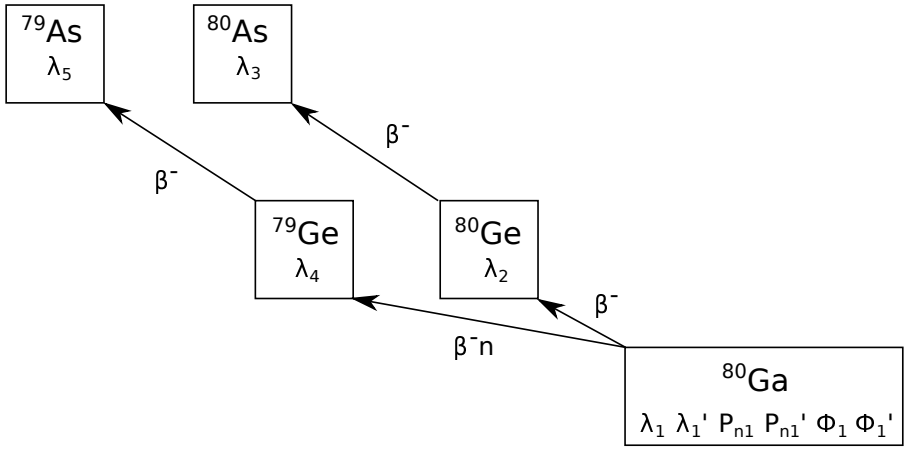

Figure 3.17 – Decay chain of ^{80g}Ga and ^{80m}Ga. The isotopes and the decay parameters involved in the Bateman equation are illustrated.

3 Analysis procedure

3.1 Statistical approach of precursors

It is essential for extracting the logft and B(GT) values with high accuracy to achieve a precise counts of precursors in the beta-decay study. In In-Flight experiments, ΔE-E or ΔE-TOF spectrum usually plays the role of ion counting and precursor identification. In ISOL production mode, there is an easy way to count the number of precursors, that is to count the γ activity in the decay chain. This is possible only if some reliable absolute γ decay intensities are available. Then one can calculate the precursors' counts through backstepping method using absolute β branching ratios I_β, P_n values and solving the proper Bateman equation system. For example, if the number of 265 keV γ-rays number originating from $1^+ \rightarrow 1^+$ in ^{80}As is extracted from the γ spectrum, one can calculate the number of ^{80}Ge according to the previously measured I_β value of ^{80}Ge and P_n of ^{80}Ga. One should emphasize, however, that the results from this method depend on the accuracy of previous experimental results I_β and P_n.

$$\begin{cases} \frac{dN_1(t)}{dt} &= -\lambda_1 N_1(t) + \phi, & (^{80g+m}Ga) \\ \frac{dN_2(t)}{dt} &= -\lambda_2 N_2(t) + (1-P_{n1})\lambda_1 N_1(t), & (^{80}Ge) \\ \frac{dN_3(t)}{dt} &= -\lambda_3 N_3(t) + \lambda_2 N_2(t), & (^{80}As) \\ \frac{dN_4(t)}{dt} &= -\lambda_4 N_4(t) + P_{n1}\lambda_1 N_1(t), & (^{79}Ge) \\ \frac{dN_5(t)}{dt} &= -\lambda_5 N_5(t) + \lambda_4 N_4(t), & (^{79}As) \end{cases} \tag{3.4}$$

Here, an alternative methodology was used, allowing the determination of the activity of the precursors and the intensity of the radioactive beam from the total β spectrum by handling the Bateman equations. The decay path of the source ^{80}Ga created by accumulation of the beam depends on both the decay parameters λ_i and P_{ni} as presented in Figure 3.17. This chain is described by a couple of linear differential equations 3.4 where $\phi_1(\phi_1'$ from isomer) is production rate of ^{80}Ga,

P_{n1} (P'_{n1}) is the probability of β-delayed neutron emission (P_n=0 for other isotopes in the chain) and λ_i corresponds to decay constant (i = 1, .., 5 is the index of corresponding isotopes). One should remember that there are two components in the ^{80}Ga collected beam: ground state ^{80g}Ga and isomeric state ^{80m}Ga.

$$\begin{cases} A^{tol}_{col}(t) = \sum_{i=1}^{5} A^{col}_i(t) = \sum_{i=1}^{5} \lambda_i N^{col}_i(t) \\ A^{tol}_{dec}(t) = \sum_{i=1}^{5} A^{dec}_i(t) = \sum_{i=1}^{5} \lambda_i N^{dec}_i(t) \end{cases} \tag{3.5}$$

$$A^{tol}(t) = \begin{cases} bg, & 0 < \mathrm{t} < 0.5 \\ A^{tol}_{col}(t) + bg, & 0.5 < \mathrm{t} < 5.5 \\ A^{tol}_{dec}(t) + bg, & 5.5 < \mathrm{t} < 10.5 \end{cases} \tag{3.6}$$

This Bateman equation has analytic solutions. So it can be handled by hand. The first one is the same as Equation 3.4. In fact, only the second and the third ones are needed to be handled. The last two are just the same as these two. So, the solutions can be obtained easily through changing parameters. Since all the parameters, λ_i and P_n, in equations 3.4 are known, and if the background(bg) is already estimated through fitting the first 0.5 s spectrum of β activity, the only parameter left in equations 3.4 is ϕ (beam intensity). So, one can figure out the exact solution but just using one value of A^{tol}_{col}(t) or A^{tol}_{dec}(t) at any time t. In addition, during the experiments β activity curve was recorded as a function of time. So, one can also extract ϕ by fitting the β activity curve with function 3.5 or 3.6. In the end, the number of precursor ^{80}Ga will be obtained through the integration of β particles' counts 3.7 and efficiency parameter of β detector.

$$\begin{cases} N^{exp}_{\beta} = \int_0^{10.5} A^{tol,exp}_{\beta}(t)\, dt \\ N^{decayed}_{^{80}Ga} = \frac{N^{exp}_{\beta} - N^{bg}_{\beta}}{\epsilon_{\beta}} \end{cases} \tag{3.7}$$

Actually, for ^{80}Ga, there are two free parameters (unknowns) in the Bateman equation ϕ_1 and ϕ'_1 but only one equation. One method is to create two equations through changing the beam collection and decay times like in [127]. It is impossible to handle two parameters with one equation. In addition, the fitting of the β curve with ϕ_1 and ϕ'_1 also failed. One possible reason is that the half-lives of ^{80g}Ga and ^{80m}Ga are too close. Furthermore, by this method, it is difficult to determine whether the fitting results correspond to a global minimum instead of a local minimum because the fitting process will stop when it converges to a local minimum in the 2D plane of ϕ_1 and ϕ'_1. The complementary method taken in this data analysis is to set only one ϕ_1 during the Bateman equation handling process with one halflife the weighted value of ^{80g}Ga and ^{80m}Ga. Then one can separate the ϕ_1 into two values according to the isomer ratio. Figure 3.18 presents the fitting result of β activity with the first two parts of function 3.6. Eq. 3.8 is the counts of precusor ^{80}Ga.

$$\begin{aligned} N^{decayed}_{^{80m}Ga} &= 1.41(8) \times 10^8 \\ N^{decayed}_{^{80g}Ga} &= 2.40(8) \times 10^8 \end{aligned} \tag{3.8}$$

There are 3.81(2)$\times 10^8$ decayed ^{80}Ga isotopes collected during the 13h experimental time. The

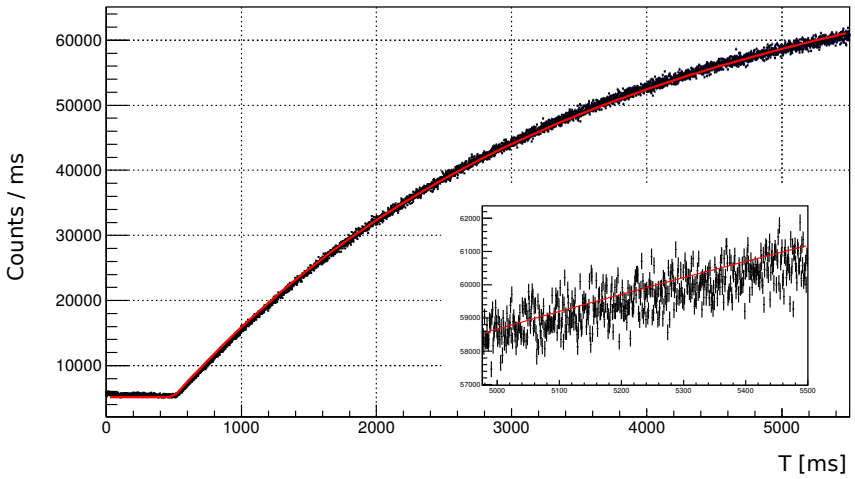

Figure 3.18 – β activity plot $A^{tol}(t)$ of ^{80}Ga decay chain and its fitting curve.

uncertainty on this number originates from the uncertainties on λ_i, P_n, the errors in the determination of beam intensity ϕ (taking into account the errors in background measurements and the error of $A^{tol}(t)$) and the error of the efficiency of β detector. Note that the error on β detector's efficiency will not contribute to the errors of logft and B(GT) values as ϵ_β was not used during these calculation, which is because the γ-rays' counting is also from beta-gated γ spectrum.

3.2 β-γ-γ coincidence technique

It is very important for the beta-decay study of neutron-rich nuclei to suppress the background coming from the ambient activity and possible collection off the tape in the γ spectrum through β-γ coincidence as shown in Figure 3.2.

In the second step, various γ-γ matrixes were built, taking into account the γ-rays following a β signal and being detected within a time window. The γ-γ coincidence relationships are used to build the decay level scheme. The coincidence time window was set according to the time resolution of different detectors as shown in Figure 5.20. The perfect value is 6σ (FWHM = 2.355 σ) that guarantees that $\sim 100\%$ events were included. In the data analysis of ^{80}Ga, 20 ns was adoped for $LaBr_3$-$LaBr_3$ matrix and $LaBr_3$-$LaBr_3$+NaI matrix and 50 ns for HPGe-HPGe matrix, 50 ns for HPGe-PARIS($LaBr_3$ or $LaBr_3$+NaI) matrix.

The matrix in Figure 3.19 is a symmetry matrix. Its X and Y axis are filled with same information, γ-ray energies from β-γ-γ coincidence events involving HPGe detectors (Clover and coaxial HPGe). Except for the clear crossing points formed by the γ coincidences one can also observe oblique and continuous lines from the Compton scattering due to a very close detection geometry. Note that in order to obtain the γ-γ coincidence information, "multiplicity greater or equal 2" was set, which means the condition for matrix filling is that there are at least 2 γ-rays detected in one decay event. A comparison between the projection spectrum from matrix (Figure 3.19) and the original spectrum from HPGe is presented in Figure 3.20. Some information can be extracted from this comparison such as judging that a γ-ray transition goes directly to the ground state or to an excited states.

The procedure to extract the γ-γ coincidence is as follows: 1. Put a gate on the interesting peak

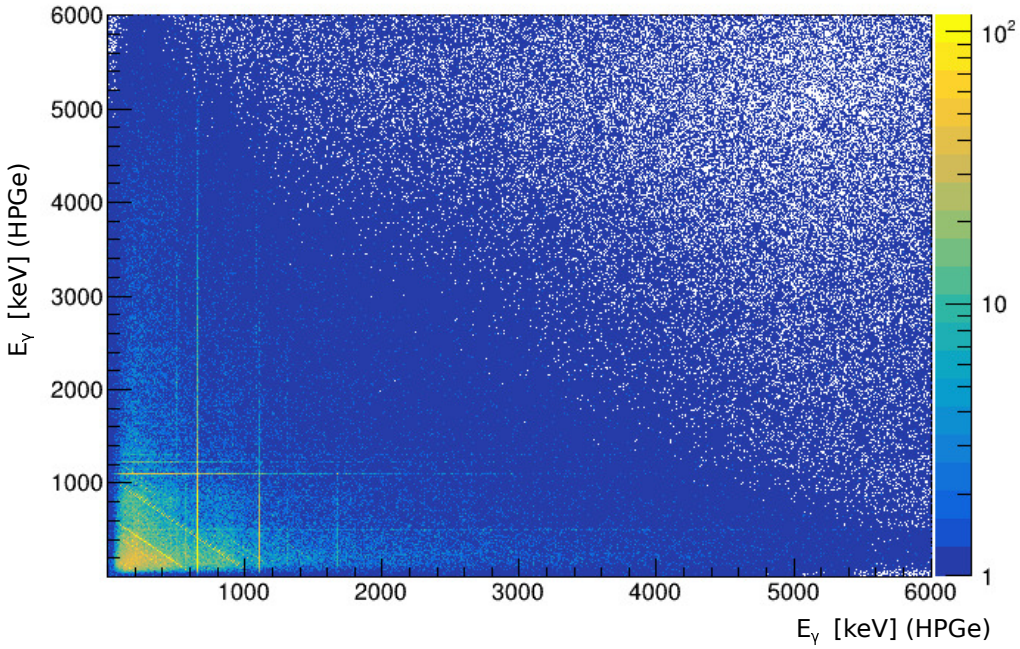

Figure 3.19 – Symmetric γ-γ matrix filled by γ-rays from HPGe detectors with 2.10×10^7 entries.

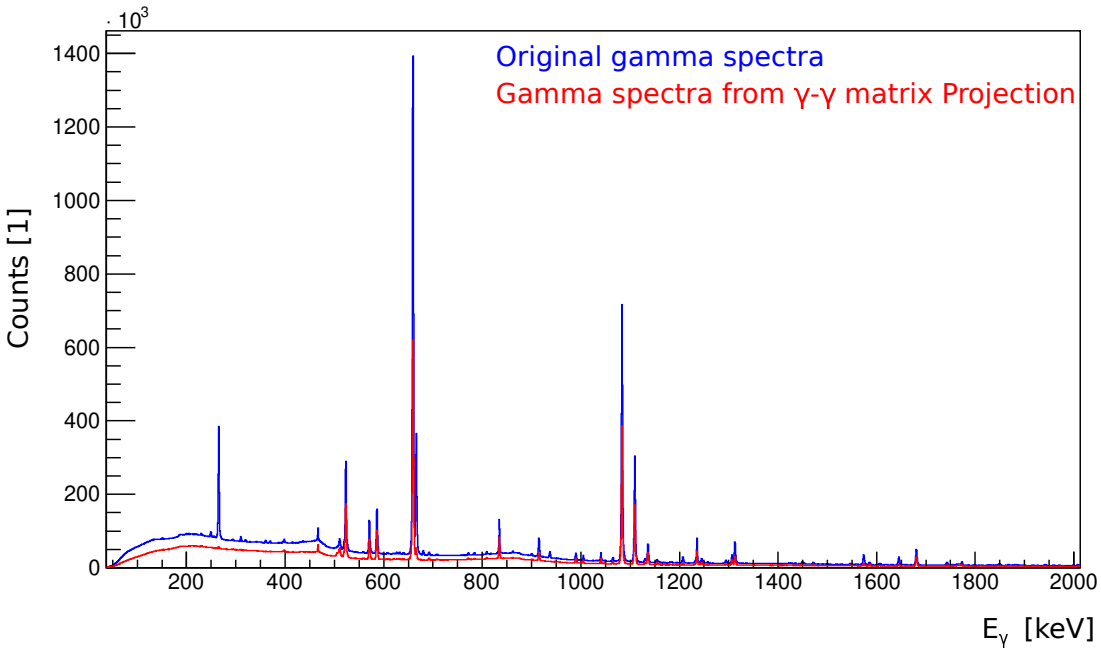

Figure 3.20 – Comparison between projection spectrum from Figure 3.19 and the original spectrum from HPGe detectors.

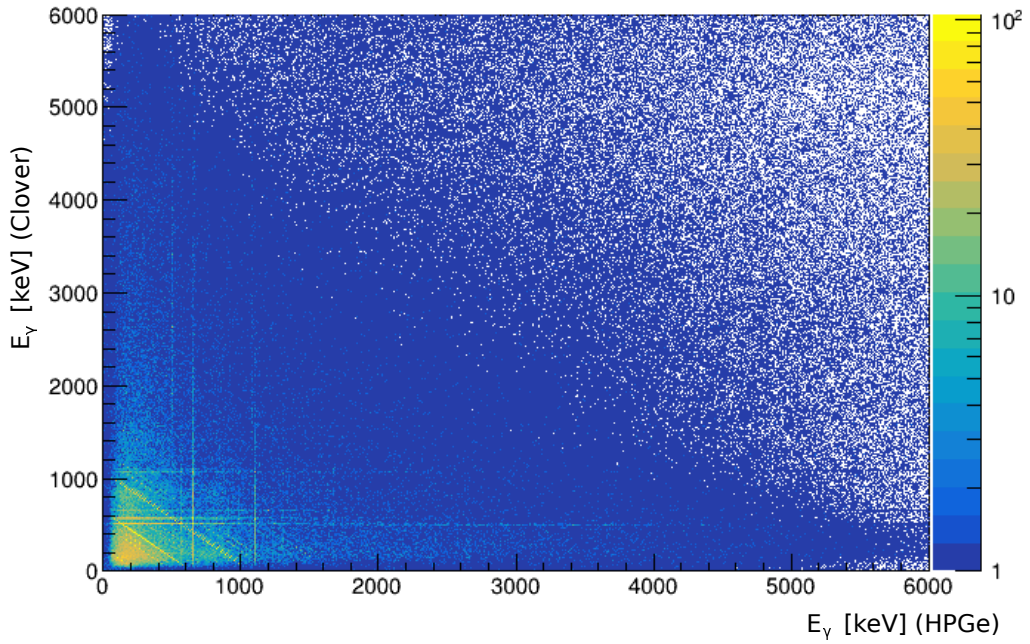

Figure 3.21 – γ-γ matrix filled with coincident events between CLOVER and any of the five HPGe detectors.

γ_1 and get the gated spectrum; 2. Then put two equally wide gates on left and right background and obtain an average background-gated spectrum. Now, one can achieve a background suppressed spectrum through spectrum substraction; 3. Check the coincidence: take same action but putting a gate on the coincident γ_2 to check if γ_1 is visible or not; 4. Confirm the coincidence: repeat operations 1 and 2 but shifting the gate a little bit to left-half or right-half of the interesting peak γ_1 to see that γ_2 decreases (real coincidence) or remains invariant (fake coincidence). Some β-γ-γ coincidence spectra will be shown in the next chapter.

To extract different information, different matrices are needed. For example, Figure 3.21 was made in order to get clearer coincidence spectra in the busy region located around ∼1750 keV which is object of an intense controversy [140, 127] taking advantage of clover's good energy resolution. In order to reduce the Compton scattering background and obtain higher efficiency, one can add-back signals from the four CLOVER crystals together and then build a matrix from coincidences between coaxial HPGe events and add-backed CLOVER events, the later being considered as a single detector. This matrix is thereafter called "cloverAddback-coaxial" matrix; see Figure 3.22. Compared with Figure 3.21, one can observe that the full energy γ-line is obviously brighter and the background in the low energy region is suppressed dramatically. The main drawback of this data sorting strategy is that, by considering the CLOVER detector as a single detector, the granularity is reduced and hence the coincidence set is poorer. This is because, in non-add-back mode, for building the high resolution decay level scheme in the low energy region, coincidence can happen between 4 clover crystals and coaxial HPGe while in add-back mode, coincidence can only happen between clover and coaxial.

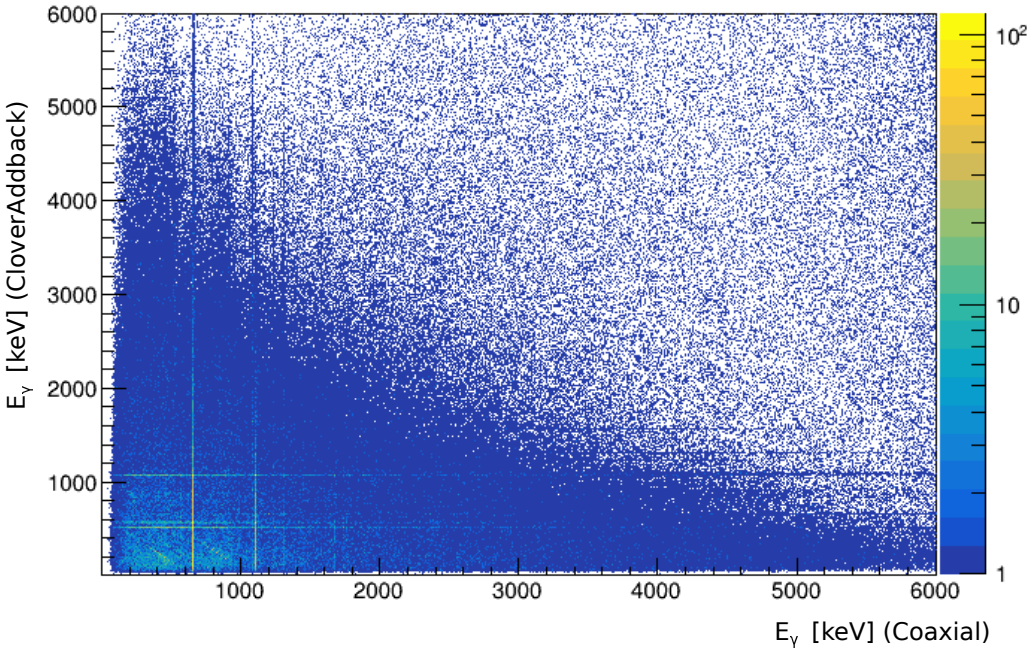

Figure 3.22 – γ-γ matrix filled by coincident γ-rays from Clover-addback and Coaxial detectors.

3.3 Unique characteristic of a hybrid array: PARIS + HPGe

In principle, for the measurement of γ radiations, the best candidate detector should own excellent energy and time resolution, good photopeak (full energy) efficiency and no internal radiation. Actually and obviously, such perfect detector does not exist. Though HPGe detectors provide the best energy resolution at the moment, the price of HPGe crystal, the time resolution and the full-energy peak efficiency at high energy region ($>$ 6 MeV) are far from being ideal.

Therefore, in order to reach the goals of our experiment, a hybrid modular array was employed to measure the γ-rays over the whole Q_β window 10.312(4) MeV. Both advantages of PARIS (high detection efficiency Figure 3.16) and HPGe (high energy resolution Figure 3.7) are combined. The main idea is to put a narrow gate (4 keV) on a peak in the HPGe spectrum to further clean the γ spectrum of PARIS. However, due to the complexity of PARIS array and its unique characteristics, several different combinations or modes can be used depending on the need, such as achieving higher statistics to reduce the statistical error bar or making some physical signal more visible at the cost of statistics. This section will introduce and present the advantages, disadvantages and difference of each mode.

3.3.1 Multiplicity analysis

Another characteristic property of the PARIS array is its high granularity that allows for the measurement of beta-delayed gamma-ray multiplicity. The value of multiplicity is determined by the detectors' geometrical efficiency, detectors' granularity and the multiplicity property of the state's deexcitation.

Conditions set on the multiplicity parameter (Figure 3.23) may help suppress further the background when performing the β-γ-γ coincidence, by enhancing the full energy peak with respect to the

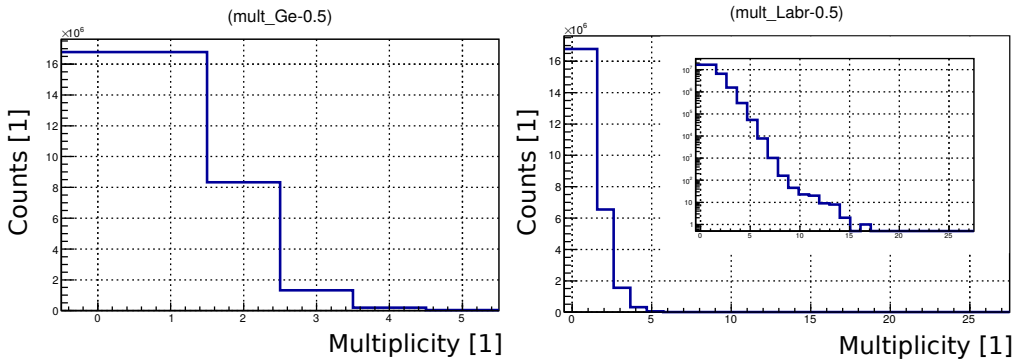

Figure 3.23 – Left: multiplicities of HPGe detectors; Right: multiplicities of $LaBr_3$ crystals fired by γ-rays with full energy deposition.

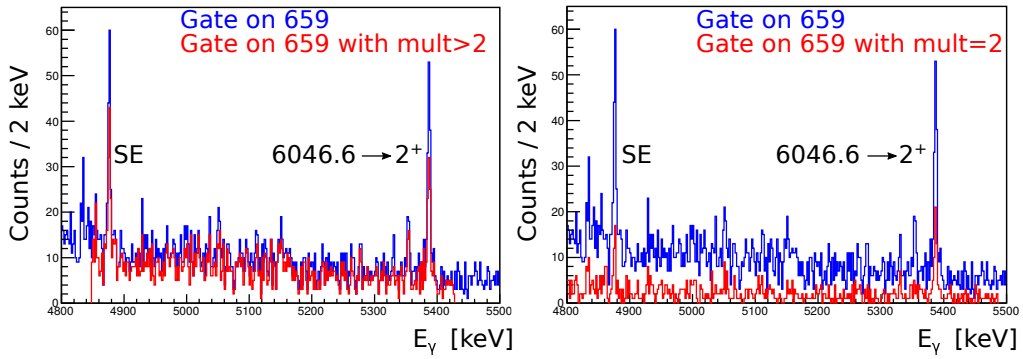

Figure 3.24 – The role of multiplicity value in the cascade confirmation of γ deexcitation and full energy peaks identification.

double- and first-escape peaks. For example, in the cascade of "6046.6 keV (state) $\rightarrow 2^+ \rightarrow 0^+$", there are two γ-rays emitted, 5387 keV and 659 keV. So, in principle, the value of multiplicity is 2. But, due to the electron pair production, followed by its annihilation, there are strong single-escape peak (losing one 511 keV γ) and double-escape peak (losing two 511 keV γ) especially in the high energy region (>3 MeV). This phenomenon is more serious for HPGe detector than for $LaBr_3$ scintillator. So, based on this reasoning, the single-escape peak is suppressed in the gated spectra when imposing a multiplicity condition of two, as shown with the right spectra in Figure 3.24. On the contrary, the single-escape peak is enhanced in the same spectrum when imposing a multiplicity number of 3 or more, as shown with the left spectra in Figure 3.24.

This multiplicity-condition based technique is very useful to unambiguously recognize escape peaks (like the 4876 keV peak visible in the left panel of Fig. 3.24. This technique also helps the attribution of high energy transitions to a given gamma cascade and hence its placement in the level scheme (for example, the placement of the 5387 keV transition).

3.3.2 Comparison of different combination modes for PARIS

$LaBr_3$ work separately, NaI as veto detector

The basic, easy mode of PARIS data sorting is to let $LaBr_3$ phoswich detectors work separately, while using NaI as veto detectors to eliminate the incomplete energy deposition events (associated to γ photons scattering out from rear-end direction) and which amounts to giving a Compton suppression role to these detectors. The biggest advantage of this mode is that one can obtain a very clean γ spectrum with pretty low (almost zero) and clean background. As can be seen in Fig. 3.25, using this sorting mode, the high energy background in the region extending from neutron separation energy to Q_β is reduced to only ∼40 events (on a total of 10^8 gamma events in the spectrum). This unique capability, which is due to the composite LaBr3/NaI phoswich nature of PARIS, allows a direct evaluation of the high energy background. This in contrast to situations met with 4π calorimeters made out of a single layer of homogeneous scintillator material, typically NaI [73], where this background receives an important contribution from gamma events summation. Ultra-high-energy γ-rays are obviously visible and their presence is convincing in the 6-8 MeV region of the spectra. Furthermore, in Figure 3.25, the overlap of non-add-back and add-back spectra shows the existence of states in the energy region above S_n represented by the difference between the two spectra.

In principle, this analysis mode could be combined with other PARIS unique properties like its granularity. One could perform γ-ray multiplicity, angular distribution and angular correlation analysis.

To complete the analysis exploiting this sorting mode, two coincidence matrices were built, One matrix contains energies of individual $LaBr_3$ and HPGe gamma events (see Fig. 3.26). It takes the advantage of high energy resolution of HPGe detectors that one can put a super narrow gate of 4 keV on the HPGe spectrum to obtain coincidence spectra. The other one contains energies of individual LaBr3 and sum of spectra from $LaBr_3$ and NaI crystal. Note that sum of spectra here is not add-back of the signals from $LaBr_3$ and NaI crystals. The difference is in the former one giving up the crossing signals between $LaBr_3$ and NaI as shown in Figure 3.13. It aims to guarantee the non-distortion of γ spectra, caused by the different responses of $LaBr_3$ and NaI crystal, at the cost of losing some crossing γ events. This matrix can also realise coincidence with putting a narrow gate also but the "gate" has higher statistics strengthening the possibility of coincidence compared with the first matrix.

$LaBr_3$ add-back completely, NaI as veto detector

This second analysis mode, which I call "LaBr3 add-back completely", allows using PARIS in a Total Absorption Spectroscopy (TAS) like mode, adding the vetoing capabilities provided by the second shell of NaI detectors. It is with this analysis mode that the spectrum in blue of Fig. 3.25 was obtained. This configuration can provide a minimum value for γ width above S_n: $\frac{\Gamma_\gamma}{\Gamma_\gamma+\Gamma_n}$ due to the lack of γ-rays that escape out of NaI shell. One solution is to enlarge the size of inside $LaBr_3$ crystal, or one can add-back the signals in the ouside NaI crystals at the cost of background contamination and simulation dependence.

Figure 3.27 shows a coincidence matrix containing energies of wholly add-backed and HPGe events, NaI-vetoed $LaBr_3$ events. One can clearly see the global population of some particular high-lying states

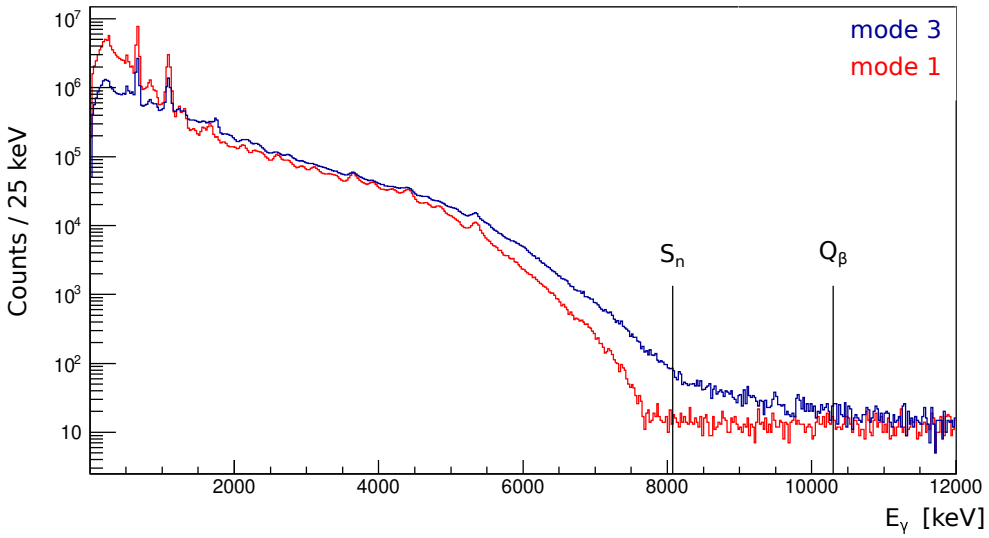

Figure 3.25 – Red: γ spectrum from PARIS when $LaBr_3$ works separately and NaI as veto detectors. Blue: γ spectrum from PARIS by complete add-back of all $LaBr_3$ detectors and NaI as veto from outside shell.

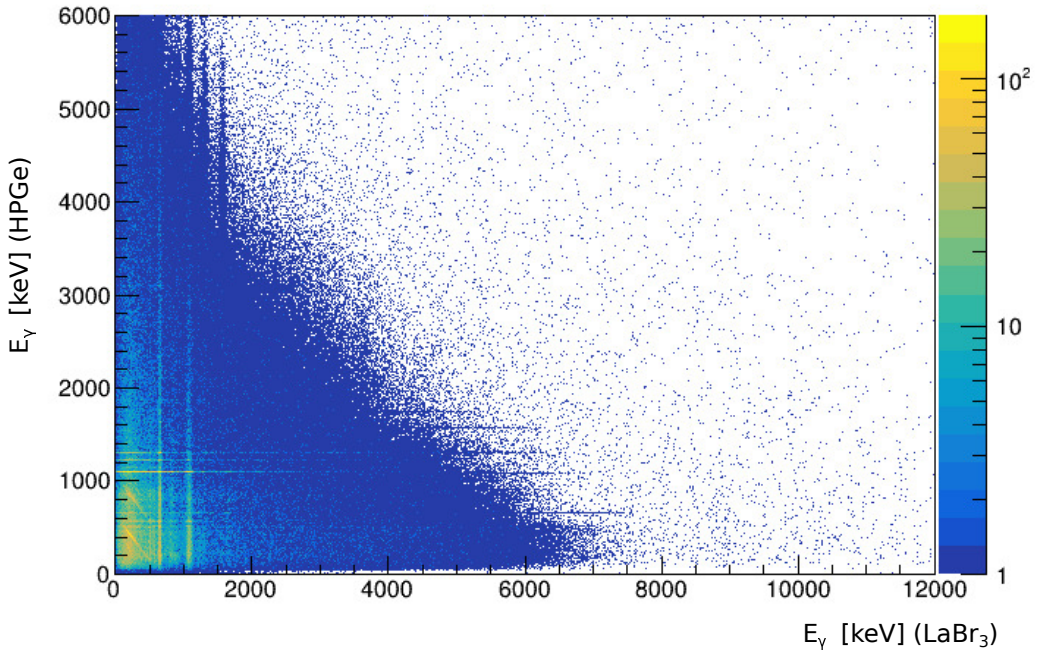

Figure 3.26 – γ-γ coincidence matrix filled by energies of γ-rays events from $LaBr_3$ (working individually and NaI as veto) and HPGe detectors with entries 2.77×10^7.

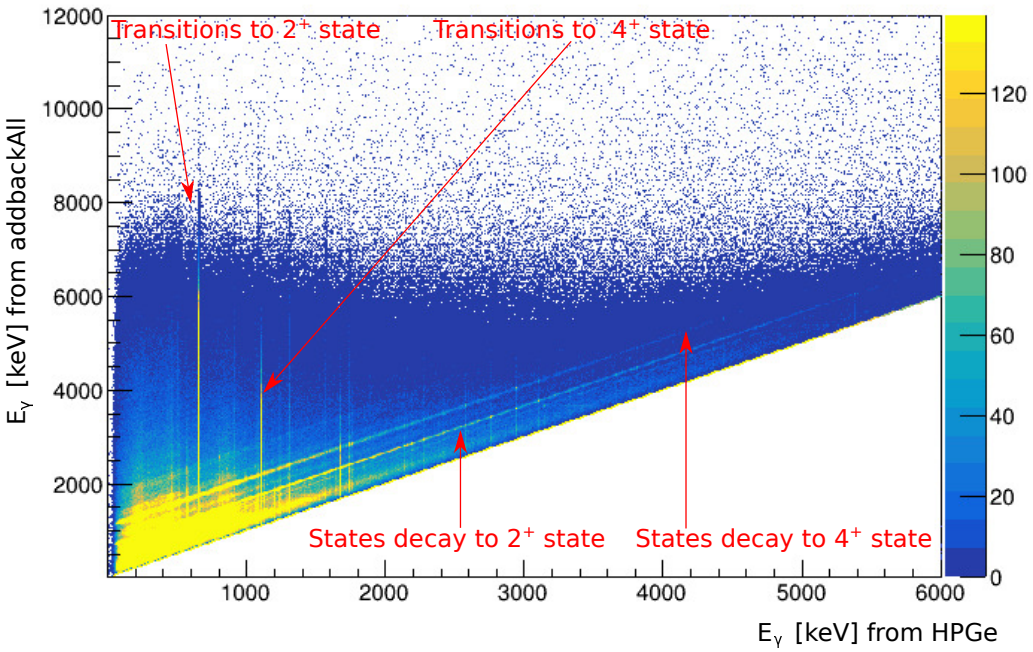

Figure 3.27 – γ-γ coincidence matrix filled by energies of γ-rays events from All-Detectors-Add-back (in PARIS, NaI work as veto detectors) and HPGe detectors.

which deexcite to the 2^+ and 4^+ states.

Sum_LaBr$_3$_NaI (phoswich individually) coincidence with HPGe detector

This third sorting mode consists in generating the sum of the spectrum recorded by the $LaBr_3$ and the NaI per individual phoswich. This summed spectrum is used to build two types of coincidence matrices: phoswich sum spectrum versus HPGe energy as shown in Figure 3.28, and phoswich sum spectra between themselves. These coincidence modes generate the highest statistics coincidence spectra and help make visible weak but interesting coincident transitions.

Clover coincidence with Coaxial

To build a rich decay level scheme of ^{80}Ga, two HPGe detectors were employed in the experiment to compensate for the PARIS insufficiency in energy resolution. The low-energy part (below 6 MeV) level scheme presented in the next chapter was obtained from HPGe-HPGe coincidence matrices. To improve the CLOVER photopeak detection efficiency one can build add-back signals considering the four CLOVER crystals. One can then treat the CLOVER detector as a single detector and look for coincidences with the single-crystal coaxial detector. However, the coincidence probability is reduced from C_5^2 to C_2^2, i.e. by a factor ten and this procedure is not well adapted for this close geometry, low-granularity Ge setup (contrary to large Ge arrays like EUROBALL or GALILEO).

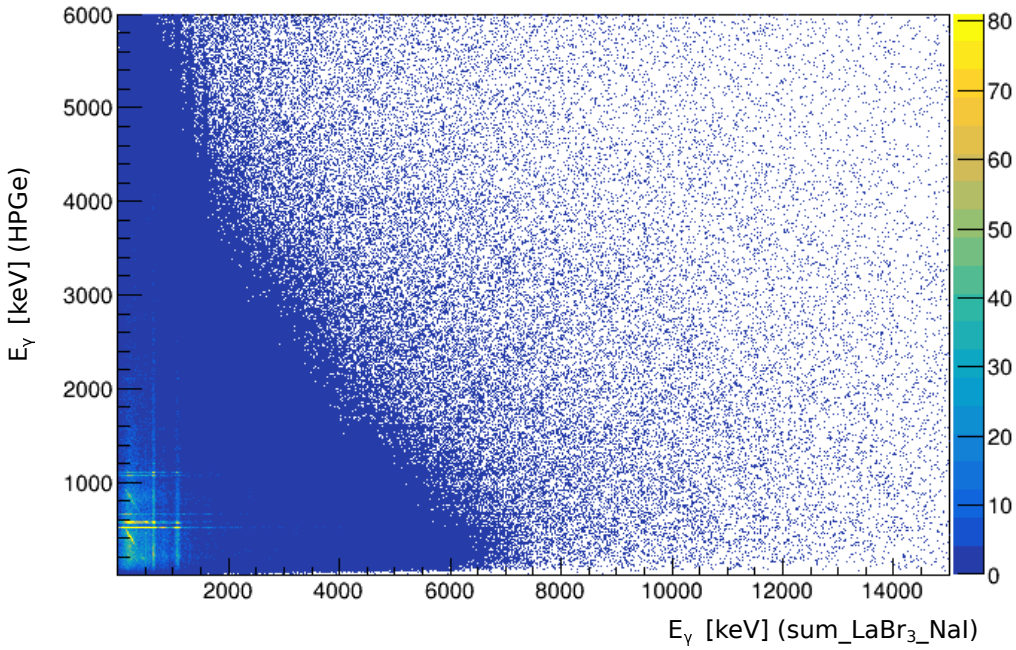

Figure 3.28 – γ-γ coincidence matrix: γ-rays energies from HPGe detectors are plotted along the y axis; γ-rays energies from $LaBr_3$ and NaI (sum spectrum) are presented along the x axis.

3.4 β-feeding identification

The "X" value method

In order to obtain two separated decay level schemes of ^{80g}Ga and ^{80m}Ga, it is essential to identify the β-feeding precursor for each state of the daughter nucleus. To achieve this goal we will use here a method based on the measurement of each individual γ-line apparent half-life. In order to achieve this goal, we will use the so called "X" value method which was first introduced in Ref. [42]. It is based on the following hypotheses (experimental and shell model calculation results): the spins and parity of the two β-decay states $^{80g+m}$Ga are 3^- and 6^- determined from laser spectroscopy measurement and related analysis based on shell model [141]. Therefore, beta-decay of ^{80m}Ga (3^-) would primarily populate states of spin-parity 2^-, 3^-, 4^- through allowed transitions and 2^+, 3^+, 4^+ through first-forbidden non-unique (ffnu) transitions; Similarly, 5^-, 6^-, 7^- and 5^+, 6^+, 7^+ states are primarily populated by ^{80g}Ga beta-decay. Therefore, considering allowed and ffnu transitions, there is no overlap between states directly β-fed by the two isomers. An overlap would be only possible via first-forbidden unique (ffu) transitions with logft > 8, according to systematic analysis of massive nuclei especially in A=80 region [21]. So, if ffu occurs, the crossed beta-feeding can happen to states of 5^+ or 4^+. Contribution from ffu would originate from some unobserved indirect feedings or strong structure effects.

In the following, a quantity "X" is proposed to help in assessing the belonging of the excited states of ^{80}Ge to one of ^{80g}Ga and ^{80m}Ga decay schemes. For each excited state of ^{80}Ge, one determines an apparent half-life ($T^A_{1/2}$) from a specific γ-ray's activity curve like in Figure 4.1 or a weighted value of a

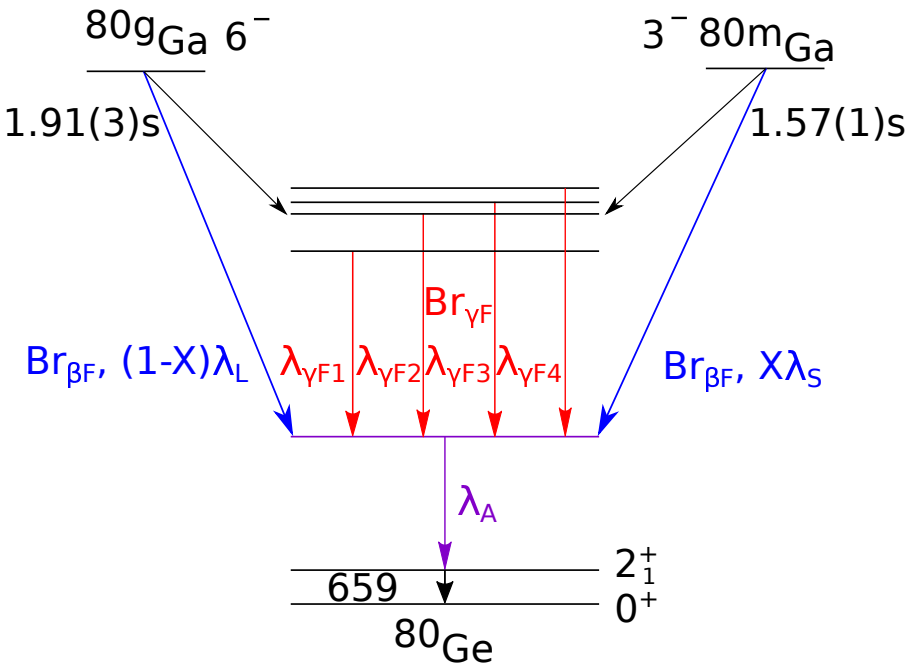

Figure 3.29 – Schematic diagram of "X" equation: involved parameters when building the "X" equation for a given state in purple.

few of γ-rays emitted from this same state in ^{80}Ge. The value of this apparent half life is the result of several contributions: the fractional direct β feeding from ^{80g}Ga (Br$_{\beta F}$X), fractional direct beta feeding from ^{80m}Ga (Br$_{\beta F}$(1-X)), the half-life of ^{80m}Ga ($T^S_{1/2}$), the half-life of ^{80g}Ga ($T^L_{1/2}$), the branching ratio of γ-feeding (Br$_{\gamma F}$), the weighted half-life of γ-rays taking part into this γ-feeding ($T^{\gamma F}_{1/2}$). It is important to point out that, due to the previous comments on forbidden direct beta feeding overlap, the parameters Br$_{\beta F}$X and Br$_{\beta F}$(1-X) should be 1 or 0 strictly. In real life they are not, and we may assume that this is mostly due to the effect of the unobserved feeding (i.e. a Pandemonium effect). One of the main objectives of this work is precisely to show, for this X parameter extraction, the definitive contribution of a hybrid spectroscopy device including PARIS modules in comparison with the results obtained by Verney et al. [42] with traditional spectroscopic means. Figure 3.29 presents the schematic diagram of the relationships between these parameters, and Eq. 3.9 gives the equation relating these parameters.

$$\lambda_A = \frac{Br_{\beta F}}{Br_{\beta F}+Br_{\gamma F}}[X\lambda_S+(1-X)\lambda_L]+\frac{Br_{\gamma F}}{Br_{\beta F}+Br_{\gamma F}}\lambda_{\gamma F} \tag{3.9}$$

where $\lambda = \ln 2/T_{1/2}$, $T^S_{1/2}$ and $T^L_{1/2}$ are the new measured values of ^{80m}Ga and ^{80g}Ga, 1.57(1) s and 1.91(3) s, respectively as introduced at the beginning of this chapter. Br$_{\beta F}$ + Br$_{\gamma F}$ = 1 for a given state in ^{80}Ge. Then, one can derive the equation of X as Eq. 3.10

$$X = \frac{1}{R}\frac{1/T^{\gamma F}_{1/2}-1/T^A_{1/2}}{1/T^L_{1/2}-1/T^S_{1/2}}+\frac{1/T^L_{1/2}-1/T^{\gamma F}_{1/2}}{1/T^L_{1/2}-1/T^S_{1/2}} \tag{3.10}$$

Where $\lambda_{\gamma F} = \ln 2/T^{\gamma F}_{1/2}$ is the apparent decay constant associated with the γ-feeding (weighted

average value), so called (observed) indirect feeding, $T_{1/2}^{\gamma F}$ that was taken as the weighted average of all the γ-rays of indirect feeding as shown in Eq. 3.12 and associated error formula Eq. 3.13. R = Br/(Br+F) is the proportion of the direct β-feeding contribution in the total (direct+indirect) feeding of one given state. It can be calculated directly from the difference between the γ-ray counts of deexcitation and γ-feedings Eq. 3.11. It is important to point out that the precision on the extracted X values relies primarily on the available statistics, and its accuracy (or meaningfulness) relies on the capability to detect all indirect feeding strength, including at high energy.

$$R = \frac{C_{\gamma-from-\beta-feeding}}{C_{all-\gamma-of-deexcitation}} \tag{3.11}$$

$$\overline{T}_{1/2}^{\gamma F} = \sum_{i=1}^{n} Br_{\gamma Fi} T_{1/2(\gamma_i)} \tag{3.12}$$

$$\overline{\Delta T}_{1/2}^{\gamma F} = [\sum_{i=1}^{n} (\Delta Br_{\gamma Fi} T_{1/2(\gamma i)})^2 + (Br_{\gamma Fi} \Delta T_{1/2(\gamma i)})^2]^{\frac{1}{2}} \tag{3.13}$$

Then, X is used to try to attribute each state fed in ^{80}Ge to one of the two decay schemes. Levels with values X = 0 are considered as perfect candidates to the decay scheme of longer-lived ^{80g}Ga (6^-) and X = 1 to the decay scheme of shorter-lived isomer ^{80m}Ga (3^-). Besides the ideal situations, the actual actions taken are: (1). x<0.4, belong to gs decay; (2). x>0.6, belong to isomer decay; (3). 0.4<x<0.6, belong to both. This standard was taken for the purpose of achieving precisely as possible isomer ratio, precursor absolute decayed population of ^{80g}Ga and ^{80m}Ga and the related logft and B(GT) values. After the analysis, only 12 states were assigned to simultaneous direct β-feeding from both ^{80g}Ga and ^{80m}Ga, out of a total of 81 populated states. In the following, I introduce two complementary techniques to confirm the decay scheme assignment obtained from the X parameter method..

Decay ratio comparison method

Another method that can be used to identify the precursors of beta-decay is the comparison spectrum under different beta-activity curves. It profits from the discrepancy of the ground state and isomer, $^{80g+m}$Ga, half-lives. For example, one can put a gate on the beta-activity curve 5.5 s - 8 s (period 1), after beam collection, to obtain a gated spectrum (black one) in Figure 3.30. Next, the same operation can be taken but on 8 s - 10.5 s (period 2) to get the red spectrum. Then, one can immetiately observe some survived peaks in period 2 being relatively weaker than others like the two γ-lines with star mark, just two examples. It demonstrates the precursor populating these beta-delayed γ-rays has a shorter half-lives than another one. This would be ^{80m}Ga. Consequently, 809.1(3) keV γ-rays deexcitation from 4324.2(6) keV (3^-) state and 915.1(3) keV deexcitation from 1574.1(4) keV 2^+ state are asigned to beta-feeding by ^{80m}Ga purely. For a certain γ-ray, Eqs. 3.14 and 3.15 present the ideal ratios of statistics between period 1 and 2, which are calculated based the assumption that there are 10000 precusors of each ^{80}Ga isomer and ground state at 5.5 s. This assmption does not affect the ratio

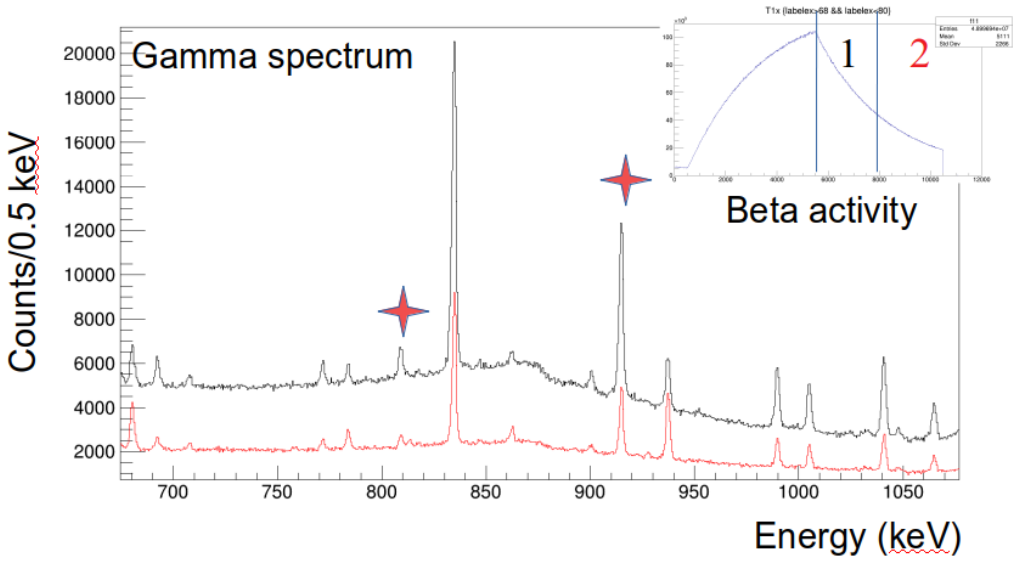

Figure 3.30 – β-gated γ spectra; Black: coincidence with β particles in "1" region in β activity curve; Red: coincidence with β particles in "2" region; γ-lines with red star: the related energy states populating these γ-rays were assigned to ^{80m}Ga β-feeding because of its relative faster decaying rate from "1" period to "2" period.

value.

$$\begin{cases} N_{^{80m}Ga} & = 10000 & t = 5.5s \\ N_{^{80m}Ga} & = 3316(23) & t = 8s \\ N_{^{80m}Ga} & = 1100(11) & t = 10.5s \\ R_{1/2} & = \frac{6684(23)}{2216(25)} = 3.02(3) & \end{cases} \tag{3.14}$$

$$\begin{cases} N_{^{80g}Ga} & = 10000 & t = 5.5s \\ N_{^{80g}Ga} & = 4036(57) & t = 8s \\ N_{^{80m}Ga} & = 1629(33) & t = 10.5s \\ R_{1/2} & = \frac{5964(57)}{2407(66)} = 2.48(7) & \end{cases} \tag{3.15}$$

I_γ comparison method with different fission systems

Last method is to compare the relative γ-ray intensities in different fissioning systems as they produce different isomeric ratios with high and low angular momentum (σ_h/σ_l). For example, through this comparison, it was understood that the isomeric ratio (relative yield in fission of ^{80}Ga fragments under isomeric 3^- form) was higher in photo-fission ^{238}U(γ,n$_f$,f) (data from this and previous work [42] in ALTO) than in thermal neutron induced fission ^{235}U(n$_{th}$,f) (data from Hoff and Fogelberg [142]). This empirical observation is used here as an additional verification criterion: if a γ-ray relative intensity is higher than in Ref. [142], one can reach the conclusion that the related state populated by this γ-transition was β-fed by short-lived ^{80m}Ga.

Figure 3.31 presents the relative intensities of the β-delayed γ-rays emitted by the $^{80g+m}$Ga source measured in this experiment as a function of the evaluated values in NNDC [126] which uniquely originate from the thermal neutron data of Ref. [142]. One can observe that there is a distribution relative to "X = Y" line. Therefore, γ-rays located above this line (stronger) can be generally assigned to ^{80m}Ga β-feeding and those below this line (weaker) are assigned to ^{80g}Ga β-feeding. This conclusion is based on the assumption that there is no simultaneous β-feeding from the ground state and the isomer.

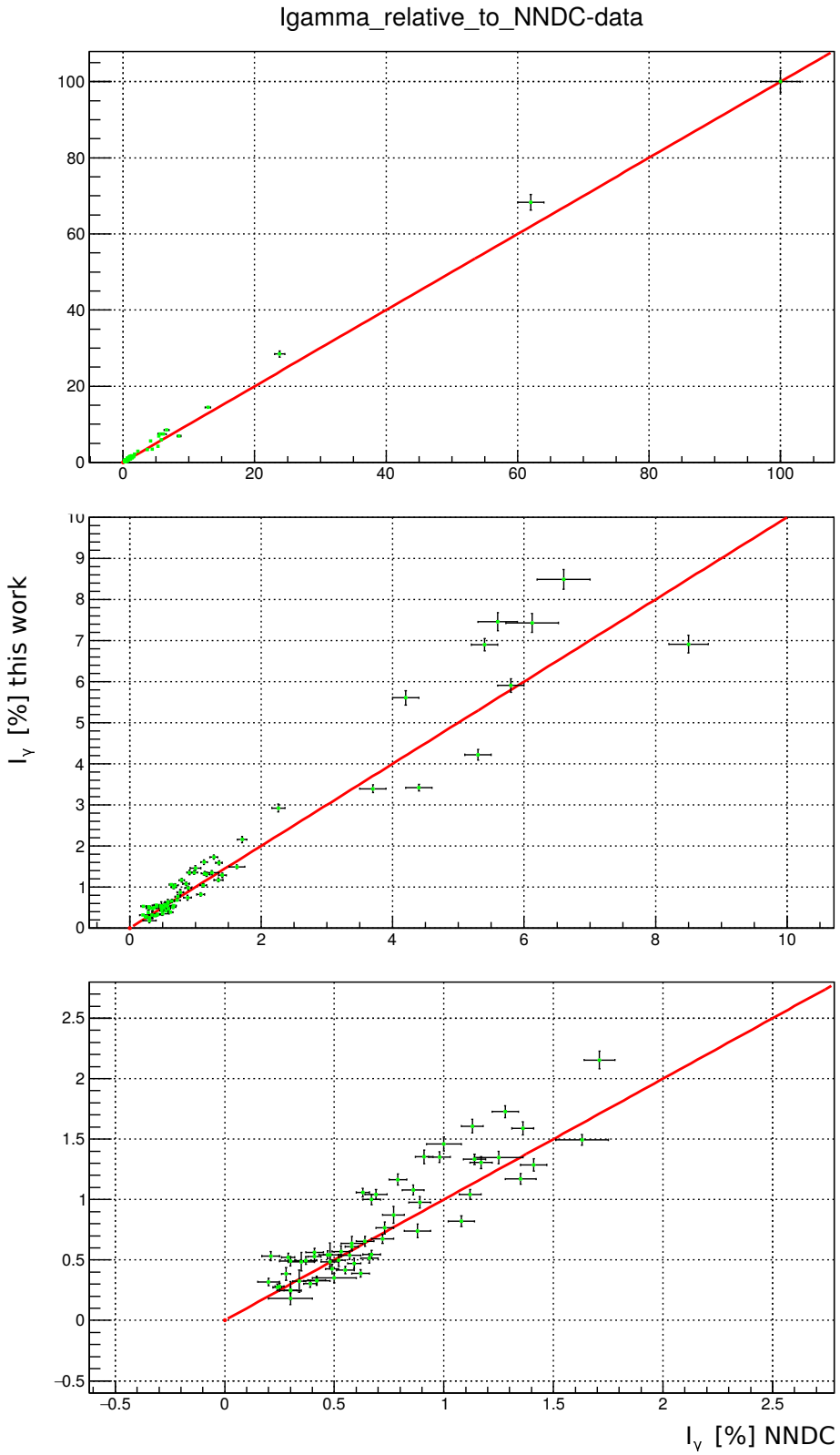

Figure 3.31 – Relative γ intensities of transitions in ^{80}Ge observed in this work from photo-fission of ^{238}U (vertical axis) as a function of relative γ intensities from the evaluated values [126] from thermal neutron-induced fission of ^{235}U [142] (horizontal axis). The two plots in the bottom are the zoom-in of the first one.

4 Experimental results for $^{80g+m}$Ga β-decay study

Sommaire

1 Half-lives of ^{80g}Ga and ^{80m}Ga

The intrinsic γ or neutron decay lifetimes of excited levels in the daughter nucleus ($<$ ns) are negligible compared to the beta-decay lifetime ($>$ tens of ms) of the mother nucleus. As a consequence, the time distribution of all decay emission products: β, β and neutrons, will obey the same Bateman equation system. The β-decay half-lives of the two precursors ^{80g}Ga and ^{80m}Ga can then be extracted from observed ^{80}Ge gamma lines activities.

The differential equation 4.1 gives the evolution of the β-decaying state population N(t) as a function of time, and equation 4.2 is a convenient variant of 4.1. The solution functions 4.3 and 4.4 were used to fit the curve of γ-rays to obtain the half-lives of precusors $^{80g+m}$Ga from each recorded γ ray activity curve. It must be emphasized that the present extraction of individual ^{80g}Ga and ^{80m}Ga half-lives is impossible to achieve from a fit of the β activity curve alone because of their too close values. I have checked that an analysis like the one performed in Ref. [143] is therefore impossible here.

$$dN(t) = \phi dt - \lambda N(t) dt \tag{4.1}$$

$$\int_{N_0}^{N(t)} \frac{1}{\frac{\phi}{\lambda} - N(t)} d(\frac{\phi}{\lambda} - N(t)) = \int_{t_0}^{t} -\lambda \, dt \tag{4.2}$$

$$N_t = \begin{cases} bg, & 0 < \text{t} < 0.5\text{s} \\ \frac{\phi}{\lambda}(1 - e^{-\lambda(t-0.5)}) + bg, & 0.5 < \text{t} < 5.5\text{s} \\ \frac{\phi}{\lambda}(1 - e^{-\lambda(5.5-0.5)})(e^{-\lambda(t-5.5)}) + bg, & 5.5 < \text{t} < 10.5\text{s} \end{cases} \tag{4.3}$$

$$A_{E\gamma} = \lambda N(t) \tag{4.4}$$

In Eq. 4.3, N_t is the population of the β-decaying state (or β-decay precursor) at a given time t, ϕ is the production yield (or intensity, ions/s or s^{-1}) of this state in the beam, and λ is the associated decay rate. Eq. 4.4 is the activity of a γ line at energy E_γ. As an example, Figure 4.1 shows the fitting results of 467 keV γ-ray ($8^+ \rightarrow 6^+$) with the function 4.4, including background, population growth(beam collection) and decay parts.

In the previous study of ^{80}Ga decay at ALTO [42], the half-life of the longest-lived β-decaying state ^{80g}Ga was assigned as 1.925(134) s from the study of the activity pattern of the 467 keV γ line. The choice of 467 keV γ-ray deexciting from the 8^+ level at 3445.11 keV appeared reasonable since this level was observed being fed uniquely by the J = 6 isomer at that time. However, this must be re-investigated in view of the recent study of ^{80}Ga decay of Ref. [127] where new transitions populating this 8^+ state were discovered. Meanwhile, The question of the half-life of the shortest lived beta-decaying state ^{80m}Ga must be re-investigated too because in the study of Ref. [42] most of the γ-ray transitions characterized by the shortest half-lives were unfortunately not placed in the level scheme due to too weak intensity. Therefore, the authors of this work chose the shortest of those values (which corresponds to the γ-ray at 2554.95 keV) was taken as the most probable half-life of the

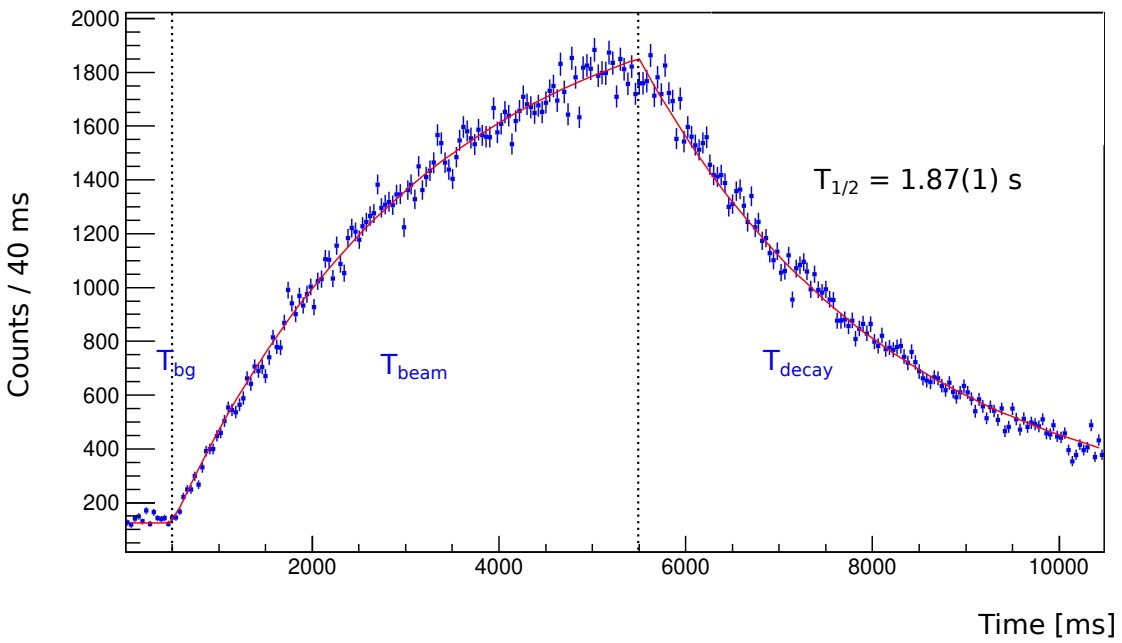

Figure 4.1 – 467 keV γ-ray activity curve from $8^+ \rightarrow 6^+$ deexcitation.

shortest-lived ^{80}Ga β-decaying state, 1.317(155) s [42].

In the present work, thanks to the superior statistics compared to Ref. [42], I propose to introduce a new method to determine the half-lives of $^{80g+m}$Ga relying on the use of the highest-energy γ-lines. Considering the small gamma strength originating from above S_n in ^{80}Ge, $\Gamma_\gamma/(\Gamma_\gamma + \Gamma_n) = 3.2(4)\%$, the principle of this method is to select the states which deexcite with high energy γ-rays but are fed uniquely by ^{80g}Ga or ^{80m}Ga β-decay (no higher γ-feeding). The selection of these γ-rays is based on three conditions: 1) the state depopulated by this γ transition receives no unobserved high-energy gamma population, because, otherwise it would originate from neutron-unbound levels; 2) it receives no observed lower-energy γ population either because lower-energy γ-rays should be observed if existing due to higher detection efficiency of detectors in the lower energy region; 3) "X" value of this state is clear, discriminating ^{80g}Ga and ^{80m}Ga definitely. For extraction of the half-life of ^{80g}Ga, the 4443.6(7) keV (depopulating the 6187.1(7) keV state) and 4835.7(7) keV (corresponding to 6578.5(9) keV state) γ-rays were used. Similarly, for ^{80m}Ga, 3750.5(6), 4207.8(7), 4238.8(7), 4412.8(7), 4665.3(8), 4678.5(7), 4729.6(7), 5387.4(8), 5353.7(8) keV γ-rays were taken. This selected set of γ lines is represented by red points in Fig. 4.3 which represents the half-lives of all individual gamma line activities as a function of their energies. In this figure, one observes a clear splitting in the high energy region and the scattering between the half-lives of the ground state and the isomer in the lower energy region. The extraction of the half-life values originates from the analysis of gamma-activity time patterns like the one shown in Fig. 4.1. A background subtraction procedure was applied which consisted in subtracting average of left and right background time distribution spectrum, especially for the weak peaks in case of being dominated by the background as the background of γ spectrum (Compton scattering γ-rays) also has a half-life as shown in Figure 4.2.

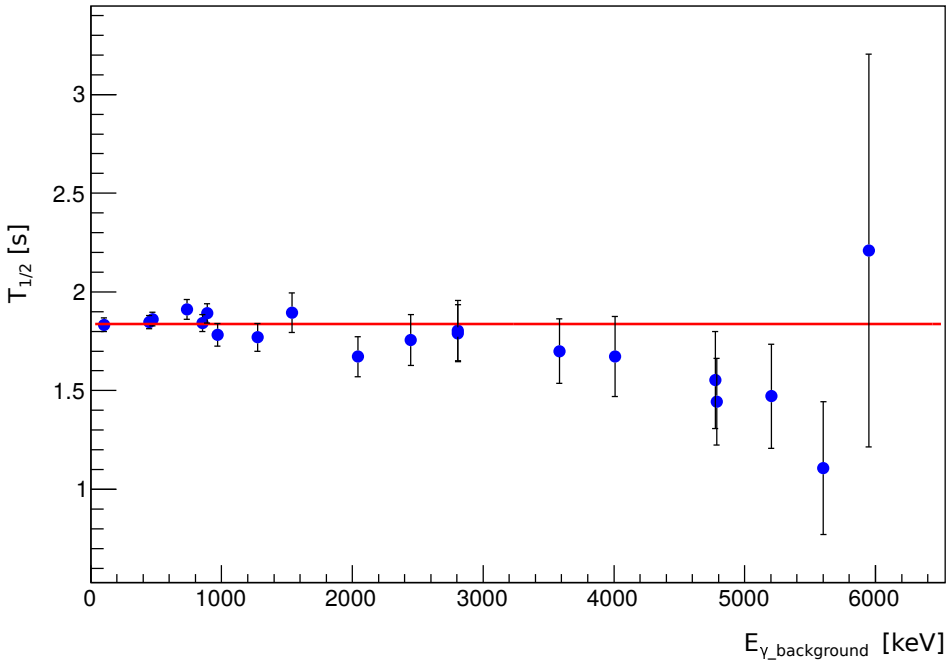

Figure 4.2 – $T_{1/2}$ distribution of background γ-rays. The method used is the same as that for the 467 keV γ-ray but without background suppression. One can easily observe the deviation from the average value, 1.83(1) s, in the high energy region, which is an evidence that there are more γ-rays populated by shorter-lived isomer ^{80m}Ga β-decay than by ^{80g}Ga in this region. This trend is in good agreement with the one observed in Fig. 4.3.

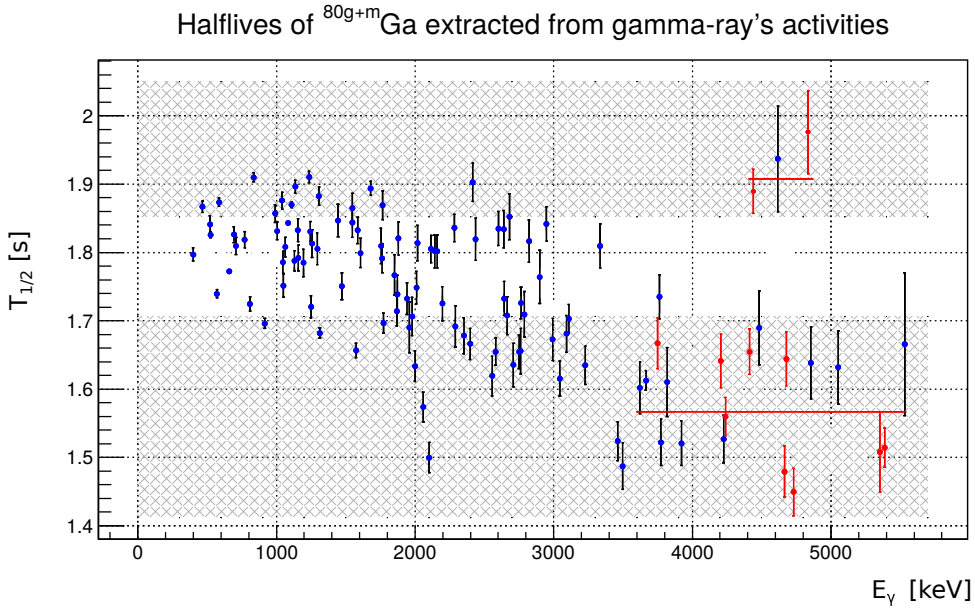

Figure 4.3 – Measured (apparent) half-lives of all individual gamma-line activities associated with the decay of the mixed $^{80g+m}$Ga source. Red points show data used to extract half-lives of ^{80g}Ga and ^{80m}Ga. The red lines are the fitting curves. The splitting in the higher energy region and scattering in the lower energy region are easily observed

$$\overline{T}_{1/2} = \frac{\sum_{i=1}^{n} \frac{T_{1/2(\gamma_i)}}{[\Delta T_{1/2(\gamma_i)}]^2}}{\sum_{i=1}^{n} \frac{1}{[\Delta T_{1/2(\gamma_i)}]^2}} \tag{4.5}$$

$$\Delta\overline{T}_{1/2} = [\sum_{i=1}^{n} \frac{1}{[\Delta T_{1/2(\gamma_i)}]^2}]^{-\frac{1}{2}} \tag{4.6}$$

Formula 4.5 and 4.6 were applied to calculate the $T_{1/2}$ (^{80g}Ga), $T_{1/2}$ (^{80m}Ga) and their error bars using the selected 2 and 9 γ-rays separately [116] and the final results are given by Eq. 4.7 and 4.8 below. This methodology of experimental error analysis is also the one adopted by "ROOT Fit" procedure applied to Figure 4.4.

$$^{80m}Ga : T_{1/2} = 1.57(1)s \tag{4.7}$$

$$^{80g}Ga : T_{1/2} = 1.91(3)s \tag{4.8}$$

In the present work, a total of 114 characteristic half-lives of activities of beta-delayed γ-rays could be determined, which are shown in a graphical way in Figure 4.3. Among them 75 were assigned to the decay of ^{80g}Ga and 64 of ^{80m}Ga according to "X" methodology illustrated in Figure 3.29. Therein, 25 γ-rays are populated commonly by both isomers.

Figure 4.4 displays the half-lives of the ground and isomeric states from this work (Red points) and previous experimental results (blue and black). $T_{1/2}$ = 1.676(14) s is adopted by Nuclear Data Sheets in 2005 that is a weighted average value from several measurements [144]. At that time, the isomeric state of ^{80}Ga have not been discovered. It was found in 2010 through laser spectroscopy [141]. Then, D. Verney et al. measured the half-lives of the ground and isomeric states through beta-delayed γ spectroscopy and obtained 1.3(2) s and 1.9(1) s [42]. They were evaluated and adopted by NNDC database [126]. The result obtained in the present work for $T_{1/2}$(^{80g}Ga) confirms the one of ref. [42] but with much better precision. However, the half-life of ^{80m}Ga found here is larger than the previous result in Ref. [42]. In Ref. [42], the authors chose to propose the shortest γ-activity half life as the most probable value for ^{80m}Ga, this is not the choice made here. As can be seen in 4.4, the previous adopted value 1.676 s is approximately situated at middle position between the two extremes of the $T_{1/2}$ values of ^{80m}Ga and ^{80g}Ga. Similar phenomenon occurs for the $T_{1/2}$ extracted from neutron activity: 1.77(24) s [123], which can be interpreted as an evidence that both ^{80}Ga ground state and isomer are neutron precursors.

2 β-delayed γ spectra

2.1 β-γ coincidence spectra

The β-gated γ spectrum measured during experiment (with the mass-separator set on A = 80 during ~13 h) is presented in Figures 4.5, 4.6 and 4.7. Totally, a number of 3.54 $\times$ $10^8$$\beta$ particles were recorded. One can observe the β-delayed γ-rays (peaks) belonging to daughter and granddaughter

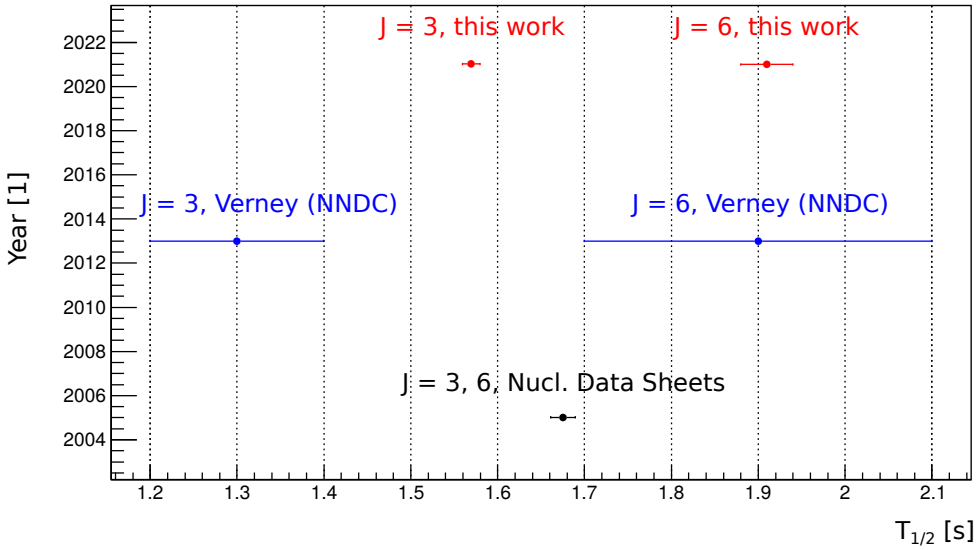

Figure 4.4 – $T_{1/2}$ for the ground and isomeric states of ^{80}Ga. Red: measured presently through specially selected γ-rays (see Figure 4.3); Blue: proposed by D. Verney [42] (adopted by NNDC currently [126]) through two γ-rays, $8^+ \rightarrow 6^+$ and shortest-lived one. Black: adopted value by Nuclear Data Sheets in 2005 [144].

nuclei ^{80}Ge, ^{80}As and ^{80}Se with different marks. In addition, γ-ray deexcitation of nucleus ^{79}Ge, populated through beta-delayed neutron emission of ^{80}Ga, is also detected.

No other γ-rays were observed in the spectrum, which proves the beam purity, ensured by the triple selectivity: reaction selectivity (photo-fission is the only process), mass selectivity, and Z selectivity through laser-ionization in ALTO ISOL facility.

So, in conclusion, as can be seen in these spectra, the γ-lines characterizing the activity of the nucleus of interest, ^{80}Ga, are clearly visible and play a dominant role. It is the higher electron beam intensity (10μA) and a successful laser ion source that guarantee the cleanness of these spectra. All these γ-rays populated through deexcitation of the excited states of ^{80}Ge following the β-decay of ^{80}Ga allowed us to improve and enrich the decay level scheme of ^{80}Ge.

2.2 β-γ-γ coincidence spectra

It is essential for building and enriching the decay level schemes of ^{80g}Ga and ^{80m}Ga to reconstruct all β-fed γ-ray cascades. Therefore, the β-γ-γ coincidence technique was used to assign the new γ transitions to ^{80}Ge and check the previous results. Figures 4.8 and 4.9 present the 659 keV ($2_1^+ \rightarrow 0_1^+$) γ-line gated γ spectra (blue ones). To remove the influence of background, the gated spectra are background suppressed through spectra substraction. Wherein the background spectrum is taken as average of spectra taken left and right of the peak of interest. The analysis shows that the strongest contribution to the background around 659 keV originates from the strongest lines of the ^{80}Ge decay scheme: 1108, 1109 and 1236 keV. This is clearly manifested by the diagonals shown in Figure 3.19 "HPGe-HPGe" matrix. They are suppressed when using add-back modes as described in the previous chapter. Some minor components survive the background subtraction like two structures around 400

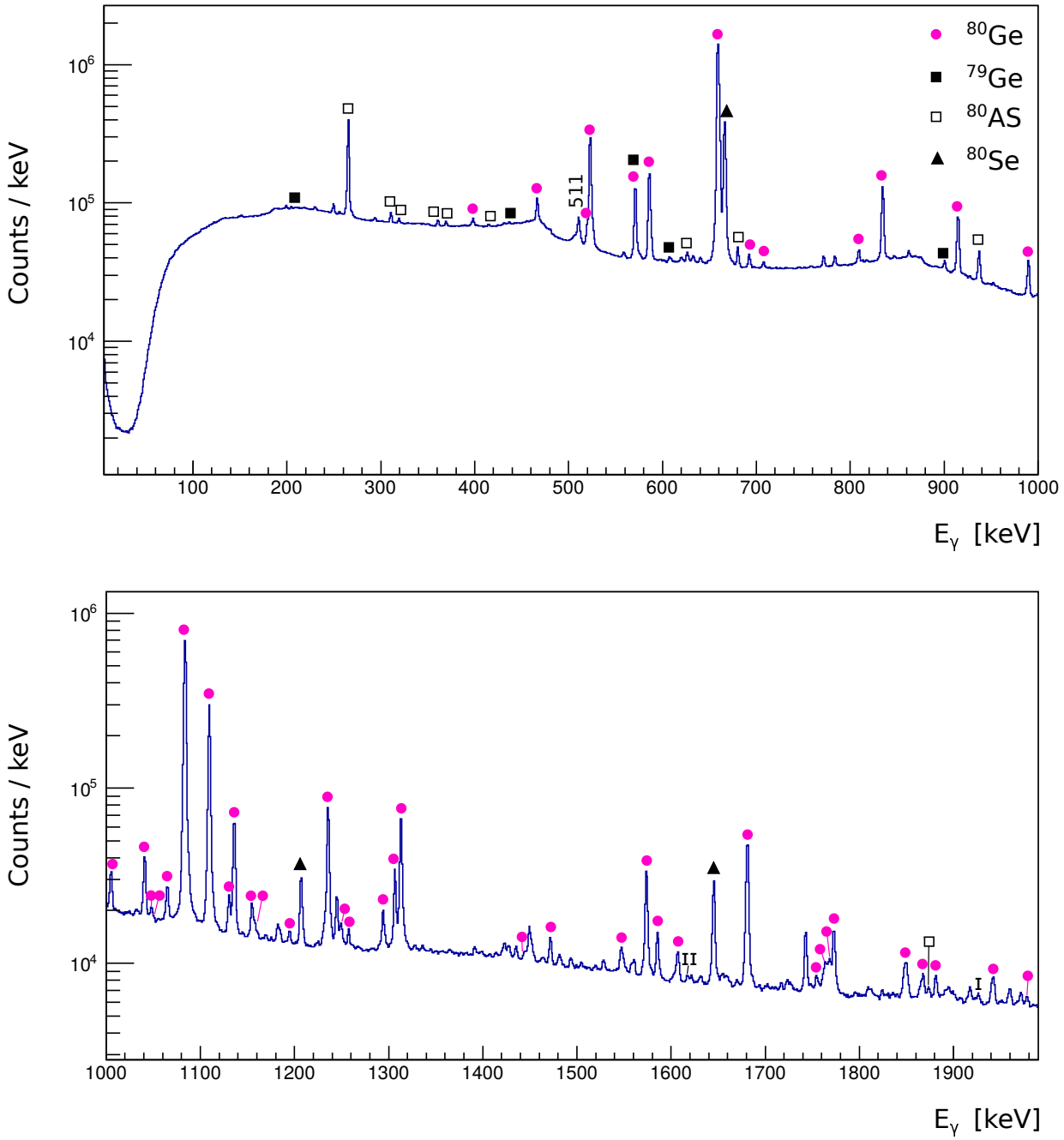

Figure 4.5 – β-gated γ spectra in the range 0 to 2000 keV. The marked lines are attributed to transitions in daughter nuclei: filled circles = ^{80}Ge; filled squares = ^{79}Ge; empty squares = ^{80}As and filled triangles = ^{80}Se. I and II symbols denote single- and double-escape peaks, respectively.

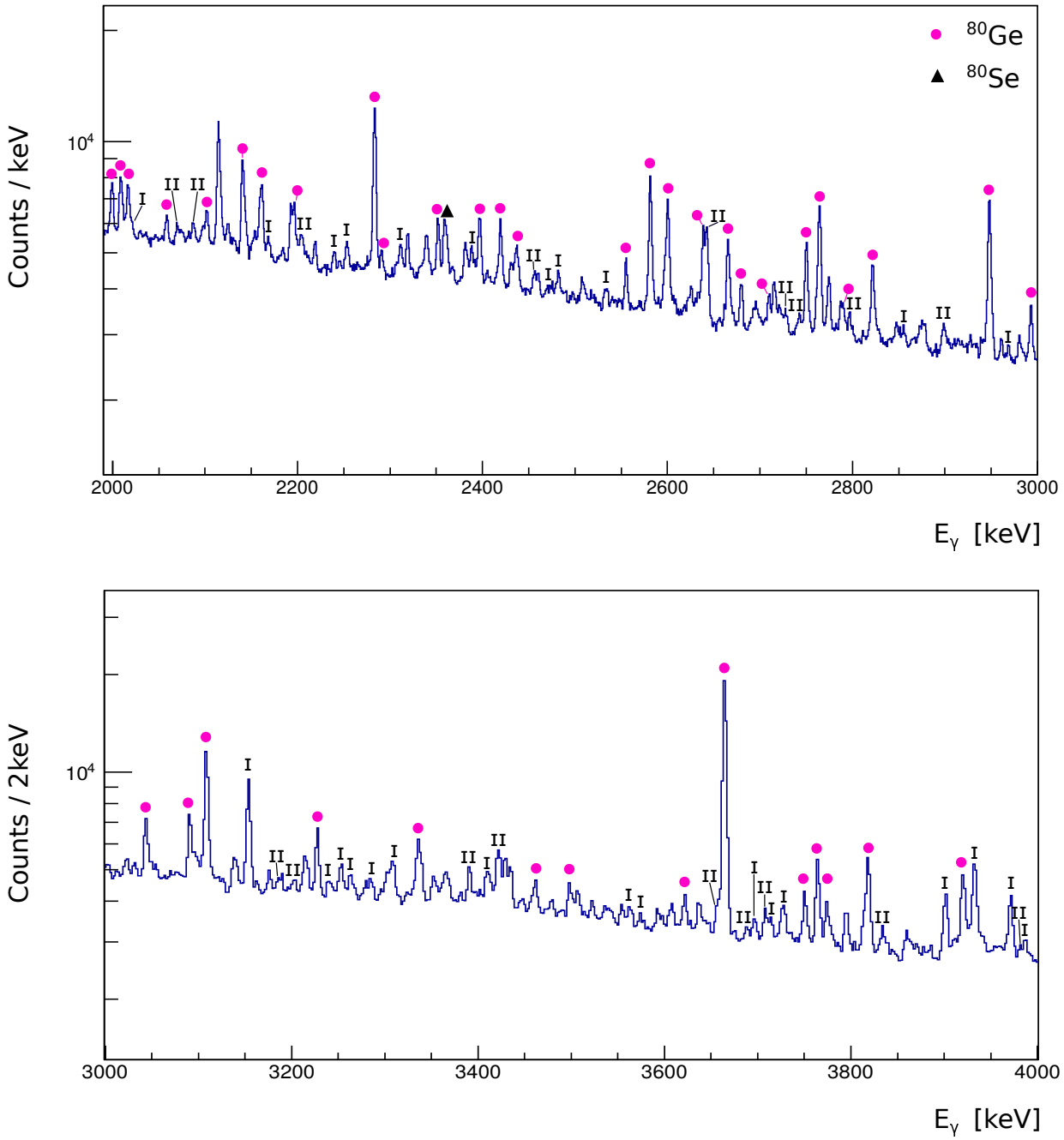

Figure 4.6 – β-gated γ spectra in the range 2000 to 4000 keV. The marked lines are attributed to transitions in daughter nuclei: filled circles = ^{80}Ge and filled triangles = ^{80}Se. I and II symbols denote single- and double-escape peaks, respectively.

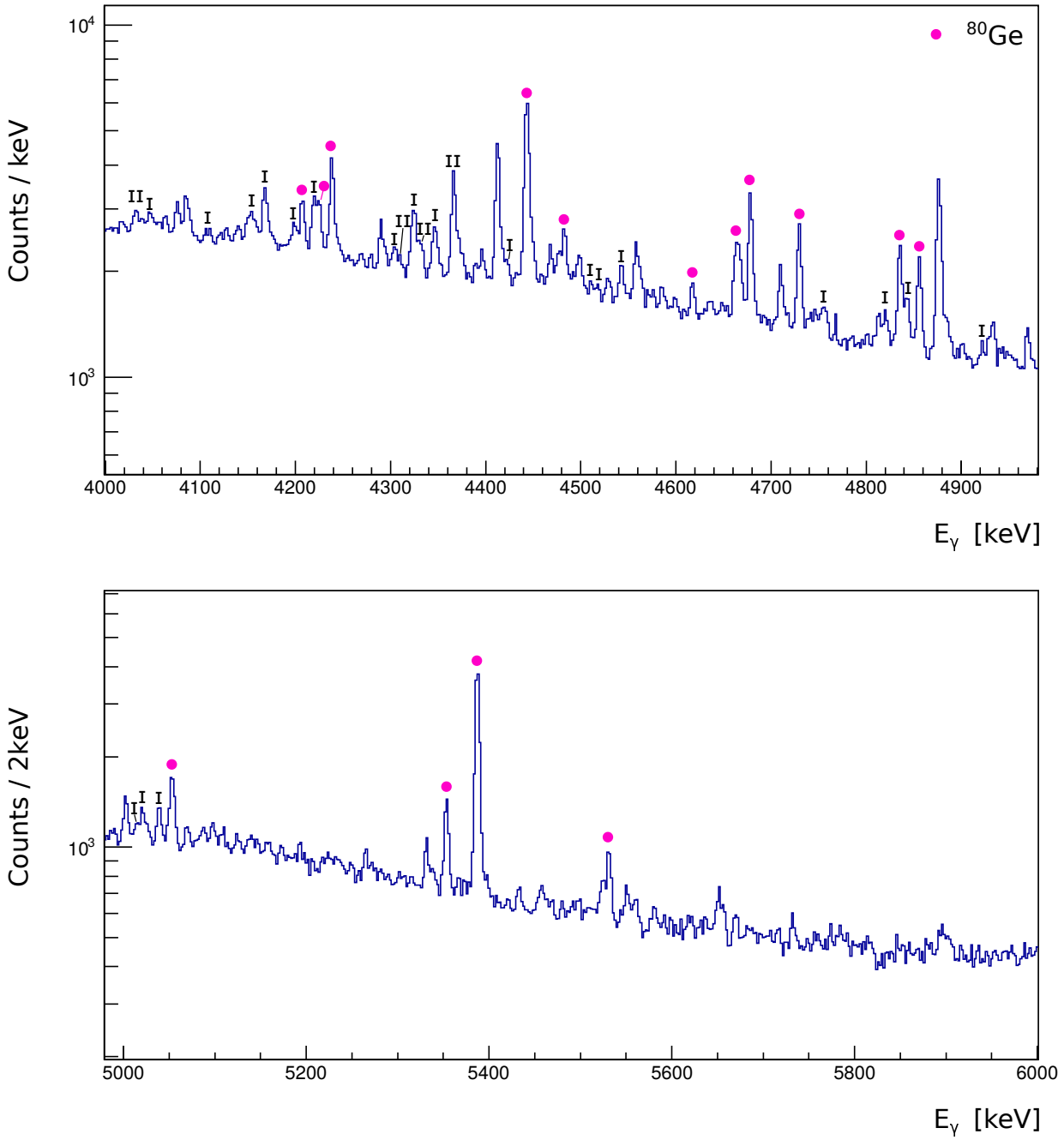

Figure 4.7 – β-gated γ spectra in the range 4000 to 6000 keV. The marked lines are attributed to transitions in daughter nuclei (filled circles = ^{80}Ge). I and II symbols denote single- and double-escape peaks, respectively.

keV in Figure 4.8.

A convenient way to distinguish between real and random coincidences is to superpose ungated and gated spectra. The relative intensity of the peaks associated with real coincidences is strongly increased in the gated spectra. To illustrate this, both ungated (black) and gated spectra are represented in Figures 4.8 and 4.9.

Additional spectra gated by 915 ($2_2^+ \rightarrow 2_1^+$) and 1574 keV ($2_2^+ \rightarrow 0_1^+$) γ-rays are presented in Figures 4.10 and 4.11.

In the process of decay scheme construction, to make the coincidence relationships between the γ-rays convincing enough, an opposite gating procedure is necessary. For example, the cascade connecting the four levels 6187 keV $\rightarrow$ 1742.9 keV $\rightarrow$ 659.3 keV $\rightarrow$ 0 keV contains three gamma transitions at 4444, 1083 and 659 keV. Therefore, 4444 keV peak is obviously visible when gating on 1083 keV γ-ray as shown in Figure 4.12 upper spectrum. Conversely, 1083 and 659 keV γ-rays must be clearly visible in the spectrum gated on 4444 keV γ-line as presented Figure 4.12 lower spectrum. Furthermore, their intensity ratio in the gated spectrum should be consistent with the detector efficiency ratios. These intensity considerations provide a useful additional verification criterion for the validity of the reality of the coincidence and the validity of the placement of the associated transition in the level scheme. For example, one can use this method to judge whether a γ-ray has coincidence with 1083 and 1109 keV γ-rays simultaneously or with just one of them.

In the present work, γ transitions and levels were assigned when an unambiguous (following the above criteria) coincidence relationship has been established.

2.3 β-delayed "Ultra"-high-energy γ-rays

Figure 4.13 shows the β-gated γ spectrum in the high energy region recorded with PARIS spectrometer. The region located above 5.6 MeV is of particular interest because it contains γ rays originating exclusively from the ^{80}Ga β decay as the Q values of daughter nuclei ^{80}Ge and ^{80}As are 2679(4) keV and 5545(4) keV, respectively [126]. In particular, in model 1, as described in Table 3.4, shown with red line in Figure 4.13, the background is easily and clearly distiguished and counted. Based on this determination of background, the background of spectrum from mode 3 with blue line is obviously visible and clearly starts above Q_β value. Compared to the previous spectrum, the excess of counts that is found in the energy region extending from S_n to Q_β must be attributed to the decay of states which are located there. This is because this excess of counts corresponds either to correctly reconstructed single γ transitions that connect directly these levels to the ground state, or to summed cascades originating from the depopulation of levels in the same region.

In order to study the highest-energy part of the γ spectrum which is dominated by Compton scattering and escape events the following PARIS-data sorting mode was used: 1) add-back between the nine $LaBr_3$ crystals within a 9-fold cluster; 2) outer-shell NaI crystals work as anticoincidence veto detectors. The energy resolution and detection efficiency of PARIS under this configuration can be found in chapter 3 experimental setup section. As can be seen in Fig. 4.14(a), high-energy γ-ray events, spectra endpoint and backgrounds are easily visible and distinguishable. It must be emphasized that, thanks to the specific properties of PARIS correctly exploited through this sorting method, one can

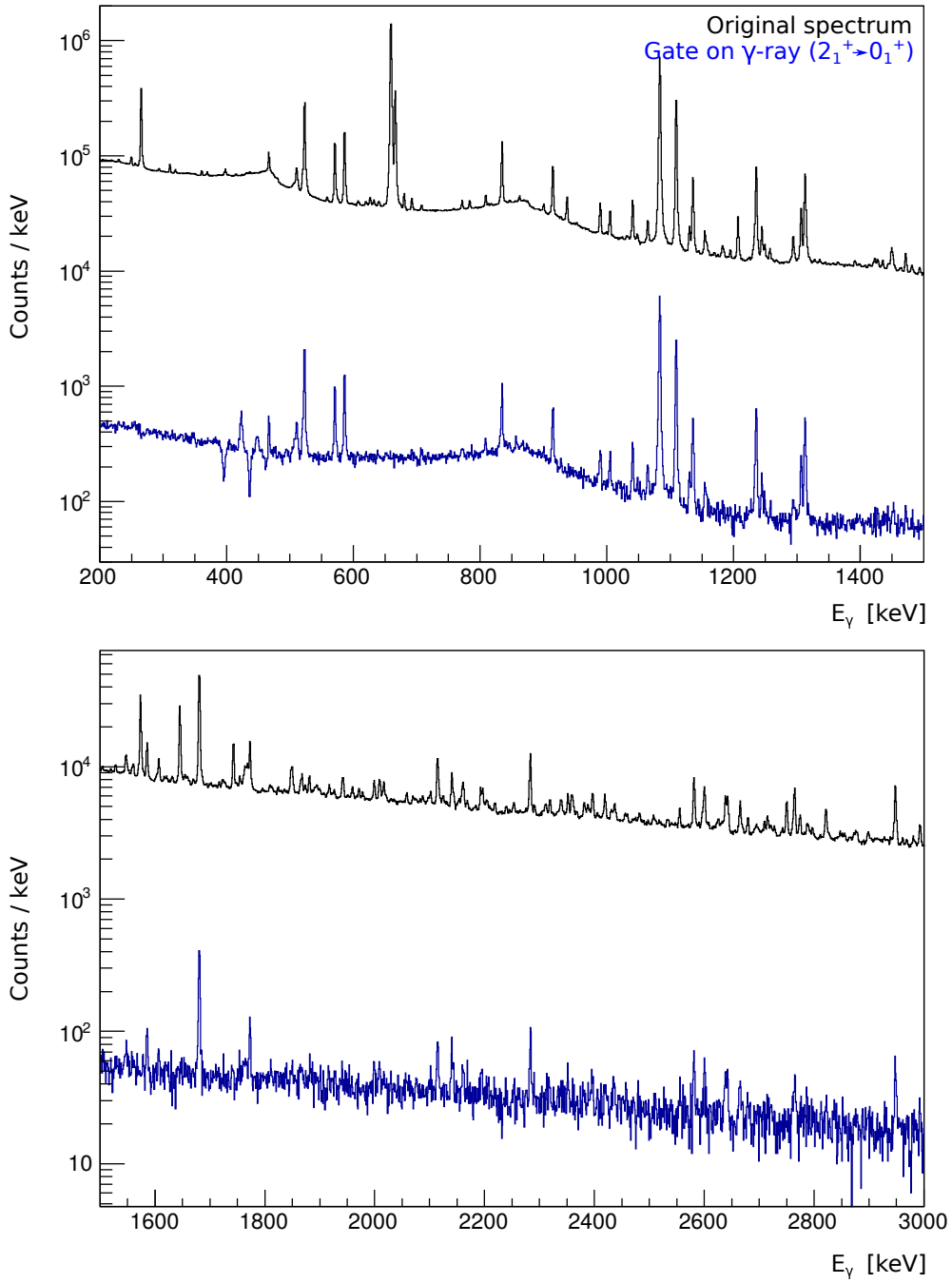

Figure 4.8 – Black: original β-γ coincidence spectra (β triggered); Blue: the β-γ-γ coincidence and background suppressed spectra with gating on 659 keV γ-line ($2_1^+ \rightarrow 0_1^+$ in ^{80}Ge) in the energy range 200-3000 keV.

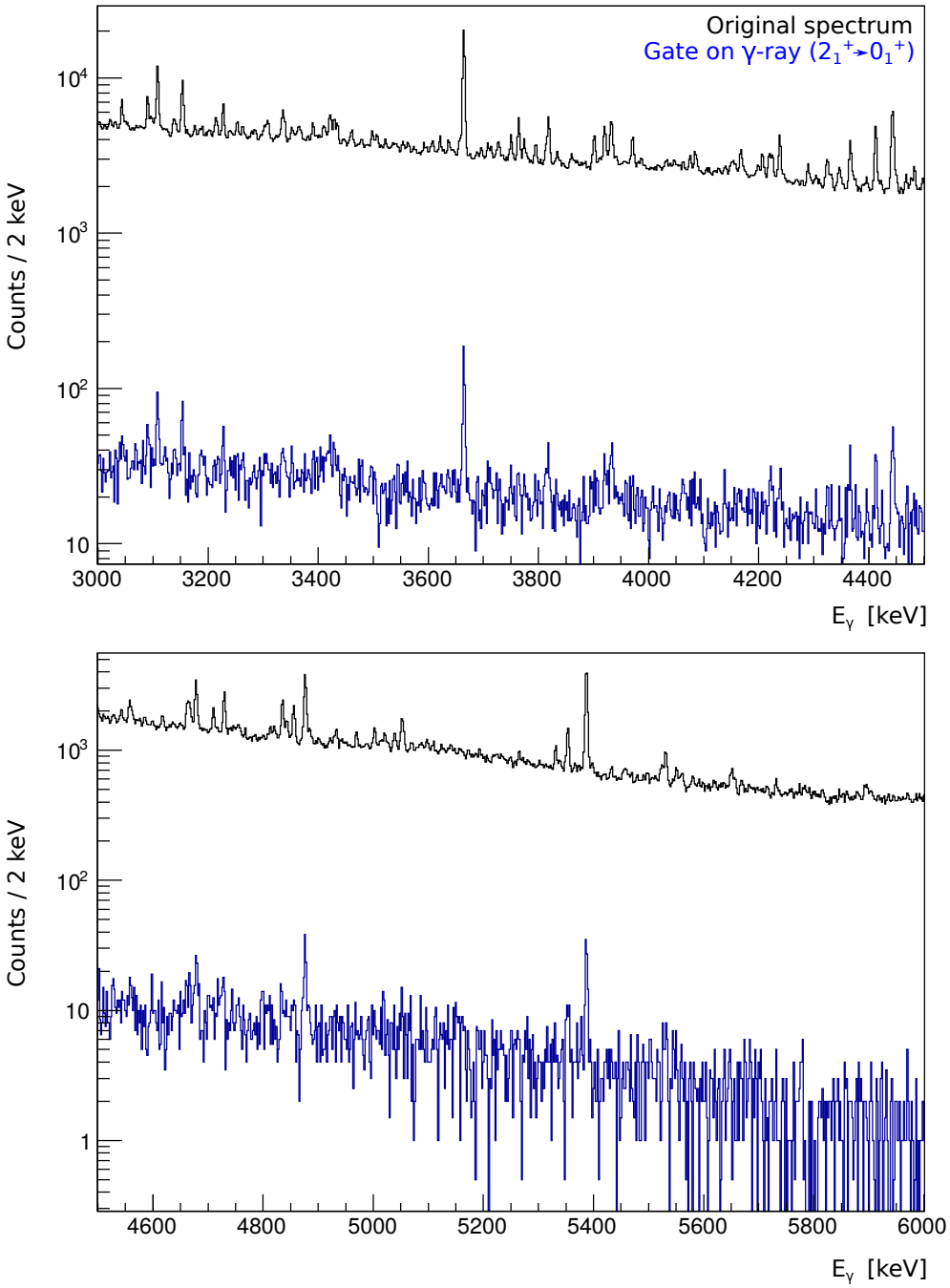

Figure 4.9 – Black: original β-γ coincidence spectra (β triggered); Blue: the β-γ-γ coincidence and background suppressed spectra with gating on 659 keV γ-line ($2_1^+ \rightarrow 0_1^+$ in ^{80}Ge) in the energy range 3000-6000 keV.

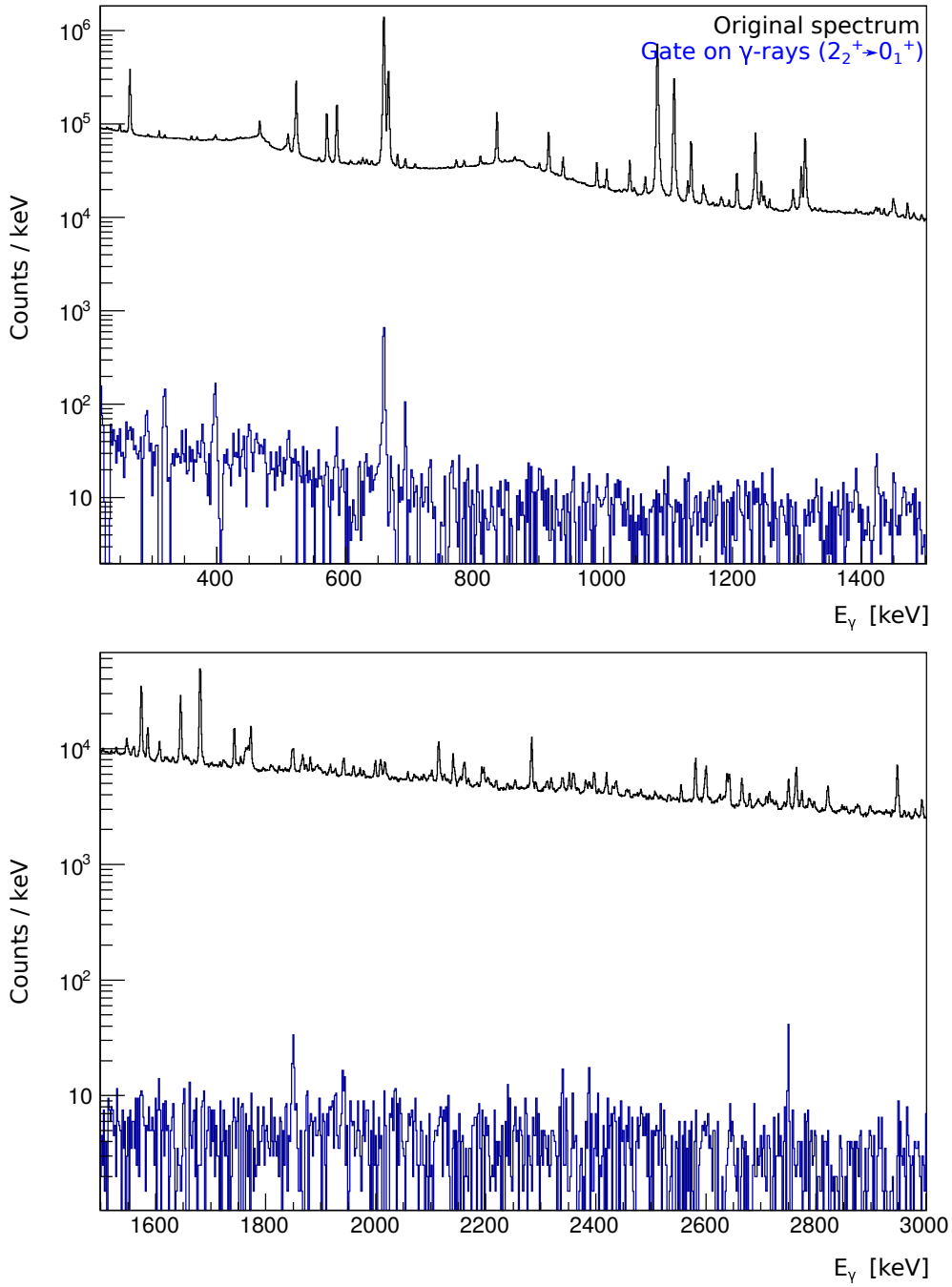

Figure 4.10 – Black: original β-γ coincidence spectra (β triggered); Blue: the β-γ-γ coincidence and background suppressed spectra with gating on 915 ($2_2^+ \rightarrow 2_1^+$ in ^{80}Ge) and 1574 keV ($2_2^+ \rightarrow 0_1^+$ in ^{80}Ge) γ-lines in the energy range 0-3000 keV.

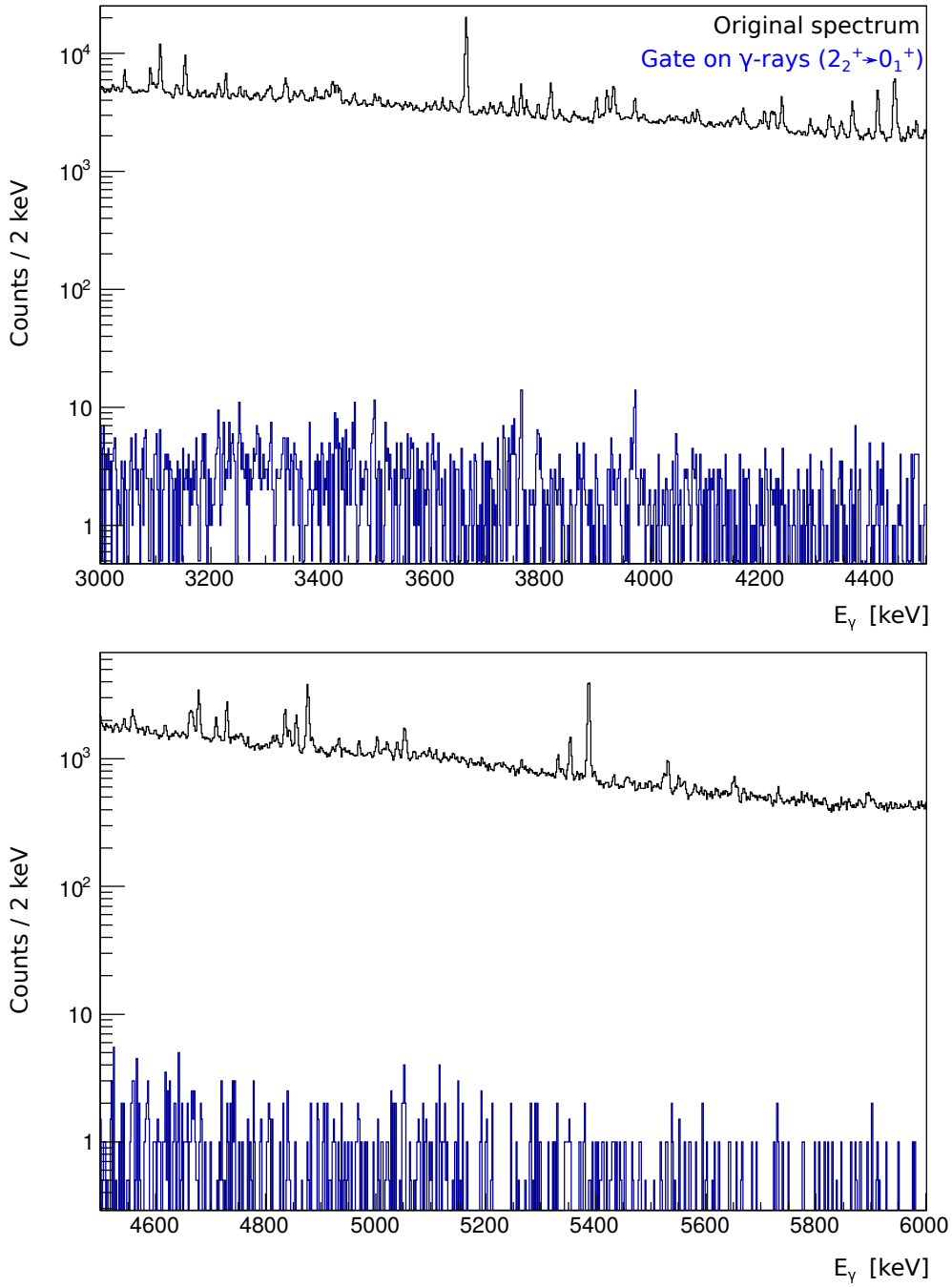

Figure 4.11 – Black: original β-γ coincidence spectra (β triggered); Blue: the β-γ-γ coincidence and background suppressed spectra with gating on 915 ($2_2^+ \rightarrow 2_1^+$ in ^{80}Ge) and 1574 keV ($2_2^+ \rightarrow 0_1^+$ in ^{80}Ge) γ-lines in the energy range 3000-6000 keV.

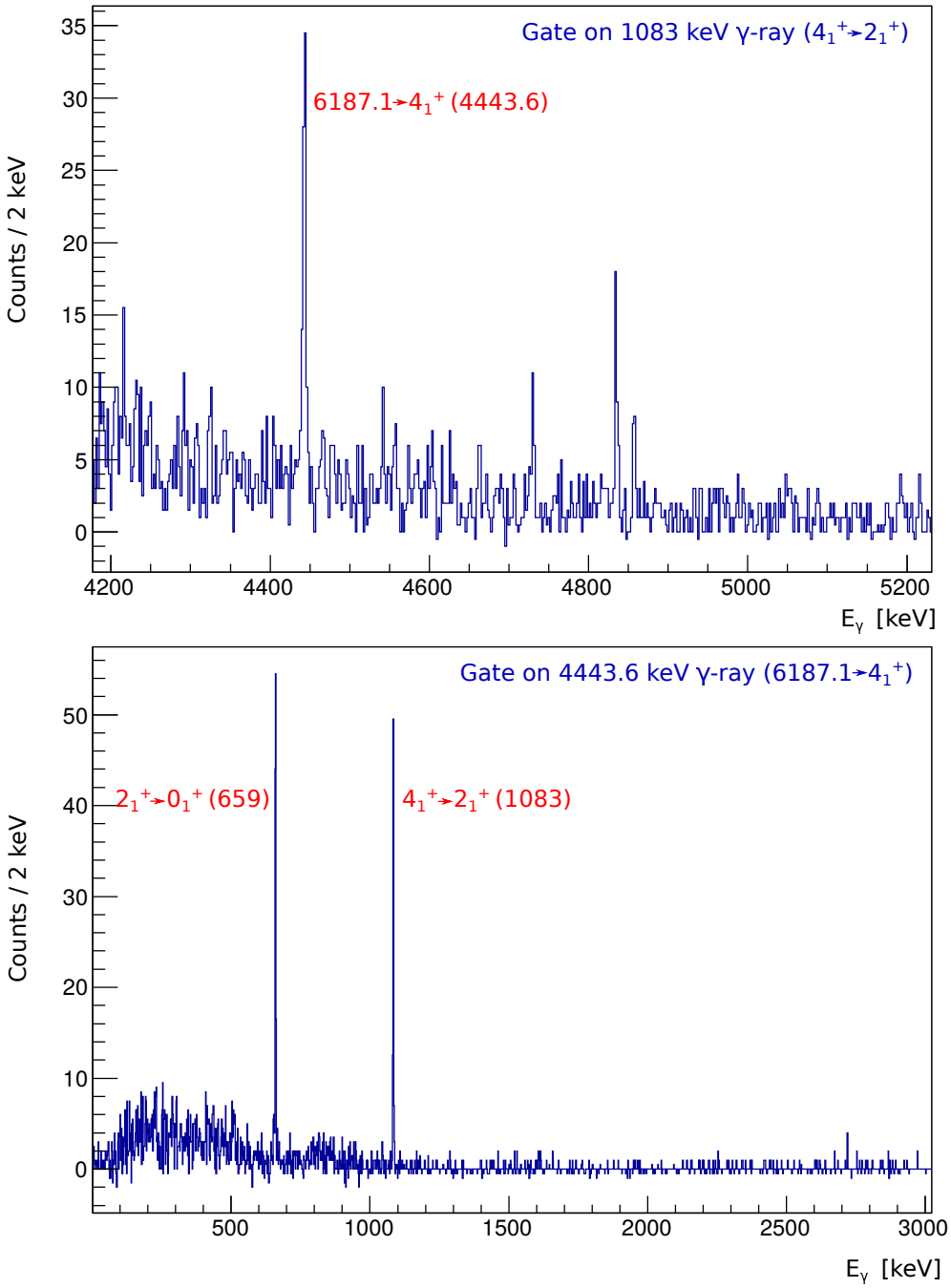

Figure 4.12 – Top: The β-γ-γ coincidence spectrum with gating on 1083 keV ($4_1^+ \rightarrow 2_1^+$) γ-line. One can clearly observe the 4444 keV γ-ray; Bottom: The β-γ-γ coincidence spectrum with gating on 4444 keV (6187 keV $\rightarrow 4_1^+$) γ-line. One can obviously see 659 ($2_1^+ \rightarrow 0_1^+$) and 1083 keV γ-rays. Thus, one can confirm that the three transitions belong to the cascade 6187 keV $\rightarrow 4_1^+ \rightarrow 2_1^+ \rightarrow 0_1^+$.

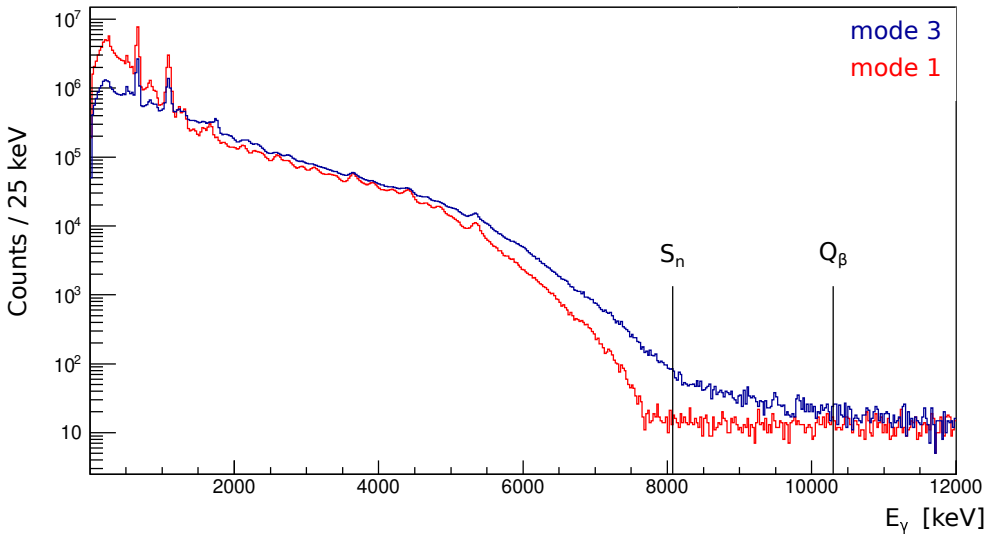

Figure 4.13 – Red: γ spectrum from PARIS under mode 1 data sorting procedure, as described in Table 3.4. Blue: γ spectrum from PARIS under mode 3 data sorting procedure, as described in Table 3.4.

extract directly the higher-energy part of the γ spectrum without resorting to Monte-Carlo techniques or to any theoretical assumption on the γ strength distribution. This is, in particular, a dramatic improvement over the first study of the high-energy regions of β-delayed spectra that was initiated at ALTO with the work of Gottardo et al. [43].

In order to understand the physics behind the structures observed in this high energy part of the γ strength populated in β decay, detailed information was extracted including level energy, β transition half-life, B(GT) and their decay pattern to derive the spin-parity information. As shown in Figure 4.14(b), one can observe distinctly resolved full-energy peaks and their associated single-escape peaks in the PARIS spectrum gated by 659 keV events in HPGe detectors corresponding to the $2^+ \rightarrow 0^+$ transition of ^{80}Ge. The peaks appearing in these HPGe-gated PARIS spectra can be unambiguously interpreted as originating from direct transitions from an excited state located at 7.8 MeV excitation energy to the first-excited 2^+ state of ^{80}Ge. For further verification, the reversed coincidence spectrum is showed in Figure 4.14(c).

As explained earlier, the advantage of using a mixed ^{80g}Ga (J^π=6^-) + ^{80m}Ga(J^-=3^π) source is to populate excited states of ^{80}Ge over a very large spin range. But in order to be able to make hypotheses on γ transitions multipolarities from the observed decay patterns and to assign spins and parities to the ^{80}Ge levels one should disentangle the two ^{80g}Ga and ^{80m}Ga decay schemes. As explained above, this is achieved by using a method based on the measurement of the half-life of a beta-delayed γ-ray. This apparent half-life receives two contributions: 1) direct β-feeding branches from the ground and isomeric states and their half-lives; 2) indirect γ-feeding from the depolulation of higher-lying states and their half-lives. To each level we attributed a quantity X that includes these different contributions and that should take a value 1 and 0 if the level receives β population from ^{80g}Ga J=6 and ^{80m}Ga J=3 respectively. As shown in Fig. 4.15(b), this method was validated with states of well established spins and parities: 2_1^+, 2_2^+, 4^+, 6^+ and 8^+. Figure 4.15(a) presents the activity curve of the 7212(53)

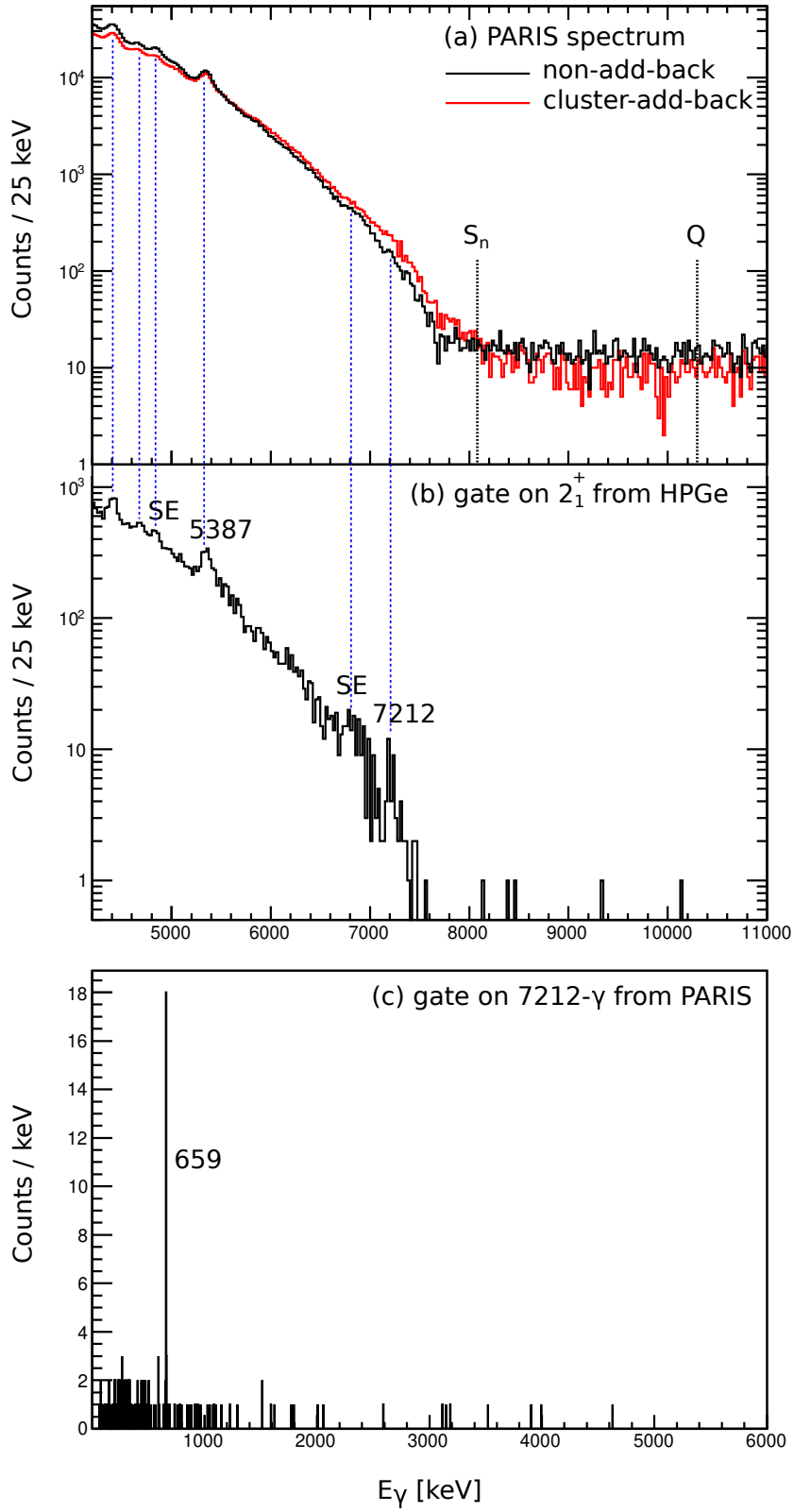

Figure 4.14 – The highest-energy part of the gamma spectra. (a): The γ-ray energy spectrum as measured in coincidence with β particles from $LaBr_3$ scintillators in PARIS when outer-shell NaI crystals work as veto detectors. Red: Same as black one but signals in $LaBr_3$ inside one cluster were added back; (b): γ-rays in (a) black spectrum in coincidence with 659 keV ($2^+ \rightarrow 0^+$) γ-ray from HPGe detectors; (c): The inverse coincidence: γ-ray registered in HPGe detectors in coincidence with 7212 keV γ-ray from PARIS-$LaBr_3$ scintillator (NaI as veto)

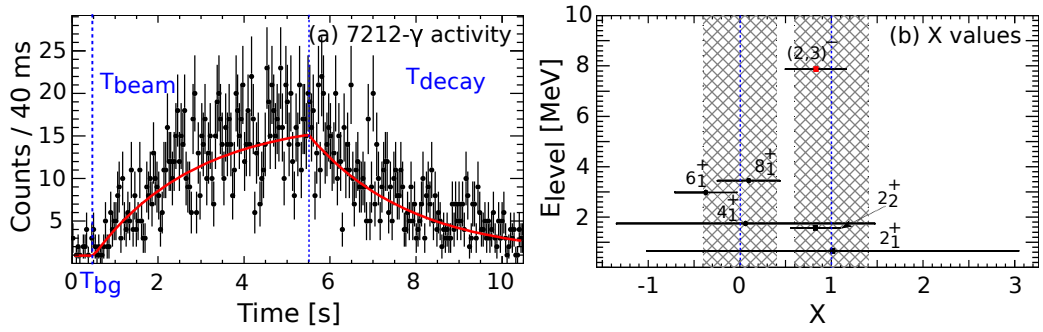

Figure 4.15 – β-feeding identification with "X" value method: (a): 7212 keV γ-ray activity curve and its fit with function 4.4; (b): X value of 7871(53) keV state together with some well-identified states.

keV γ-line and its fit with function Eq. 4.4. The derived X value for the 7.8 MeV state is 0.8(3). So, it is assigned to a 3^- β feeding with 83% confidence. The energy of another state is 8.0 MeV, which is not obvious in Figure 4.14 spectrum. As discussed earlier, real simultaneous direct feeding from both ^{80g}Ga and ^{80m}Ga can occur only if one of the two beta transitions is of first-forbidden unique nature. In consideration of lower possibility of 1U transition compared to allowed and first nonunique forbidden transition [21], the condition took for cross β-feeding is that X value located between 0.4 - 0.6. It is arbitrary due to large error bar of "X" values for many states. In addition, for allowed transition, the candidate high-lying states populated by 6^- are $(5,6,7)^-$ whose deexcitation gamma to 2^+ is unlikely. Consequently, X value provides reasonable and reliable evidence that theses two high-lying states can only be fed by isomer 3^- of ^{80}Ga.

For the extraction of the accurate β-decay intensity, the pure beam technique was used. One can extract the precursor's abundance through handling its Bateman equation using β particle activities data, i.e. the (5) nuclei involved in present data, which promises the results I_β, logft and B(GT) independent of granddaughter's data [145]. Once the construction of the separated decay level schemes is achieved, one can count 3^- and 6^- β-feeding statistics. Based on this, the beam ratio of the ground and isomeric states was achieved. The extracted absolute I_β of this high lying state, 7871(53) keV, is 1.01(11)%. The related logft is 4.91(7). First-forbidden β transitions to well established levels in ^{80}Ge are observed in the present work with logft larger than 6.3. This is consistent with the review of Ref. [21] where 98% of first-forbidden β transitions are characterized with logft larger than 6. Therefore, this high-lying state was unambiguously assigned to be populated through allowed Gamow-Teller β transition instead of forbidden transition. Based on this analysis, the spin-parity of these two high-lying states at 7.8 and 8.0 MeV can be proposed to be $(2,3,4)^-$ according to our data. The multipolicities of the related γ transition deexciting to 2^+ could be E1, M2, E3; E1, M2, E3 and M2, E3, respectively.

Considering Weisskopf single-particle estimates for transition probabilities, for same energy of the transition, the probability decreases ∼3 magnitudes when multipolarity increases 1 and for same multipolarity, the possibility of electric transition is ∼2-3 magnitudes stronger than magnetic transition [146]. Therefore, the most likely nature of electromagnetic transitions from canditate states $(2,3,4)^-$ to 2^+ is E1.

3 Decay level scheme of ^{80g}Ga

3.1 I_γ^{rel} for ^{80g}Ga and ^{80m}Ga

I_γ^{rel} in this work (before separation) compared with previous work

For the β-decay study of ^{80}Ga, the difficulty lies in the presence of two β-decaying states $^{80g+m}$Ga simultaneously produced in ISOL mode, but, with varied isomeric fraction depending on the primary production reaction (for instance thermal neutron-induced fission or photo-fission).

Different isomeric ratios in the beams obtained with different reactions obviously lead to a spread of the relative intensities of the γ-lines relative to the strongest one, I_γ^{rel}, in the decay of the mixed sources obtained by collecting these beams. Figure 4.16 shows the relative intensities of the β-delayed γ-rays emitted by the $^{80g+m}$Ga source measured in this experiment and previous work of P. Hoff et al. [142] and B. Tastet et al. [117]. The intensities are given relative to the one of the 659.2 keV line. The error bar in the parenthesis presents the statistical error coming from the parameters of fitting. During the calculation process, the error propagation formula was used as shown in Formula 4.9. Detailed error analysis can be found in book [147].

$$\begin{cases} \sigma_x^2 & \simeq \lim\limits_{N\to\infty} \frac{1}{N} \sum[(u_i-\bar{u})(\frac{\partial x}{\partial u}) + (\nu_i-\bar{\nu})(\frac{\partial x}{\partial \nu}) + \cdots]^2 \\ \sigma_x^2 & \simeq \lim\limits_{N\to\infty} \frac{1}{N} \sum[(u_i-\bar{u})^2(\frac{\partial x}{\partial u})^2 + (\nu_i-\bar{\nu})^2(\frac{\partial x}{\partial \nu})^2 + 2(u_i-\bar{u})(\nu_i-\bar{\nu})(\frac{\partial x}{\partial u})(\frac{\partial x}{\partial \nu}) + \cdots] \\ \sigma_x^2 & \simeq \sigma_u^2(\frac{\partial x}{\partial u})^2 + \sigma_\nu^2(\frac{\partial x}{\partial \nu})^2 + \cdots + 2\sigma_{u\nu}^2(\frac{\partial x}{\partial u})(\frac{\partial x}{\partial \nu}) + \\ \sigma_x^2 & \simeq \sigma_u^2(\frac{\partial x}{\partial u})^2 + \sigma_\nu^2(\frac{\partial x}{\partial \nu})^2 + \cdots \end{cases} \tag{4.9}$$

The I_γ^{rel} in P. Hoff et al. work was obtained from the neutron-induced fission and results in B.Tastet also obtained from ALTO but with different UC_x target thickness. So, the I_γ^{rel} in this work is quite close to B. Tastet's, however, it varies a lot when compared with P. Hoff's. The γ-rays marked with purple color and up arrow deexcite from states β-fed exclusively by the ^{80g}Ga 6^- state: 466.7 keV from $8^+ \to 6^+$, 1083.6 keV from $4^+ \to 2^+$, 1109.5 keV from $5^- \to 4^+$ and 1236.7 keV from $6^+ \to 4^+$. These γ-rays are obviously relatively stronger than in the results of P. Hoff et al.. The γ-rays marked with red color and down arrow, 915.1 keV from $2_2^+ \to 2_1^+$ and 1573.6 keV from $2_2^+ \to 0_1^+$, have clearly weaker intensities than P. Hoff's. There are less data in B.Tastet et al. work but they support these observations.

Hence, a clear conclusion is obtained that more ^{80g}Ga with 6^- (less ^{80m}Ga with 3^-) was produced in ALTO photo-fission ^{238}U(γ,n$_f$,f) than that in thermal neutron-induced fission ^{235}U(n$_{th}$,f). These observations can be used as additional evidence helping to identify the states β fed by ^{80g}Ga or ^{80m}Ga. For instance, 2_2^+ state is assigned to ^{80m}Ga β-feeding definitely.

I_γ^{rel} separation for ^{80g}Ga and ^{80m}Ga

The first step of separating the I_γ^{rel} is to split the statistics of 659.2 keV γ-line, which can be obtained through counting the γ-feeding and β-feeding to this state in each decay level sheme of ^{80g}Ga and ^{80m}Ga. There is no β-feeding to 659 keV state (2^+) in the scheme of ^{80g}Ga (6^-). In addition, this

E_γ	I_γ in this work (error)	I_γ in P. Hoff	I_γ in B. Tastet
398.60	0.35(4)	0.50(10)	
466.72	1.59(5) ↑	1.36(5)	1.60(20)
520.04	1.35(5)	1.25(11)	
523.13	14.41(40)	12.90(40)	11.70(20)
571.07	5.90(17)	5.80(20)	5.50(10)
586.16	8.48(24)	6.60(40)	7.70(20)
659.25	100.00(281)	100.00(300)	100.00(100)
692.56	0.61(3)	0.58(3)	0.67(8)
707.87	0.25(3)	0.30(3)	
771.58	0.54(3)	0.47(2)	0.46(6)
809.13	0.77(5)	0.73(4)	
834.61	7.46(22)	5.60(30)	7.20(50)
915.08	4.22(13) ↓	5.30(20)	4.20(20)
989.78	1.61(6)	1.13(5)	1.50(10)
1005.16	1.35(6)	0.91(4)	0.82(8)
1040.86	2.15(7)	1.71(7)	1.70(10)
1047.68	0.18(5)	0.30(10)	
1064.89	0.98(5)	0.89(5)	
1083.62	68.27(204) ↑	62.00(200)	67.40(100)
1109.47	28.43(85) ↑	23.80(80)	28.10(50)
1130.73	1.31(5)	1.17(5)	1.13(8)
1135.98	5.60(17)	4.20(20)	5.30(2)
1154.68	0.87(7)	0.77(5)	0.71(8)
1157.53	0.32(9)	0.34(3)	
1235.66	7.36(23) ↑	6.20(40)	7.90(20)
1244.82	1.17(5)	0.79(4)	
1249.27	0.52(3)	0.29(3)	
1294.18	1.04(4)	0.69(5)	0.40(10)
1306.68	2.92(9)	2.26(10)	2.60(20)
1312.93	6.91(22)	8.50(30)	7.50(40)
1471.75	0.55(4)	0.67(4)	
1547.17	0.50(3)	0.37(5)	
1560.08	0.25(8)	0.30	
1573.56	3.41(8) ↓	4.40(20)	4.20(20)
1585.30	1.06(4)	0.63(3)	0.68(8)
1680.53	6.90(15)	5.40(20)	6.40(20)
1772.56	1.49(4)	1.63(12)	1.00(10)
1850.19	1.00(4)	0.67(4)	
1880.97	0.32(3)	0.20	
1941.71	0.47(4)	0.59(3)	
1999.73	0.39(3)	0.62(4)	
2009.32	0.50(5)	0.52(3)	
2016.95	0.38(5)	0.28(2)	
2114.98	1.33(4)	1.14(5)	
2141.04	0.74(6)	0.88(6)	
2160.86	0.54(10)	0.48(5)	
2283.33	1.73(5)	1.28(6)	
2351.71	0.30(3)	0.39(3)	
2396.52	0.53(4)	0.41(3)	
2555.11	0.27(3)	0.24(2)	
2581.14	1.04(4)	1.12(5)	
2600.22	1.08(4)	0.86(5)	
2638.40	0.53(4)	0.21(4)	
2665.37	0.54(3)	0.57(5)	
2750.39	0.66(4)	0.64(4)	
2764.51	0.82(4)	1.08(6)	
2821.85	0.56(3)	0.41(4)	
2948.16	1.35(4)	0.98(5)	
3044.13	0.43(4)	0.49(3)	
3091.07	0.42(3)	0.55(4)	
3108.86	1.17(4)	1.35(7)	
3335.99	0.48(8)	0.35(6)	
3664.55	3.39(10)	3.70(20)	
3764.28	0.49(6)	0.48(4)	
3818.58	0.64(6)	0.58(5)	
3920.35	0.49(4)	0.30(5)	
3971.47	0.33(3)	0.42(6)	
4238.79	0.57(5)	0.53(4)	
4412.80	0.68(4)	0.72(5)	
4443.61	1.46(6)	1.00(8)	
4678.48	0.51(4)	0.66(4)	
4729.64	0.33(3)	0.42(4)	
5387.39	1.29(5)	1.41(6)	
5353.72	0.28(3)	0.25(2)	

Figure 4.16 – I_γ^{rel} in this work (mixed source) compared with previous works from P. Hoff [142] and B. Tastet[117]

splitting is based on the assumption that the missing γ-rays, too weak to be detected, feeding 659.2 keV state are the same for the decay scheme of ^{80g}Ga and ^{80m}Ga as shown in the formula 4.10 below. In counting the γ feeding to the 2^+ state it was necessary to separate, using the same procedure, the mixed activities of lines at 915 keV, 1083 keV, 1312 keV, 1606 keV and 2642 keV γ-rays. After this process, one can obtain the number of counts of 659 keV belonging to each decay level scheme. As presented in Eq. 4.11, there are $1.24(3) \times 10^8$ γ-rays belonging to the decay scheme of ^{80g}Ga while $0.975(25) \times 10^8$ to the one of ^{80m}Ga. By using this method, the statistics of all γ-rays can be separated into two groups. Then, two tables comprising individual γ-rays' information of the ground and isomeric precusors can be obtained.

$$\begin{cases} C_{659\_measured\_total} & = C_{659\_from\_^{80g}Ga} + C_{659\_from\_^{80m}Ga} \\ C_{659\_from\_observed\_\gamma\_and\_\beta\_feeding\_in\_^{80g}Ga} & = \sum_{i=1}^{n} C_{\gamma\_feeding} \\ C_{659\_from\_observed\_\gamma\_and\_\beta\_feeding\_in\_^{80m}Ga} & = \sum_{i=1}^{n} C_{\gamma\_feeding} + C_{\beta\_feeding} \\ R & = \frac{C_{659\_from\_observed\_\gamma\_and\_\beta\_feeding\_in\_^{80g}Ga}}{C_{659\_from\_observed\_\gamma\_and\_\beta\_feeding\_in\_^{80m}Ga}} \end{cases} \tag{4.10}$$

$$\begin{cases} C_{659\_from\_^{80g}Ga} & = 1.24(3) \times 10^8 (56.0(6)\%) \\ C_{659\_from\_^{80m}Ga} & = 0.975(25) \times 10^8 (44.0(5)\%) \end{cases} \tag{4.11}$$

The hypotheses (a bit arbitrary) that were used to achieve this separation are the following: If "X $>$ 0.6", the related state is assigned to ^{80g}Ga β-feeding; if "X $<$ 0.4", it is assigned to ^{80m}Ga β-feeding; if "$0.4 \leqslant$ X $\leqslant$ 0.6", the assignment is to ^{80g}Ga β-feeding and ^{80m}Ga feeding simultaneously. For the last group situation, especially the weak transitions, more data are particularly needed in the future to verify further.

3.2 Tabular information of γ-rays

A total of 70 β-delayed γ transitions assigned to the precusor nucleus ^{80g}Ga are reported in Tables 4.1 and 4.2. Among them, 30 γ-rays are observed for the first time (red color line in the decay level scheme in Figures 4.17 and 4.18).

Based on this analysis, there are 10 states located in 0.4 - 0.6 region of "X" value: 1972.9, 3423.4, 3515.5, 3610.7, 3721.1, 3752.2, 4029.3, 4408.2, 4462.5 and 5806.3 keV states. If simultaneous β-feeding occurs, at least one of ^{80g}Ga and ^{80m}Ga β-decay must proceed through first-forbidden unique transition. The result on the 1972.9 keV state is in good agreement with previous work in ALTO [42] in which it was also identified as simultaneously fed by the ground state (g.s.) and the isomer.

Low-lying states located at 659.3, 1574.1, 1742.9, 2266.0, 2852.3 and 2978.5 keV excitation energy, involve 22 transitions which are common to both g.s. and isomer decay schemes. These are the lines at: 398, 523, 571, 586, 659, 693, 915, 1050, 1083, 1109, 1249, 1312, 1573, 1606, 1772, 1867, 1941, 1978, 2009, 2196, 2290, 2665 keV. They all required a separation of their counting statistics to extract I_γ^{rel} in ^{80g}Ga and ^{80m}Ga individual decay schemes.

The results on I^{rel} are presented in Table 4.1. The spin-parity assignments of initial and final

states will be discussed in the next chapter. The uncertainties of I_γ^{rel} values come from the statistics. The error-propagation formula was used during the calculation process.

3.3 Decay level scheme of ^{80g}Ga

From the present data, one can place 45 excited states populated in the β-decay level scheme of ^{80g}Ga as shown in Figures 4.17 and 4.18. Twenty one states are reported for the first time. The scheme was built based on the γ-γ coincidence relationships.

The excitation energy of states were obtained through calculating the weighted average value of distinct deexcitation cascades. For example, for the state at 5801.1(7) keV excitation energy that last was obtained by considering the three following deexcitation cascades 2948.2(5) + 2852.3(5), 2821.9(5) + 2978.5(5) and 2115.0(4) + 3686.9(6). The weight (proportion) is according to the strength (I_γ^{rel}) of three γ-rays 2948(5), 2821.9(5) and 2115.0(4). They are 2.42(9)%, 1.01(6)% and 2.39(9)% individually. Then a weighted energy level of 5801.1 keV state is obtained. The uncertainty 0.7 keV is also a weighted results of three cascades.

The I_β values were calculated using the balance of the observed feeding and depopulating γ activities, which means that for a given state, the β feeding is the difference between the γ-feeding to and γ-decay from this state. The cumulated values of I_β from ^{80g}Ga and ^{80m}Ga only reach $\sim$ 80%, one can conclude that some states are missing in this work especially in the high energy around S_n (8.08 MeV) region. These states would deexcite to some low-lying states like 1742.9, 2266.0, 2852.3, 2978.5, 3423.4, 3445.3, 3515.5, 3686.9, 3988.3 and 4026.2 keV. In order to avoid being overweighted, the I_β of these states were just given an upper limit in this work. The error analysis of I_β is the same as in the aformentioned parts.

The logft value calculations were performed using the NNDC online procedure [148], and, therein, the $T_{1/2}$, E_{energy} and I_β were from this work and the used Q_β was taken from the ENSDF evaluated result [126].

4 Decay level scheme of ^{80m}Ga

4.1 Tabular information of γ-rays

The relative γ-ray intensities, I_γ^{rel}, following the β-decay of ^{80m}Ga are listed in Tables 4.3 and 4.4. The analysis procedure is the same as in the case of ^{80g}Ga. Totally, there are 65 γ-rays recorded in this work, in which 38 are detected and reported for the first time. The corresponding initial and final states information of γ-transitions are also provided in the tables. The detailed assignment process will be discussed in the discussion chapter. The γ-γ coincidence relationship can be discovered in the decay level scheme.

One should note that there are 10 states that are cross-β-feeding as mentioned before and 6 of the low-lying states (populated by γ-transition) are appearing in both decay level schemes of ^{80g}Ga and ^{80m}Ga. All of this brings 22 of cross-appearance γ-rays.

Table 4.1 – Gamma transitions in the decay of ^{80g}Ga to ^{80}Ge.

E_γ (keV)	I_γ^{rel}	E_{level}^{i} (keV)	J_i^π	E_{level}^{f} (keV)	J_f^π
398.6 3		1972.2 4	(4^+)	1574.1 4	2^+
466.7 3	2.85 11	3445.3 6	8^+	2978.5 5	6^+
520.0 3	2.42 10	3498.6 6	$(5,6,7)^+$	2978.5 5	6^+
523.1 3	25.83 85	2266.0 5	(4^+)	1742.9 4	4^+
571.1 3		3423.4 6		2852.3 5	(5^-)
586.2 3		2852.3 5	(5^-)	2266.0 5	(4^+)
659.2 3	100.0 35	659.3 3	2^+	0	0^+
692.6 3	1.09 6	2266.0 5	(4^+)	1574.1 4	2^+
707.9 3	0.45 5	3686.9 6	$(5,6)^+$	2978.5 5	6^+
771.6 3	0.97 6	3037.2 5	$(5,6)^+$	2266.0 5	(4^+)
834.6 3	13.37 46	3686.9 6	$(5,6)^+$	2852.3 5	(5^-)
915.1 3		1574.1 4	2^+	659.3 3	2^+
989.8 3	2.88 11	4413.1 7	$(5,6,7)^+$	3423.4 6	
1005.2 3	2.43 11	4933.5 7	$(6,7)^-$	3988.3 6	$(5,6)^-$
1040.9 3	3.86 15	5573.7 7	$(5,6,7)^-$	4532.8 6	$(5,6)^-$
1047.7 3	0.32 9	4026.2 6	(5^-)	2978.5 5	6^+
1050.8 4		4029.3 7		2978.5 5	6^+
1064.9 3	1.75 9	3037.2 5	$(5,6)^+$	1972.2 4	(4^+)
1083.6 3		1742.9 4	4^+	659.3 3	2^+
1109.5 3		2852.3 5	(5^-)	1742.9 4	4^+
1130.7 3	2.34 10	3396.8 6	$(5,6)^+$	2266.0 5	(4^+)
1136.0 3	10.03 36	3988.3 6	$(5,6)^-$	2852.3 5	(5^-)
1154.7 3	1.57 13	5567.8 7	$(5,6,7)^-$	4413.1 7	$(5,6,7)^+$
1157.5 4	0.58 16	3424.0 6	(4^+)	2266.0 5	(4^+)
1194.8 3	0.43 5	4173.3 6	(4^+)	2978.5 5	6^+
1235.7 3	13.19 47	2978.5 5	6^+	1742.9 4	4^+
1244.8 3	2.09 9	5233.1 7	$(5,6,7)^-$	3988.3 6	$(5,6)^-$
1249.3 3		3515.5 6	(4^+)	2266.0 5	(4^+)
1257.6 3		4944.5 7	$(6,7)^-$	3686.9 6	$(5,6)^+$
1294.2 3	1.87 8	3037.2 5	$(5,6)^+$	1742.9 4	4^+
1306.7 3	5.24 19	4993.5 7	$(6,7)^-$	3686.9 6	$(5,6)^+$
1312.9 3		1972.2 4	(4^+)	659.3 3	2^+
1444.3 4	0.31 5	4422.6 6	(4^+)	2978.5 5	6^+
1547.2 4	0.89 6	5233.1 7	$(5,6,7)^-$	3686.9 6	$(5,6)^+$
1548.5 5	0.89 6	4993.5 7	$(6,7)^-$	3445.3 6	8^+
1573.6 3		1574.1 4	2^+	0	0^+
1585.3 3	1.90 7	5573.7 7	$(5,6,7)^-$	3988.3 6	$(5,6)^-$
1606.7 4		2266.0 5	(4^+)	659.3 3	2^+
1680.5 3	12.37 35	4532.8 6	$(5,6)^-$	2852.3 5	(5^-)
1753.5 4	0.53 5	4732.1 6	$(4,8)^+$	2978.5 5	6^+
1763.5 3	0.71 43	4615.8 6	(4^+)	2852.3 5	(5^-)
1766.7 5	1.16 45	5453.6 8	$(5,6,7)^-$	3686.9 6	$(5,6)^+$
1772.6 4		3515.5 6	(4^+)	1742.9 4	4^+
1850.2 3	1.79 8	3424.0 6	(4^+)	1574.1 4	4^+
1867.8 7		3610.7 8	(5^+)	1742.9 4	4^+
1881.0 4	0.57 6	5567.8 7	$(5,6,7)^-$	3686.9 6	$(5,6)^+$
1941.7 4		3515.5 6	(4^+)	1574.1 4	2^+
1978.3 5		3721.1 6		1742.9 4	4^+
2009.3 4		3752.2 6		1742.9 4	4^+
2017.0 4	0.69 10	5703.8 7	$(5,6,7)^-$	3686.9 6	$(5,6)^+$
2115.0 4	2.39 9	5801.1 7	$(5,6,7)^-$	3686.9 6	$(5,6)^+$
2141.0 4	1.33 10	4933.5 7	$(6,7)^-$	2852.3 5	(5^-)
2160.9 3	0.97 18	6187.1 7	(5^-)	4026.2 6	(5^-)
2196.5 4		4462.5 6	(4^+)	2266.0 5	(4^+)
2283.3 4	3.10 10	4026.2 6	(5^-)	1742.9 4	4^+

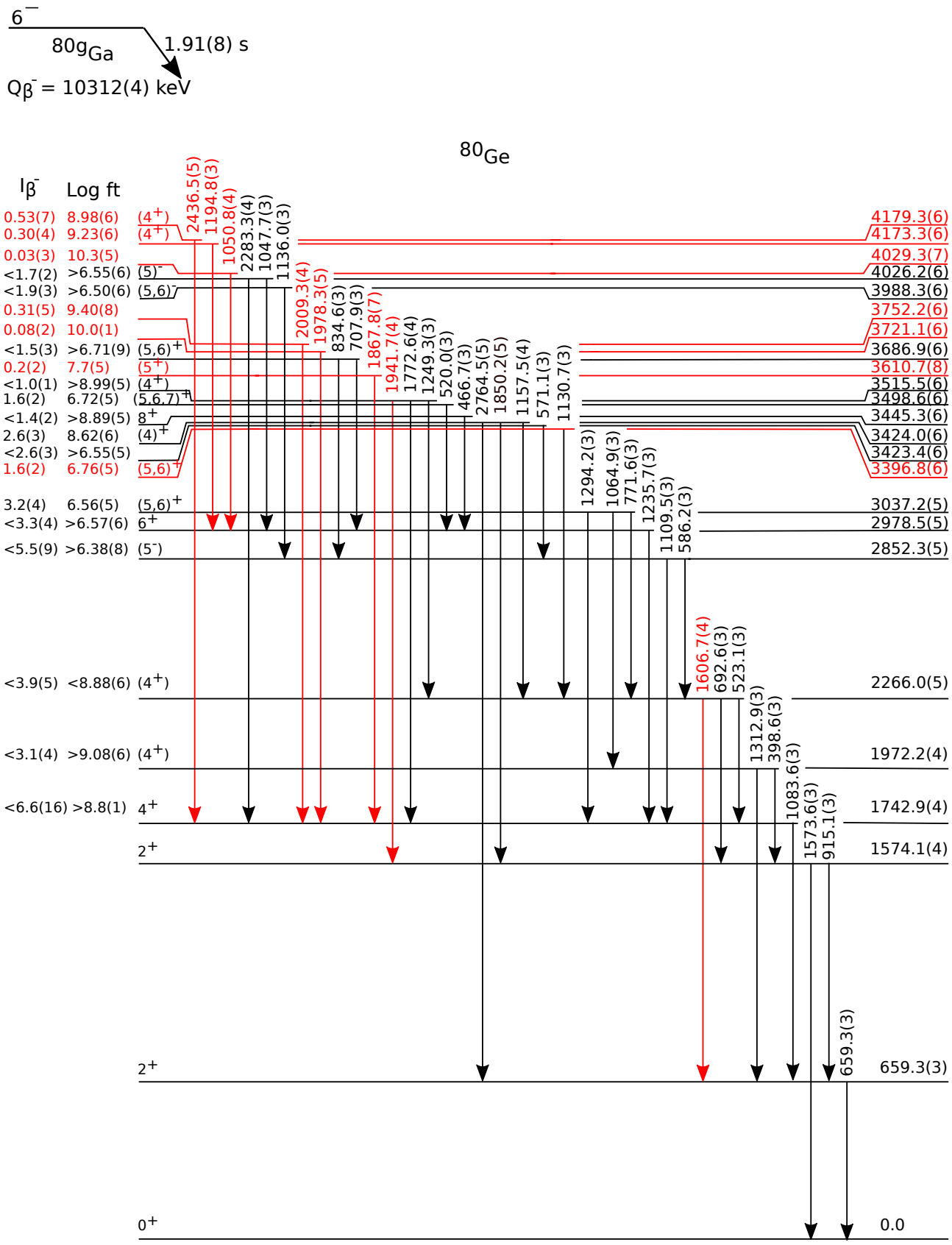

Figure 4.17 – Level scheme of ^{80}Ge up to 4.2 MeV in energy populated following the β-decay of ^{80g}Ga (6^-). For the sake of clarity the decay scheme has been split in two sections with the one for the higher energies plotted in Figure 4.18.

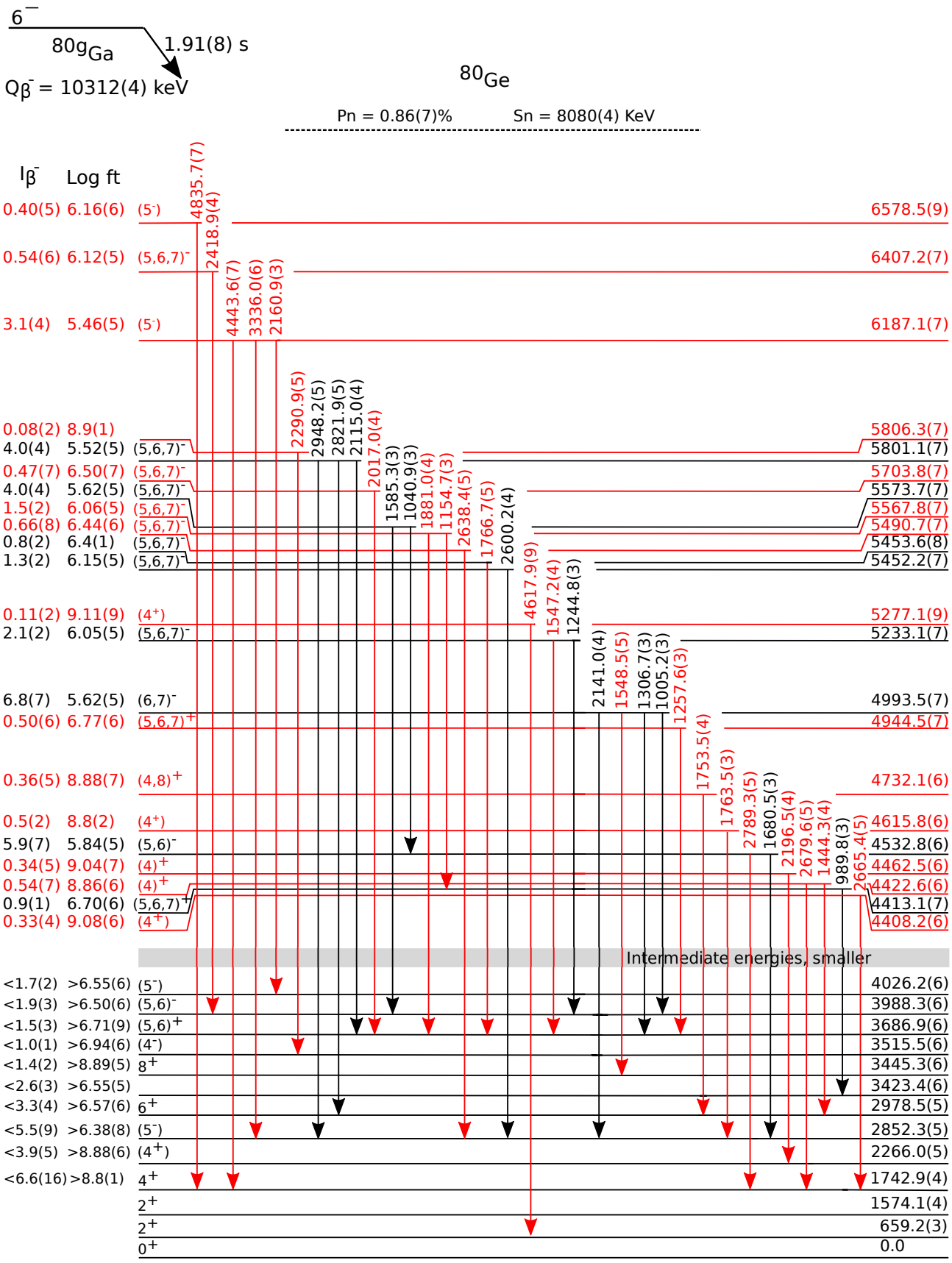

Figure 4.18 – Level scheme of ^{80}Ge populated following the β-decay of ^{80g}Ga (6^-) containing the high-lying states between 4.2 and 8 MeV in energy.

Table 4.2 – Gamma transitions in the decay of ^{80g}Ga to ^{80}Ge (continue).

E_γ (keV)	I_γ^{rel}	E_{level}^i (keV)	J_i^π	E_{level}^f (keV)	J_f^π
2290.9 5		5806.3 7		3515.5 6	(4^+)
2418.9 4	0.79 6	6407.2 7	$(5,6,7)^-$	3988.3 6	$(5,6)^-$
2436.5 5	0.78 8	4179.3 6	(4^+)	1742.9 4	4^+
2600.2 4	1.93 8	5452.2 7	$(5,6,7)^-$	2852.3 5	(5^-)
2638.4 5	0.95 7	5490.7 7	$(5,6,7)^-$	2852.3 5	(5^-)
2665.4 5		4408.2 6	(4^+)	1742.9 4	4^+
2679.6 5	0.47 5	4422.6 6	(4^+)	1742.9 4	4^+
2764.5 5	1.47 8	3424.0 6	(4^+)	659.3 3	2^+
2789.3 5	0.12 4	4532.8 6	$(5,6)^-$	1742.9 4	4^+
2821.9 5	1.01 6	5801.1 7	$(5,6,7)^-$	2978.5 5	6^+
2948.2 5	2.42 9	5801.1 7	$(5,6,7)^-$	2852.3 5	(5^-)
3336.0 6	0.87 14	6187.1 7	(5^-)	2852.3 5	(5^-)
4443.6 7	2.62 11	6187.1 7	(5^-)	1742.9 4	4^+
4617.9 9	0.15 5	5277.1 9	(4^+)	659.3 3	2^+
4835.7 7	0.59 7	6578.5 9	(5^-)	1742.9 4	4^+

4.2 Decay level scheme of ^{80m}Ga

As presented in Figures 4.19 and 4.20, 48 of excited states of ^{80}Ge were populated by ^{80m}Ga β-decay and 34 of these states are proposed for the first time (with red color) in current work. Of the 34 new states, 26 are located interestingly above 4 MeV. It means the I_β of low-lying states were overweighted in previous work, which was caused by the so-called Pandemonium effect. The details will be discussed in the Pandemonium effect and B(GT) distribution sections of the discussion chapter. The states a 7871(53) keV and 7996(53) keV were constructed based on the observation of "ultra"-high-energy γ-rays, 7181(53) keV and 7337(53), by PARIS array. The I_β, logft and their uncertainty analysis procedures are the same as aforementioned. The spin-parity assignment will be discussed in the next chapter.

5 Fast timing

Thanks to the good time resolution of $LaBr_3$(Ce) scintillator in PARIS, fast timing measurements become possible. As introduced in the detector characteristic part, $LaBr_3$ owns 1.65(2) ns time resolution (FWHM) at 1083 keV. It is super convenient for the nanosecond level half-life measurement.

Figure 4.21(a) presents the "t2plastic-energy" two-dimensional where t2plastic refers to the time of γ-rays relative to plastic detector, which takes the faster-response advantage of plastic scintillator. When putting a "CUTG" (red region in Figure 4.21(a)) and projecting on the γ-ray energy axis, one will obtain the γ-rays with a delayed-tail immediately as shown in Figure 4.21(b). Four γ-rays in the cascade of $8^+ \rightarrow 6^+ \rightarrow 4^+ \rightarrow 2^+ \rightarrow 0^+$ are obviously visible in the "selected" spectrum Figure 4.21(b), which is contributed by the 8^+ isomer. Figure 4.21(c) presents the "t2plastic" spectrum of the 467 keV ($8^+ \rightarrow 6^+$) γ-ray and a background reference 1500 keV, in which, the time resolution of $LaBr_3$ detector and the delayed-tail part of the 467 keV γ-ray are clearly distinguishable. One can fit the tail part only and extract the half-life of 8^+. The half-life of 8^+ extracted in this work is 3.08(6) ns in good agreement with previous work operated with BaF_2 scintillator [126].

Table 4.3 – Gamma transitions in the decay of ^{80m}Ga to ^{80}Ge.

E_γ (keV)	I_γ^{rel}	E_{level}^i (keV)	J_i^π	E_{level}^f (keV)	J_f^π
398.6 3		1972.2 4	(4^+)	1574.1 4	2^+
523.1 3		2266.0 5	(4^+)	1742.9 4	4^+
571.1 3		3423.4 6		2852.3 5	(5^-)
586.2 3		2852.3 5	(5^-)	2266.0 5	(4^+)
659.2 3		659.3 3	2^+	0	0^+
692.6 3		2266.0 5	(4^+)	1574.1 4	2^+
809.1 3	1.73 8	4324.2 6	(3^-)	3515.5 6	(3^-)
915.1 3		1574.1 4	2^+	659.3 3	2^+
1050.8 4		4029.3 7		2978.5 5	6^+
1083.6 3		1742.9 4	4^+	659.3 3	2^+
1109.5 3		2852.3 5	(5^-)	1742.9 4	4^+
1235.7 3	16.64 40	2978.5 5	6^+	1742.9 4	4^+
1249.3 3		3515.5 6	(3^-)	2266.0 5	(4^+)
1312.9 3		1972.2 4	(4^+)	659.3 3	2^+
1471.8 3	1.23 6	4324.2 6	(3^-)	2852.3 5	(5^-)
1573.6 3		1574.1 4	2^+	0	0^+
1606.7 4		2266.0 5	(4^+)	659.3 3	2^+
1772.6 4		3515.5 6	(3^-)	1742.9 4	4^+
1867.8 7		3610.7 8	(5^+)	1742.9 4	4^+
1941.7 4		3515.5 6	(3^-)	1574.1 4	2^+
1978.3 5		3721.1 6		1742.9 4	4^+
1999.7 4	0.88 5	4851.8 6	$(3,4)^-$	2852.3 5	(5^-)
2009.3 4		3752.2 6		1742.9 4	4^+
2058.9 4	0.34 4	4324.2 6	(3^-)	2266.0 5	(4^+)
2101.9 4	0.49 5	4074.1 6	(5^+)	1972.2 4	(4^+)
2196.5 4		4462.5 6	(4^+)	2266.0 5	(4^+)
2290.9 5		5806.3 7		3515.5 6	(3^-)
2351.7 4	0.68 5	4324.2 6	(3^-)	1972.2 4	(4^+)
2396.5 4	1.19 7	4139.4 6	$(3,4)^-$	1742.9 4	4^+
2555.1 4	0.62 4	3214.4 5	(5^+)	659.3 3	2^+
2581.1 4	2.36 7	4324.2 6	(3^-)	1742.9 4	4^+
2642.4 5	2.49 8	3301.6 5	(5^+)	659.3 3	2^+
2665.4 5		4408.2 6	(4^+)	1742.9 4	4^+
2709.9 5	0.27 5	4682.1 7	(5^+)	1972.2 4	(4^+)
2750.4 5	1.48 7	4324.2 6	(3^-)	1574.1 4	2^+
2762.3 5	0.26 4	6185.7 8	$(3,4)^-$	3423.4 6	2^+
2993.2 5	0.93 6	4736.1 6	$(3,4)^-$	1742.9 4	4^+
3044.1 5	0.96 7	3703.4 6	$(2,3,4)^+$	659.3 3	2^+
3091.1 5	0.94 5	3750.3 6	$(2,3,4)^+$	659.3 3	2^+
3108.9 5	2.65 8	4851.8 6	$(3,4)^-$	1742.9 4	4^+
3228.0 5	0.90 6	3887.3 6	$(2,3,4)^+$	659.3 3	2^+
3461.8 6	0.21 4	5035.9 7	(1^+)	1574.1 4	2^+
3498.1 6	0.49 6	5072.1 7	$(2,3)^-$	1574.1 4	2^+
3621.7 6	0.42 6	5364.5 7	$(3,4)^-$	1742.9 4	4^+
3664.6 6	7.67 0.17	4324.2 6	(3^-)	659.3 3	2^+
3750.5 6	0.58 6	5324.5 8	$(2,3)^-$	1574.1 4	2^+
3764.3 6	1.10 10	5338.1 7	$(2,3)^-$	1574.1 4	2^+
3774.4 7	0.49 8	5517.2 8	$(3,4)^-$	1742.9 4	4^+
3818.6 6	1.44 10	4477.8 7	$(2,3)^-$	659.3 3	2^+
3920.4 6	1.11 7	4579.6 7	$(2,3)^-$	659.3 3	2^+
4207.8 7	0.57 7	6473.8 8	$(3,4)^-$	2266.0 5	(4^+)
4225.1 8	0.47 8	4884.4 8	$(2,3,4)^+$	659.3 3	2^+
4238.8 7	1.29 8	6211.0 8	$(3,4)^-$	1972.2 4	(4^+)
4412.8 7	1.53 6	5072.1 7	$(2,3)^-$	1574.1 4	2^+

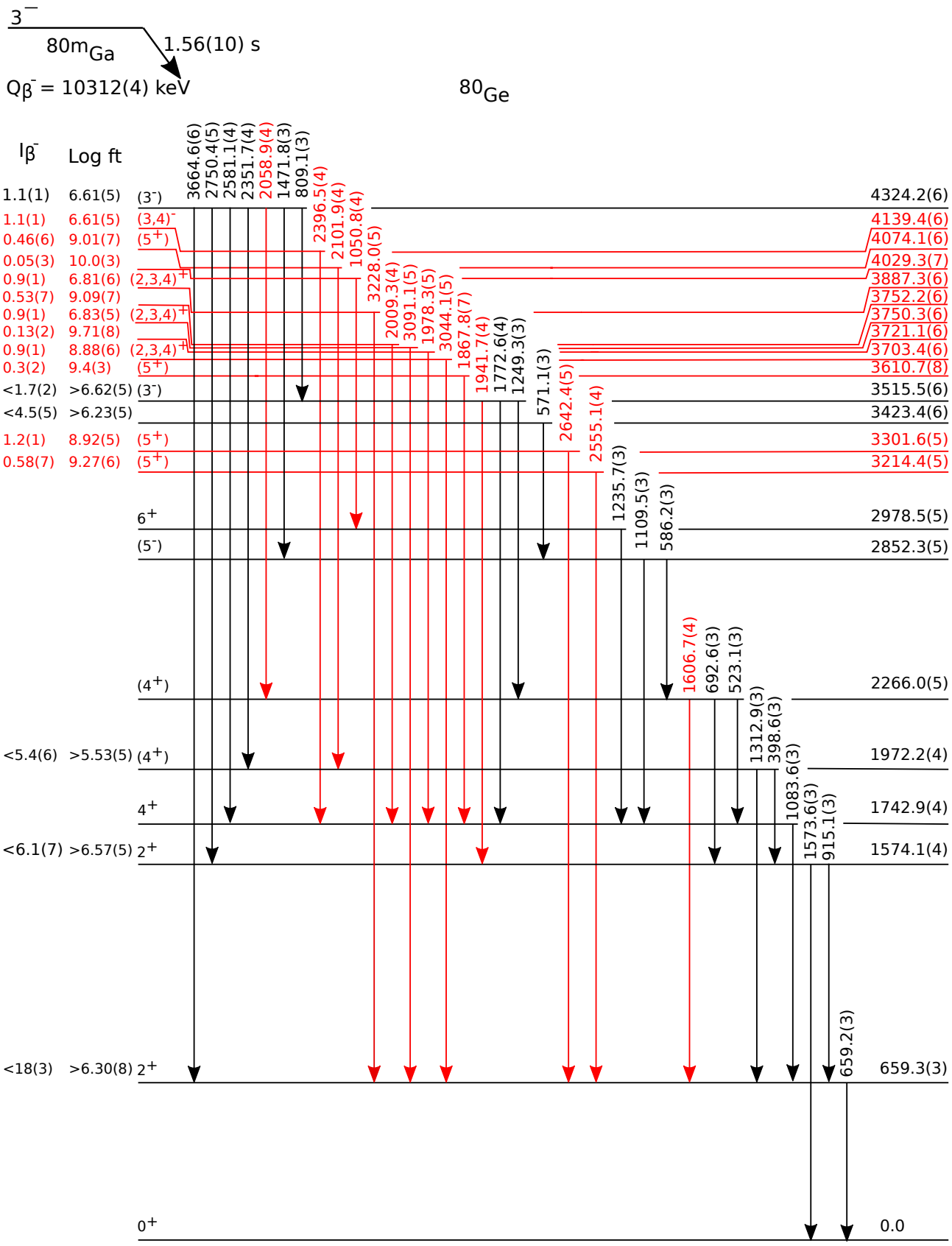

Figure 4.19 – Level scheme of ^{80}Ge up to 4.4 MeV in energy populated following the β-decay of ^{80m}Ga (3^-). For the sake of clarity the decay scheme has been split in two sections with the one for the higher energies plotted in Figure 4.20.

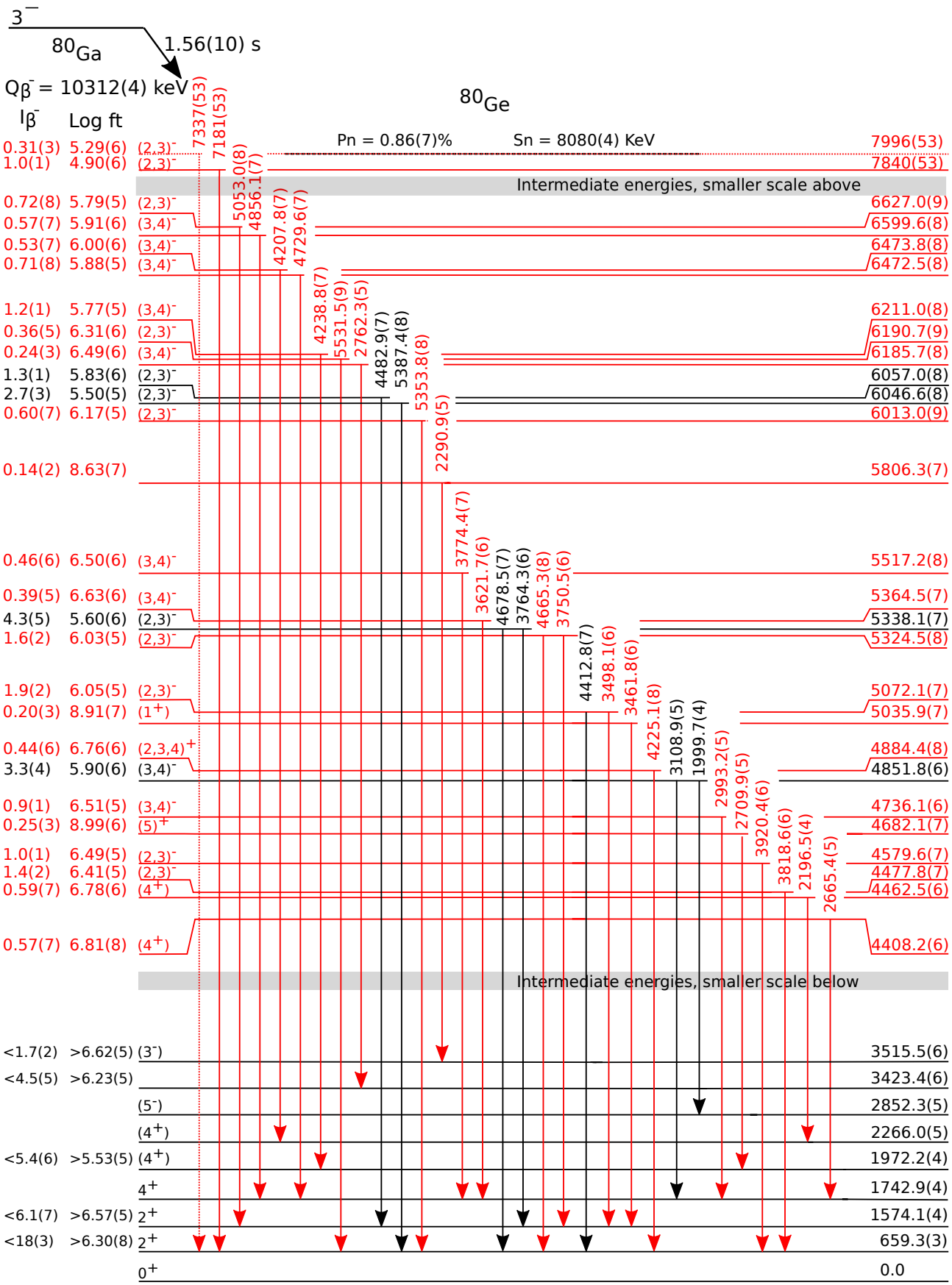

Figure 4.20 – Level scheme of ^{80}Ge populated following the β-decay of ^{80m}Ga (3^-) containing the high-lying states between 4.4 and 8 MeV in energy. Dashed arrows indicate tentatively placed transitions.

Table 4.4 – Gamma transitions in the decay of ^{80m}Ga to ^{80}Ge (continue).

E_γ (keV)	I_γ^{rel}	E_{level}^i (keV)	J_i^π	E_{level}^f (keV)	J_f^π
4482.9 7	0.68 4	6057.0 8	$(2,3)^-$	1574.1 4	2^+
4665.3 8	1.13 9	5324.5 8	$(2,3)^-$	659.3 3	2^+
4678.5 7	1.16 7	5338.1 7	$(2,3)^-$	659.3 3	2^+
4729.6 7	0.75 6	6472.5 8	$(3,4)^-$	1742.9 4	4^+
4856.1 7	0.60 5	6599.6 8	$(3,4)^-$	1742.9 4	4^+
5053.0 8	0.77 6	6627.0 9	$(2,3)^-$	1574.1 4	2^+
5353.8 8	0.63 5	6013.0 9	$(2,3)^-$	659.3 3	2^+
5387.4 8	2.91 9	6046.6 8	$(2,3)^-$	659.3 3	2^+
5531.5 9	0.39 5	6190.7 9	$(2,3)^-$	659.3 3	2^+
7181 53	1.08 6	7840 53	$(2,3)^-$	659.3 3	2^+
7337 53	0.33 2	7996 53	$(2,3)^-$	659.3 3	2^+

For the hundred picosecond half-life measurement with $LaBr_3$, the deconvolution procedure is needed. The related procedure under development currently will be used to extract other states appearing in the 4.21(b) red spectrum. For the dozen of picosecond half-life measurements by $LaBr_3$, central-shift method works. However, the detector response function of energy (time walk function) is mandatory, whcih requires a very long time source calibration for the setup.

$$8^+ isomer : T_{1/2} = 3.08(6) ns \tag{4.12}$$

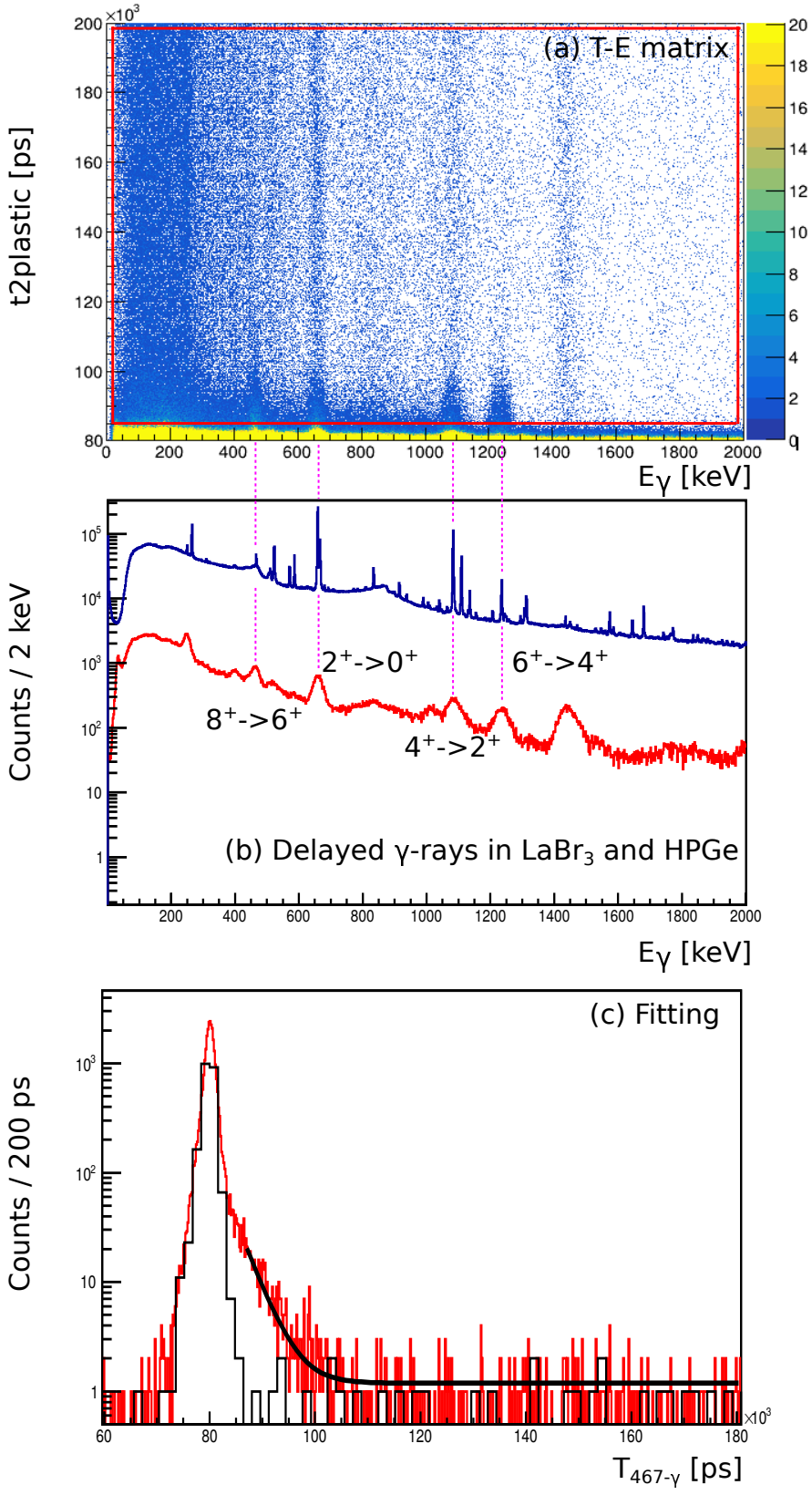

Figure 4.21 – (a): t2plastic-energy two-dimensional spectrum of $LaBr_3$ channel-14; (2): γ-rays energy spectrum with delayed-tails in t2plastic projected from (a) red pane region; (3): t2plastic spectrum of 467 keV γ-ray and its fitting.

5 Discussion

Sommaire

1 Structure of ^{80}Ge

1.1 Spin-parity assignment

Spin-parity assignment

The spin assignment of states in ^{80}Ge was performed according to the values of logft. The reference are global statistics for the whole nuclear chart [21] where logft value is 3-4 for super-allowed β-decay, 4-8 for allowed transition, 6-9 for first forbidden (FF) transition, 8-11 for first unique (1U) transition and local standard. Due to the fact that the 0_1^+, 2_1^+, 4_1^+, 6_1^+ and 8_1^+ are well identified in ^{80}Ge, the transitions $6^-(^{80g}Ga)\rightarrow 4_1^+$, $6^-(^{80g}Ga)\rightarrow 6_1^+$ and $6^-(^{80g}Ga)\rightarrow 8_1^+$ can provide a local reference of FF and 1U for the β-transition type identification as shown in Table 5.1. Likewise, $3^-(^{80m}Ga)\rightarrow 2_1^+$, $3^-(^{80m}Ga)\rightarrow 2_2^+$, $3^-(^{80m}Ga)\rightarrow 4_2^+$ (notice that the 3^- does not feed 4_1^+ according to "X" analysis, see Table 5.3) can also give references of FF as shown in Table 5.2.

Table 5.1 – Logft of spin-parity well-known states in ^{80}Ge populated by ^{80g}Ga.

$6^- \rightarrow 6_1^+$	$6^- \rightarrow 4_1^+$	$6^- \rightarrow 8_1^+$
>6.57(6)	>8.8(1)	>8.89(5)

Table 5.2 – Logft of spin-parity well-known states in ^{80}Ge populated by ^{80m}Ga.

$3^- \rightarrow 2_1^+$	$3^- \rightarrow 2_2^+$	$3^- \rightarrow 4_2^+$
>6.30(8)	>6.57(5)	>5.35(5)

Based on this analysis, among the β-transitions of ^{80g}Ga, the allowed transition character was assigned if the "logft<6.6", which populated $(5,6,7)^-$ states; ff was assigned if "logft>6.6 and logft<6.8", which populated $(5,6,7)^+$ states; 1U was assigned if "logft>6.8" and the logft value was calculated again using 1U formula, which populated $(4,8)^+$. For ^{80m}Ga, the same identifying standards were adopted. Therefore, allowed transitions populated $(2,3,4)^-$ states; ff populated $(2,3,4)^+$ states; 1U populated $(1,5)^+$ states. This analysis is based on the hypothesis that the spin-parities of $^{80g+m}$Ga (6^- and 3^-) are correct [141], and that the second forbidden transition with "logft>11" in the global statistics [21] was negligible. Combined with this β-transition identification, the candidate (tentative) spin-parities of states of ^{80}Ge were given on the priority consideration of E1, E2 and M1 multipolarities.

The final results are presented in Table 5.3 and Table 5.4. A total number 43 of β-decays from the 6^- state was determined and 44 from the 3^- state. Furthermore, the acumulated I_β for $^{80g+m}$Ga are (79.0 ± 2.5)% and (85.3 ± 3.6)% individually, which means there are around 20% and 15% β branch ratios still unobserved in this work. It is easily understood as there are only two states being measured in this work in the energy range 6.6-8.08 (S_n) MeV, which is caused by "Pandemonium effect". It is the high detection effiency of PARIS that guaranteed the observation of these two states. The unobserved γ-rays, for low-lying states, could significantly decrease the deduced β-feedings and consequently increase the logft values. Therefore, the logft values of low-lying states in $^{80g+m}$Ga decay level scheme were just provided as minimum values. This operation can guarantee the branch ratio of low-lying states non-overweighted. Beside I_β, logft and J^π information, the "X" value of each state

was also presented in the table as it the critical information for the separation of decay level scheme.

Two assumptions were made in deduced logft values calculations process. First, no β-feeding to the ^{80}Ge ground state was assumed as 3^-(^{80m}Ga) β-decaying to 0^+ needs second unique β-transition (2U) with logft larger than 12, which is negligible and 6^-(^{80g}Ga) β-decaying to 0^+ is almost impossible. The second assumption was that there is a few unobserved γ intensities for the high-lying states (logft without ">" marks).

The spin-parity of states populated by β-transition with reduced logft values less than 6.0, can be adopted with high confidence. In other words, these transitions can be assigned to Gamow-Teller transitions. For the states with β-transition logft value between 6 to 6.6, their spin-parity assignments are regarded as tentative due to the serious competition between allowed and FF β-transitions. Particularly, the later is essential for medium neutron-rich nuclei due to phase space and nuclear structure reasons. In addition, their competition is important in the nuclear astrophysics r-process modeling process.

Furthermore, Fermi decay would populate 3^- and 6^- states in ^{80}Ge, but such transitions only happen with low logft values to isobaric analog states (IAS) which are located at much higher energy than levels observed in these studies. In addition, isospin mixing in the low-lying states (below S_n 8.08 MeV) is expected to be extremely small, which is reflected in the logft values. One can find there is no state which has ∼3.5 logft value.

Logft systematic analysis of N = 49 isotones

Logft values are one of the most important observables in the β-decay study. Logft values are affected by the nuclear structure of the parent and daughter nuclei. It is also important experimental data that can be used to inform the theory development.

In this subsection, a systematical analysis of logft values of N=49 isotones was performed as shown in Table 5.5 including $^{78}_{29}Cu_{49} \rightarrow ^{78}_{30}Zn_{48}$, $^{80}_{31}Ga_{49} \rightarrow ^{80}_{32}Ge_{48}$, $^{82}_{33}As_{49} \rightarrow ^{82}_{34}Se_{48}$ and $^{84}_{35}Br_{49} \rightarrow ^{84}_{36}Kr_{48}$. Then, one can have a global view of β-decay properties in this mass region. More importantly, it can provide a reference to determine the types of β-transition.

In $^{78}_{29}Cu_{49} \rightarrow ^{78}_{30}Zn_{48}$ case, the allowed and FF transitions have a large difference and lack 1U data. However, in the cases of $^{80}_{31}Ga_{49} \rightarrow ^{80}_{32}Ge_{48}$ and $^{82}_{33}As_{49} \rightarrow ^{82}_{34}Se_{48}$, there are somes overlaps of the logft values between allowed and FF transitions. In the case of $^{84}_{35}Br_{49} \rightarrow ^{84}_{36}Kr_{48}$, the logft values of allowed and FF transitions are differentiable. Whereas, generally, there is a law one can observe clearly, in which along the proton number (Z) increasing the logft values of allowed and FF transitions also increase. It means that in N = 49 isotones from exotic to stability the allowed and FF β-decay probalities decrease, which keeps super good agreement with nuclear characteristics. This systematic analysis also supports the standards adopted in this work.

In this neutron-rich region, it is often difficult to separate allowed from FF transitions since FF becomes significant for neutron-rich nuclei. The latter makes a critical contribution to the nuclear matrix element compared with the allowed transitions. It also plays an important role in the understanding of supernova explosions and heavy element nucleosynthesis. The measured logft of allowed and FF could provide important reference for the nuclear β-decay theory development like understanding of

Table 5.3 – Excited states information of ^{80}Ge β-feeding by ^{80g}Ga (6^-).

E_{state} (keV)	I_β	logft	J^π	"X"
1742.9 4	<6.6 16	>8.8 1	4^+	0.06(140)
1972.9 4	<3.1 4	>9.08 6	(4^+)	0.60(32)
2266.0 5	<3.9 5	>8.88 6	(4^+)	0.33(95)
2852.3 5	<5.5 9	>6.38 8	(5^-)	-0.24(117)
2978.5 5	<3.3 4	>6.57 6	6^+	-0.37(0.34)
3037.2 5	3.2 4	6.56 5	$(5,6)^+$	0.25(16)
3396.8 6	1.6 2	6.76 5	$(5,6)^+$	0.31(25)
3423.4 6	<2.6 3	>6.55 5		0.56(32)
3424.0 6	2.6 3	8.62 6	(4^+)	0.40(31)
3445.3 6	<1.4 2	>8.89 5	8^+	0.10(34)
3498.6 6	1.6 2	6.72 5	$(5,6,7)^+$	0.17(24)
3515.5 6	<1.0 1	8.99 5	(4^+)	0.55(42)
3610.7 8	0.2 2	7.7 5	(5^+)	0.52(585)
3686.9 6	<1.5 3	>6.71 9	$(5,6)^+$	-0.74(171)
3721.1 6	0.08 2	10.0 1		0.54(135)
3752.2 6	0.31 5	9.40 8		0.42(70)
3988.3 6	<1.9 3	>6.50 6	$(5,6)^-$	-0.33(74)
4026.2 6	<1.7 2	>6.55 6	(5^-)	0.16(66)
4029.3 7	0.03 3	10.3 5		0.41(589)
4173.3 6	0.30 4	9.23 6	(4^+)	0.32(75)
4179.3 6	0.53 7	8.98 6	(4^+)	0.22(67)
4408.2 6	0.33 4	9.08 6	(4^+)	0.54(44)
4413.1 7	0.9 1	6.70 6	$(5,6,7)^+$	0.05(89)
4422.6 6	0.54 7	8.86 6	(4^+)	0.14(54)
4462.5 6	0.34 5	9.04 7	(4^+)	0.49(63)
4532.8 6	5.9 7	5.84 5	$(5,6)^-$	0.02(22)
4615.8 6	0.5 2	8.8 2	(4^+)	0.30(414)
4732.1 6	0.36 5	8.88 7	$(4,8)^+$	0.25(67)
4944.5 7	0.50 6	6.77 6	$(5,6,7)^+$	0.24(42)
4993.5 7	6.8 7	5.62 5	$(6,7)^-$	0.12(14)
5233.1 7	2.1 2	6.05 5	$(5,6,7)^-$	0.18(20)
5277.1 9	0.11 2	9.11 9	(4^+)	-0.07(197)
5452.2 7	1.3 2	6.15 5	$(5,6,7)^-$	0.18(25)
5453.6 8	0.8 2	6.4 1	$(5,6,7)^-$	0.10(258)
5490.7 7	0.66 8	6.44 6	$(5,6,7)^-$	0.19(48)
5567.8 7	1.5 2	6.06 5	$(5,6,7)^-$	0.20(39)
5573.7 7	4.0 4	5.62 5	$(5,6,7)^-$	0.11(15)
5703.8 7	0.47 7	6.50 7	$(5,6,7)^-$	0.24(95)
5801.1 7	4.0 4	5.52 5	$(5,6,7)^-$	0.22(13)
5806.3 7	0.08 2	8.9 1		0.59(121)
6187.1 7	3.1 4	5.46 5	(5^-)	0.13(32)
6407.2 7	0.54 6	6.12 5	$(5,6,7)^-$	0.01(45)
6578.5 9	0.40 5	6.16 6	$(5)^-$	-0.16(71)

Table 5.4 – Excited states information of ^{80}Ge β-feeding by ^{80m}Ga (3^-).

E_{state} (keV)	I_β	logft	J^π	"X"
659.3 3	<18 3	>6.30 8	2^+	1.01(203)
1574.1 4	<6.1 7	>6.57 5	2^+	0.83(27)
1972.2 4	<5.4 6	>5.53 5	(4^+)	0.60(32)
3214.4 5	0.58 7	9.27 6	(5^+)	0.82(72)
3301.6 5	1.2 1	8.92 5	(5^+)	0.46(30)
3423.4 6	<4.5 5	>6.23 5		0.56(32)
3515.5 6	<1.7 2	>6.62 5	$(3)^-$	0.55(42)
3610.7 8	0.3 2	9.4 3	(5^+)	0.52(585)
3703.4 6	0.9 1	8.88 6	$(2,3,4)^+$	0.83(69)
3721.1 6	0.13 2	9.71 8		0.54(135)
3750.3 6	0.9 1	6.83 5	$(2,3,4)^+$	0.65(55)
3752.2 6	0.53 7	9.09 7		0.42(70)
3887.3 6	0.9 1	6.81 6	$(2,3,4)^+$	0.77(65)
4029.3 7	0.05 3	10.0 3		0.41(589)
4074.1 6	0.46 6	9.01 7	(5^+)	1.25(115)
4139.4 6	1.1 1	6.61 5	$(3,4)^-$	0.67(57)
4324.2 6	1.1 1	6.61 5	(3^-)	0.72(12)
4408.2 6	0.57 7	6.81 8	$(2,3,4)^+$	0.54(44)
4462.5 6	0.59 7	6.78 6	$(2,3,4)^+$	0.49(63)
4477.8 7	1.4 2	6.41 5	$(2,3)^-$	0.85(74)
4579.6 7	1.0 1	6.49 5	$(2,3)^-$	1.17(67)
4682.1 7	0.25 3	8.99 6	(5^+)	0.76(175)
4736.1 6	0.9 1	6.51 5	$(3,4)^-$	0.65(61)
4851.8 6	3.3 4	5.90 6	$(3,4)^-$	0.60(22)
4884.4 8	0.44 6	6.76 6	$(2,3,4)^+$	1.15(191)
5035.9 7	0.20 3	8.91 7	(1^+)	1.16(221)
5072.1 7	1.9 2	6.05 5	$(2,3)^-$	0.84(41)
5324.5 8	1.6 2	6.03 5	$(2,3)^-$	0.76(58)
5338.1 7	4.3 5	5.60 6	$(2,3)^-$	0.60(46)
5364.5 7	0.39 5	6.63 6	$(3,4)^-$	0.88(14)
5517.2 8	0.46 6	6.50 6	$(3,4)^-$	1.16(169)
5806.3 7	0.14 2	8.63 7		0.59(121)
6013.0 9	0.60 7	6.17 5	$(2,3)^-$	1.22(84)
6046.6 8	2.7 3	5.50 5	$(2,3)^-$	1.19(32)
6057.0 8	1.3 1	5.83 6	$(2,3)^-$	0.59(58)
6185.7 8	0.24 3	6.49 6	$(3,4)^-$	0.70(158)
6190.7 9	0.36 5	6.31 6	$(2,3)^-$	0.67(125)
6211.0 8	1.2 1	5.77 5	$(3,4)^-$	1.02(64)
6472.5 8	0.71 8	5.88 5	$(3,4)^-$	1.45(85)
6473.8 8	0.53 7	6.00 6	$(3,4)^-$	0.75(132)
6599.6 8	0.57 7	5.91 6	$(3,4)^-$	0.80(67)
6627.0 9	0.72 8	5.79 5	$(2,3)^-$	0.78(79)
7840 53	1.0 1	4.90 6	$(2,3)^-$	0.83(33)
7996 53	0.31 3	5.29 6	$(2,3)^-$	1.24(56)

core-collapse effect and other related calculations.

Table 5.5 – Systematic analysis of logft values of N=49 isotones. Data from NNDC [126].

	$^{78}_{29}Cu_{49} \rightarrow ^{78}_{30}Zn_{48}$	$^{80}_{31}Ga_{49} \rightarrow ^{80}_{32}Ge_{48}$	$^{82}_{33}As_{49} \rightarrow ^{82}_{34}Se_{48}$	$^{84}_{35}Br_{49} \rightarrow ^{84}_{36}Kr_{48}$
allowed	5.5(1)	6.38(8)	6.57(16),5.37(6)	6.74(6)
ff	6.2(3)	6.57(6),6.30(8),6.57(5)	6.65(17),6.43(17)	7.70(6),7.2(1), 7.4(1),7.5(1)
1U		8.89(5)	8.9(5),9.5(3),8.65(17)	9.46(7)

1.2 Systematic analysis of Ge isotopes

Shell structure and collectivity of N=48 isotones

After the previous analysis of the neutron and proton shells evolution near ^{78}Ni and the comment on under-lying physics, the focus is moved to the shell structure of N=48 isotones and the location of ^{80}Ge. Figure 5.1(b) presents the N=50 gap derived from the difference of two-neutron binding energy in N = 52 and N = 50, which keeps good agreement with the upper left part of Figure 1.11 derived from binding energy of ground states of N = 49 and N=51. Furthermore, the two neutron separation energy of N = 48 is also plotted in Figure 5.1. There are two interesting things to comment on here. Firstly, the N=50 shell gap keeps a minimum value at Z = 32 with 3.450(5) MeV while its maximum value is at Z = 38 or Z = 50. Secondly, the figure of S_{2n} between N = 48 and N = 50 "sausage" shape: at its two poles (Z = 28 and Z = 40) the S_{2n} curves are very near, whereas in between they are more distant. It means that the Ge isotopes, located between two poles of proton magic number, are looser bound than other neighbor isotones.

The $E(2_1^+)$ values along the chains of N = 48 and N = 50 isotones are presented in Figure 5.2. Both exhibit two local maximums at Z = 28 (Ni) and Z = 40 (Zr) attributed to spin-orbit coupling (OS) and harmonic oscillator (HO) shell closure, respectively. These assessments are reinforced by their low B(E2) values, implying a quadrupole non-collectivity. Additionally, the difference of $E(2_1^+)$ energy (noted $E(2_1^+)$ gap) between N = 48 and N = 50 is also shown in Figure 5.2 in which two strong peaks emerge at Z = 28 and Z = 40. This is in good agreement with Figure 5.1. It is due to the double magic character of $^{78}_{28}Ni_{50}$ and $^{90}_{40}Zr_{50}$ when another double magic nucleus ^{100}Sn still keeps its mystery. On the contrary, in Fig. 5.2(a) the $E(2_1^+)$ values for ^{80}Ge an ^{82}Se are the lowest of the N=48 isotopic chain. This is an indication for higher collectivity. The fact that the maximum of quadrupole collectivity emerges already at ^{80}Ge in the N = 48 isotones chain, two neutron away from magic number N = 50, is amazing and justifies the interest toward this nucleus for studying the collectivity in the nuclear structure, binding energy and nuclear force near the magic number region (spherical symmetry from HO theory).

Figure 5.3 displays the experimental B(E2)↑ ($0_1^+ \rightarrow 2_1^+$) reduced transition probabilities for N = 48 and N = 50 isotones as functions of proton numbers, between 28 and 40-42, measured from Coulomb excitation experiments [126]. It sheds light on the behavior of nuclear collectivity in the N = 48 and N = 50 isotopes between neutron-rich nuclei together with nuclei in stability valley. One can observe that the B(E2)↑ value increases from Z = 30 to Z = 34 and then decreases until the minimum Z = 40. One can draw two conclusions. Firstly, the quadrupole E2 excitations are quenched and as well

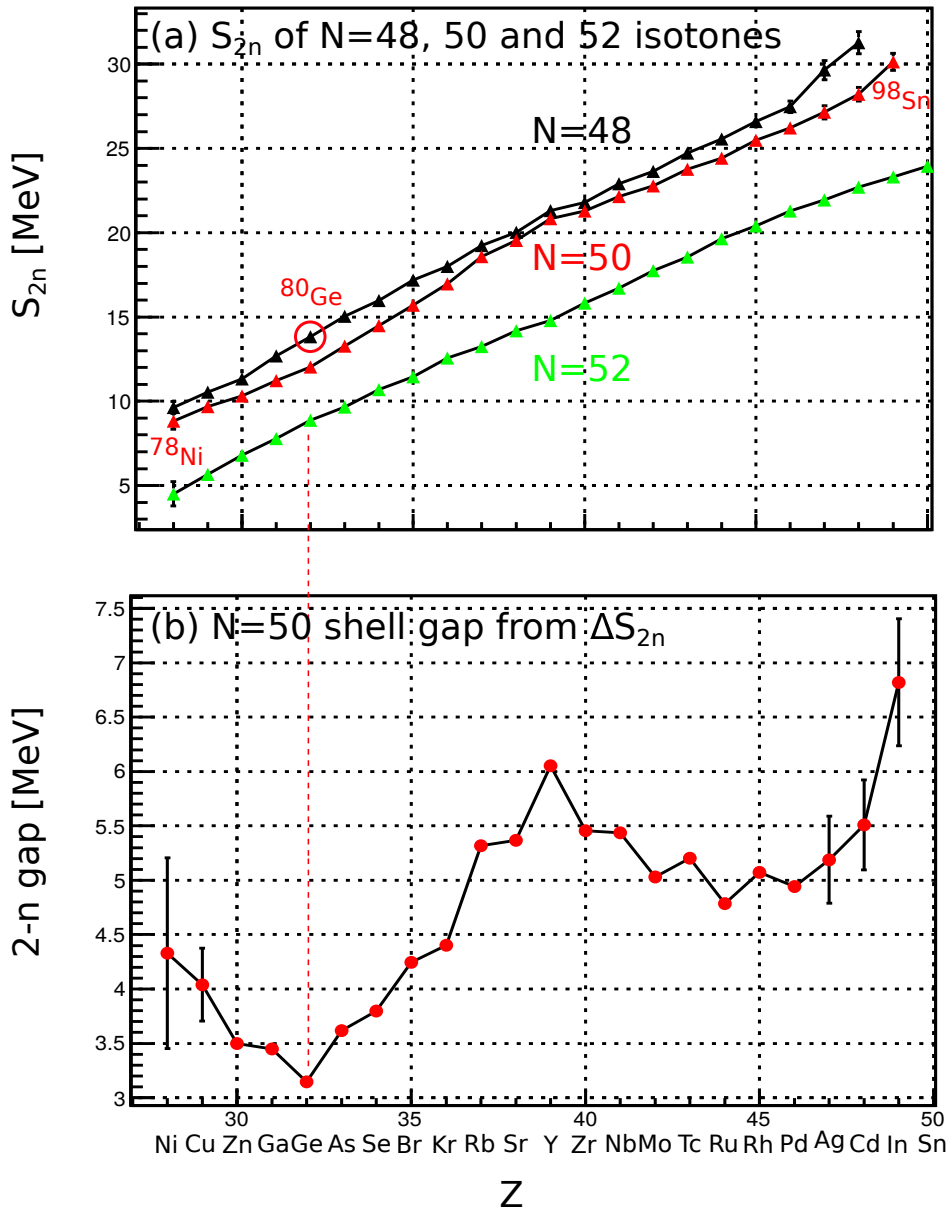

Figure 5.1 – a) Two-neutron binding energy of N=48,50,52 isotones chains and b) N=50 shell gaps extracted from ΔS_{2n}. Data comes from AME2020 [36].

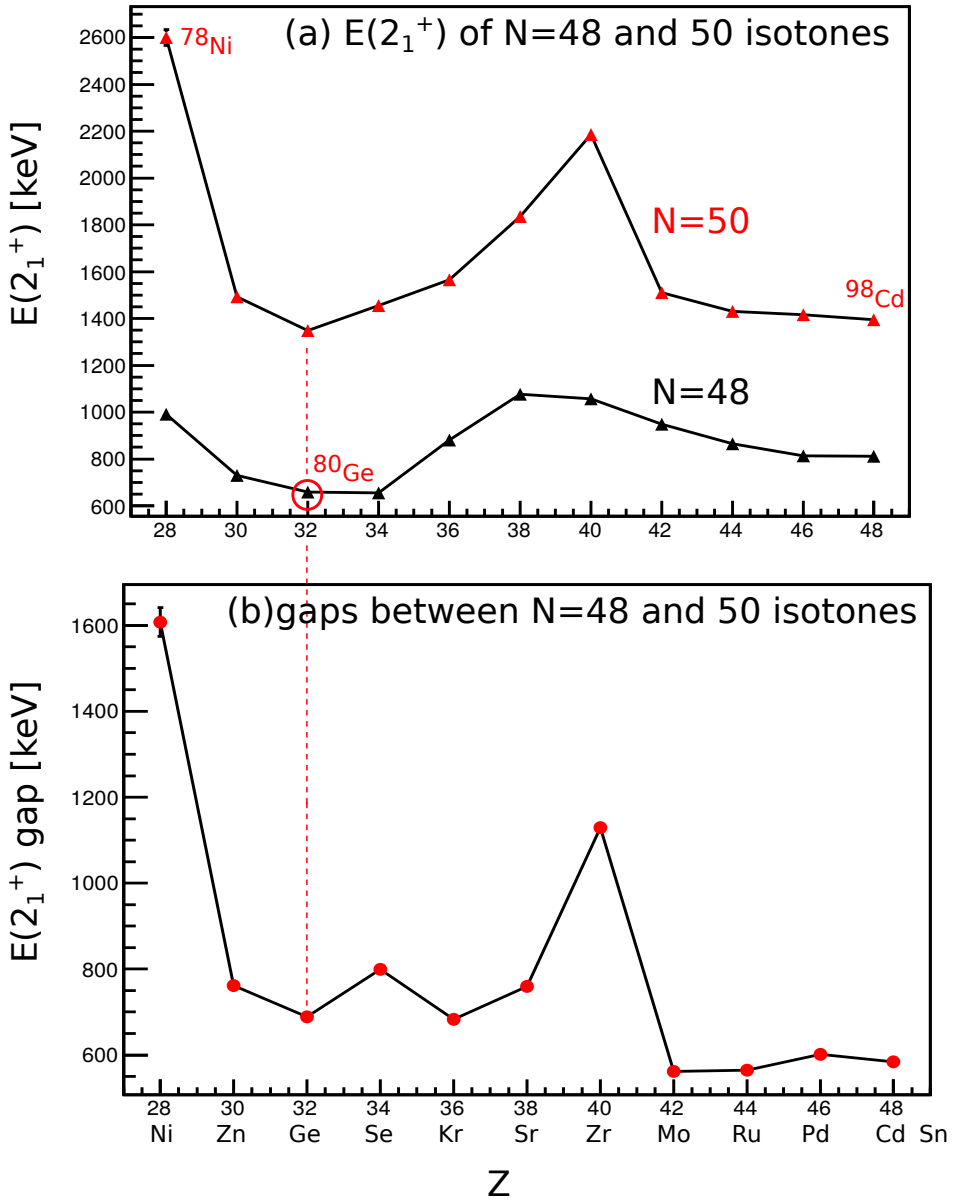

Figure 5.2 – a) E(2_1^+) of N = 48 and N = 50 isotones chain and b) their difference. Data comes from ENSDF [126].

exhausted at closed shell (Z=28 and Z=40) because any excitation has to overcome the large gap and also because of, from collective point of view, spherical symmetry of double magic nuclei. Secondly, inversely, the mid-shell nuclei Z = 32 (Ge) and Z = 34 (Se), which have free levels for their excitation, exhibit the highest B(E2)↑ values among the N = 48 and N = 50 isotones. This highest collectivity is correlated with larger deformation. In conclusion, from the B(E2)↑ curves in the nuclei of this region, ^{80}Ge has a stronger collectivity, which is consistent with the previous analysis.

Furthermore, the excitation energy of 8^+ isomeric states of N = 48 isotones chain are compared in Figure 5.4. These 8^+ isomers have been determined as built on two neutron-hole configuration $\nu g_{9/2}^{-2}$ before Z = 40. This was determined thanks to g factor measurement of 8^+ states and comparison with g factor of $9/2^+$ state [149]. Therefore, the energy of 8^+ states can reveal the 2 neutron hole potential V_{2h} in the N = 48 isotones chain. ^{80}Ge (Z = 32) together with ^{82}Se (Z = 34) have the maximum values of 8^+ energy in accordance with largest V_{2h} which is in good agreement with their large collectivity as shown in Figure 5.2 and Figure 5.3.

$$g(8^+[\nu g_{9/2}^{-2}]) = g(9/2^+[\nu g_{9/2}^{-1}]) = -0.243(4) \quad (from\ ^{87,88}Sr[149]) \tag{5.1}$$

Collectivity of ^{80}Ge

From a shell model point of view the level structure of ^{80}Ge is complex especially for the high-lying states in which the excitations require the so-called large-scale shell model. A reasonable picture for the low-lying excited states is that of four protons primarily in the $f_{5/2}$, $p_{3/2,1/2}$ and $g_{9/2}$ orbits coupled to two neutron holes in the $g_{9/2}$ orbit. An inert core of ^{68}Ni is assumed. However, considering that the β-transition can occur in the deep-bound neutron, the core could be degenerated to ^{56}Ni or even collapes.

Another difficulty to study the ^{80}Ge structure in β-decay is that there are the ground state and isomer β-feeding to ^{80}Ge simultaneously, whereas these $^{80g+m}$Ga have quite different structure. As shown in Table 5.6, from the laser spectroscopy measurement [150], ^{80m}Ga presents a smaller quadrupole deformation than ^{80g}Ga, and its electric-quadrupole moment is smaller. Furthermore, from the shell model calculation [141], ^{80g}Ga and ^{80m}Ga have the same configuration $\pi f_{5/2}^1 \otimes \nu g_{9/2}^{-1}$ that couples to 6^- and 3^-, respectively. However, these two states possess opposite magnetic-dipole moments as for ^{80g}Ga it is positive and for ^{80m}Ga it is negative. It demonstrates that they have different weights in the proton and neutron components while they have the same configuration. ^{80g}Ga has more neutron contribution while ^{80m}Ga has more proton contribution. Of course, the fact that their spins are different is important. All of these differences of ^{80g}Ga and ^{80m}Ga make the determination of the structure of daughter nucleus ^{80}Ge complex. Nevertheless, this complexity implies a rich harvest of information for nuclear structure in the β-decay study. The spin difference of these two isomers enlarge the spin window, reducing the disadvantage of nuclear structure study through β-decay. In the consideration of allowed, FF and 1U, spin 1-8 are available for ^{80}Ge. One picture of this complexity is provided by the level scheme. One can see that the level scheme presented in this work shows a rather high level density with no significant gaps above 3 MeV.

In order to study the collectivity of ^{80}Ge, an analysis of some systematics of Ge isotopes was

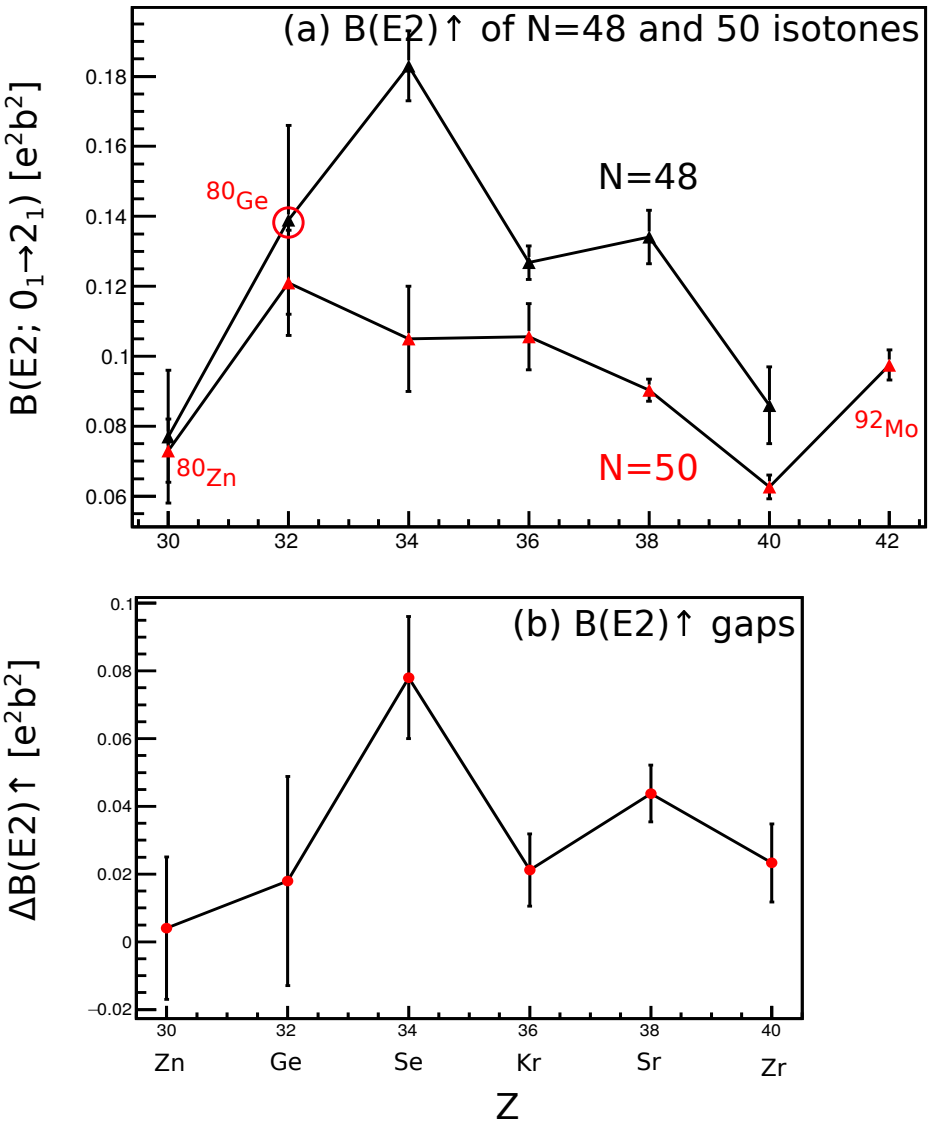

Figure 5.3 – a) B(E2)↑ of N = 48 and N = 50 isotones chains and b) their difference as function of proton number. Data comes from ENSDF [126].

Table 5.6 – The magnetic-dipole moments and electric-quadrupole moments of ^{80g}Ga and ^{80m}Ga measured in the laser spectroscopy study [150].

A	I	$\mu(\mu_n)$	Q_s(efm^2)
80g	6	+0.061(29)	+47.8(27)
80m	3	-1.435(5)	+37.5(21)

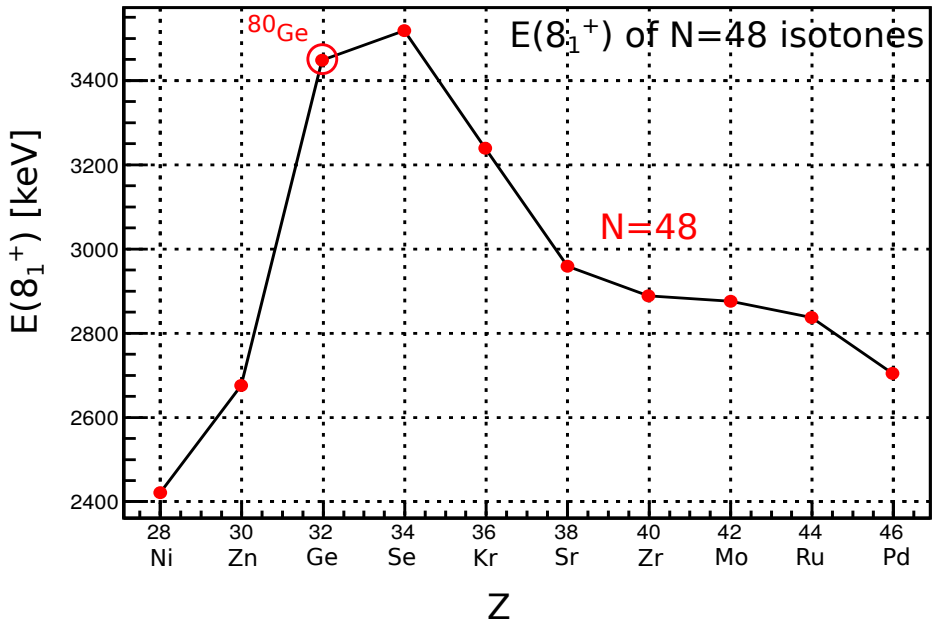

Figure 5.4 – Energy of 8_1^+ states relative to 0_1^+ for the N = 48 isotones as a function of the proton number. Data comes from ENSDF [126].

performed. In the nuclear triaxial deformation research, the even–even Ge isotopes have attracted much attention and many endeavors have been used including experimental and theoretical work. In ^{72,74,76,78}Ge, the γ-bands have been experimentally observed, which are the evidences of the triaxiality [38, 39, 40, 41]. However, insufficient experimental evidence can be discovered to distinguish between a γ-soft or γ-rigid asymmetry (remains elusive). For the purpose of investigating the nuclear collective motion, the B(E2)↑ of Ge isotopes are drawn in Figure 5.5. In addition, B(E2)↑ of Ni(Z=28) and Zn(Z=30) isotopes are also presented together with the difference of their B(E2) value (Fig. 5.5 bottom). One interesting phenomenon appears in the curve of the B(E2) difference of Z = 28 and Z = 30 where the minimum values occur at the two closed shell N = 28 and N = 50 while the maximum appears at the sub-closed shell N = 40. It is attributed to the super quenched B(E2) at $^{68}_{28}$Ni$_{40}$. Moreover, the behavior of the B(E2) function of the Ge isotopes is quite different, when compared with Ni isotopes, as it keeps fast increasing beyond N = 40 and until N = 42. Then, it decreases toward N=50. However, ^{80}Ge still possesses large B(E2) value close to the one in the stable ^{70}Ge. And Ge isotopes present quite larger B(E2) values when compared with Ni and Zn isotopes.

Figure 5.6 presents potential energy surface of ^{80}Ge from the CEA calculation. It supports the triaxial deformation in ^{80}Ge. Some signals of gamma vibration have been found in the present work of this thesis through β-delayed spectroscopy of ^{80}Ge in ALTO data. However, a further confirmation measurement is needed.

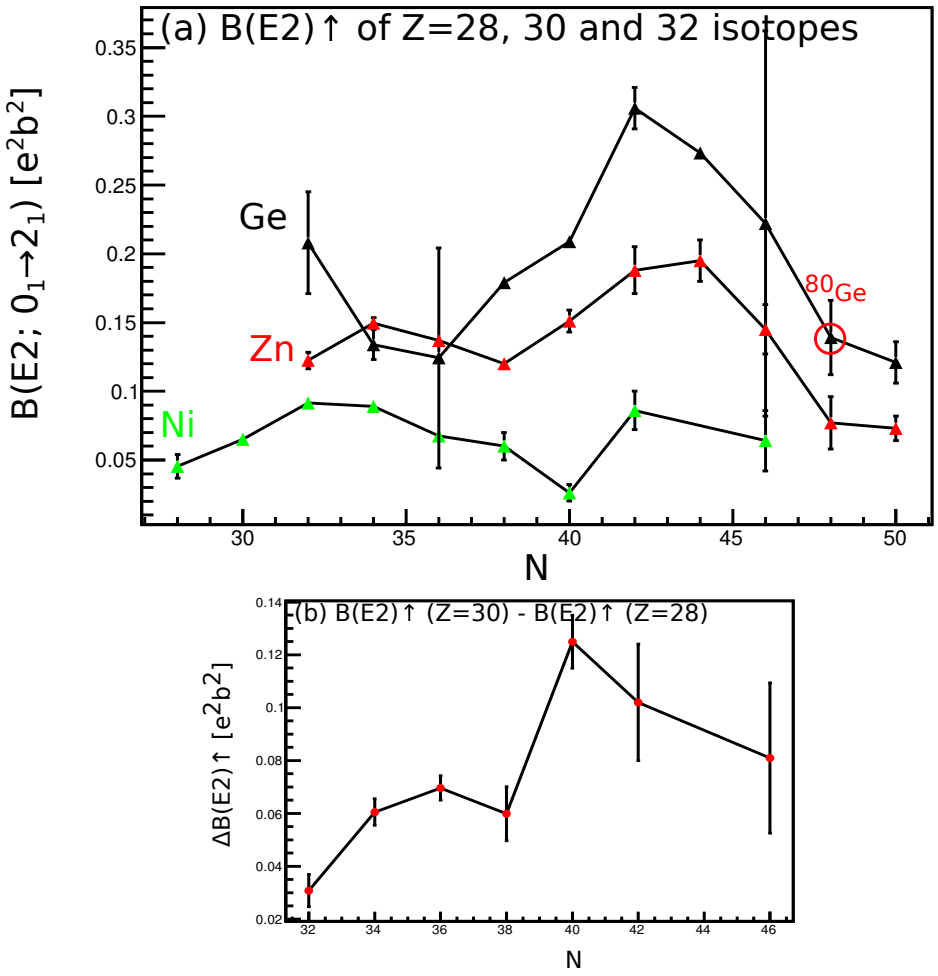

Figure 5.5 – a) B(E2)↑ of Z = 28, 30, 32 isotopes chains and b) the difference between Z = 28 and Z = 30 as functions of neutron number. Data comes from ENSDF [126].

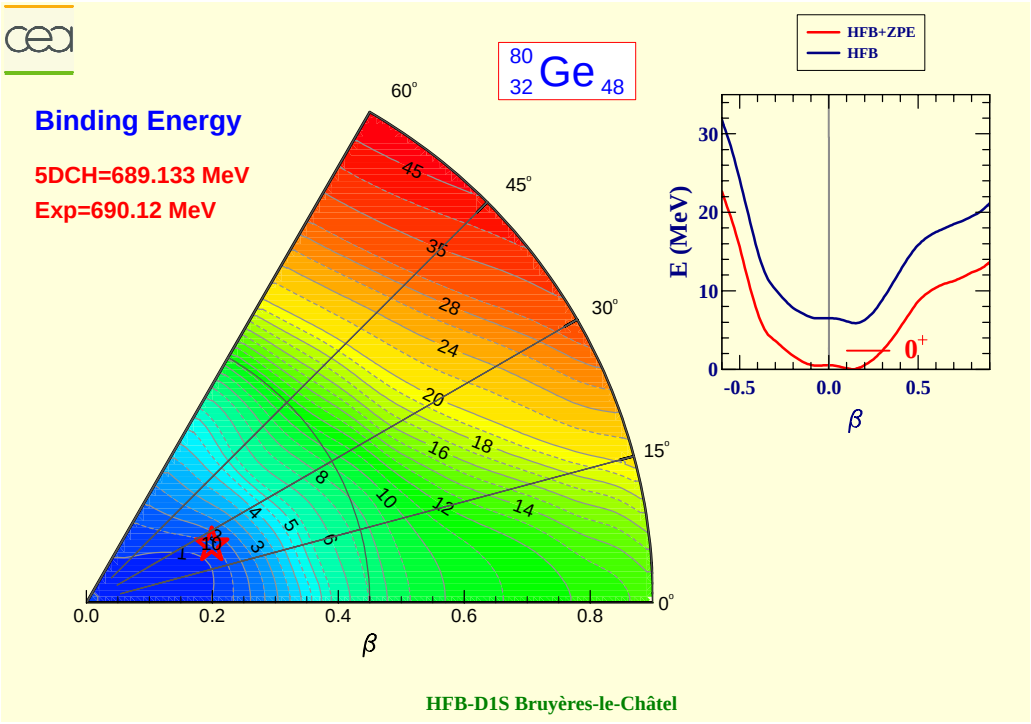

Figure 5.6 – The potential energy surfaces for ^{80}Ge from CEA Hartree-Fock-Bogoliubov calculations based on the D1S Gogny.[151]

2 Experimental evidence for PDR in ^{80}Ge

In this thesis, we firstly report on the study of PDR built on quadrupole collectivity with medium spin and its decay pattern in the exotic nucleus ^{80}Ge through ^{80}Ga (Z = 31; N = 49; $J^P_{isomer} = 3^-$; $J^P_{gs} = 6^-$[141]; Q_β = 10.312(4) MeV [152] with high isospin asymmetry of 0.23) β decay study. This endeavor was triggered by the unexpected observation of "ultra"-high-energy γ-rays (8-9 MeV) in the β-delayed emission products of ^{83}Ga [43] and β-delayed neutron-emission probabilities study that provides side evidence for the existence of PDR in the N = 50 region [76]. In addition, nuclei in this region are considered to be dominated by near-spherical features, which provides an opportunity to investigate the shell structure effect. However, quadrupole and octupole, asymmetric by reflexion, deformations also have been observed in ^{80}Ge [42, 153]. This brings the chance to survey nuclear structure effects from another degree freedom, i.e. visualized macroscopic view point or so-called collective motion such as two-phonon vibration. Folding with the B(GT) measurements, all these data provide a direct insight into the structure and the collectivity of the PDR through investigating its state's wave function, configuration, spin parity, isospin character and decay pattern. The aim of this study is to broaden the existence frontier of PDR along the spin dimension and reveal the importance of the role of the complex 2p2h configurations mixed with the 1p1h constituent, which are prominent components in β decay [17].

Figure 4.14(a) shows the β-gated γ spectrum at the high energy region detected by PARIS spectrometer where above 5.6 MeV only beta-delayed emissions from ^{80}Ga occured as the Q value of daughter nuclei ^{80}Ge and ^{80}As are 2679(4) keV and 5545(4) keV [152]. In order to suppress the Comp-

ton scattering and escape events caused background and extract relatively accurate B(GT) value, the following PARIS-data sorting modes were used: 1) $LaBr_3$ works individually; 2) add-back between the 9 $LaBr_3$ crystals within a 9-fold cluster; 3) add-back between the 27 $LaBr_3$ crystals within 3 clusters. For these modes, outer-shell NaI crystals work as anticoincidence veto detectors. The energy resolution and detection efficiency of PARIS are 53 keV and 0.3% at 7.2 MeV under mode 3 [154]. As can be seen in Fig. 4.14(a), high-energy γ-ray events, spectra endpoint and backgrounds are easily visible and distinguishable. It must be emphasized that, thanks to the specific properties of PARIS, correctly exploited through this sorting method, one can extract directly the higher-energy part of the γ spectrum without resorting to Monte-Carlo techniques or to any theoretical assumption on the γ strength distribution.

In order to investigate the structure of the high-lying states, the detailed information: level energy, spin, parity, β transition half-life, B(GT) and their decay pattern were extracted. As showed in Fig. 4.14(b), two distinct resolved full-energy peaks survived in PARIS spectrum of photons detected in coincidence with a 659 keV photon from the $2^+ \rightarrow 0^+$ transition of ^{80}Ge and detected with the HPGe detectors. The peaks in this spectrum result from direct feeding transitions of the excited states at 7.8 and 8.0 MeV into the first-excited 2^+ state of ^{80}Ge. For a further verification, the reversed coincidence spectrum is showed in Fig. 4.14(c).

For the assignment of the multipolarity of γ transitions, it is essential to separate the decay level schemes for the ^{80g}Ga and ^{80m}Ga. The half-life of a beta-delayed γ-ray is contributed to by: 1) direct β-feeding branch ratio from the ground state and isomer and their half-lives; 2) indirect γ-feeding from the depopulation of higher-lying states and their half-lives. The "X", value of 3^- isomer β feeding branch ratio, formula [42] covering these parameters was used to assign each level. In principle, X = 0 and X = 1 mean the pure 6^- and 3^- feeding, respectively. The X value distributions of the spin-parity definite states 2_1^+, 2_2^+, 4^+, 6^+ and 8^+ in Fig. 4.15(b) affirm the validity of the approach applied. Fig. 4.15(a) presents the activity curve of 7212(53) keV γ-ray and its fitting by a A(τ,Φ), function of γ-line half-life τ and level state's population intensity Φ. The derived X values for the 7.8 and 8.0 MeV states are 0.8(3) and 1.2(6), respectively. So, they are assigned to 3^- β feeding with 83% and 100% confidence. Note that if cross β-feeding happens, at least one isomer needs to take first unique forbidden (1U) β transition. Considering the lower probability of 1U transition compared to allowed and first nonunique forbidden transition [21], the condition for cross β-feeding is that the X value would lie between 0.4 and 0.6. In addition, assuming the allowed transition, the candidate high-lying states populated by 6^- are $(5,6,7)^-$ of which deexcitation to 2^+ are quite difficult to be observed. Consequently, the X value provides reasonable and reliable evidence that these two high-lying states can only be fed by the isomer 3^- of ^{80}Ga as shown in Fig. 5.7.

For the extraction of the accurate β-decay intensity, the pure beam technique was used. The significance is that one can extract the precursor's abundance through handling its Bateman equation using β particle activities data, 5 nuclei involved in present data, which promises the results I_β, logft and B(GT) independent of granddaughter's data [145]. Once the construction of the separated decay level schemes has been achieved, one can count 3^- and 6^- β-feeding statistics. Based on this, the beam ratio of two isomers was achieved. The extracted absolute I_β of these two high lying states are 1.01(11)% and 0.31(3)%. The related logft are 4.91(7) and 5.29(6). Comparison with the logft values

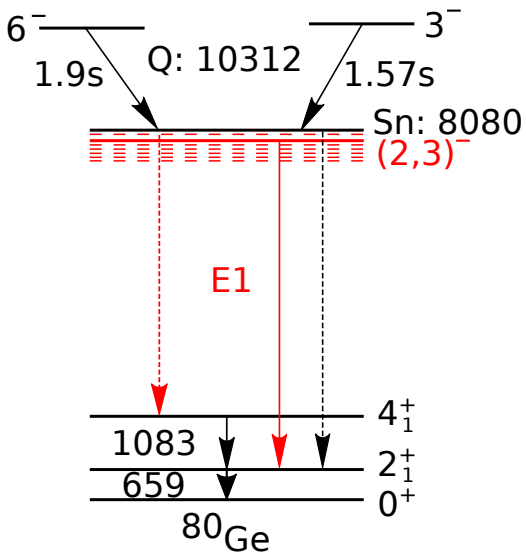

Figure 5.7 – Diagram of PDR in ^{80}Ge.

of the first-forbidden β transitions, from J^π firmly assigned states, occuring in ^{80}Ga of which logft values are larger than 6.3 (as listed in Table I) and together with the statistical information of the experimental logft values between levels of firmly assigned J^π states of 3900 β transitions (where 98% first-forbidden β transition whose logft are larger than 6 [21]), therefore, enable to assign that these two high-lying states were populated through allowed Gamow-Teller β transition instead of forbidden transition unambiguously. Based on this analysis, the spin-parity of these two states are determined to be $(2,3,4)^-$ experimentally. The related γ transition multipolarity deexciting to 2^+ could be E1, M2, E3; E1, M2, E3 and M2, E3 respectively. In addition, PDR based on 4_1^+ would be too weak to get resolved peaks. But some events survived clearly at the endpoint of the background-free spectrum that corresponds to a 7.9 MeV state when gating on $4_1^+ \rightarrow 0^+$ γ rays, like Fig. 4.14b.

According to the electromagnetic transition probabilities of nuclei, considering single-particle transitions in the framework of the shell model, for a fixed energy difference, the probability decreases by $\sim$3 orders of magnitude when the multipolarity increases by one order 1 and for a given polarity. The possibility of an electric transition being $\sim$2-3 magnitudes stronger than magnetic transition [146]. Therefore, the most probable transition to be observed from canditate states $(2,3,4)^-$ to 2^+ is E1. To verify this deduction, theoretical calculations were performed using 2p2h-QRPA$*$ model. In these calculations 1p-1h type excitations are considered, called 2qp excitations, the pairing being active for neutrons as well for protons in ^{80}Ge. We perform calculations on top of HFB single-particle spectrum corresponding to the ^{80}Ge ground state but also on top of HFB single-particle spectrum associated with an excited 2qp configuration, these calculations are noted as QRPA$*$. Note that 2p2h interaction, multi-correlation, is consistent with the quantum nonlocality property of the quantum system. Isovector PDR with configuration of 2p2h located at high energy was assigned while 1p1h populates lower energy PDR states in ^{208}Pb study [55]. Actually most 1^- states can not be considered as simple neutron 1p1h states. Table 5.3 shows the calculated state's energy, logft, B(GT), spin-parity and γ transition multipolarity. Especially B(GT) is powerful to check the final state's wave function and configurations after β-decay. Note that PDR must be distinguished from neutron separation thresh-

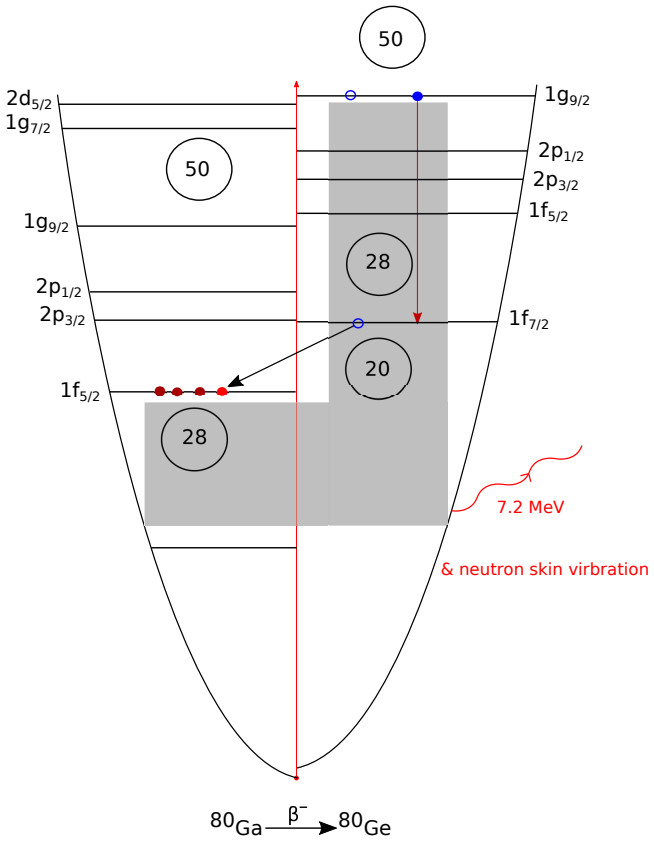

Figure 5.8 – Diagram of microscopic mechanism of PDR in ^{80}Ge.

old effect indicating γ ray emits from nuclear S_n energy level. This is observed in data of ^{80}Ge in PARIS spectra when using add-back-all configuration and is also observed in ^{82}Ga β-delayed γ emisson spectrum in HPGe detectors [155].

The results were compared to cutting-edge QRPA and two particle two hole (2p2h) coupling two phonon (2p) model, which accurately described the E1 strength of the ^{116,120}Sn and ^{68}Ni. The model has been extended to calculate the PDR built on an excited configuration. For 7.8 MeV state, the configuration is $(\pi 1f_{5/2})^2\ (\nu 1g_{9/2})^{-1}\ (\nu 1g_{9/2})^1\ (\nu 1f_{7/2})^{-1}$, neutron decay from core shell $\nu 1f_{7/2}$ was adopted during calculation as shown in Fig. 5.8. From B(E2) measurements and related shell model calculation, 2_1^+ state is dominated by proton configuration $(\pi 1f_{5/2})^2(\pi 2p_{3/2})^2$ and $(\pi 1f_{5/2})^4$ (about 50% in total). On the neutron side, the main configuration is $(\nu 1g_{9/2})^{-2}$ that dominates the neutron wave functions of 2_1^+ (about 80%) and they tend to be coupled to 2^+ in 2_1^+, whereas in the 2_2^+ state they mostly coupl to 0^+; larger amplitude of neutron $[(\nu 1g_{9/2})^{-2}]^{J=2^+}$ configuration for 2_1^+ state was vertified by larger contribution of $A_n = 13.3$ (e fm^2) to the $2_1^+ \rightarrow 0_{gs}^+$ E2 transition while $A_n = 0.8$ (e fm^2) in $2_2^+ \rightarrow 0_{gs}^+$ [156, 153]. More overlap of the wave functions between 7.8 MeV state and 2_1^+ can explain the preferred γ transition between them rather than deexciting to 2_2^+ or 0_{gs}^+. From microscopic point of view, the agreement between the present observation and the QRPA$*$ model calculations that assume a neutron β-decay from isospin saturated core suggests that the enhanced E1 transition from near neutron emission threshold in ^{80}Ge can be related to the

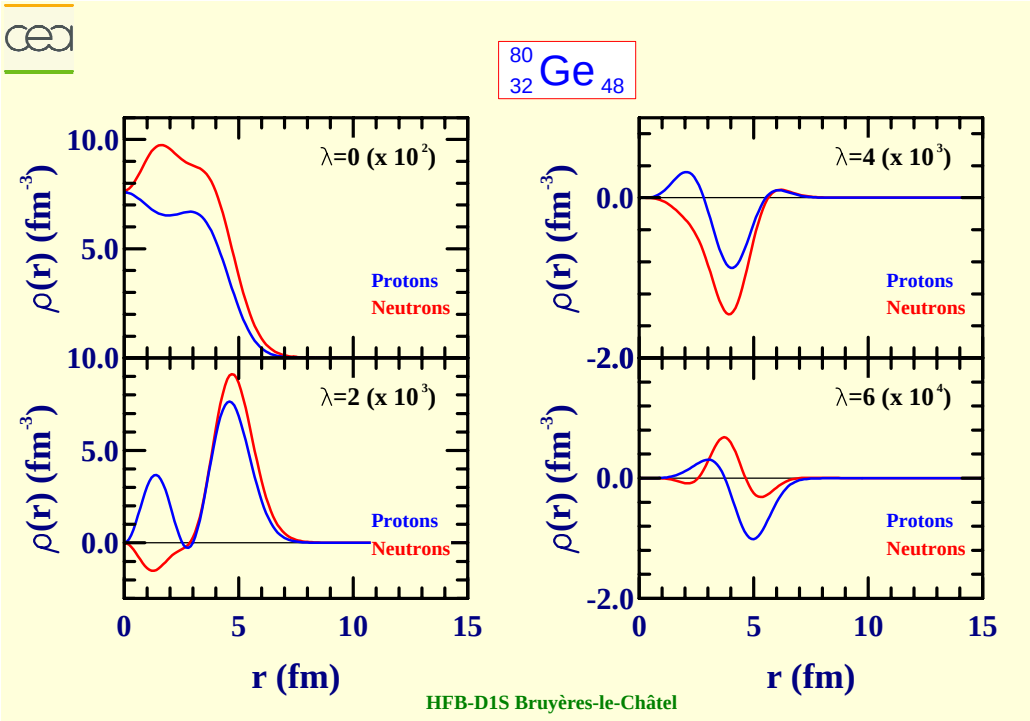

Figure 5.9 – Radial matter densities for ^{80}Ge [151].

neutron skin which is, from theoretical calculations [157], around 0.19 fm, also shown in Fig. 5.9 calculate by CEA theoretical group [151]. This skin oscillates during the deexcitation process. In addition, the observision of this quadrupole collectivity based PDR can be explained by the effect of the angular momentum: some of the populated levels, which can only deexcite to 0^+_{gs} with photon carrying large orbital angular momentum, are strongly hindered. From macroscopic point of view, ^{80g}Ga and ^{80m}Ga have the largest electric-quadrupole moments in the $^{65,67,69,75,79-82}$Ga isotopes [150]. For QRPA$*$ model calculation, the excited configuration has a rather large quadrupole deformation that is consistent with the precusor's shape of ^{80m}Ga. Therefore, the large shape overlap between PDR and 2^+_1 states causes the PDR states "prefer" decay to 2^+_1 instead of 2^+_2 and 0^+_{gs}. Indeed, the respective quadrupole deformation parameters β_2 values of 2^+_1 and 2^+_2 are 0.155(9) and $0.053^{0.008}_{0.009}$ [153]. So, the PDR decay to the 2^+_1 is from quadrupole deformation to quadrupole instead of spherical shape, because of the wave function overlap between these two states, i.e. the two neutron hole component, which corresponds to short-range correlations that cause the nuclear deformation. ^{80}Ge compared to ^{82}Ge has two neutron hole, which dominates the short-range correlation, therefore, dominating the decay pattern of PDR.

Therefore, the decay pattern of PDR, direct to the 0^+_{gs} or to low-lying states, strongly depends on the nuclear structure. The neglect of the components of the excited states based PDR can potentially lead to incorrect statistical results.

For implications, the results of present measurement is an evidence for questioning the completeness of electric dipole polarizabilities measured by proton scattering and, especially, photon absorption. For hadron methodology, E1 strength and angular momentum transfer depend on the beam energy and projectile species when the later is limited to $1\hbar$ angular momentum transfer. From the Connection

research between the PDR and the neutron skin Δr_{np}, the strength of PDR is proportional to the thickness of nuclear skin. Hence, compared with the recent PREX-2 result, the current PDR strength of ^{208}Pb is downweighted due to absence of medium-spin PDR components that built on excited states and GDR components built on excited states, which is not easy to be measured because of high contamination in low energy region; small-angle scattering in (p,p$\prime$) experiment and spin transfer limitation in photoabsorption data. Therefore, we suggest to perform a further measurement of dipole polarizability built on excited states in ^{208}Pb for a more complete electric dipole response function to accurate the Δr_{np} value, which is the potential way to solve the discrepancy of the neutron skin value of ^{208}Pb between extracted from PREX2 and dipole polarizability measurement, considering their uncertainty, at least 10% of PDR is missing in ^{208}Pb in later measurement presently [67] informed by PREX2 [158]; 50% missing given the central value. The study will be a cornerstone to determine symmetry energy is soft or the opposite at nuclear densities. In addition, the effect of isospin on the PDR deserves to be investigated in the future. Moreover, interestingly, the results of present work would trigger the study of the relationship between PDR width and nuclei temperature. And, high resolution gamma spectroscopy and parity measurement need to be measured in the future for ^{80}Ge.

In summary, we extend PDR border along the spin dimention. We have here presented the first experimental search of a medium-spin pygmy dipole resonance built on quadrupole collectivity in the neutron-rich ^{80}Ge nucleus using β-decay technique. Pure beam and background-free spectrum technique make the extracted data logft, B(GT) independent of the accuracy of other nucleus's and simulation data. Evidence is found for the presence of sizeable strength energetically located below the GDR and centered at 7.8 MeV. This structure is similar to what has been found in IVGDR, but is more sensitive to the probe species [67]. Our results support the suggestion that the decay of PDR states is not the inverse reaction to its excitation by photons. This result is in rather good agreement with theoretical calculations and, typically, provides evidence for the incompleteness of polarizability measured by current experiments as it depends on selected reactions, which can get neutron skin and slope of the symmetry energy L in the EOS downweighted. The present result for new structure of pygmy dipole resonance opens interesting future perspectives with other medium-spin neutron-rich nuclei β-decay and further instrumentation for parity measurement such as POLAREX at ALTO. In fact, it will be very interesting for the study of the structure and the decay pattern of medium-spin PDR in nuclei far from stability to measure more in detail and systematically the termperature-dependence of the width of electric dipole response.

3 B(GT) distribution of ^{80g}Ga and ^{80m}Ga

Figure 5.10 presents the cumulative experimental β-decay intensities with statistical uncertainties of ^{80g}Ga and ^{80m}Ga in this work. In order to compare with previous work, results of P. Hoff [142] was also drawn with black points. In this work, for ^{80g}Ga, a total of (79.1±2.5)% I_β up to 6.5 MeV was obtained. For ^{80m}Ga, (85.3±3.6)% was achieved up to 8 MeV. The unobserved states contribute to the missing parts. Additionally, the extracted β-decay intensities were also used to calculate the logft values and then the related B(GT).

If comparing the $\sum I_\beta$ of ^{80g}Ga with the previous unseparated results, one can get obviously that

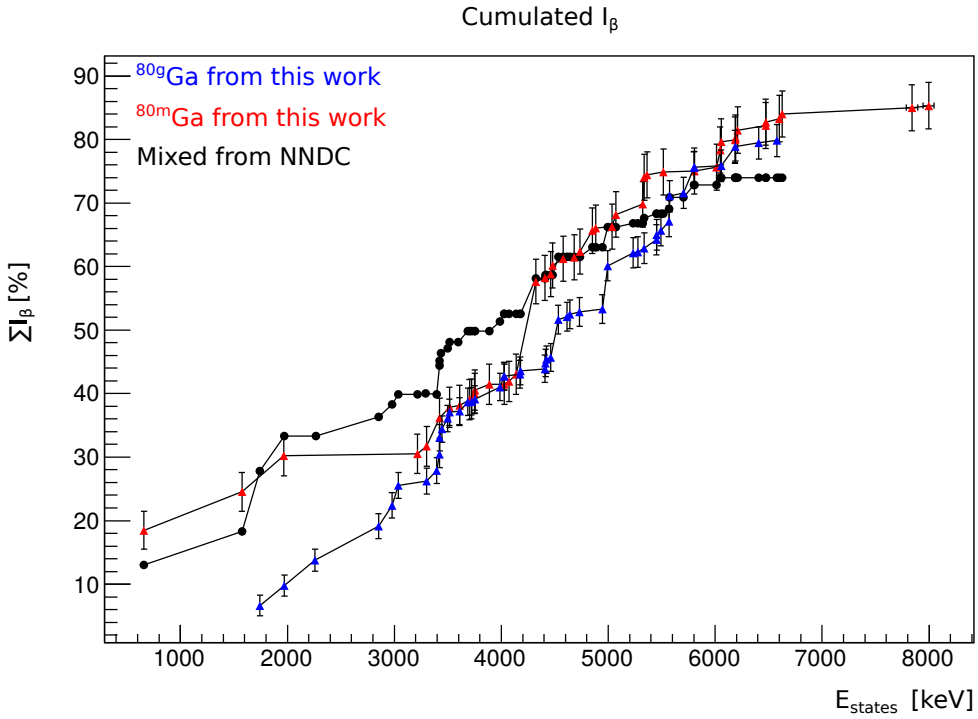

Figure 5.10 – Cumulative β-decay intensity of $^{80g+m}$Ga versus excitation energy of the final states in ^{80}Ge. Red and Blue data come from this work. Black data come from P. Hoff [142].

the former value is smaller than the later's before 5 MeV and then surpasses it quickly at 5.6 MeV. $\sum I_\beta$ of ^{80g}Ga obtains a fast rise from 5 to 6.4 MeV, which demonstrates that there are a intense β-transitions with strong strength in this energy region a indication for allowed transitions. If making a comparison between $\sum I_\beta$ of ^{80m}Ga with the previous results, the former is less than the later's between 2 to 4.3 MeV and then surpasses super fast at 4.5 MeV. One important contribution is the strong β-transition at 4324.2(6) keV states with I$_\beta$ value of 14.6(16)%. In conclusion, in previous work the I$_\beta$ values were overweighted in the low-energy region and downweighted in the high-energy region. It was caused by the so-called pandemonium effect the missing of unobserved high-energy γ-ray.

The nuclear structure including the shape (oblate or prolate) and deformation parameter β_2 effects the distributions of I$_\beta$.

Figure 5.11 presents the experimental B(GT) strength distribution up to S$_n$ (8.08 MeV). The B(GT) with values 0 of previous work indicates the absence of these level states in ^{80}Ge. One can find that most absence concentrates on the energy region of 4.5-8 MeV. In addition, two new measured states at S$_n$ region by PARIS have very larger B(GT) than others due to the rapid decrease of phase space even though the I$_\beta$ is not very large.

Figure 5.12 shows the cumulative B(GT). The total Gamow-Teller strength to states within this energy window is measured to be 0.071(3) for ^{80}Ga and 0.150(8) for ^{80m}Ga. The error bars include the error of Q$_\beta$ value, error of half-lives (from this work), error of I$_\beta$ and error of E$_{states}$. In the case of B(GT) comparison of ^{80g}Ga between this work and P. Hoff [142], the cumulative B(GT) relatively keep coincidence before 5.5 MeV peculiarly for the tendency. However, the acumulated B(GT) of this work

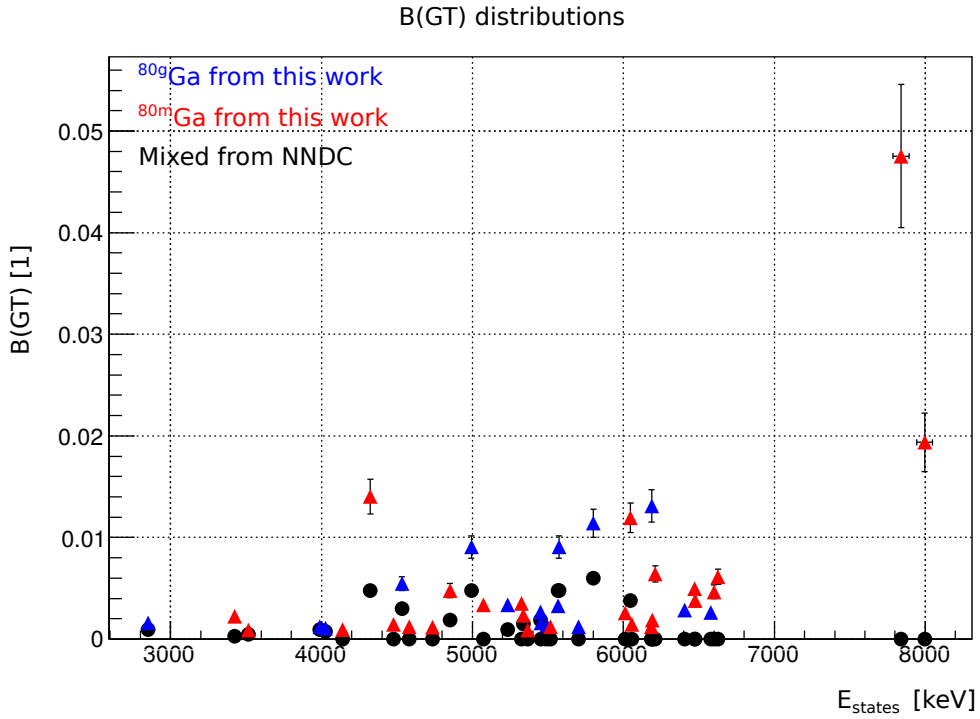

Figure 5.11 – B(GT) distributions of ^{80g}Ga and ^{80m}Ga from this work with red and blue colors and B(GT) distributions obtained from previous mixed decay level scheme [142] with black color.

continue to rise rapidly from 5.5 to 6.5 MeV when these data was unobserved in the previous work. For ^{80m}Ga, the B(GT) difference was enhanced from 4.2 MeV to 6 MeV and then was strengthened obviously from 6 MeV to 8 MeV. In the end, the cumulative B(GT) value of this work is four times of P. Hoff's as shown in the Figure 5.12 down. This conclusion keep good consistence with cumulated I_β analysis as it is contributed by the absence of high-lying states due to Pandemonium effect.

4 Decay-heating of $^{80g+m}$Ga

Decay level schemes of fission products are used to calculate the decay heat energy released in nuclear reactors. The precise data is critical input parameter for the models describing β-decay properties. Decay heating is the only energy source of heat in the nuclear fuel after reactor shutdown. The Nuclear Energy Agency (NEA) provided a list of fission products those are important for the analysis of decay heat [23].

Figure 5.13 shows the relative intensities of γ-rays versus the nergy of γ-rays. In order to compare with the data from ENSDF, the unseparated I_β values are used. There are plenty of new γ-rays were observed in this work especially in the high energy region. A comparison of previous experimental data [126] and this work was presented. The average γ-ray energy determined from this new decay schemes. As presented in the Figure 5.14, average γ-ray energy of $^{80g+m}$Ga β-decay from this work increases 87(17) keV compared with ENSDF data from 1108(12) keV to 1194(11) keV with (7.8 $\pm$ 1.6)% enhanced ratio. But, the analysis here only provided a minimum enhancement due to the absences of counting of single and double escapes peaks.

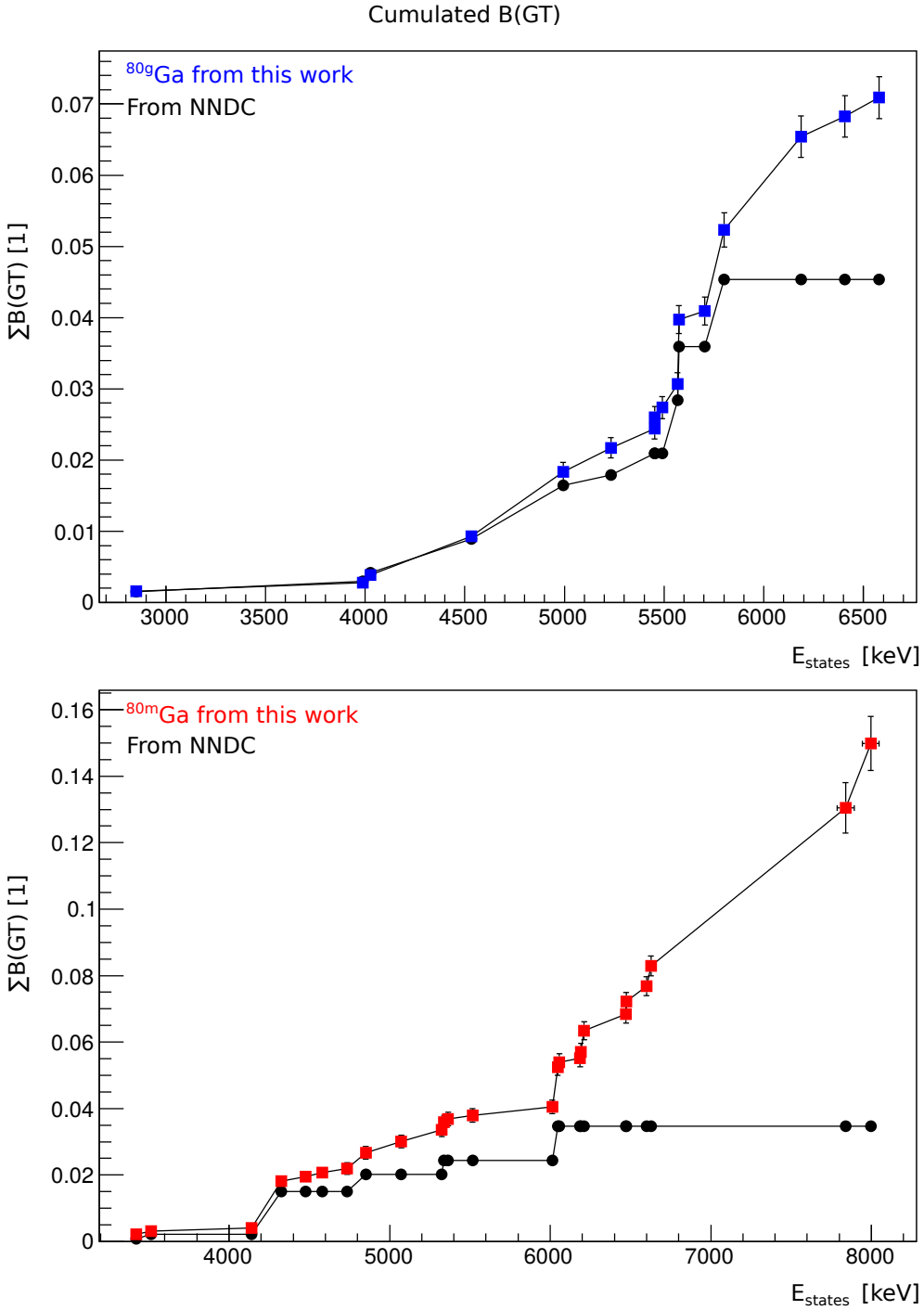

Figure 5.12 – Cumulative B(GT) with statistic uncertainties of $^{80g+m}$Ga versus excitation energy of the final states in ^{80}Ge. For the purpose of comparison, previous results were split and presented separately as well.

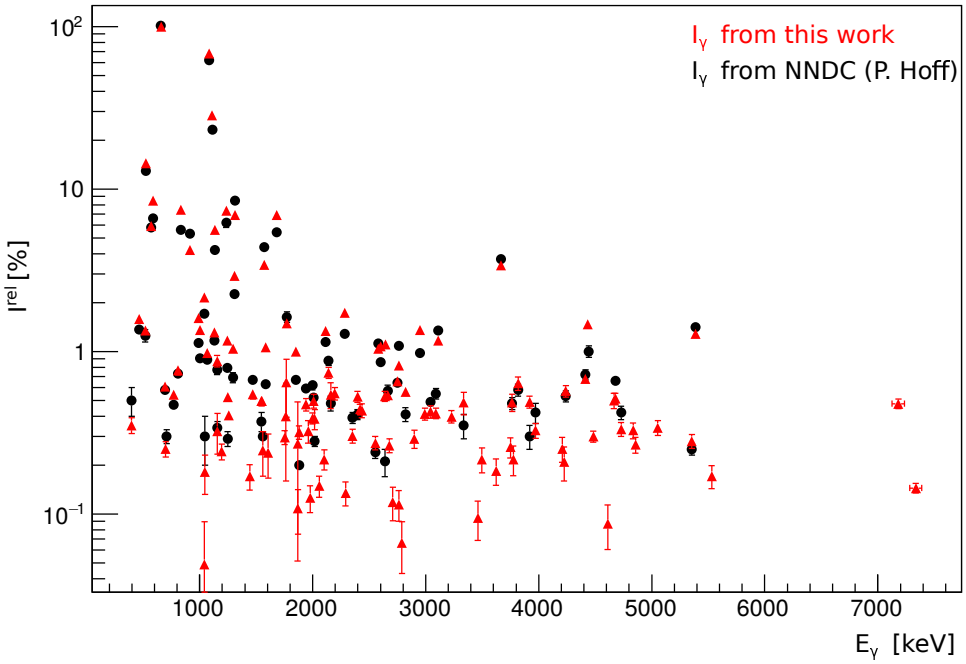

Figure 5.13 – The intensity of γ-rays relative to 659.2 keV γ-ray versus γ-energy.

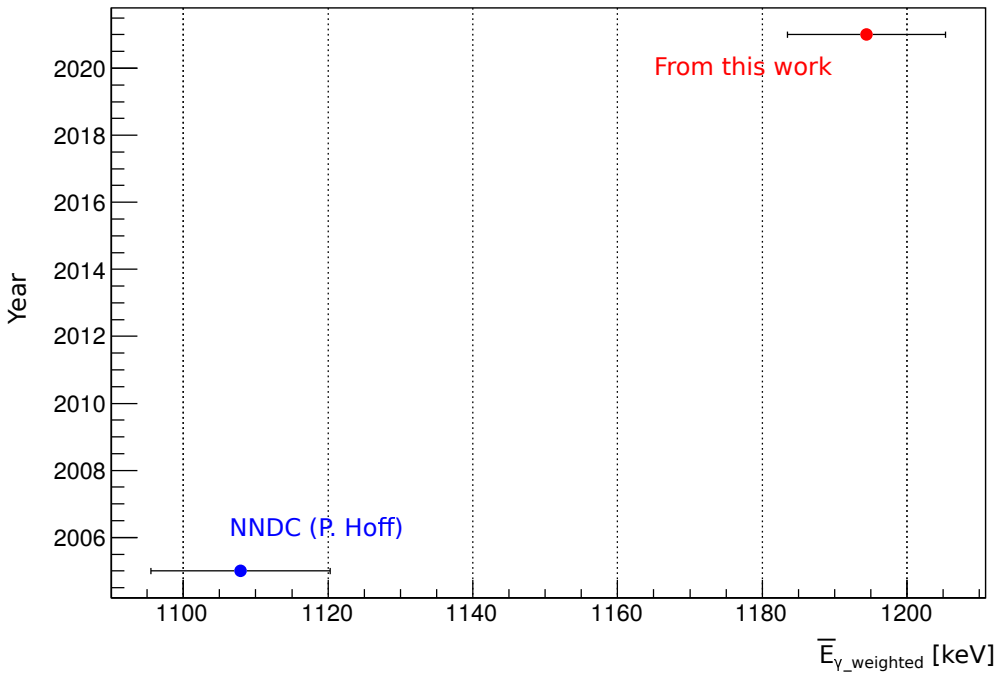

Figure 5.14 – Shift of average γ-ray energy emitted in the β-decay of $^{80g+m}$Ga from previous results [126] and this work.

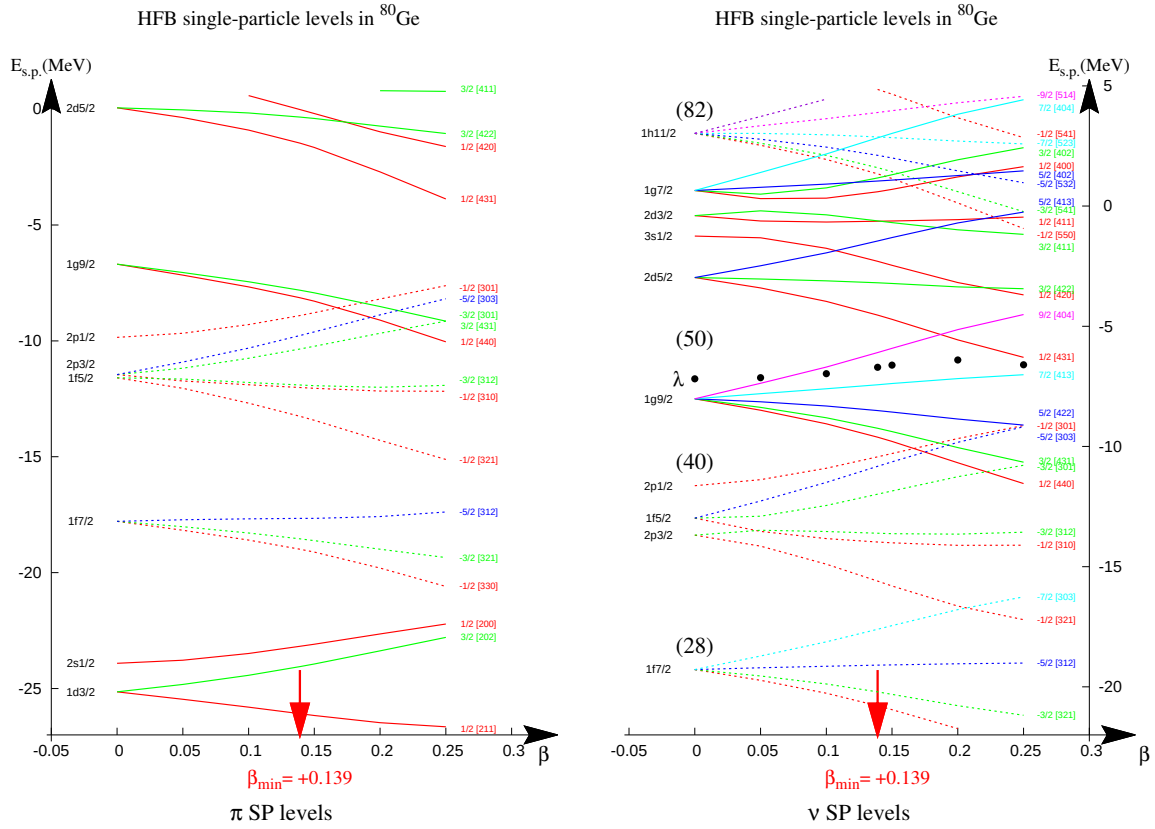

Figure 5.15 – Single particle energy level in ^{80}Ge associated with the ground state using Hartee-Fock Bogolyubov method.

5 Reproduction of experimental data from theoretical calculation: QRPA* method

Single-particle level spectrum from HFB calculation

The first step of theoretical calculation is to obtain the single-particle level spectrum (the equivalent of the Nilsson diagram, but self-consistent in HFB) of deformed or spherical nuclei in their ground state using Hartee-Fock Bogolyubov method method with D1 Gogny force as shown in Fig. 5.21.

Reproduction of B(GT)

Then, this single-particle level spectrum is validated by reproducing B(GT) distribution as presented in Figures 5.16 and 5.17. The good agreement between experimental data and theoretical result, especially for ^{80m}Ga implies that the D1S effective interaction does a good job in this mass region. The single-particle level spectrum (the sequence of single-particle levels and their density) is well reproduce.

As Fig. 5.17 shows, one can easily observe that there three large jumps in cumulative B(GT) distribution of ^{80m}Ga and two in ^{80m}Ga. These jumps are interpreted as doorways of Gamow-Teller β

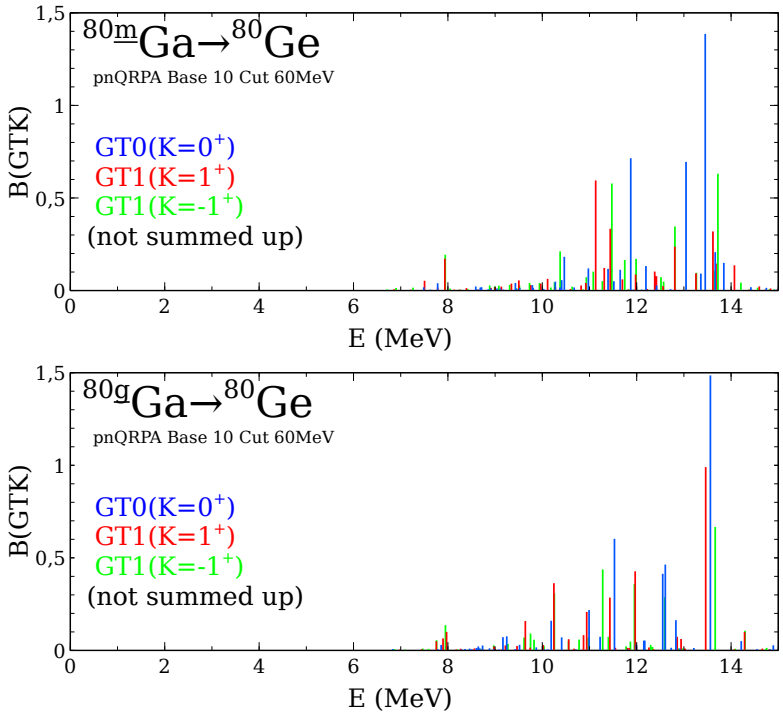

Figure 5.16 – B(GT) distributions of ^{80g}Ga and ^{80m}Ga from microscopic QRPA calculations. Different color corespond to different angular momentum component in the symmetry axis.

transition contributed by $\nu f_{5/2} \rightarrow \pi f_{5/2}$ (first one), $\nu p_{3/2} \rightarrow \pi p_{3/2}$ (second one) or/and $\nu p_{1/2} \rightarrow \pi p_{1/2}$ (second one), $\nu f_{7/2} \rightarrow \pi f_{5/2}$ (third one) or/and $\nu g_{9/2} \rightarrow \pi g_{9/2}$ (third one). The configurations of the two doorways happened in ^{80m}Ga are same as the first two in ^{80m}Ga.

Ground state based B(E1) using QRPA method

QRPA is the natural framework for exploring high energy E1 excitations. This framework allows also the description of β-decay with charge exchange. The starting point of calculations is a HFB calculation. The minimization of the HFB potential energy (here axial) allows to determine the β deformation and the single particle level spectrum at this minimum. At this point it would be good to show not only the single-particle level evolution with the elongation but also their sequence at the deformaton minimizing the HFB energy, i.e 0.139 for ^{80}Ge.

Then all the 2qp excitations can be calculated. They are the building blocks of the phonon excitations predicted by the QRPA/pn-QRPA. The phonon excitations for a given K are coherent summations the 2qp excitations with ΔK. Once they are determined, one can get the strength function: dipole, qadrupole, octupole, etc, and GT in the case of pn-QRPA.

From QRPA calculations, about the E1 strength distribution in ^{80}Ge, the high energy part (IVGDR) is located at around 17 MeV as shown in Fig. 5.18 upper one that is in total adequation of the values calculated from the goldhaber formula (18.6 MeV), the goldhaber/Teller formula (17.40 MeV) and the phenomenological one Bertsh, Tsai (17.16 MeV). The lower energy part (PDR), one can observe in particular a state at 7.9 MeV as shown in Fig. 5.18 middle one and its density function of neutron and proton in Fig. 5.18 bottom one. One can easily observe that there is a

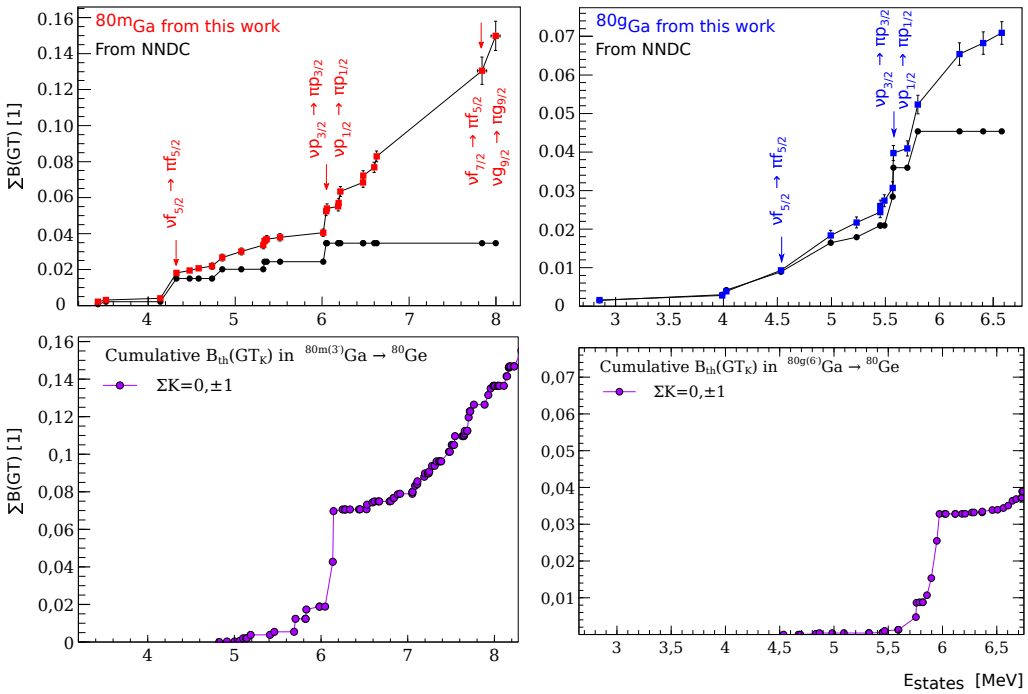

Figure 5.17 – Cumulative B(GT) with statistic uncertainties of $^{80g+m}$Ga versus excitation energy of the final states in ^{80}Ge. For the purpose of comparison, previous results were split and presented separately. Top two from experimental measurements. Bottom two from microscopic HFB+QRPA calculations.

neutron skin vibration in the symmetry (z) direction in this 7.9 MeV state. Fig. 5.19 presents the main 2qp excitations components of this 7.8 MeV state in which many 2qp excitations are involved, demonstrating a rather collective origin instead of 1p1h state.

Excited states based B(E1) using QRPA∗ method

However, experimentally, we have observed an important E1 strength connected not to the ground state but to the 2^+_1. In a first and rough approximation, in order to reproduce this experimental results we have calculated the E1 strength obtained when starting not from the minimum of HFB potential energy but in from the minimum of HFB energy associated with an excited configuration. Two excited configurations have been used, the main configuration building the first K=2^+ as shown in Fig. 5.20. The configuration of 2^+ is presented in Fig. 5.21. All the two excited configurations lead to a PDR state lying at around 7.3 MeV that is in very good agreement with our experimental observation.

The HFB process can also be used to obtain the single-particle level spectrum associated with a one- or several- quasi-particle excitations. It allows for example to obtain the excitation energies of N-qp (isomeric) state. In this work we have performed HFB calculations, not only for obtaining the single-particle level spectrum associated with the ground state (0 qp excitation) but also the ones lowering the excitation energy of different 2qp excitations, those 2qp found to be principal building blocks (or 2qp components) of the first $K^\pi=2^+$ QRPA excited state.

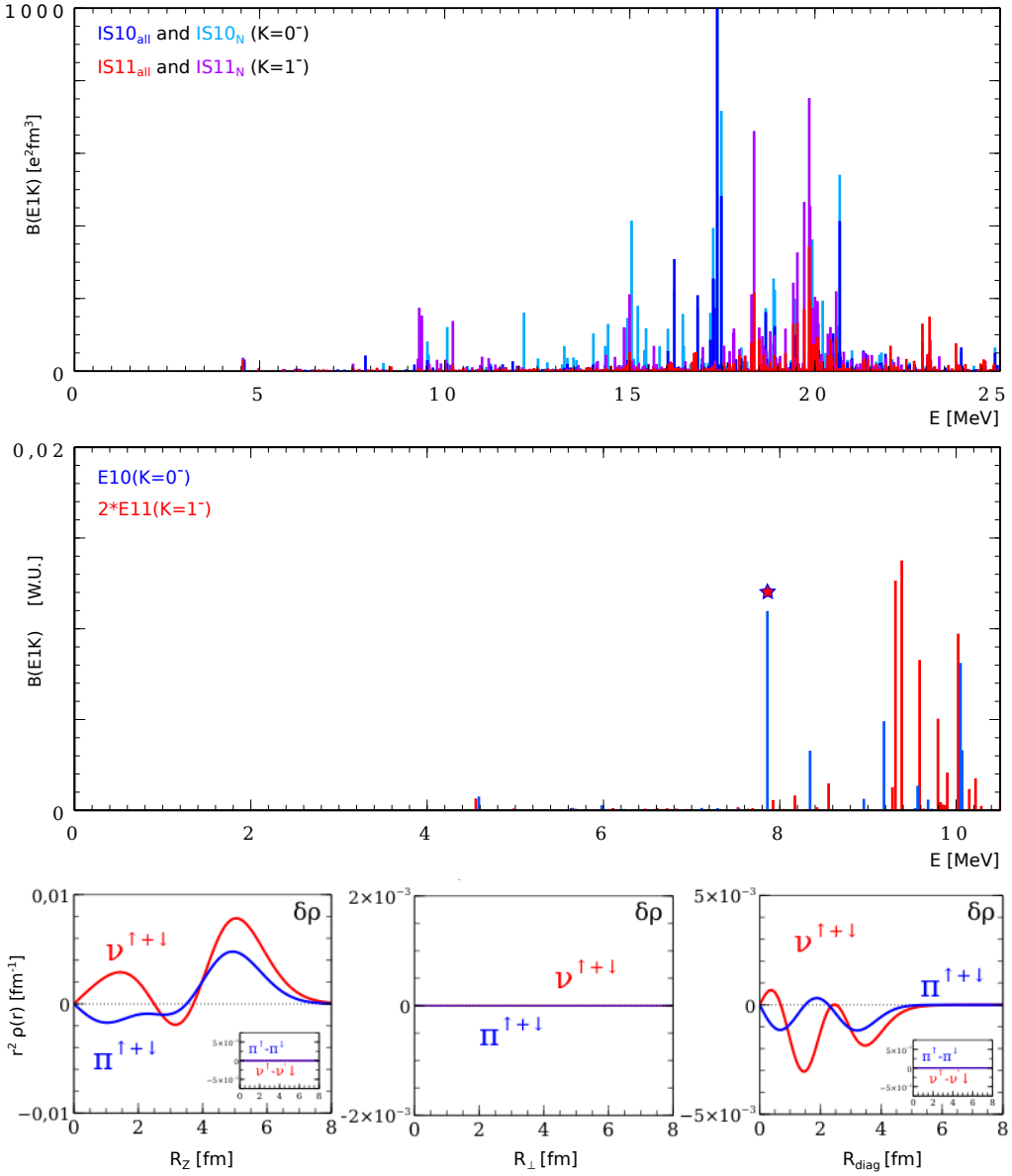

Figure 5.18 – B(E1) distributions of ^{80}Ge from microscopic calculations. Different color corespond to different angular momentum component in the symmetry axis. Top: up to 25 MeV. Middle: up to 10 MeV. Bottom: density function of neutron and proton in symmetry, vertical direction relative to symmetry axis and radii direction of 7.8 MeV state.

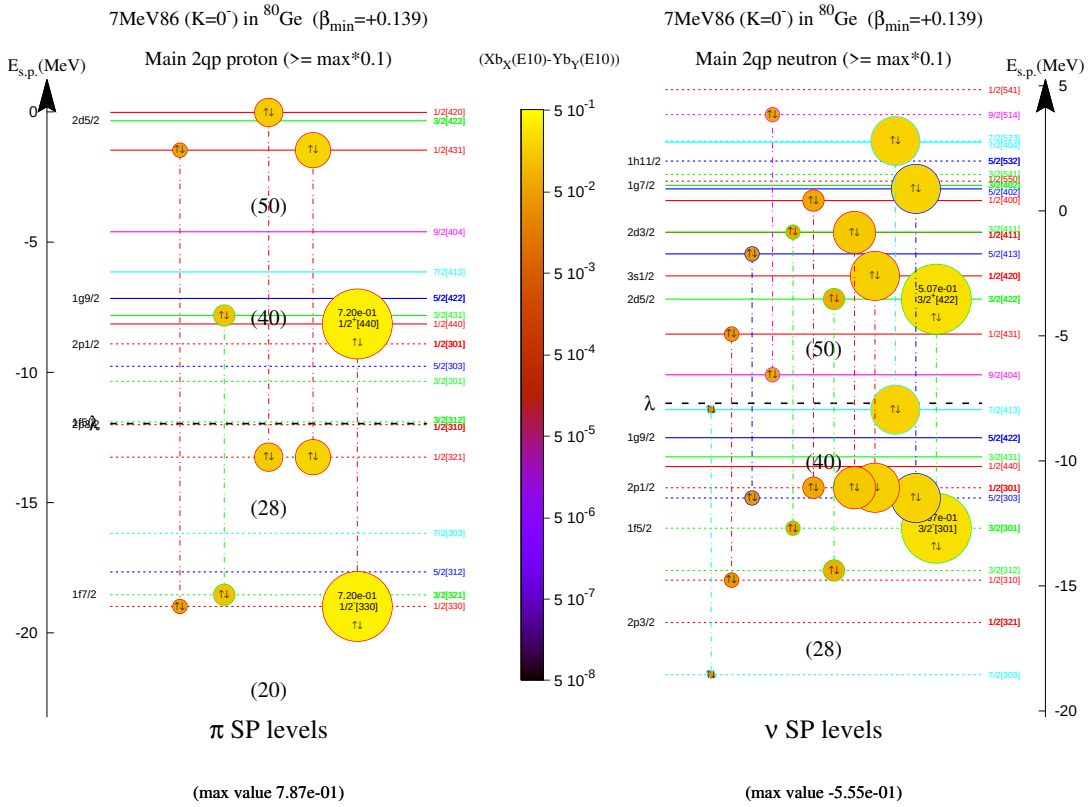

Figure 5.19 – Main 2qp excitations components of 7.8 MeV state in QRPA calculation.

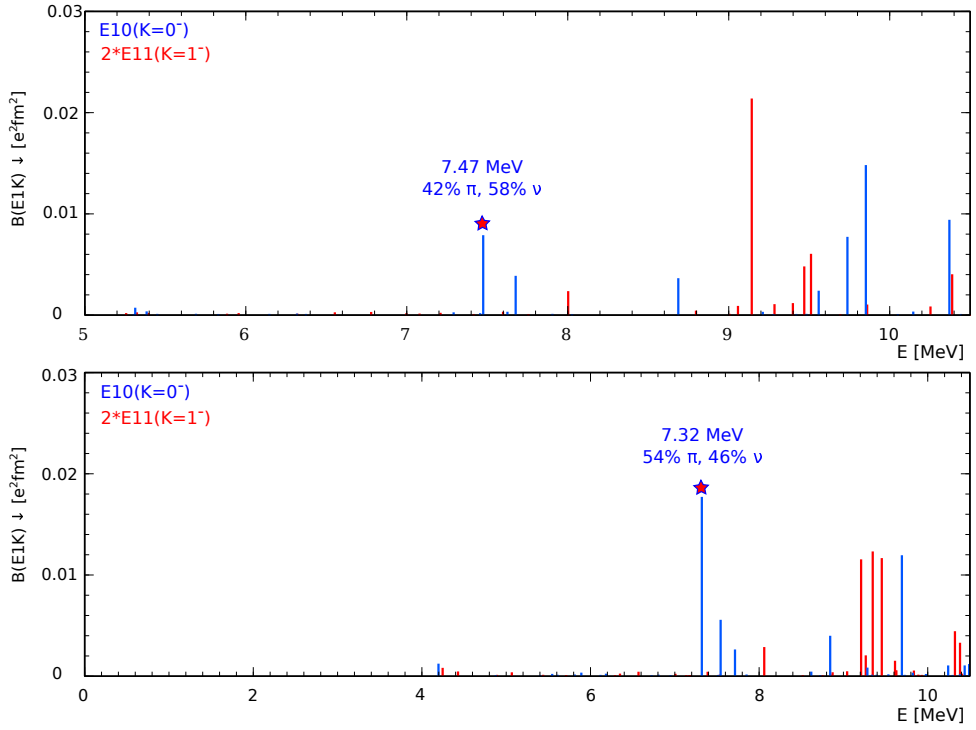

Figure 5.20 – B(E1) distributions of ^{80}Ge from microscopic QRPA* calculations. Up: block 7/2↑ 3/2↓ in proton. Bottom: 5/2↑ 1/2↓ in proton.

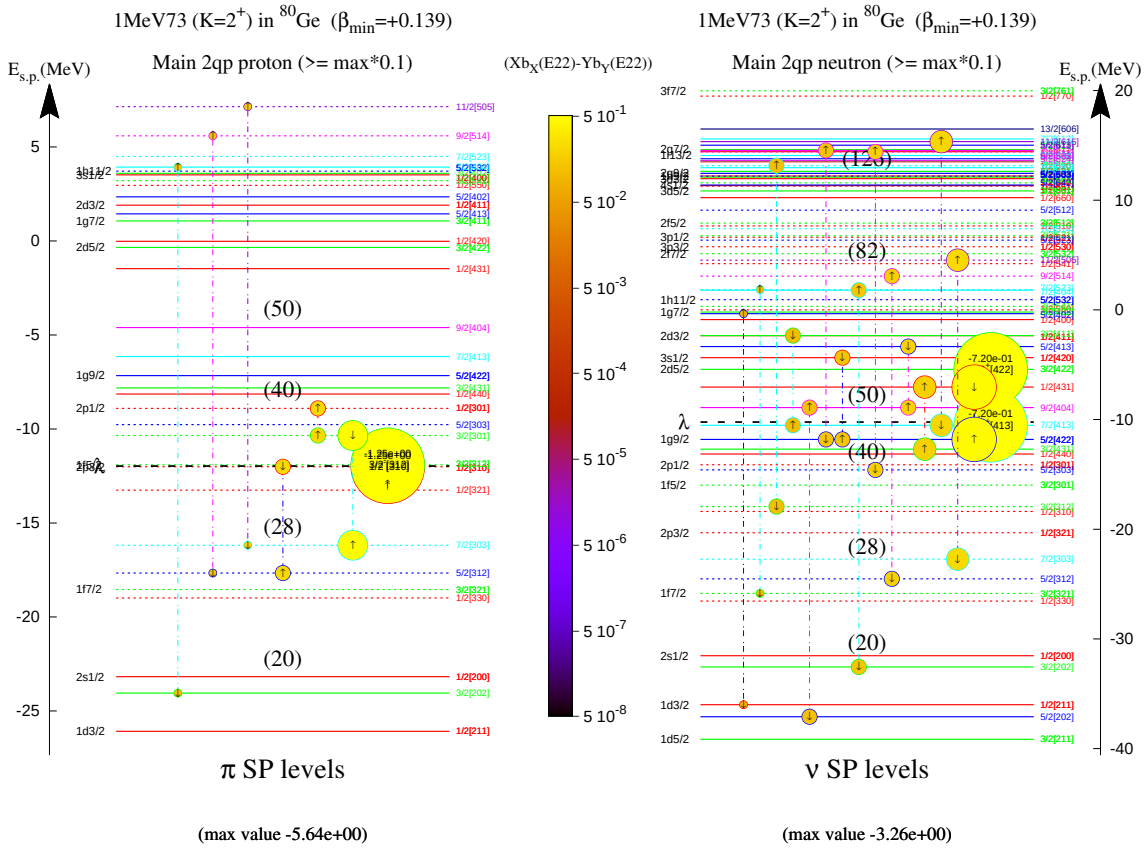

Figure 5.21 – Components of 1.73 MeV 2^+ state in QRPA calculation.

The nature of this state can be analysed when looking to the main 2qp excitations, in the first order of magnitude of 2qp E1 strength. Each of these 2qp is represented by circles that are connected. The size and the color of the circles gives the magnitude of their E1 contribution as shown in Figures 5.19 and 5.20. We can see that many 2qp excitations are involved, indicating a rather collective origin instead of 1p1h state, which illustrates the microscopic mechanism of the 7.8 MeV PDR state observed in this thesis.

6 Conclusions and outlook

Sommaire

1 Conclusions

In order to improve the understanding of the structure in the neutron threshold (S_n) region of exotic nuclei and the influence of this structure on the B(GT), a mixed $^{80g+m}$Ga source was collected at the BEDO decay station of the ALTO Isotope Separation On Line facility in Orsay. The ^{80g}Ga and ^{80m} Ga β-decaying states having spin-parity 6^- and 3^- respectively, this source has the advantage that it can populate an unusually large spin-range of daughter states in the nucleus ^{80}Ge. To achieve the goals of this thesis, a hybrid γ spectrometer composed of PARIS ($NaI/LaBr_3$) phoswich detectors associated to high resolution Ge detectors was used. A detailed data analysis is presented in this manuscript.

The conclusions of this thesis covers three aspects: manifestation of PDR in ^{80}Ge, separated decay level schemes of ground state ^{80g}Ga and isomeric state ^{80m}Ga and precisely determined B(GT) in the whole Q_β window.

Manifestation of PDR in ^{80}Ge

In this manuscript, I have here presented the first experimental search of a medium-spin pygmy dipole resonance built on quadrupole collectivity in the neutron-rich ^{80}Ge nucleus using β-decay technique, which extends PDR border along spin dimension. Pure beam and background-free spectrum technique make the extracted data including logft and B(GT) independent of simulation data and any theoretical hypothesis. Evidence is found for the presence of sizeable strength energetically located below the GDR and centered at 7.8 MeV. This structure is more sensitive to the probe species. Our results support that the decay of PDR states is not the inverse reaction to its excitation by photons. This result is in rather good agreement with theoretical calculations using nucleons-blocked HFB+QRPA method and, typically, provides evidence for the incompleteness of polarizability measured by current experiments as it dependents on selected reactions. The present result for new structure of pygmy dipole resonance opens interesting future perspectives with other medium-spin neutron-rich nuclei β-decay and further instrumentation for parity measurement such as POLAREX at ALTO.

Separated decay level schemes of ^{80g}Ga and ^{80m}Ga

For ^{80g}Ga, a total of 70 β-delayed γ transitions are assigned to the precusor nucleus ^{80g}Ga as reported in Tables 4.1 and 4.2. Among them, 30 γ-rays are observed for the first time. For each γ-line, information of energy (E_γ), absolute intensity (I_γ^{abs}), relative intensity (I_γ^{rel}), activity half-life ($T_{1/2}(activity)$) are extracted. Totally, 45 excited states populated are placed in the β-decay level scheme of ^{80g}Ga as shown in Figures 4.17 and 4.18. Twenty one states are reported for the first time. For each state, information of energy (E_{state}), absolute β-feeding intensity (I_β), logft, "X", and spin-parity (J^π) are extracted.

For ^{80m}Ga, totally, there are 65 γ-rays recorded in this work, in which 38 are detected and reported for the first time. For each γ-line, the same information as in ^{80g}Ga are extracted. As presented in Figures 4.19 and 4.20, 48 of excited states of ^{80}Ge were populated by ^{80m}Ga β-decay and 34 of these states are proposed for the first time (with red color) in current work. Of the 34 new states, 26 are located interestingly above 4 MeV. It means the I_β of low-lying states were overweighted in previous

work, which was caused by the so-called Pandemonium effect.

Precisely determined B(GT)

In this work, for ^{80g}Ga, a total of (79.1±2.5)% I_β up to 6.5 MeV was obtained. For ^{80m}Ga, (85.3±3.6)% was achieved up to 8 MeV. The unobserved states contribute to the missing parts. When compared with previous work, the I_β values were overweighted in the low-energy region and downweighted in the high-energy region. It was caused by the so-called pandemonium effect, the missing of unobserved high-energy γ-ray.

Figure 5.11 presents the experimental B(GT) strength distribution up to S_n (8.08 MeV). Most newly discovered data in this theis concentrates on the energy region of 4.5-8 MeV. In addition, two new measured states at S_n region by PARIS have very larger B(GT) than others due to the rapid decrease of phase space even though the I_β is not very large. Figure 5.12 shows the cumulative B(GT). The total Gamow-Teller strength to states within this energy window is measured to be 0.071(3) for ^{80}Ga and 0.150(8) for ^{80m}Ga. In the case of B(GT) comparison of ^{80g}Ga between this work and P. Hoff [142], the cumulative B(GT) relatively keep coincidence before 5.5 MeV peculiarly for the tendency. However, the acumulated B(GT) of this work continue to rise rapidly from 5.5 to 6.5 MeV when these data was unobserved in the previous work. For ^{80m}Ga, the B(GT) difference was enhanced from 4.2 MeV to 6 MeV and then was strengthened obviously from 6 MeV to 8 MeV. In the end, the cumulative B(GT) value of this work is four times of P. Hoff's as shown in the Figure 5.12 down.

2 Outlook

Searching for γ band in ^{80}Ge

Triaxial deformation has been a subject of much interest in the study of nuclear structure especially in the region with magic number, which challenges the traditional knowledge: spherical symmetry performance in closed shell nuclei (from shell model) and demonstrates the fundamental role of collective motion in nuclei. This mechanism was interpreted as quantum mechanical self-organization. Low-lying structures of Ge isotopes have attracted many experimental and theoretical endeavors. Experimental evidence of triaxial deformation (axial asymmetry) in ^{72,74,76,78}Ge has been found [38, 39, 40]. However, insufficient experimental evidence can be discovered to distinguish between a γ-soft or γ-rigid asymmetry (remains elusive). Now, a increasingly intense debate concentrates on the shape evolution of Ge isotopes as weather $^{80,82}Ge_{48,50}$ remains triaxiality and γ-soft or opposite as publication [41]: ^{74}Ge from soft to rigid triaxiality toward closed shell N=50? Taking advantages of high detection efficiency and angular correlation measurement ability of new generation γ detectors array like recent launched AGATA in INFN(Legnaro) or GRETA in Argonne coupled with mass spectrometer like PRISMA make it be possible to observe γ-band in ^{80,82}Ge including spin-parity measurement using deep inelastic scattering. This kind of experiment will shine a light on the nuclear collective motion in N=50 closed shell.

Investigate Pandemonium effect in ^{80}Ga β-decay study via TAS technique

Hitherto, the debate about the existence of real Pandemonium effect still continues between those who believe that 100% I_β is never available for high resolution γ-ray specstoscopy (HRS) method due to Pandemonium effect, many γ-rays de-excite from weak states (especially states above S_n) hide in background in γ spectrum, and those who believe that one can achieve 100% I_β if the statistic is enough through HRS technique. The former got supports (evidences) from recent TAS results that β-feeding branch ratio, I_β, of low-energy states were overweighted due to lack of indirect high-energy γ-feeding to these states in mostly previous β-decay study. The latter receives confidence from the knowledge that the states in nuclei are totally discrete even above S_n.

In the case of ^{80}Ga in this thesis, for ^{80g}Ga, a total of (79.1±2.5)% I_β up to 6.5 MeV was obtained. For ^{80m}Ga, (85.3±3.6)% was achieved up to 8 MeV. The contributors for the missing parts could be next two or one of them: insufficient statistic and "real" Pandemonium effect.

Therefore, based on the already existing data and research method accumulated in this thesis, ^{80}Ga could be a good candidate for investigating real Pandemonium effect and its caused percentage in the missing I_β in the close future. The method is to make a comparison between HRS technique with sufficient statistic, increasing beam time from 13h to one week and enhancing detection efficiency with more HPGe detectors and PARIS clusters, and TAS technique.

A Résumé en Français

Sommaire

1 Présentation et motivations

Le noyau atomique a été découvert en 1911 par Ernest Rutherford grâce à l'expérience de la feuille d'or de Geiger-Marsden en 1909 [1]. En tant que système fini auto-organisé à plusieurs corps, il présente à la fois des excitations microscopiques à une seule particule et macroscopiques collectives. Ces deux visions constituent les deux facettes d'un même objet qui peuvent être conciliées à travers des théories microscopiques grâce aux récents développements théoriques [2, 3, 4]. Les degrés de liberté d'une seule particule se manifestent par une structure en couches [5, 6] fournissant une interprétation de l'observation des nombres magiques tandis que les degrés de liberté collectifs sont en général associés à la vibration et/ou à la rotation de diverses formes nucléaires [7, 8, 9, 10, 11] fournissant l'interprétation de l'observation de la spectroscopie de bandes rotationnelles.

Le but de ce chapitre est de fournir une revue générale de la théorie de la désintégration β et des défis existants dans la compréhension du processus de désintégration nucléaire β, comme le montre la figure *A*.1. La structure de la distribution de force β et son implication pour l'étude nucléaire sont également introduites. De plus, l'évolution de structure le long de la chaîne isotonique N=50 vers le noyau doublement magique difficile à atteindre ^{78}Ni est introduite. Dans cette introduction, nous introduisons les concepts derrière le modèle en couches nucléaire tels que présentés dans la Fig. *A*.2, le modèle collectif et la force nucléaire. Des résultats expérimentaux obtenus au cours des dernières décennies dans ces régions exotiques sont également présentés. Le débat existant concernant l'évolution de la collectivité dans les isotopes Ge riches en neutrons vers N=50 est également introduit dans ce chapitre. Cette découverte pourrait fournir un début de solution à la question ouverte de l'épaisseur de la peau des neutrons de ^{208}Pb.

Des résultats expérimentaux récents sur une compétition γ/neutron exceptionnellement forte après une désintégration β dans les noyaux de Ge riches en neutrons ont été interprétés comme une manifestation possible des effets de la résonance dipolaire pygmée (PDR). La possibilité d'utiliser la désintégration β comme sonde supplémentaire (complémentaire) pour étudier les états collectifs de haute altitude dans les noyaux exotiques est présentée ici.

Enfin, trois nouveaux paysages expérimentaux d'étude de la désintégration β sont introduits : la spectroscopie de désintégration assistée par piège, TAGS et PARIS.

2 Production de faisceaux d'ions radioactifs à ALTO et montage expérimental

L'exploitation de faisceaux de noyaux exotiques est la nouvelle direction de la science nucléaire et, sûrement, une condition préalable à la recherche des caractéristiques fondamentales de ces noyaux exotiques. Le développement de nouvelles techniques a permis de rendre accessible expérimentalement des noyaux de plus en plus exotiques, ce qui offre la possibilité de comprendre la structure des noyaux exotiques présentant de nouveaux phénomènes non observés dans les noyaux stables. Proche de la limite d'existence neutron, ces phénomènes sont déclenchés par la forte asymétrie des isospins ou leur faible énergie de liaison. Ce chapitre présentera les méthodes de production du faisceau d'ions radioactifs, ^{80}Ga à ALTO France, y compris la photo-fission, la source d'ions et les techniques utilisées

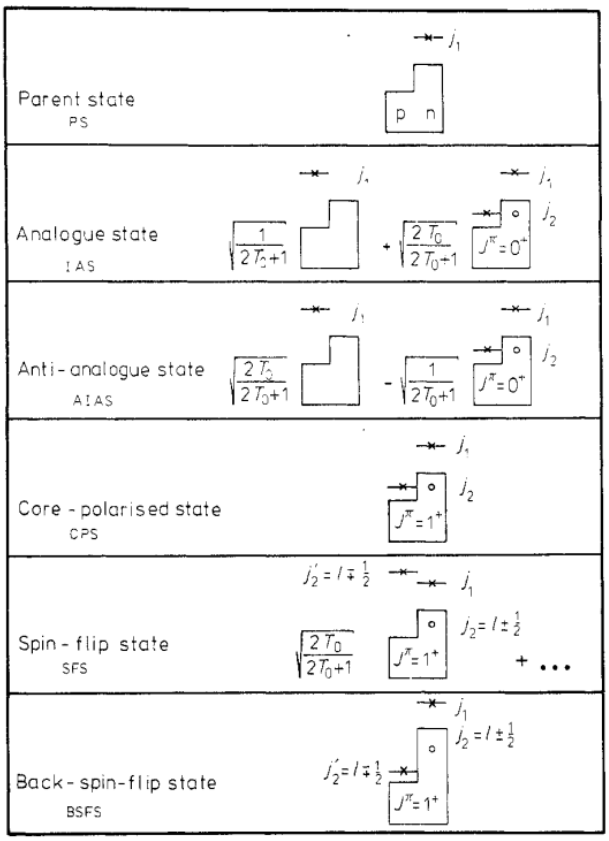

Figure A.1 – Les configurations qui épuisent la force β dans la décroissance β Gamow-Teller : états anti-analogue isobarique, états spin-flip, états back-spin-flip et états de cœur polarisé. Ces états épuisent également la force M1 γ dans la décroissance γ de l'état isobarique analogue (IAS) qui est peuplé par la transition β de Fermi supperallowed [12].

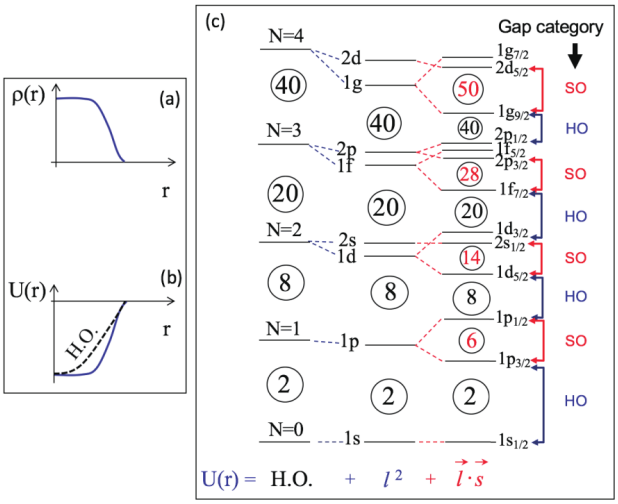

Figure A.2 – (a) distribution de la densité des nucléons dans les noyaux ; (b) un potentiel moyen (ligne pleine) et une approximation par un potentiel d'oscillateur harmonique (ligne pointillée). (c) La structure en couches avec des nombres magiques : voir les détails dans [25].

dans la séparation en ligne des isotopes.

La spectroscopie γ-retardée β de ^{80}Ge a été réalisée en profitant de la présence de PARIS à ALTO en juillet 2019 aux côtés de la spectroscopie γ-retardée β de ^{80,82,83,84}Ge avec un temps de faisceau 10.03h, 4.90h, 39.03h, 15.52h respectivement. Cette recherche est une étude en série des isotopes du gallium dans BEDO (étude de la désintégration BEta à Orsay). Ce programme vise à étudier la structure nucléaire de la région des isotopes riches en neutrons, au voisinage de ^{78}Ni.

BEDO est un dispositif expérimental à bande mobile de pointe actuellement exploité à ALTO, qui offre la possibilité de construire un système de détection plus complexe avec un faisceau radioactif offert par l'achèvement d'une nouvelle section de ligne de faisceau secondaire à ALTO. BEDO est dédié aux études de structure nucléaire après désintégration β des produits de fission riches en neutrons produits à ALTO. La trajectoire de la bande dans BEDO est définie pour maximiser l'espace disponible autour du point de collection du faisceau, idéalement 4π, permettant le positionnement le plus proche des différents types de détecteurs pour atteindre l'efficacité maximale. Le châssis de support mécanique a également été conçu pour accueillir divers ensembles détecteurs : le point de collection du faisceau est entouré d'un scintillateur cylindrique en plastique pour la détection β comme déclencheur d'un événement de désintégration β, 2 HPGe et 3 clusters PARIS comprenant 27 détecteurs phoswitch $LaBr_3$ + NaI pour une prise de temps rapide et une mesure des rayons γ à haute énergie. Dans cet assemblage hybride, les HPGe étaient utilisés pour maintenir une très grande résolution dans la gamme 0 à 6 MeV pour supprimer la contamination des descendants, et PARIS était pour la région de désintégration des précurseurs purs de 6 à 10 MeV. Les réglages permettant de couvrir la fenêtre Q_β entière visent à extraire les informations détaillées des états excités et à traiter simultanément l'effet Pandémonium.

3 Analyse des données expérimentales

Le système d'acquisition de données FASTER (FASTER DAQ) enregistre tous les signaux sur chaque canal indépendamment dans un mode sans déclenchement. Les événements reçoivent un horodatage et sont enregistrés dans l'ordre chronologique dans le format spécifique du système FASTER. Étant donné que l'analyse des données a été effectuée à l'aide du logiciel ROOT, les données générées par le FASTER DAQ au format FASTER ont été converties au format ROOT pour un traitement ultérieur. Les données ont été stockées dans les arbres ROOT (TTree) et chacun a plusieurs branches contenant des informations spécifiques comme deux valeurs ADC avec le temps d'intégration du signal long et court, le temps, l'étiquette (identification du détecteur). Le type de données de chaque branche a été déclaré en fonction de la taille des informations qu'elle contenait, ce qui a permis d'optimiser la taille des données en compressant chaque branche indépendamment. En particulier, les branches pourraient être lues indépendamment les unes des autres selon les besoins de l'utilisateur. L'analyse des données a été séparée en deux étapes : 1. Reconstruction des événements physiques (alignement temporel des détecteurs, étalonnage énergétique et coïncidence avec les particules β). 2. Trier et organiser davantage les données en fonction des relations entre les événements physiques, y compris la construction de diverses matrices de coïncidences, l'application de procédures d'*AddBack* pour le CLOVER et de PARIS, etc.

La première étape de l'analyse des données est la construction d'événements physiques à partir de données brutes. Un événement sera considéré comme physique s'il provient de la désintégration β d'un noyau. Ainsi, les événements considérés sont les particules β, les rayons γ et les neutrons. Au cours de ce processus, le temps de référence (temps d'horloge zéro) adopté est le signal du détecteur β considérant que la particule β est le signal de désintégration β et la réponse rapide du scintillateur (inférieur à la ns). Une longueur de fenêtre de 500 ns a été adoptée pour la construction d'événements afin d'éviter de perdre des données pertinentes (puisqu'au moins un état excité de ^{80}Ge est déjà connu pour être un isomère ns). Comme dit précédemment, un événement physique est considéré comme provenant de la désintégration bêta d'un noyau collecté sur la bande, cela signifie qu'il faut considérer une condition supplémentaire liée au cycle de la bande : avec le ^{80}Ga, la particule β doit être détectée dans une fenêtre temporelle correspondant à la durée de collecte du faisceau + 10 s.

La deuxième étape consiste à construire des relations de coïncidence entre événements physiques comme le remplissage de matrices γ-γ (HPGe-HPGe, HPGe-$LaBr_3$, HPGe-$LaBr_3$(cluster addback), HPGe-$LaBr_3$(addback all), HPGe-$LaBr_3$+NaI, All-All et ainsi de suite), clover, PARIS addback et timing rapide et ainsi de suite. Dans cette étape, la fenêtre temporelle pour la coïncidence γ-γ a été fixée à 50 ns, ce qui est suffisant compte tenu de la résolution temporelle des détecteurs telle qu'introduite dans la section de configuration expérimentale.

Dans les deux sous-sections suivantes, la procédure d'analyse des données est décrite en détail. Dans un premier temps, je détaille toutes les corrections des procédures d'étalonnage appliquées aux données brutes. Dans la deuxième partie, je détaille la procédure d'analyse et les principales informations qui en sont extraites en mettant l'accent sur la détermination de la durée de vie de ^{80g}Ga et ^{80m}Ga et la détermination des durées de vie individuelles des deux états isomériques.

4 Résultats expérimentaux pour $^{80g+m}$Ga étude de la désintégration β

Afin d'améliorer la compréhension de la structure dans la région du seuil d'émission neutron (S_n) des noyaux exotiques et l'influence de cette structure sur le B(GT), une source mixte $^{80g+m}$Ga a été collectée à la station de désintégration BEDO de l'installation ALTO Isotope Separation On Line à Orsay. Les états ^{80g}Ga et ^{80m} Ga ayant respectivement une parité de spin de 6^- et 3^-, cette source a l'avantage de pouvoir remplir un plage de spin inhabituellement large des états fils dans le noyau ^{80}Ge. Pour atteindre les objectifs de cette thèse, un spectromètre hybride γ composé de détecteurs phoswich PARIS (NaI/$LaBr_3$) associés à des détecteurs Ge haute résolution a été utilisé. Une analyse détaillée des données est présentée dans ce manuscrit.

Les résultats de cette thèse couvrent trois aspects : la manifestation de la RDP dans ^{80}Ge, les schémas de niveau de décroissance séparés de l'état fondamental ^{80g}Ga et l'état isomérique ^{80m}Ga et la distribution de B(GT) déterminée avec précision toute la fenêtre Q_β.

Manifestation of PDR in ^{80}Ge

Dans ce manuscrit, j'ai présenté ici la première recherche expérimentale d'une résonance dipolaire pygmée à spin moyen construite sur une collectivité quadripolaire dans le noyau ^{80}Ge riche en neutrons en utilisant la technique de désintégration β, qui étend la frontière de la PDR le long de la dimension de spin. La technique du faisceau pur et du spectre sans fond rend les données extraites, y compris logft et B(GT), indépendantes des données de simulation et de toute hypothèse théorique. Des preuves sont trouvées pour la présence d'une force importante située énergétiquement sous la GDR et centrée à 7,8 MeV. Cette structure est plus sensible à la sonde utilisée. Nos résultats confirment que la décroissance des états PDR n'est pas la réaction inverse à son excitation par des photons. Ce résultat est en assez bon accord avec les calculs théoriques utilisant la méthode HFB + QRPA bloquée par les nucléons et, généralement, fournit la preuve de l'incomplétude de la polarisabilité mesurée par les expériences actuelles car elle dépend des réactions sélectionnées. Le présent résultat d'une nouvelle structure de résonance dipolaire pygmée ouvre des perspectives futures intéressantes avec d'autres noyaux à spin moyen riches en neutrons par décroissance β et d'autres instruments pour la mesure de la parité tels que POLAREX à ALTO.

Separated decay level schemes of ^{80g}Ga and ^{80m}Ga

Pour ^{80g}Ga, un total de 70 transitions γ retardées β sont attribuées au noyau précurseur ^{80g}Ga, comme indiqué dans les tableaux 4.1 et 4.2. Parmi eux, 30 raies γ sont observées pour la première fois. Pour chaque raie γ, information d'énergie (E_γ), intensité absolue (I_γ^{abs}), intensité relative (I_γ^{rel}), la demi-vie d'activité ($T_{1/2}(activité)$) sont extraites. Au total, 45 états excités peuplés sont placés dans le schéma de niveau de désintégration β de ^{80g}Ga, comme illustré dans les figures 4.17 et 4.18. Vingt et un États sont observés pour la première fois. Pour chaque état, informations sur l'énergie (E_{state}), l'intensité d'alimentation β absolue (I_β), logft, "X" et le spin-parité (J^π) sont extraits.

Pour ^{80m}Ga, au total, il y a 65 raies γ enregistrées dans ce travail, dont 38 sont observées pour la première fois. Pour chaque ligne γ, les mêmes informations que dans ^{80g}Ga sont extraites. Comme présenté dans les figures 4.19 et 4.20, 48 des états excités de ^{80}Ge ont été peuplés par ^{80m}Ga β -decay et 34 de ces états sont proposés pour la première fois (avec la couleur rouge) dans les travaux présentés ici. Sur les 34 nouveaux états, 26 sont situés de manière intéressante au-dessus de 4 MeV. Cela signifie que les I_β des états de faible altitude étaient surpondérés dans les travaux précédents, ce qui était causé par ce que l'on appelle l'effet Pandémonium.

5 Débat

Dans ce travail, pour ^{80g}Ga, un total de (79.1±2.5)% de la force β jusqu'à 6.5 MeV a été observée. Pour ^{80m}Ga, (85,3±3,6)% a été atteint jusqu'à 8 MeV. Les états non observés contribuent aux parties manquantes. Par rapport aux travaux antérieurs, les valeurs I_β étaient surpondérées dans la région à basse énergie et sous-pondérées dans la région à haute énergie. Cela a été causé par ce qu'on appelle l'effet pandémonium, l'absence de rayons γ de haute énergie non observés.

La figure 5.11 présente la distribution expérimentale de la force B(GT) jusqu'à S_n (8,08 MeV). La

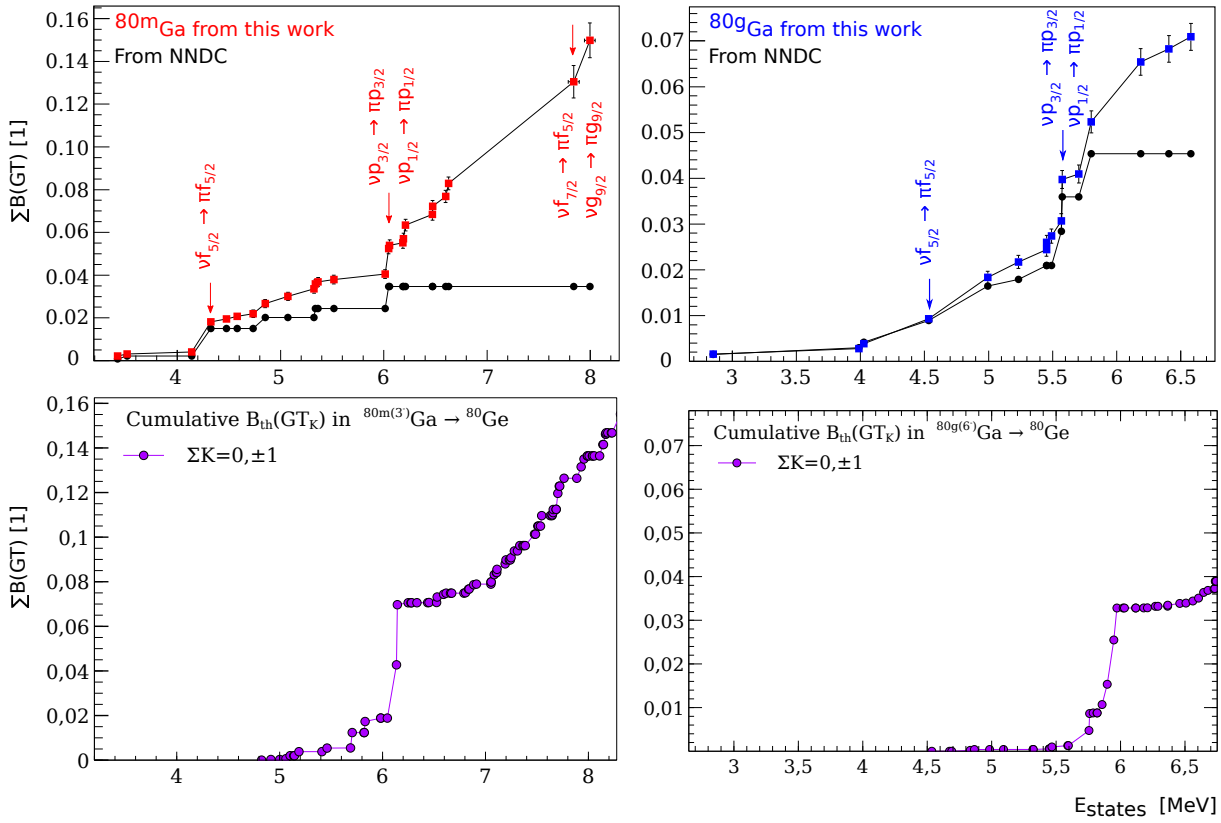

Figure A.3 – B(GT) cumulé avec des incertitudes statistiques de $^{80g+m}$Ga par rapport à l'énergie d'excitation des états finaux dans ^{80}Ge. Aux fins de comparaison, les résultats précédents ont été divisés et présentés séparément. Les deux du haut présentent les mesures expérimentales. Et les deux du bas sont obtenues à partir de calculs microscopiques HFB + QRPA.

plupart des données récemment découvertes dans cette thèse se concentrent sur la région d'énergie de 4,5 à 8 MeV. De plus, deux nouveaux états mesurés dans la région S_n par PARIS ont un B(GT) très plus grand que les autres en raison de la diminution rapide de l'espace des phases même si le I_β n'est pas très grand. La figure 5.12 montre le B(GT) cumulé. La force totale de Gamow-Teller aux états dans cette fenêtre d'énergie est mesurée à 0,071(3) pour ^{80}Ga et 0,150(8) pour ^{80m}Ga. Dans le cas de la comparaison B(GT) de ^{80g}Ga entre ce travail et P. Hoff [142], les B(GT) cumulés conservent relativement une coïncidence avant 5,5 MeV particulièrement pour la tendance. Cependant, les B(GT) cumulés de ces travaux continuent d'augmenter rapidement de 5,5 à 6,5 MeV alors que ces données n'étaient pas observées dans les travaux précédents. Pour ^{80m}Ga, la différence B(GT) a été augmentée de 4,2 MeV à 6 MeV, puis a été renforcée évidemment de 6 MeV à 8 MeV. Au final, la valeur B(GT) cumulée de ce travail est quatre fois celle de P. Hoff comme le montre la figure 5.12 ci-dessous.

6 Conclusions et perspectives

Les conclusions de cette thèse couvrent trois aspects : la manifestation de la RDP dans ^{80}Ge, les schémas de niveau de décroissance séparés de l'état fondamental ^{80g}Ga et l'état isomérique ^{80m}Ga et

la distribution de B(GT) déterminée avec précision dans toute la fenêtre Q_β.

Dans la sous-section sur les perspectives, deux expériences sont proposées avec "la recherche de la bande γ dans ^{80}Ge" et "l'étude de l'effet pandémonium dans l'étude ^{80}Ga β-decay via la technique TAS "

Bibliography

[1] Ernest Rutherford. Lxxix. the scattering of α and β particles by matter and the structure of the atom. *The London, Edinburgh, and Dublin Philosophical Magazine and Journal of Science*, 21(125):669–688, 1911.

[2] Krishna Kumar. Intrinsic quadrupole moments and shapes of nuclear ground states and excited states. *Physical Review Letters*, 28(4):249, 1972.

[3] Thomas Schäfer. Fermi liquid theory: A brief survey in memory of gerald e. brown. *Nuclear Physics A*, 928:180–189, 2014.

[4] Takaharu Otsuka, Yusuke Tsunoda, Takashi Abe, Noritaka Shimizu, and Piet Van Duppen. Underlying structure of collective bands and self-organization in quantum systems. *Physical review letters*, 123(22):222502, 2019.

[5] Maria Goeppert Mayer. On closed shells in nuclei. ii. *Physical Review*, 75(12):1969, 1949.

[6] Otto Haxel, J Hans D Jensen, and Hans E Suess. On the" magic numbers" in nuclear structure. *Physical Review*, 75(11):1766, 1949.

[7] James Rainwater. Nuclear energy level argument for a spheroidal nuclear model. *Physical Review*, 79(3):432, 1950.

[8] A Bohr and BR Mottelson. *Nuclear Structure Benjamin*, volume 2. 1975.

[9] Aage Bohr. *The coupling of nuclear surface oscillations to the motion of individual nucleons*. Munksgaard, 1952.

[10] Aage Bohr and Ben R Mottelson. The original papers on the unified model. *K. Dan. Vidensk. Selsk. Mat. Fys. Medd*, 27:16, 1953.

[11] Aa Bohr and BR Mottelson. *Nuclear Structure vol. 1 WA Benjamin*. 1969.

[12] HV Klapdor and CO Wene. Structures in the beta strength function and consequences for nuclear physics and astrophysics. *Journal of Physics G: Nuclear Physics*, 6(9):1061, 1980.

[13] Benedetta Belfatto and Zurab Berezhiani. Are the ckm anomalies induced by vector-like quarks? limits from flavor changing and standard model precision tests. *arXiv preprint arXiv:2103.05549*, 2021.

[14] GC Branco, JT Penedo, Pedro MF Pereira, MN Rebelo, and JI Silva-Marcos. Addressing the ckm unitarity problem with a vector-like up quark. *arXiv preprint arXiv:2103.13409*, 2021.

[15] P Gysbers, Gaute Hagen, JD Holt, Gustav R Jansen, Titus D Morris, P Navrátil, T Papenbrock, S Quaglioni, A Schwenk, SR Stroberg, et al. Discrepancy between experimental and theoretical β-decay rates resolved from first principles. *Nature Physics*, 15(5):428–431, 2019.

[16] A Belley, CG Payne, SR Stroberg, T Miyagi, and JD Holt. Ab initio neutrinoless double-beta decay matrix elements for ca 48, ge 76, and se 82. *Physical Review Letters*, 126(4):042502, 2021.

[17] D Gambacurta, M Grasso, and J Engel. Gamow-teller strength in ca 48 and ni 78 with the charge-exchange subtracted second random-phase approximation. *Physical Review Letters*, 125(21):212501, 2020.

[18] YF Niu, ZM Niu, Gianluca Colo, Enrico Vigezzi, et al. Particle-vibration coupling effect on the β decay of magic nuclei. *Physical review letters*, 114(14):142501, 2015.

[19] Klaus Grotz and Hans Volker Klapdor. *The weak interaction in nuclear, particle and astrophysics*. CRC Press, 1990.

[20] JC Hardy and IS Towner. Superallowed 0+→ 0+ nuclear β decays: 2020 critical survey, with implications for v ud and ckm unitarity. *Physical Review C*, 102(4):045501, 2020.

[21] Balraj Singh, JL Rodriguez, SSM Wong, and JK Tuli. Review of logftvalues in β decay. *Nuclear Data Sheets*, 84(3):487–563, 1998.

[22] T Wakasa, H Sakai, H Okamura, H Otsu, S Fujita, S Ishida, N Sakamoto, T Uesaka, Y Satou, MB Greenfield, et al. Gamow-teller strength of 90 nb in the continuum studied via multipole decomposition analysis of the 90 zr (p, n) reaction at 295 mev. *Physical Review C*, 55(6):2909, 1997.

[23] AL Nichols. Nuclear data requirements for decay heat calculations. In *Lectures given at the Workshop on Nuclear Reaction Data and Nuclear Reactors: Physics, Design and Safety, Trieste, Italy*, volume 25, 2002.

[24] Y Abgrall, G Baron, E Caurier, and G Monsonego. The 8 particle-8 hole rotational band in 16o. *Physics Letters B*, 26(2):53–55, 1967.

[25] Takaharu Otsuka. Emerging concepts in nuclear structure based on the shell model. *arXiv preprint arXiv:2201.05443*, 2022.

[26] Aage Niels Bohr and Benjamin Roy Mottelson. Collective and individual-particle aspects of nuclear structure. *Dan. Mat. Fys. Medd.*, 27(CERN-57-38):1–174, 1953.

[27] Aage Niels Bohr and Ben R Mottelson. *Nuclear Structure (In 2 Volumes)*. World Scientific Publishing Company, 1998.

[28] Sven Gösta Nilsson. Binding states of individual nucleons in strongly deformed nuclei. *Dan. Mat. Fys. Medd.*, 29(CERN-55-30):1–69, 1955.

[29] Chen-Ning Yang and Robert L Mills. Conservation of isotopic spin and isotopic gauge invariance. *Physical review*, 96(1):191, 1954.

[30] Ian Johnston Rhind Aitchison and Anthony JG Hey. *Gauge theories in particle physics, Volume II: QCD and the Electroweak Theory*. CRC Press, 2003.

[31] Norbert Kaiser, R Brockmann, and Wolfram Weise. Peripheral nucleon-nucleon phase shifts and chiral symmetry. *Nuclear Physics A*, 625(4):758–788, 1997.

[32] E Epelbaoum, Walter Gloeckle, and Ulf-G Meißner. Nuclear forces from chiral lagrangians using the method of unitary transformation (i): Formalism. *Nuclear Physics A*, 637(1):107–134, 1998.

[33] Evgeny Epelbaum, H-W Hammer, and Ulf-G Meißner. Modern theory of nuclear forces. *Reviews of Modern Physics*, 81(4):1773, 2009.

[34] K Alder and RM Steffen. The electromagnetic interaction in nuclear spectroscopy ed wd hamilton, 1975.

[35] O Sorlin and M-G Porquet. Nuclear magic numbers: New features far from stability. *Progress in Particle and Nuclear Physics*, 61(2):602–673, 2008.

[36] Meng Wang, WJ Huang, FG Kondev, G Audi, and S Naimi. The ame 2020 atomic mass evaluation (ii). tables, graphs and references. *Chinese Physics C*, 45(3):030003, 2021.

[37] K Sieja and F Nowacki. Shell quenching in ni 78: A hint from the structure of neutron-rich copper isotopes. *Physical Review C*, 81(6):061303, 2010.

[38] AD Ayangeakaa, RVF Janssens, CY Wu, JM Allmond, JL Wood, S Zhu, M Albers, S Almaraz-Calderon, B Bucher, MP Carpenter, et al. Shape coexistence and the role of axial asymmetry in 72ge. *Physics Letters B*, 754:254–259, 2016.

[39] AD Ayangeakaa, RVF Janssens, S Zhu, D Little, J Henderson, CY Wu, DJ Hartley, M Albers, K Auranen, B Bucher, et al. Evidence for rigid triaxial deformation in ge 76 from a model-independent analysis. *Physical review letters*, 123(10):102501, 2019.

[40] AM Forney, WB Walters, CJ Chiara, RVF Janssens, AD Ayangeakaa, J Sethi, J Harker, M Alcorta, MP Carpenter, G Gürdal, et al. Novel δ j= 1 sequence in ge 78: Possible evidence for triaxiality. *Physical review letters*, 120(21):212501, 2018.

[41] JJ Sun, Z Shi, XQ Li, H Hua, C Xu, QB Chen, SQ Zhang, CY Song, J Meng, XG Wu, et al. Spectroscopy of 74ge: From soft to rigid triaxiality. *Physics Letters B*, 734:308–313, 2014.

[42] D Verney, B Tastet, K Kolos, F Le Blanc, F Ibrahim, M Cheikh Mhamed, E Cottereau, PV Cuong, F Didierjean, G Duchene, et al. Structure of ge-80 revealed by the beta decay of isomeric states in ga-80: Triaxiality in the vicinity of ni-78. *Physical Review C*, 87(5), 2013.

[43] A Gottardo, D Verney, I Deloncle, S Péru, C Delafosse, S Roccia, I Matea, C Sotty, C Andreoiu, C Costache, et al. Unexpected high-energy γ emission from decaying exotic nuclei. *Physics Letters B*, 772:359–362, 2017.

[44] D Savran, T Aumann, and A Zilges. Experimental studies of the pygmy dipole resonance. *Progress in Particle and Nuclear Physics*, 70:210–245, 2013.

[45] Muhsin N Harakeh and Adriaan Woude. *Giant Resonances: fundamental high-frequency modes of nuclear excitation*, volume 24. Oxford University Press on Demand, 2001.

[46] Brendan T Reed, Farrukh J Fattoyev, Charles J Horowitz, and Jorge Piekarewicz. Implications of prex-2 on the equation of state of neutron-rich matter. *Physical Review Letters*, 126(17):172503, 2021.

[47] GA Bartholomew. Neutron capture gamma rays. *Annual review of nuclear science*, 11(1):259–302, 1961.

[48] Radhe Mohan, M Danos, and LC Biedenharn. Three-fluid hydrodynamical model of nuclei. *Physical Review C*, 3(5):1740, 1971.

[49] P-G Reinhard and Witold Nazarewicz. Information content of a new observable: The case of the nuclear neutron skin. *Physical Review C*, 81(5):051303, 2010.

[50] J Piekarewicz. Pygmy resonances and neutron skins. *Physical Review C*, 83(3):034319, 2011.

[51] A Klimkiewicz, Nils Paar, P Adrich, M Fallot, K Boretzky, T Aumann, D Cortina-Gil, U Datta Pramanik, Th W Elze, H Emling, et al. Nuclear symmetry energy and neutron skins derived from pygmy dipole resonances. *Physical Review C*, 76(5):051603, 2007.

[52] Stéphane Goriely. Radiative neutron captures by neutron-rich nuclei and the r-process nucleosynthesis. *Physics Letters B*, 436(1-2):10–18, 1998.

[53] Stéphane Goriely, Elias Khan, and Mathieu Samyn. Microscopic hfb+ qrpa predictions of dipole strength for astrophysics applications. *Nuclear Physics A*, 739(3-4):331–352, 2004.

[54] A Avdeenkov, Stéphane Goriely, S Kamerdzhiev, and S Krewald. Self-consistent calculations of the strength function and radiative neutron capture cross section for stable and unstable tin isotopes. *Physical Review C*, 83(6):064316, 2011.

[55] M Spieker, A Heusler, BA Brown, T Faestermann, R Hertenberger, G Potel, M Scheck, N Tsoneva, M Weinert, H-F Wirth, et al. Accessing the single-particle structure of the pygmy dipole resonance in pb 208. *Physical Review Letters*, 125(10):102503, 2020.

[56] A Bracco, EG Lanza, and A Tamii. Isoscalar and isovector dipole excitations: Nuclear properties from low-lying states and from the isovector giant dipole resonance. *Progress in Particle and Nuclear Physics*, 106:360–433, 2019.

[57] Nils Paar, Dario Vretenar, Elias Khan, and Gianluca Colo. Exotic modes of excitation in atomic nuclei far from stability. *Reports on Progress in Physics*, 70(5):691, 2007.

[58] J Endres, D Savran, AM Van den Berg, P Dendooven, M Fritzsche, MN Harakeh, J Hasper, HJ Wörtche, and A Zilges. Splitting of the pygmy dipole resonance in ba 138 and ce 140 observed in the (α, α γ) reaction. *Physical Review C*, 80(3):034302, 2009.

[59] D Savran, M Babilon, AM Van den Berg, MN Harakeh, J Hasper, A Matic, HJ Wörtche, and A Zilges. Nature of the pygmy dipole resonance in ce 140 studied in (α, α γ) experiments. *Physical review letters*, 97(17):172502, 2006.

[60] J Endres, E Litvinova, D Savran, PA Butler, MN Harakeh, S Harissopulos, R-D Herzberg, R Krücken, A Lagoyannis, N Pietralla, et al. Isospin character of the pygmy dipole resonance in sn 124. *Physical review letters*, 105(21):212503, 2010.

[61] Nils Paar, YF Niu, Dario Vretenar, and Jie Meng. Isoscalar and isovector splitting of pygmy dipole structures. *Physical review letters*, 103(3):032502, 2009.

[62] EG Lanza, A Vitturi, E Litvinova, and D Savran. Dipole excitations via isoscalar probes: The splitting of the pygmy dipole resonance in 124 sn. *Physical Review C*, 89(4):041601, 2014.

[63] CT Angell, SL Hammond, HJ Karwowski, JH Kelley, M Krtička, E Kwan, A Makinaga, and G Rusev. Evidence for radiative coupling of the pygmy dipole resonance to excited states. *Physical Review C*, 86(5):051302, 2012.

[64] Marcus Scheck, V Yu Ponomarev, T Aumann, J Beller, M Fritzsche, J Isaak, JH Kelley, E Kwan, N Pietralla, R Raut, et al. Decay pattern of the pygmy dipole resonance in 60 ni. *Physical Review C*, 87(5):051304, 2013.

[65] J Isaak, D Savran, M Krtička, MW Ahmed, J Beller, E Fiori, J Glorius, JH Kelley, B Löher, N Pietralla, et al. Constraining nuclear photon strength functions by the decay properties of photo-excited states. *Physics Letters B*, 727(4-5):361–365, 2013.

[66] B Löher, D Savran, T Aumann, J Beller, M Bhike, N Cooper, V Derya, M Duchêne, J Endres, A Hennig, et al. The decay pattern of the pygmy dipole resonance of 140ce. *Physics Letters B*, 756:72–76, 2016.

[67] A Tamii, I Poltoratska, P von Neumann-Cosel, Y Fujita, T Adachi, CA Bertulani, J Carter, M Dozono, H Fujita, K Fujita, et al. Complete electric dipole response and the neutron skin in pb 208. *Physical review letters*, 107(6):062502, 2011.

[68] Marcus Scheck, Stoyan Mishev, V Yu Ponomarev, R Chapman, LP Gaffney, ET Gregor, N Pietralla, Pietro Spagnoletti, D Savran, and GS Simpson. Investigating the pygmy dipole resonance using β decay. *Physical review letters*, 116(13):132501, 2016.

[69] V Yu Ponomarev, Ch Stoyanov, N Tsoneva, and M Grinberg. Boson forbidden low-energy e1-transitions in spherical nuclei. *Nuclear Physics A*, 635(4):470–483, 1998.

[70] Konstantin R Mashtakov, V Yu Ponomarev, Marcus Scheck, Sean W Finch, Johann Isaak, M Zweidinger, O Agar, C Bathia, T Beck, J Beller, et al. Structure of high-lying levels populated in the 96y→ 96zr β decay. *Physics Letters B*, page 136569, 2021.

[71] Danilo Gambacurta and Marcella Grasso. Quenching of gamow-teller strengths and two particle – two hole configurations. 2021.

[72] Haruki Kurasawa, Toshio Suzuki, and Nguyen Van Giai. Role of the dirac sea in the quenching of gamow-teller strength. *Physical review letters*, 91(6):062501, 2003.

[73] JL Tain, E Valencia, A Algora, J Agramunt, B Rubio, S Rice, W Gelletly, P Regan, A-A Zakari-Issoufou, Muriel Fallot, et al. Enhanced γ-ray emission from neutron unbound states populated in β decay. *Physical review letters*, 115(6):062502, 2015.

[74] Artemis Spyrou, Sean N Liddick, Farheen Naqvi, Benjamin P Crider, Alexander C Dombos, Darren L Bleuel, B Alex Brown, A Couture, L Crespo Campo, M Guttormsen, et al. Strong neutron-γ competition above the neutron threshold in the decay of co 70. *Physical review letters*, 117(14):142701, 2016.

[75] JC Hardy, LC Carraz, B Jonson, and PG Hansen. The essential decay of pandemonium: a demonstration of errors in complex beta-decay schemes. *Physics Letters B*, 71(2):307–310, 1977.

[76] D Verney, D Testov, F Ibrahim, Yu Penionzhkevich, B Roussière, V Smirnov, F Didierjean, K Flanagan, S Franchoo, E Kuznetsova, et al. Pygmy gamow-teller resonance in the n= 50 region: New evidence from staggering of β-delayed neutron-emission probabilities. *Physical Review C*, 95(5):054320, 2017.

[77] FJ Fattoyev, J Piekarewicz, and Charles J Horowitz. Neutron skins and neutron stars in the multimessenger era. *Physical Review Letters*, 120(17):172702, 2018.

[78] I Bombaci, A Drago, D Logoteta, G Pagliara, and I Vidana. Was gw190814 a black hole–strange quark star system? *Physical Review Letters*, 126(16):162702, 2021.

[79] DM Rossi, P Adrich, F Aksouh, H Alvarez-Pol, T Aumann, J Benlliure, M Böhmer, K Boretzky, E Casarejos, M Chartier, et al. Measurement of the dipole polarizability of the unstable neutron-rich nucleus ni 68. *Physical review letters*, 111(24):242503, 2013.

[80] E Margaret Burbidge, Geoffrey Ronald Burbidge, William A Fowler, and Fred Hoyle. Synthesis of the elements in stars. *Reviews of modern physics*, 29(4):547, 1957.

[81] Karlheinz Langanke and G Martinez-Pinedo. Nuclear weak-interaction processes in stars. *Reviews of Modern Physics*, 75(3):819, 2003.

[82] Y-Z Qian and GJ Wasserburg. Where, oh where has the r-process gone? *Physics Reports*, 442(1-6):237–268, 2007.

[83] S Rinta-Antila, T Eronen, V-V Elomaa, U Hager, J Hakala, A Jokinen, P Karvonen, H Penttilä, J Rissanen, T Sonoda, et al. Decay study of neutron-rich zirconium isotopes employing a penning trap as a spectroscopy tool. *The European Physical Journal A*, 31(1):1–7, 2007.

[84] P Delahaye, Bertram Blank, and S Sturm. Trap-assisted spectroscopy with rextrap. *Nuclear Instruments and Methods in Physics Research Section B: Beam Interactions with Materials and Atoms*, 266(19-20):4647–4651, 2008.

[85] Magdalena Kowalska, Sarah Naimi, J Agramunt, A Algora, D Beck, Bertram Blank, Klaus Blaum, Ch Böhm, Ch Borgmann, M Breitenfeldt, et al. Trap-assisted decay spectroscopy with isoltrap. *Nuclear Instruments and Methods in Physics Research Section A: Accelerators, Spectrometers, Detectors and Associated Equipment*, 689:102–107, 2012.

[86] C Weber, P Müller, and PG Thirolf. Developments in penning trap (mass) spectrometry at mll-trap: Towards in-trap decay spectroscopy. *International Journal of Mass Spectrometry*, 349:270–276, 2013.

[87] C Delafosse, A Goasduff, A Kankainen, D Verney, and et al. First trap-assisted decay spectroscopy of the 81ge ground state. *The European Physical Journal A*, 2022.

[88] E Valencia, JL Tain, A Algora, J Agramunt, E Estevez, MD Jordan, B Rubio, S Rice, Patrick Regan, William Gelletly, et al. Total absorption γ-ray spectroscopy of the β-delayed neutron emitters br 87, br 88, and rb 94. *Physical Review C*, 95(2):024320, 2017.

[89] Franco Camera and Adam Maj. *PARIS White Book*. Institute of Nuclear Physics Polish Academy of Sciences, 2021.

[90] H Geissel, G Munzenberg, and K Riisager. Secondary exotic nuclear beams. *Annual Review of Nuclear and Particle Science*, 45(1):163–203, 1995.

[91] Alex C Mueller and Bradley M Sherrill. Nuclei at the limits of particle stability. *Annual review of nuclear and particle science*, 43(1):529–583, 1993.

[92] HL Ravn, P Bricault, G Ciavola, P Drumm, B Fogelberg, E Hagebø, Marc Huyse, R Kirchner, W Mittig, A Mueller, et al. Comparison of radioactive ion-beam intensities produced by means of thick targets bombarded with neutrons, protons and heavy ions. *Nuclear Instruments and Methods in Physics Research Section B: Beam Interactions with Materials and Atoms*, 88(4):441–461, 1994.

[93] PT Hosmer, H Schatz, A Aprahamian, O Arndt, RRC Clement, A Estrade, K-L Kratz, SN Liddick, PF Mantica, WF Mueller, et al. Half-life of the doubly magic r-process nucleus ^{78}ni. *Physical review letters*, 94(11):112501, 2005.

[94] Yu Khazov, AA Rodionov, S Sakharov, and Balraj Singh. Nuclear data sheets for a= 132. *Nuclear Data Sheets*, 104(3):497–790, 2005.

[95] Otto R Frisch and John A Wheeler. The discovery of fission. *Physics Today*, 20(11):43–52, 1967.

[96] F Clapier, AC Mueller, J Obert, O Bajeat, M Ducourtieux, A Ferro, A Horbowa, L Kotfila, C Lau, H Lefort, et al. Exotic beams produced by fast neutrons. *Physical Review Special Topics-Accelerators and Beams*, 1(1):013501, 1998.

[97] C Lau, B Roussière, D Verney, O Bajeat, F Ibrahim, F Clapier, E Cottereau, C Donzaud, M Ducourtieux, S Essabaa, et al. Recent studies to improve release properties from thick isotope separator on-line fission targets. *Nuclear Instruments and Methods in Physics Research Section B: Beam Interactions with Materials and Atoms*, 204:246–250, 2003.

[98] F Ibrahim, J Obert, O Bajeat, JM Buhour, D Carminati, F Clapier, C Donzaud, M Ducourtieux, JM Dufour, S Essabaa, et al. Photofission for the production of radioactive beams: Experimental data from an on-line measurement. *The European Physical Journal A-Hadrons and Nuclei*, 15(3):357–360, 2002.

[99] F Ibrahim, D Verney, M Lebois, B Roussière, S Essabaa, S Franchoo, S Gales, D Guillemaud Mueller, C Lau, F Le Blanc, et al. The alto facility at ipn orsay and study of neutron rich nuclei in the vincinity of 78ni. *Nuclear Physics A*, 787(1-4):110–117, 2007.

[100] William T Diamond. A radioactive ion beam facility using photofission. *Nuclear Instruments and Methods in Physics Research Section A: Accelerators, Spectrometers, Detectors and Associated Equipment*, 432(2-3):471–482, 1999.

[101] Yu Ts Oganessian, SN Dmitriev, J Kliman, OA Maslov, G Ya Starodub, AG Belov, and SP Tretiakova. Rib production with photofission of uranium. *Nuclear Physics A*, 701(1-4):87–95, 2002.

[102] JT Caldwell, EJ Dowdy, BL Berman, RA Alvarez, and P Meyer. Giant resonance for the actinide nuclei: Photoneutron and photofission cross sections for u 235, u 236, u 238, and th 232. *Physical Review C*, 21(4):1215, 1980.

[103] E Jacobs, H Thierens, D De Frenne, A De Clercq, P D'hondt, P De Gelder, and AJ Deruytter. Product yields for the photofission of u 238 with 12-, 15-, 20-, 30-, and 70-mev bremsstrahlung. *Physical Review C*, 19(2):422, 1979.

[104] M Cheikh Mhamed, S Essabaa, C Lau, M Lebois, B Roussiere, M Ducourtieux, S Franchoo, D Guillemaud Mueller, F Ibrahim, JF LeDu, et al. Rib production by photofission in the framework of the alto project: First experimental measurements and monte-carlo simulations. *Nuclear Instruments and Methods in Physics Research Section B: Beam Interactions with Materials and Atoms*, 266(19-20):4092–4096, 2008.

[105] Julien Guillot, Brigitte Roussière, Sandrine Tusseau-Nenez, Denis S Grebenkov, and Maxime Ignacio. Influence of density and release properties of ucx targets on the fission product yields at alto. *Nuclear Instruments and Methods in Physics Research Section B: Beam Interactions with Materials and Atoms*, 468:1–7, 2020.

[106] B Roussière, F Ibrahim, J Sauvage, O Bajeat, N Barré, F Clapier, E Cottereau, C Donzaud, M Ducourtieux, S Essabaa, et al. Release properties of ucx and molten u targets. *Nuclear*

Instruments and Methods in Physics Research Section B: Beam Interactions with Materials and Atoms, 194(2):151–163, 2002.

[107] B Roussière, O Bajeat, N Barré, C Bourgeois, F Clapier, E Cottereau, C Donzaud, M Ducourtieux, S Essabaa, D Guillemaud-Mueller, et al. Release of kr, ag, sn, i and xe from ucx targets. *Nuclear Instruments and Methods in Physics Research Section B: Beam Interactions with Materials and Atoms*, 246(2):288–296, 2006.

[108] Julien Guillot and Brigitte Roussière. UC_x ISOL target, 2021.

[109] Karolina Kolos. *Probing the nuclear structure in the vicinity of 78Ni via beta decay spectroscopy of 84Ga*. PhD thesis, Université Paris Sud-Paris XI, 2012.

[110] Ulrich Köster. *Yields and spectroscopy of radioactive isotopes at LOHENGRIN and ISOLDE*. PhD thesis, Technical University ät München, 2000.

[111] F. Le Blanc. Resonant laser beam ionization (ris) at alto. `https://alto.ijclab.in2p3.fr/installation/alto-leb/rialto/`, 2021.

[112] Matthieu Lebois. Rapport d'activité pour la plateforme alto 2020. `https://www.in2p3.cnrs.fr/sites/institut_in2p3/files/page/2020-04/3-Doc-LEBOIS.pdf`, 2021.

[113] William P Jesse and John Sadauskis. Ionization by alpha particles in mixtures of gases. *Physical Review*, 100(6):1755, 1955.

[114] GS Hurst, MG Payne, SD Kramer, and JP Young. Resonance ionization spectroscopy and one-atom detection. *Reviews of Modern Physics*, 51(4):767, 1979.

[115] Harald Friedrich and H Friedrich. *Theoretical atomic physics*, volume 3. Springer, 2006.

[116] Alexandre A Radzig and Boris M Smirnov. *Reference data on atoms, molecules, and ions*, volume 31. Springer Science & Business Media, 2012.

[117] Benoît Tastet. *Structure des noyaux de gallium, de germanium et d'arsenic riches en neutrons autour de N= 50 et Développement d'une source d'ionisation laser à ALTO*. PhD thesis, Université Paris Sud-Paris XI, 2011.

[118] K Peräjärvi, UC Bergmann, VN Fedoseyev, A Joinet, U Köster, C Lau, J Lettry, H Ravn, M Santana-Leitner, Isolde Collaboration, et al. Studies of release properties of isolde targets. *Nuclear Instruments and Methods in Physics Research Section B: Beam Interactions with Materials and Atoms*, 204:272–277, 2003.

[119] Helge L Ravn and Brian W Allardyce. On-line mass separators. In *Treatise on heavy ion science*, pages 363–439. Springer, 1989.

[120] S Sundell, H Ravn, Isolde Collaboration, et al. Ion source with combined cathode and transfer line heating. *Nuclear Instruments and Methods in Physics Research Section B: Beam Interactions with Materials and Atoms*, 70(1-4):160–164, 1992.

[121] R Kirchner and E Roeckl. Investigation of gaseous discharge ion sources for isotope separation on-line. *Nuclear Instruments and Methods*, 133(2):187–204, 1976.

[122] Matthieu Lebois. *Structure des noyaux de Germanium et de Gallium riches en neutrons au-delà de N= 50 à ALTO*. PhD thesis, Université Paris Sud-Paris XI, 2008.

[123] Dmitry Testov. *Effect of shell closure N= 50 and N= 82 on the structure of very neutron-rich nuclei produced at ALTO: measurements of neutron emission probabilities and half lives of nuclei at astrophysical r-processes path*. PhD thesis, Université Paris Sud-Paris XI, 2014.

[124] P Paris, CF Liang, D Lecouturier, M Arianer, J Obert, A Caruette, A Ferro, J Fournet, JC Putaux, JL Sarrouy, et al. Description and performance of the isocele 2 separator. *Nuclear Instruments and Methods in Physics Research*, 186(1-2):91–98, 1981.

[125] Christophe Lau. *Etude de la production de faisceaux riches en neutrons par fission induite par neutrons rapides*. PhD thesis, Paris 7, 2000.

[126] Brookhaven national laboratory. Ensdf, national nuclear data center. https://www.nndc.bnl.gov/ensdf/, 2021.

[127] FH Garcia, C Andreoiu, GC Ball, A Bell, AB Garnsworthy, F Nowacki, CM Petrache, A Poves, K Whitmore, FA Ali, et al. Absence of low-energy shape coexistence in ge 80: The nonobservation of a proposed excited 0 2+ level at 639 kev. *Physical Review Letters*, 125(17):172501, 2020.

[128] PARIS collaboration. Paris collaboration website. http://paris.ifj.edu.pl/index.php?lng=en, 2021.

[129] FASTER project. Fast acquisition system for nuclear research (faster). http://faster.in2p3.fr/, 2021.

[130] M Lebois, N Jovančević, D Thisse, R Canavan, D Étasse, M Rudigier, and JN Wilson. The ν-ball γ-spectrometer. *Nuclear Instruments and Methods in Physics Research Section A: Accelerators, Spectrometers, Detectors and Associated Equipment*, 960:163580, 2020.

[131] Root developers. Data analysis framework. https://root.cern/, 2021.

[132] MT Haj-Heidari, MJ Safari, H Afarideh, and H Rouhi. Method for developing hpge detector model in monte carlo simulation codes. *Radiation Measurements*, 88:1–6, 2016.

[133] Radware team developers. Radware data analysis framework. https://radware.phy.ornl.gov/gf3/gf3.html, 2000.

[134] Geant4 collaboration. Geant4 simulation framework. https://geant4.web.cern.ch/, 2021.

[135] Huynh Dinh Chuong, Tran Thien Thanh, Vo Hoang Nguyen, Chau Van Tao, et al. Estimating thickness of the inner dead-layer of n-type hpge detector. *Applied Radiation and Isotopes*, 116:174–177, 2016.

[136] C Ghosh, V Nanal, RG Pillay, KV Anoop, N Dokania, Sanjoy Pal, MS Pose, G Mishra, PC Rout, Suresh Kumar, et al. Characterization of paris labr3 (ce)-nai (tl) phoswich detectors up to eγ 22 mev. *Journal of Instrumentation*, 11(05):P05023, 2016.

[137] SAINT-GOBAIN. Lanthanum bromide labr3(ce) eu sds. https://www.crystals.saint-gobain.com/document-center, 2014.

[138] M Ciemała, D Balabanski, M Csatlós, JM Daugas, G Georgiev, J Gulyás, M Kmiecik, A Krasznahorkay, S Lalkovski, A Lefebvre-Schuhl, et al. Measurements of high-energy γ-rays with labr3: Ce detectors. *Nuclear Instruments and Methods in Physics Research Section A: Accelerators, Spectrometers, Detectors and Associated Equipment*, 608(1):76–79, 2009.

[139] PARIS collaborators in Lyon group. PARIS Monte Carlo simulation procedure: SToGS, 2014.

[140] A Gottardo, D Verney, C Delafosse, F Ibrahim, B Roussière, C Sotty, S Roccia, C Andreoiu, C Costache, M-C Delattre, et al. First evidence of shape coexistence in the ni 78 region: Intruder 0 2+ state in ge 80. *Physical review letters*, 116(18):182501, 2016.

[141] B Cheal, J Billowes, ML Bissell, Klaus Blaum, FC Charlwood, KT Flanagan, DH Forest, S Fritzsche, Ch Geppert, A Jokinen, et al. Discovery of a long-lived low-lying isomeric state in ga 80. *Physical Review C*, 82(5):051302, 2010.

[142] P Hoff and B Fogelberg. Properties of strongly neutron-rich isotopes of germanium and arsenic. *Nuclear Physics A*, 368(2):210–236, 1981.

[143] K Siegl, K Kolos, ND Scielzo, A Aprahamian, G Savard, MT Burkey, MP Carpenter, P Chowdhury, JA Clark, P Copp, et al. β-decay half-lives of sb 134, 134 m and their isomeric yield ratio produced by the spontaneous fission of cf 252. *Physical Review C*, 98(5):054307, 2018.

[144] Balraj Singh. Nuclear data sheets for a= 80. *Nuclear data sheets*, 105(2):223–418, 2005.

[145] Dmitry Testov. *Effect of shell closure N=50 and N=82 on the structure of very neutron-rich nuclei produced at ALTO. Measurements of neutron emission probabilities and half lives of nuclei at astrophysical r-processes path.* PhD thesis, Université Paris-Saclay, France, 2014.

[146] Fay Ajzenberg-Selove. *Nuclear spectroscopy*, volume 9. Academic Press, 2013.

[147] P. Bevington and D.K. Robinson. *Data Reduction and Error Analysis for the Physical Sciences*. McGraw-Hill Education, 2003.

[148] Brookhaven national laboratory. logft, national nuclear data center. https://www.nndc.bnl.gov/logft/, 2021.

[149] E Matthias, E Recknagel, O Hashimoto, S Nagamiya, K Nakai, T Yamazaki, and Y Yamazaki. The g-factor measurement for the 8+ isomeric state of 86sr produced in kr gas. *Nuclear Physics A*, 237(1):182–188, 1975.

[150] Gregory James Farooq-Smith, AR Vernon, J Billowes, CL Binnersley, ML Bissell, Thomas Elias Cocolios, T Day Goodacre, RP De Groote, KT Flanagan, S Franchoo, et al. Probing the ga 31 ground-state properties in the region near z= 28 with high-resolution laser spectroscopy. *Physical Review C*, 96(4):044324, 2017.

[151] M.Girod S.Hilaire. Hartree-fock-bogoliubov results based on the gogny force. http://www-phynu.cea.fr/science_en_ligne/carte_potentiels_microscopiques/carte_potentiel_nucleaire_eng.htm, 2021.

[152] Meng Wang, G Audi, FG Kondev, WJ Huang, S Naimi, and Xing Xu. The ame2016 atomic mass evaluation (ii). tables, graphs and references. *Chinese Physics C*, 41(3):030003, 2017.

[153] H Iwasaki, S Michimasa, M Niikura, M Tamaki, N Aoi, H Sakurai, S Shimoura, S Takeuchi, S Ota, M Honma, et al. Persistence of the n= 50 shell closure in the neutron-rich isotope ge 80. *Physical Review C*, 78(2):021304, 2008.

[154] Ren Li. *First attempt toward a quasi-Pandemonium free β-delayed spectroscopy of ^{80}Ge using PARIS at ALTO*. PhD thesis, Université Paris-Saclay, France, 2022.

[155] Lama Ai-Ayoubi, Iolanda Matea Macovei, and David Verney. private communication 2021.

[156] E Padilla-Rodal, A Galindo-Uribarri, C Baktash, JC Batchelder, JR Beene, R Bijker, BA Brown, O Castanos, B Fuentes, J Gomez del Campo, et al. B (e 2)↑ measurements for radioactive neutron-rich ge isotopes: Reaching the n= 50 closed shell. *Physical review letters*, 94(12):122501, 2005.

[157] Shuichiro Ebata, Takashi Nakatsukasa, and Tsunenori Inakura. Systematic investigation of low-lying dipole modes using the canonical-basis time-dependent hartree-fock-bogoliubov theory. *Physical Review C*, 90(2):024303, 2014.

[158] D Adhikari, H Albataineh, D Androic, K Aniol, DS Armstrong, T Averett, C Ayerbe Gayoso, S Barcus, V Bellini, RS Beminiwattha, et al. Accurate determination of the neutron skin thickness of pb 208 through parity-violation in electron scattering. *Physical Review Letters*, 126(17):172502, 2021.